Universidade Técnica de Lisboa
Instituto Superior Técnico

Design, optimization and integration of magnetoresistive biochips

Filipe Arroyo Cardoso

(Licenciado)

Dissertação para a obtenção do Grau de Doutor em Engenharia Física Tecnológica

Orientador : Doutor Paulo Jorge Peixeiro de Freitas

Co-Orientador : Doutor Moisés Piedade

Júri

Presidente : Presidente do Conselho Científico do IST
Vogais : Doutor Paul Galvin
Doutor Mikkel Fougt Hansen
Doutor Moisés Simões Piedade
Doutor Paulo Jorge Peixeiro de Freitas
Doutor Susana Isabel Pinheiro Cardoso de Freitas

January 2010

Universidade Técnica de Lisboa
Instituto Superior Técnico

Design, optimization and integration of magnetoresistive biochips

Filipe Arroyo Cardoso

(Licenciado)

Dissertação para a obtenção do Grau de Doutor em Engenharia Física Tecnológica

Orientador : Doutor Paulo Jorge Peixeiro de Freitas

Co-Orientador : Doutor Moisés Piedade

Júri

Presidente : Presidente do Conselho Científico do IST
Vogais : Doutor Paul Galvin
Doutor Mikkel Fougt Hansen
Doutor Moisés Simões Piedade
Doutor Paulo Jorge Peixeiro de Freitas
Doutor Susana Isabel Pinheiro Cardoso de Freitas

January 2010

Resumo

Biochips baseados em sensores magnetorestivos foram introduzido há uma década atrás no desenvolvimento de sistemas de detecção envolvendo reconhecimento biomolecular. Estes sistemas baseiam-se na utilização de sondas biológicas immobilizadas à superfície do chip que detectam moléculas alvo marcadas magneticamente. A detecção dos marcadores magnéticos é conseguida através de sensores magnetoresistivos. Entretanto, desde há alguns anos atrás, um grande investimento na construção de plataformas integradas com base neste tecnologia tem sido realizado. É esperado que estas plataformas apresentem simultâneamente uma elevada sensibilidade, sejam económicas, de fácil utilização e portáteis, integrando-se no tipo de dispositivos lab-on-a-chip. Nesta tese, dois tipos diferentes de sensores magnetoresistivos, válvulas de spin e junções de efeito tunel de spin são optimizados, desenhados e fabricados, tendo como objectivo o desenvolvimento de biochips. Estes biochips são depois integrados numa plataforma electrónica portátil a qual realiza o controlo e a aquisição de sinal dos sensores. Um sistema microfluídico é também integrado para melhorar a reprodutibilidade e a rapidez de resposta em sistemas de análise biológica. O limite de detecção da plataforma desenvolvida é determinado e posteriormente melhorado através de uma estratégia de concentração magnética, a qual é usada para atrair as moléculas de ADN alvo para as zonas sensíveis.

Em paralelo, uma arquitectura de biochip baeada numa matriz de sensores é desenvolvida por forma a aumentar consideravelmente o número de unidades sensíveis, mantendo as pequenas dimensões do chip. Estes biochips são depois optimizados e caracterizados em termos da relação sinal-ruído.

Finalmente, biochips magnetoresistivos são integrados em sistemas tipo lab-on-a-chip incluindo módulos de extração e amplicicação de ADN por PCR. Dado o sistema de PCR utilizado basear-se na tecnologia de EWOD para o transporte da amostra fluidica, o biochip é especificamente desenhado e fabricado para este efeito.

Os dispositivos desenvolvidos provaram possibilitar uma detecção competitiva de moléculas de ADN alvo em diferentes aplicações biológicas.

PALAVRAS-CHAVE : Biochips magnetoresistivos, Válvulas de spin, Junções de efeito tunel de Spin, Partículas magnéticas, microarrays de ADN

Abstract

Magnetoresistive-based biochips were introduced one decade ago to perform biomolecular recognition assays. These assays use biological probes immobilized on the chip surface to detect a magnetically labeled target biomolecule. The detection of the magnetic label fringe field is accomplished by a magnetoresistive sensor. Meanwhile, in the past few years, a great effort has been made for building up fully integrated platforms based on this technology. Such platforms are expected to be simultaneously highly sensitive, inexpensive, user-friendly and portable; type lab-on-a-chip devices. In this thesis, two different types of magnetoresistive sensors, spin valves and magnetic tunnel junctions, are optimized, designed and fabricated aiming at biochip development. These biochips are further integrated into a portable electronic platform which performs the control and acquisition of the sensor signal. A microfluidic system is also integrated to improve reproducibility and rapidness of the biological analysis. The limit of detection of the developed platform is determined and further improved by a magnetic focusing strategy, which drives the DNA targets to the sensing area.

In parallel, a matrix-based biochip architecture is developed in order to highly increase the number of sensing sites while maintaining the overall chip dimensions. Matrix-based biochips are further optimized and characterized in terms of signal-to-noise ratio.

Finally, magnetoresistive biochips are integrated in a lab-on-a-chip system including both DNA extraction and polymerase chain reaction (PCR) modules. As the PCR chip uses electrowetting on dielectric (EWOD) technology for moving the fluidic sample, a magnetoresistive biochip is specifically designed and fabricated for this purpose.

The developed devices have proved to enable a competitive detection of DNA target molecules in different biological applications.

KEY-WORDS : Magnetoresistive biochips, Spin valves, Magnetic Tunnel Junctions, Integration, Magnetic particles, DNA microarrays.

Acknowledgements

The work presented in this thesis is a very multidisciplinary work and because of that it would have been impossible to perform it without being included in a team. This team comprised people of different skills and personality. During all these years of PhD, my scientific skills and knowledge have evolved. But at least as important (if not even more important) than my scientific evolution was my character and personality evolution. For all of this, I will be forever grateful to the team I worked with and also to a group of friends and family who always accompanied me along the past few years!

I would like first to specially thank Prof. Paulo Freitas for accepting me in his research group few years before I start thinking in doing a PhD. It was his leadership and the people in his team who motivated me to start this PhD. His scientific supervision and teacher capacities were very important for me specially in the beginning of my PhD. More than the scientific background, he also taught me important issues like resource management, working with other people, projects elaboration and concretization by giving me the possibility to work in challenging national and European projects.

I thank also my co-supervisor, Prof. Moisés Piedade, for all the productive discussions and everything he taught me about electronics, noise and RF measurements.

There was a group of people with whom I directly worked since I arrived at INESC-MN and to which I am very grateful. The first person was Dr. Hugo Ferreira who taught me everything about biochips sensors and architecture and with whom I had very fruitful discussions about the work to be done. He was also the person who motivated me to start this PhD. The work I performed would have been impossible if I did not have two more people working closely with me. The first person is Dr. Verónica Martins who worked in the integration of biology to the biochip: surface chemistry. I want to thank her a lot for everything that she taught me about biology, chemistry and biological experiments planning and realization, for all the fruitful discussions that we had (and still have) and for the complementary work that we had. The second person of the team was José Germano who was responsible for developing the measurement system electronics. I want to thank him for everything that he taught me about electronics and mechanics and for all the fruitful discussions about the best way of integrating the biochip into the electronics. Finally at the end of my PhD, another person joined our team. This person was Dr. Sofia Martins and I want to thank her for all the discussions we had about antibodies and PCR experiments and for everything she taught me in about these and other biological subjects. The experience of working in such a team will stay for long time in my mind.

This team was not the only team I worked with. Another very important team for this work was the one I call the "magnetoresistive sensor team". This team comprised several people who always helped me in the sensor design, optimization and fabrication. The most important people for me were Dr. Susana Freitas and Dr. Ricardo Ferreira. Susana taught me a lot about magnetoresistive sensors deposition by ion beam and ion beam system functioning. Together with Ricardo she helped me a lot in the optimization AlOx and MgO barrier magnetic tunnel

junctions and in the deposition of spin valves. I had with both of them very fruitful discussions about magnetoresistive sensors and ways of linearization of the sensors. I am also very grateful to Ricardo for everything that he taught me about the different measurement systems (VSM, transfer curve measurement system, noise measurement system...) available at INESC-MN. Along all these years, this team comprised more people who I want also to thank. These people are Beatrice Negulescu, Piotr Wisniowski and José Almeida.

Part of my work used thin film diodes for matrix-based biochips. This work have not been possible without the great help and knowledge of Prof. João Pedro Conde and Dr. Virginia Chu. I want to thank both of them for all the discussions we had about the diodes fabrication and the diode physics itself and to be always available for discussing ideas and results. I want also to thank Prof. João Pedro Conde for all the time spent in the deposition of diodes.

This work would be impossible if there were not a group of 4 people working at INESC-MN. The first 3 people are the clean room technician José Bernardo, Fernando Silva and Virginia Soares. Their work was very important to maintain the good clean room condition for microfabrication processes. The fourth person is INESC-MN secretary Natércia Correia who was very important for all the administrative work (orders, flight booking, conference inscription, hotel booking...).

Part of this work was achieved in the framework of the European project SNIP2CHIP (NMP4-CT-2005-016833). I want first to thank everyone involved, and in special the responsible of the project Dr. Paul Galvin for the fruitful work that was developed during 3 years. I want also to thank Des Brennan, Luka Clarke and Dorothee Jary with whom I worked more closely for the project. I learned a lot of things relating to integration of different platforms with them.

Beside the people I already talked about there are a group of people which work may be directly, indirectly or not related to mine but with whom I had several discussions. I want to thank all these people for their companionship and because they made me open my mind (by asking me things or by discussing their work) to other subjects which may not be directly related to my work. This reflects a lot of knowledge that I acquired and is not directly reflected in this thesis. This group includes the following people: Teresa Adrega, Ricardo Cabeça, Francisco Delgado, Rui Chaves, Marco Donolato, Riccardo Bertacco, André Guedes, Dina Gonçalves, Diana Leitão, Milene Santos, Ana Teresa Pereira, Joana Loureiro, Marco Mercier, Maria João Almeida, Inês Perdigão, Pedro Novo, José Amaral, António Sousa, Patrícia Rosa, Tomás Dias. Beside being initially being colleagues most of these people are now friends of mine as well. There is another person included in this group that I want to specially thank since she is since long time a very good friend. Her name is Rita Macedo.

And now I am entering in another group of people which do not have anything to do with my PhD work but were very important during this period: my friends. This group can be subdivided in 4 different groups: friends from IST, friends from Scouts, friends from SA and friends from high school. The first subgroup is large and I cannot enumerate all the names. Anyway I want to thank all of them for their friendship which was maintained even if we are not working at the same place. The second group of friends include people I met when I was in the Scouts. In this group I have my oldest friends. The friends from SA are the ones with

whom I passed most of my free time in the past 3 years. For them a BIG thank you for every single things we did together (specially to Kim Lembeck, Marta Pizzighella, Fabio Silva and José Lorga). Finally, my oldest and smaller group of friends from high school. From this group I want to thank in special Miguel Neto and João Almeida who are still very good friends!

Left for the end but not the least important are my family: Francine Arroyo (my mother), Adelino Cardoso (my father) and David Cardoso (my brother). Although I was living in the same flat, I did not spend so much time with them during this PhD period. Nevertheless, they always supported me and were always on my side in the most difficult moments (specially the ones where I needed surgery). They were always interested in what I was doing even though they would not understand all the details. To them a BIG BIG thank you for everything!

Finally, the financial support that I had during all these years was also important to develop and show this work to the scientific community. Therefore, I start by thanking the Portuguese Foundation for Science and Technology (FCT) who supported me financially during 4 years through the scholarship SFRH/BD/23756/2005. I also would like to thank Prof. Paulo Freitas and INESC-Microsystems and Nanotechnologies for their continuous support in providing me laboratory conditions (measuring equipment, clean room facilities for devices fabrication and all consumable materials like magnetic particles, DNA, targets for deposition systems...), financial support for a summer course, many conferences and meetings I participate in and also for the financial support of 4 months gave for writing my thesis.

Thesis structure

This thesis describes the design and optimization of two types of magnetoresistive sensors (Spin Valve - SV and Magnetic Tunnel Junction - MTJ) for the specific biochip application. Further integration of these sensors with electronics, microfluidics and detection of biological samples are also depicted. In the whole thesis, the cgs unit system was chosen.

Chapter 1 is a short introduction to biosensors in general and more specifically DNA biosensors which is the main application for the biochips designed in this thesis. A more specific but still general introduction o magnetoresistive biosensors is further performed. This is only a general introduction since more specific introductions are made in each chapter of this thesis.

Chapter 2 describes in general the tools used in a microfabrication processes and depicts two different microfabrication processes step by step. The fabrications processes used in this thesis are based on already optimized process. However, since most of them involve integration of different technologies, some steps had to be optimized by me. On a second part, the equipment and setups used in the different measurements perform throughout the thesis are depicted. Except of some small variation in some of the setups for biochip experiments, most os these setups were mounted by other people than myself.

Chapter 3 is an analysis of magnetic nanoparticles characteristics (magnetization, susceptibility...) available in the market. The goal is to choose which magnetic particles are more suitable for DNA labeling. All the magnetic characteristics of the particles were measured and analyzed using INESC-MN equipment. Simulations were further performed to determine the average magnetic field generated by magnetic particles over a 200 μm^2 sensor. All the measurements, analysis and simulations showed in this chapter were performed by myself.

Chapter 4 is a long chapter describing the different aspects of the design and optimization of magnetoresistive sensors to obtain the maximum magnetic particle signal to noise ratio as function of the specificity of the desired bioassay. The chapter starts with an introduction on how the sensors should be designed as function of the application. Then, a simple model for the determination of magnetoresistive sensors linearity conditions is described and confirmed by experimental results with MTJs sensors. The influence of the sensor magnetic layers on the positioning of the magnetic particles on top of the sensor is further studied both theoretically and experimentally. Different measurement architectures were also depicted analyzed. After this, the two magnetic sensors used in this thesis (SV and MTJ) are introduced and their theoretical signal to noise ratio studied. In both cases, a chip design is presented and magnetic nanoparticles detection using these chips is shown and compared to simulations. Finally, the two sensors are compared in terms of magnetic particles sensitivity. In this chapter, all the design, chip fabrication experiments and simulations were performed by me with the exception of the

model for the determination of sensor linearity study which was performed in collaboration with a master degree student and the electronic platform used for the sensors comparison which was designed by a PhD study from INESC-ID in a collaboration with me.

Chapter 5 describes the 3 main integrations performed during this PhD. The first one depicts a way of increase the number of sensors in a chip without increasing the size of the chip nor the number of contacts. This system needs the incorporation of thin film diodes in series with a MTJ sensor. The noise of this device is also studied. All the design, microfabrication process optimization, microfabrication, and measurements were performed by myself. The only exception is the diode depositions which was performed by Prof. J.P. Conde. The second part integrates the magnetoresistive biochips with a microfluidic platform, surface chemistry and a measuring electronic platform. This work was performed in collaboration with two groups INESC-ID, for the electronic development, and BERG, for the surface chemistry optimization. Except from these two parts of the integrated platform which I only participated in experiments planing, I performed all the remaining integration. Finally, the integration of the magnetoresistive biochip with a standard fluidic channel and a EWOD fluidic system was developed in the framework of an European Project. The biochip design and process optimization for EWOD compatibility was performed by myself.

Chapter 6 depicts the surface chemistry optimization performed for DNA probe immobilization on gold surfaces and DNA hybridization preventing magnetic particles and DNA adsorption to the chip surface. Then, this protocol was used for limit of detection determination and improvement with the microfabricated biochips. I designed the sensors used, helped in the sensors microfabrication and performed the measurements and data analysis. The optimization of the surface chemistry was performed by my colleague from BERG and I participated in the experiments planning and some data analysis.

Chapter 7 is a general conclusion of this thesis showing the future perspectives of this work.

Contents

List of Figures

List of Tables

Chapter 1

Introduction

In the last century, the development of new technologies improved in several manners our way of living. From the improvement in telecommunication (telephone, mobile phone, internet...) to the increase in mobility (cars, airplane...) several aspect in our lives were improved in only one century.

One of the greatest advances of the XX^{th} century was the health care, which enabled us to live longer and better. Besides a better understanding of the human body working mechanism, a panoply of engines were fabricated in order to enable the prognostic, diagnostic and treatment of several diseases. Nowadays, these machines are mostly large and specialized personnel is needed to operate them.

The increasing research in nanotechnologies is permitting the development of more sensitive, faster, smaller and more user friendly diagnostics equipments. The sensitivity and rapidity of these equipments are important factors since a premature and fast diagnostic in most of the cases can be determinant in saving lives. Moreover, smaller and more user friendly equipment enables the diagnostic to be performed anywhere by a non-specialized person.

The portability of bioanalytical devices is enlarging the scope of diagnostic equipment to other applications related to public health. Food quality management, environmental monitoring, bioterrorism and controlling of epidemic diseases are some of the areas requiring portable and user-friendly detection systems. As an example, *in-situ* monitoring of toxins in meat or bacteria in water are very important diagnostics for public health. In the same way, several devices for flu and drugs/biohazard detection have been introduced in airports around the world.

However, most of the equipment available in the market for this kind of diagnostics are still limited in at least one of the fundamental requirements: sensitivity, portability, cost, rapidness and user-friendliness. In order to fulfill these four requirements, several biosensors are being integrated. An overview of the most important biosensor technologies developed so far are now described. Then magnetoresistive devices as a particle type of biosensors are introduced and discussed.

1.1 Biosensors

Biosensors are used to detect a specific interaction between two biological entities with affinity to each other. This phenomenon is called biomolecular recognition and its detection has been playing an important role in the DNA hybridization and antibody-antigen based-systems. These systems are the basis of applications such as genetic disease diagnostic, mutation detection, gene expression quantification, microorganism detection and biological warfare agent detection.

A typical biochip is composed by a biological-sensing system (bioreceptor), a transducer and an output system. The bioreceptor is a biological probe typically immobilized on the biochip surface. Through microspotting, an array of several different probes can be achieved and the whole chip is called a microarray. For example, DNA microarrays with thousands of probes can be used for the study of different genes expressions. The biomolecular recognition of the probes with an unknown target sample generates a physical or chemical changes that can be converted to an electrical signal by the transducer. In the case of DNA microarrays, the target molecules are commonly labeled by a fluorophore which fluorescence is detected by a fluorescence scanner. Finally, the electrical signals are further treated (amplified, filtered...) in order to retrieve an understandable analysis of the experiments. In DNA microarrays, this treatment is accomplished in a computer where several algorithm are used for image analysis and interpretation of the results.

A typical biomolecular recognition detection experiments need four different steps (figure 1.2):

1. Probe immobilization on the chip surface
2. Target labeling
3. Target recognition and washing
4. Signal detection

After the probes immobilization by microspotting, an unknown target sample is put in contact with the chip surface. This target sample is typically a genomic DNA which specific genes have been amplified using a polymerase chain reaction (PCR) technique [3]. The amplified DNA strands are labeled with fluorophores. After hybridization a washing step is achieved in order remove all the non-hybridized DNA strands. The stringency control of this washing step is crucial in order to avoid false negative and positive results. Finally, the chip is introduced into a fluorescence scanner which detects the light emitted by the labels.

The first microarray system using this detection technique was introduced in the market by Affymetrix, Inc. (Santa Calra, CA) [1]-[2]. These arrays include thousands of microscopic spots containing picomoles of a specific DNA probe sequence. These spots are defined by photolithography. The probes are then hybridized to target DNA or RNA sequences previously labeled by a fluorophore. The abundance of hybridized DNA is then determined by scanning the chip with a fluorescence scanner and analyzing the images and results using a specific software.

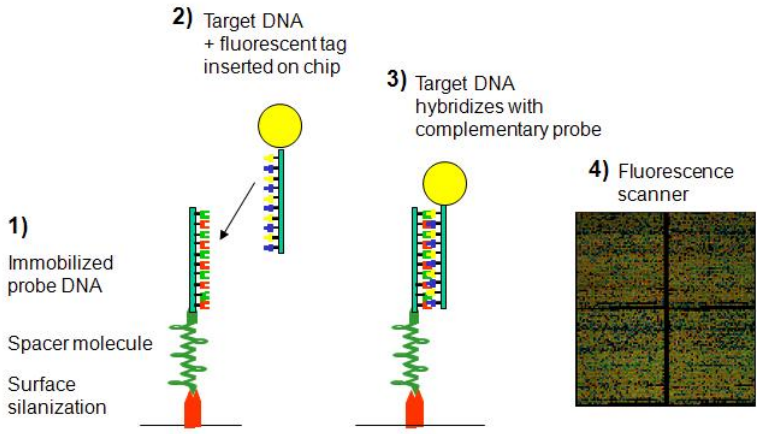

Figure 1.1: Biomolecular traget-probe hybridization detection (DNA specific case) using fluorescent labels attached to the biological targets. 1) The probe biomolecules are immobilized on the surface; 2) the labeled target biomolecules are put into contact with the probes; 3) Complementary targets hybridize to the probe; 4) An external laser-based fluorescence scanner is used for detection.

These arrays have been used in applications related to genes and gene mutations detection and gene expression determination

Since this first product, several other companies have been commercializing DNA microarrays based on fluorescence detection. An example of these devices is the Nanogen (www.nanogen.com) DNA chip incorporating an array of electrodes generating electric fields for probe arraying. The detection system includes a DNA chip cartridge with hundreds of electronically addressed probes sites, a cartridge loader and an external fluorescence scanner for detection of fluorophores. A software is provided for experiment control and data analysis. The electric fields are used to bring first probes and then target DNA strands to specific locations on the chip avoiding conventional microspotting. They can also be used to enhance the hybridization and to control the stringency of the washing step.

However, these fluorescence based systems suffer from some weaknesses. The first one is directly related to the label since its fluorescence emission is gradually reduced along the time. This phenomenon is called photo-bleaching. Moreover, some applications require higher dynamic range and sensitivity, portability, rapidity and need to be inexpensive. Since these systems are still bulky and expensive and have limited dynamic range and sensitivity due to nature of the detection principles, other devices and detection techniques have been developed.

In order to improve portability and rapidity, the integration of fluorescence-based systems have been pursued. One example is the incorporation of photodetectors (Si, amorphous Si or III-V based) in chips to detect the light emission of fluorophores [4]. Since fluorescent labels need to be optically excited, semiconductor lasers are also being integrated in the chip.

In the some biological recognition processes electron transfer phenomenon occur upon the interaction of target and probe molecules. To take advantage of this fact electrochemical detection chips are designed to capture the transferred electron enabling the detection of

biomolecular recognition. One example is the *eSensor* developed by Motorola Life Sciences (www.motorola.com). The main advantages of this system are: the target molecules do not need to be labeled and the easiness of integration.

Other physical principles are being used to avoid the photo-bleaching limitation of fluorescent labels. An approach based on Micro Electro Mechanical Systems (MEMS) have been investigate for the detection of free-labeled biological entities. These devices comprise cantilever or bridges which resonance frequency [5] or deflection [6] can be monitored. These two characteristics change with the increase of mass occurring when a target molecule interacts with an immobilized probe molecule.

Many other approaches involving different detection principles have been investigated in the past decade. This thesis is concerned with an approach involving the use of magnetoresistive sensors to detect biomolecular recognition.

1.2 Magnetoresistive Biosensors

Magnetoresistive-based biochip were introduced in 1998 by Baselt [7]. In this approach, fluorescent labels are replaced by magnetic labels. These labels are typically superparamagnetic or paramagnetic particles. The use of these kind of labels enables to overcome some limitations of the fluorescence detection such as photo-bleaching and background signal since most of biological entities are non-magnetic. The magnetic particles are covered typically with streptavidin. This protein has a high affinity to biotin. Therefore, a biotin molecule is attached the target biomolecule by a biotinylation process and the labeling is made by streptavidin-biotin interaction. The use of magnetic labels allows also the use of magnetic forces for stringency control and for focusing the biological target to the sensor area. The biomolecular recognition detection experiments steps are the same as for fluorescence detection except that magnetic labels and an integrated, highly sensitive magnetoresistive sensor are used instead of fluorophores and fluorescence scanning, respectively (figure 1.2). Magnetically labeled target molecules are put into contact to the chip surface where biomolecular probes have previously been immobilized. If the target and probe biomolecules are complementary, after a washing step the magnetic particles still remain attached to the surface. Upon magnetization by an external magnetic field, the markers generate fringe fields, which are detected by magnetoresistive sensors.

Magnetoresistive sensors are characterized by high sensitivity to measure small changes in magnetic fields. Currently these sensors are well established in the marketplace covering a diverse number of commercial applications, such as memory devices, automotive sensing equipment, navigation systems and earth field correction tools. More recently its application to the detection of biological events has been proved for the following sensors: giant magnetoresistive (GMR) multilayer sensor [7][8] [9], spin valve sensor [10] [12], planar Hall effect sensor [13] or magnetic tunnel junction sensor [14].

In the past few years, several groups have been integrating these sensors in fully controllable biochip platforms including control and acquisition electronics and microfluidics systems for sample handling [15] [16] [17]. A typical biochip-platform comprises five main components: the

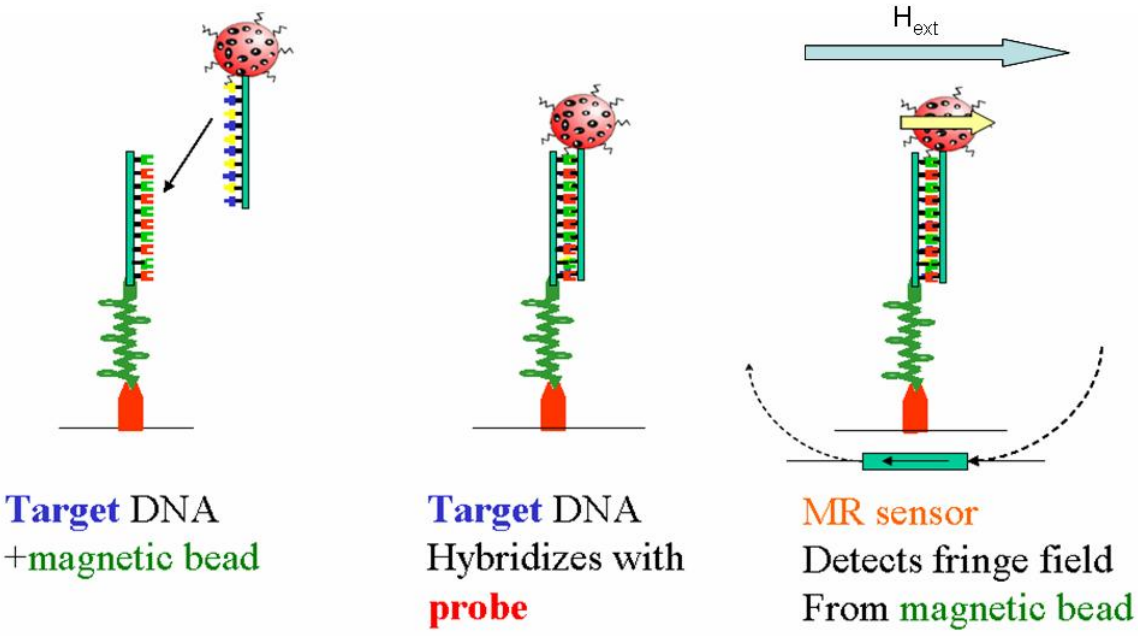

Figure 1.2: Biomolecular traget-probe hybridization detection (DNA specific case) using magnetic labels attached to the biological targets. The probe biomolecules are immobilized on the surface. Then the labeled target biomolecules are put into contact with the probes. Complementary targets further hybridize to the probes. Finally an external magnetic field is applied to magnetize the labels and therefore creating a fringe field detected by a magnetoresistive sensor.

sensing chip including the transducing elements, the magnetic particles as reporter system, the biological active interface with the biorecognition probes, the electronic circuitry for system control and transducer read-out, and also the fluidic transportation system. Each one of these five components presents their own specific difficulties towards its optimization and adaptation to a new application. However, some of the harder obstacles may be found at the interfaces between these different components upon the attempt of its fully integration.

This thesis presents a contribution toward a fully integrated device with improved sensitivity, portability, rapidity and user-friendliness. After a brief introduction of the experimental methods used along this thesis and a study of different magnetic labels, the design and optimization of two magnetoresistive sensor types (i.e. magnetic tunnel junction and spin valve sensors) are discussed for biochip applications. The integration of these sensors in a matrix-based architecture was further investigated in order to increase the number of sensing sites in a biochip. This increase gives the possibility of testing up to 256 different probes in the same chip. Furthermore, a biochip was also designed to be integrated in a portable platform including a microfluidic channel to improve the bioassay reproducibility. A step toward a lab-on-a-chip platform was also achieved by integrating magnetoresistive sensor with an on-chip PCR device in the scope of an European collaboration. Finally, after optimization of probe immobilization and target hybridization, the DNA limit of detection of the fabricated biochip was determined and improved by means of focusing the target molecules to the sensor sites.

Chapter 2

Experimental Methods

2.1 Microfabrication

The microfabrication of the devices used along this thesis is achieved by combining photolitography, etching and lift-off techniques. As the dimensions of the microfabricated structures are small when compared to some dust grains, bacteria and other impurities present in the atmosphere, the devices have to be fabricated in a controlled and dust-free environment. Consequently, all the process steps of the devices were done at INESC-MN's clean-room facilities (figure 2.1). This clean-room has two areas classified as class 100 and class 10, referring to the maximum number of dust particles larger than 1 μm per cubic feet of air in that region. There is also an adjoining area to the clean room called the grey area (class 10000).

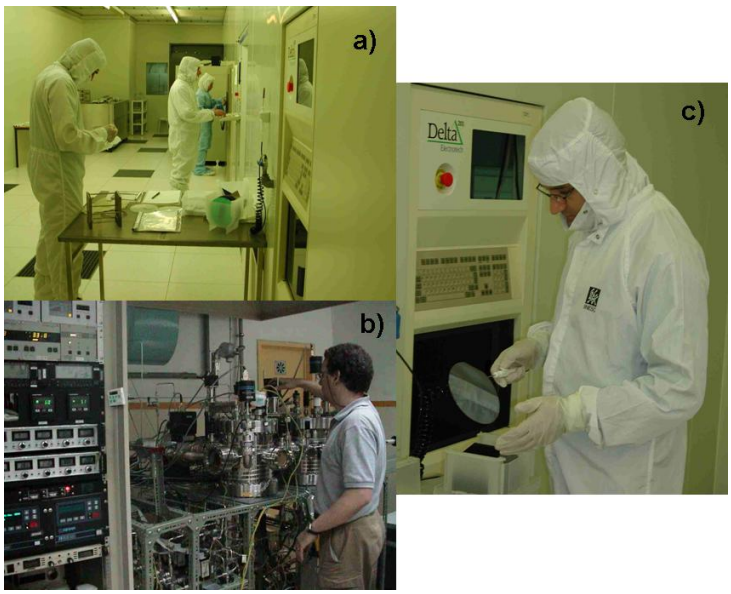

Figure 2.1: Clean-room facilities: a) clean-room class 100 b)grey area class 10000, PE-CVD machine (used for a-Si:H deposition) c) detail on clean-room garments

2.1.1 Photolithography

The goal of this procedure is to define a mask with the desired shape into a photosensitive material called photoresist (PR). To achieve this, three steps are required:

- **Coating -** Before the coating itself, the sample suffer a pretreatment in order to promote the PR adhesion. This pretreatment is made in the Vapor Prime machine and consist in the deposition of an organic compound (HDMS, Hexamethyldisilane,$C_6H_18Si_2$) under a temperature of 130°C and in vacuum. All the processes in this thesis used a positive PR (PFR 7790G 27cP, JSR Electronics) composed by a polymer, a sensitizer and a casting solvent. The spin coating is made in a Silicon Valley Group (SVG) coating system at a rotation speed of 3200 rpm during 30 seconds. For these conditions the PR has a final thickness of 1.5 μm. After the spin-coating, the PR is soft-backed at 85°C during 1 minute to remove solvents and stress while promoting adhesion.

- **Exposure -** The PR layer is exposed by a 422nm direct-write laser (DWL 2.0, Heidelberg Instruments) as defined in a mask. The system is able to resolve structures with dimension down to 0.8 μm. The mask is designed in a CAD drawing software and then converted into a laser machine language. The exposure weakens the polymer chains enabling its development.

- **Development -** Before development, the sample is baked at 110°C during 1 minute to stop uncompleted PR reactions. Then, a suitable developer (JSR Micro PTH70EG) is used to remove the exposed PR (in the case of positive PR). After 1 minute of development, the sample is washed with deionized water and dried by high speed spinning. The development is made in a SVG developing system.

2.1.2 Etch

The etching process consists in the removal of unprotected material. After patterning the PR by photolithography (figure 2.2 a)), the sample is submitted to an etching step removing all the unprotected material (figure 2.2 b)). The PR is then removed in a resist strip solution leaving only the patterned thin film. There are several methods of etching that can be used. In this thesis three main techniques were used: ion milling, reactive ion etch (RIE) and wet etch.

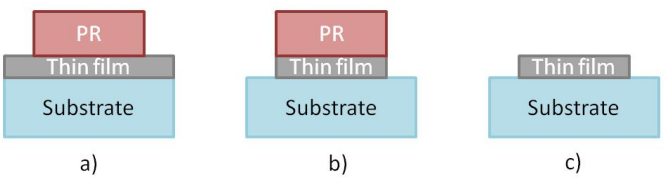

Figure 2.2: Etching process: a) patterning of the PR by photolithography b) etching of the non-protected thin film layer c) removal of the PR

Ion milling

This etching technique consists on a high energy Ar ions bombardment of the sample. The material on the sample is removed by physical impact of the Ar ions. The assist guns of the Ion Beam Deposition (IBD) systems Nordiko 3000 and Nordiko 3600 are used to perform ion milling etching. In both cases, the assist gun is set at an angle of 70° or 40° relatively to the sample surface (figures 2.3 and 2.4). In the first case, the beam is almost perpendicular to the sample and a redeposition of the etched material may occur. In critical cases where no material should be redeposited in the sample, an etching angle of 40° is used. In this configuration, the borders of the material protected by the PR ends up with a profile as shown in figure 2.4 b). In the two IBD machines at INESC-MN the etching rate of ion milling is ≈1 Å/s.

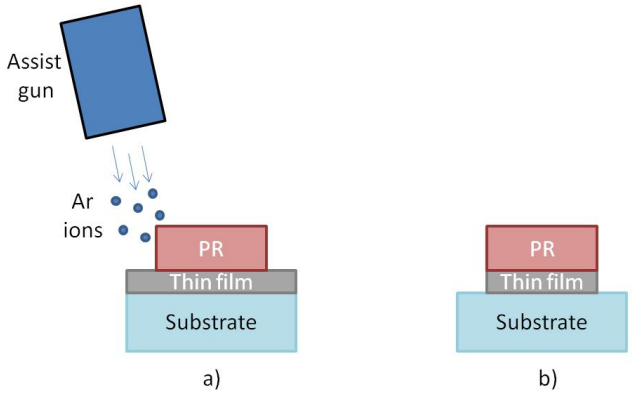

Figure 2.3: Ion milling: a) the sample is bombarded almost perpendicularly (70°) by an Ar plasma beam. b) the unprotected thin film was removed.

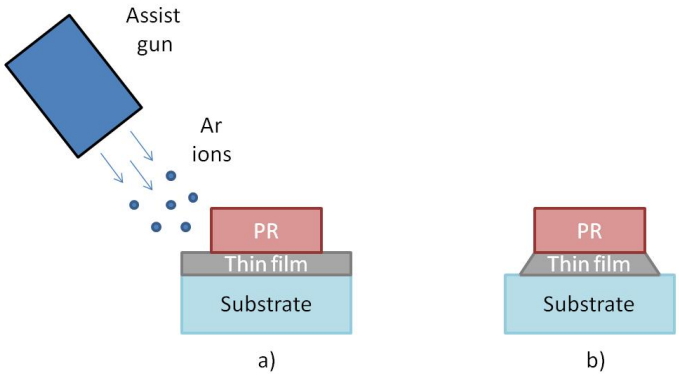

Figure 2.4: Ion milling: a) the sample is bombarded at an angle of 40° by an Ar plasma beam. b) the unprotected thin film was removed.

Reactive ion etching

The reactive ion etching (RIE) is a technique combining physical and chemical etching (figure 2.5). A plasma of CF_4, Ar and O_2 is used for selectively and anisotropically remove SiO_2, n^+-a-Si:H, p^+-a-Si:H or i-a-Si:H. This technique is performed in a LAM Rainbow 440 system.

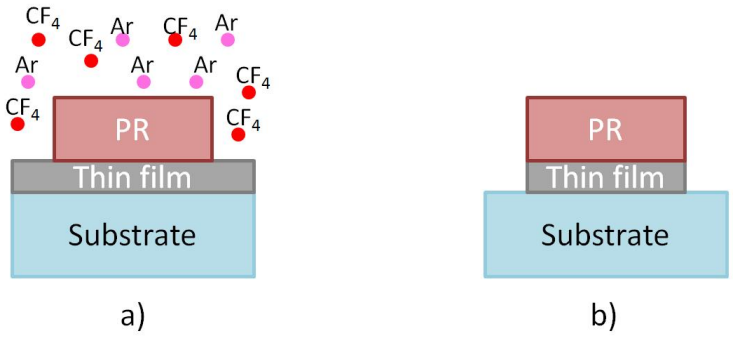

Figure 2.5: Reactive ion etching: a) the sample is etched by a plasma containing CF_4, Ar and O_2. b) the unprotected thin film was removed specifically and isotropicaly.

Wet etch

Wet etch is a technique that uses a chemical solution for material removal. The chemical solution used in this work was prepared for etching selectively an Al thin film (Aluminum etchant: solution phosphoric, nitric and acetic acid). This etching is isotropic meaning that the same amount of material is removed in all directions. Thus, the protected thin film shows a profile as depicted in figure 2.6. The etching rate at 21°C is 11 Å/s.

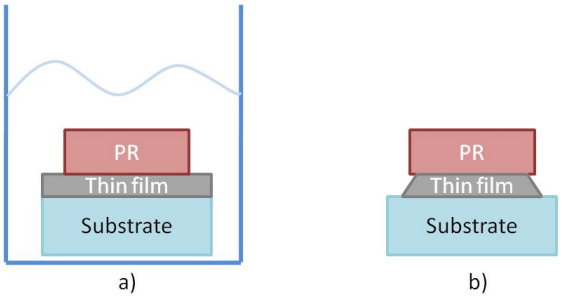

Figure 2.6: Wet etch: a) the sample is emerged in a etchant solution. b) the unprotected thin film was removed specifically and anisotropically.

2.1.3 Liftoff

Alternatively to the etching, a liftoff process can be used to pattern a thin film. As shown in figure 2.7, before the deposition of the thin film, a PR layer is patterned by photolithography.

Then, the thin film is deposited on top of it. Finally, the PR is dissolve by a resist strip solution removing in this way the material on top of it. The thin film remains where there was no PR. The resist strip solution is Microstrip 2001 (Fujifilm). The liftoff process is made at 65°C and applying ultra-sounds to accelerate the removal.

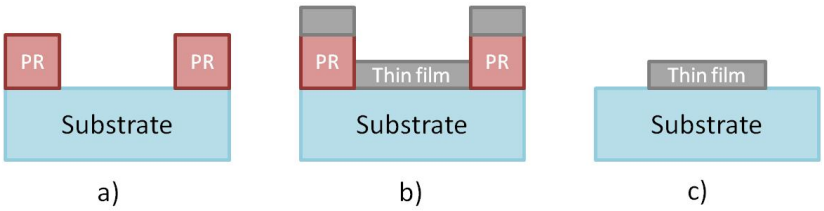

Figure 2.7: Liftoff process: a) patterning of the PR by photolithography b) deposition of a thin film layer c) removal of the PR and all the material on top of it by a resist strip solution.

2.1.4 Microfabrication runsheet

In this work several processes were optimized and accomplished. These processes can be included in two main categories: microfabrication of a biochip and fabrication of a microfluidic channel.

In this section, the microfabrication of a matrix-based magnetic tunnel junction biochip is described in detail. This process was chosen since it was the more complete and complex process accomplished in this work. On the other hand, a detailed description of the fabrication of a u-shaped microfluidic channel is made.

Microfabrication of a biochip: Magnetic tunnel junction matrix runsheet

This microfabrication process is in fact the integration of two previously optimized processes: MTJ fabrication process and diode fabrication process.They are rather standard microfabrication processes at INESC-MN and were already used by several people over the past decade. The fabrication of matrix-based magnetic tunnel junction biochip comprises 31 steps which are detailed in the run-sheet in appendix D. The steps are briefly discussed below. For a better understanding, this discussion should be accompanied by the appendix.

- **Step 1:** Substrate preparing.
  For this process, 2x1 or 1x1 inch^2 glass substrates were used. The substrate was cleaned in an Alconox solution (a detergent) and subjected to ultra-sound for 10 minutes. Then, the sample was thoroughly rinsed with isopropyl alcohol (IPA) and deionised water (DI). Finally, the sample was blow-dried with a compressed air gun.

- **Step 2:** Magnetic Tunnel Junction (MTJ) deposition.
  In INESC-MN facilities there are three deposition system used for the deposition of MTJs: Nordiko 3000 (6-target Ion beam deposition system), Nordiko 3600 (6-target Ion beam

deposition system) and Nordiko 2000 (6-target sputtering deposition system). Details in the Ion beam deposition systems and in the sputtering system can be found in [19]-[20] and [18], respectively. In Nordiko 3000, AlOx barrier MTJs were deposited while MgO barrier MTJs were deposited either in the Nordiko 3600 system or the Nordiko 2000 system. Chapter 4 depicts in detail the structure of these sensors. A reference sample with the same MTJ structure from the top electrode until the anti-ferromagnetic layer (MnPt or MnIr) was deposited. This sample will be used on step 8 as a reference for the second etch step.

- **Step 3:** TiW(N_2) 150 Å Deposition in Nordiko 7000.
  In this step a 150 Å TiW(N_2) layer was deposited over the MTJ material in Nordiko 7000 (sputtering system). This layer protects the MTJ from oxidation and corrosion. Furthermore, this layer acts as an anti-reflective layer useful for a better mask exposure. Note that this deposition was made in both main and reference samples.

- **Step 4:** Mask exposure in DWL (MTJ bottom electrode definition).
  The photoresist was coated, exposed and developed as described in section 2.1.1. In this step, the MTJ bottom electrode was defined.

- **Step 5:** MTJ+TiW(N_2) ion milling.
  The MTJ bottom electrode definition was finally obtained by removing the material that the PR was not covering. This was made by ion milling in Nordiko 3600 or Nordiko 3000 system as depicted in section 2.1.2.

- **Step 6:** Resist stripping in wet bench.
  In order to be able to proceed with the process, it is necessary to remove the PR mask. This was done by immersing the sample into Microstrip 2001 solution at a temperature of 65°C. The sample must stay in solution until all the PR is removed and eventually, ultra-sound can be applied to improve the removal. After that the sample was washed with IPA, rinsed with DI and blow-dried with a compressed air gun. The schematic representation of the final aspect of a matrix of 4 elements is presented in figure 2.8.

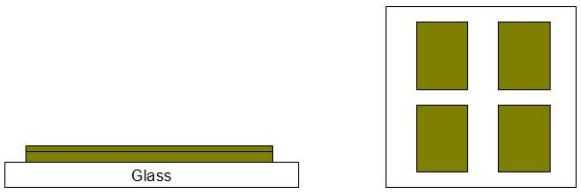

Figure 2.8: Schematic of a matrix of 4 elements after the first etch.

- **Step 7:** Mask exposure in DWL (Sensor definition).

In this step, the sensor dimension (10x2 μm^2 - 100x2 μm^2) and the contacts with the diode dimension (220x220 μm^2) were defined in PR.

- **Step 8:** MTJ top electrode ion milling.
  The MTJ was etched (by ion milling) until reaching the anti-ferromagnetic layer (see chapter 4). To know if the MTJ top electrode has already been etched, the reference sample was also etched at the same time. When there is no more material on the reference sample, it means that the top electrode was totally etched. It is preferable to perform a short over-etch in order to be sure that the sample was completely etched until the desired point.

- **Step 9:** Deposition of 1000 Å of Al_2O_3 in UHV2.
  Before stripping the PR, a passivation of 1000 Å of Al_2O_3 layer was deposited by sputtering in UHV2 system. This layer was used to prevent the top contact to become shorted with the bottom electrode. The deposition was made in a RF sputtering system.

- **Step 10:** Al_2O_3 Lift-off in wet bench.
  The liftoff of the Al_2O_3 layer was made in Microstrip 2001 and applying ultra-sounds. After this step the sample will look like the figure 2.9.

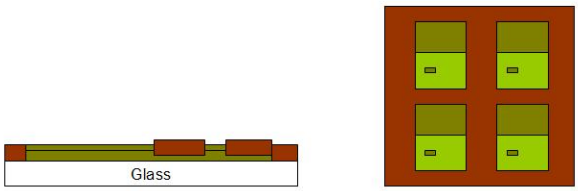

Figure 2.9: Schematic of a matrix of 4 elements after the first Al_2O_3 Lift-off.

- **Step 11:** 2000 Å Al + 150 Å TiW(N_2) (MTJ top contact, U-shaped line and diode bottom contact) deposition in Nordiko 7000.
  In this step, a 2000 Å Al + 150 Å TiW(N_2) layer was deposited by sputtering in Nordiko 7000 system. This layer will be used to make the top contact lead of the MTJ, the U-shaped line and the diode bottom contact.

- **Step 12:** Mask exposure in DWL (MTJ top contact, U-shaped line and diode bottom contact definition).
  This exposure defined the MTJ top contact, the U-shaped line and the diode bottom contact.

- **Step 13:** TiW(N_2) ion milling + Al wet etch.
  After defining the PR mask for the MTJ top contact, the U-shaped line and the diode bottom contact, the Al + TiW(N_2) which was not covered with the PR had to be removed. First of all, the 150 Å TiW(N_2) layer was removed by ion milling in Nordiko 3600 or

Nordiko 3000 because it can not be removed by wet etch. After that, the sample was put in a solution of phosphoric, nitric and acetic acid solution. This solution removed the Aluminum layer as depicted in section 2.1.2. This step is a key point on the matrix design since this metal layer cannot be shorted with second metal layer deposited later on step 23. There were several modification over the time in this step. The first modification was to use a etch instead of a liftoff step. A liftoff step may leave so called rabbit-hears which are material portions on the edge of the metal lines. These rabbit-hears may not be completely covered by the oxide deposited on step 21 thus being a point of short-circuit between this metal layer and the metal layer of step 23. Concerning the etch, initially ion milling was used to etch also the aluminum layer. However, this is a time consuming process (since the etching rate of ion milling is 1 Å/s) and the fact that the sample is bombarded so many time by ions, the sample heats. This heating effect burns the PR which turn it much more difficult to strip in the next step. The wet etching of the Al lines has two main advantages. The first one is that it is a fast process and it does not damage the sensor since it is buried into the oxide layer od step 9. The second advantage is that the edges are not sharp (see section 2.1.2). In this way even a sputtering oxide will give a good lateral coverage. In conclusion, using a wet etch process here will provide a better isolation of the first metal layer.

- **Step 14:** Resist stripping in wet bench.
  The sample was dipped on Microstrip 2001 at a temperature of 65°C. The PR was stripped from the sample as described previously on step 8. In the end, a matrix of 4 elements looked like figure 2.10 .

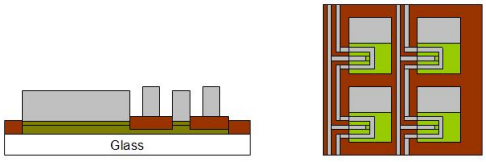

Figure 2.10: Schematic of a matrix of 4 elements after the MTJ top contact, the U-shaped line and the diode bottom contact definition.

- **Step 15:** Diode deposition in a PE-CVD machine.
  In this step, the diode was deposited on a PE-CVD system (Plasma-Enhanced Chemical Vapour Deposition). A PIN diode is composed by the following layers: 200 Å of p^+-a-Si:H, 5000 Å of i-a-Si:H and 200 Å of n^+-a-Si:H (see section 5.1.2).

- **Step 16:** Mask exposure in DWL (diode island definition).
  This exposure defined the diode island.

- **Step 17:** Reactive Ion Etch (RIE), diode island definition.

In this step, the diode island was defined by Reactive Ion Etch (section 2.1.2). This etch technique is very selective, so all the a-Si:H material not covered by the PR is removed, leaving the material below intact.

- **Step 18:**Resist stripping in wet bench.
  The PR was striped as indicated previously. After this, the sample looked like the schematic shown on figure 2.11.

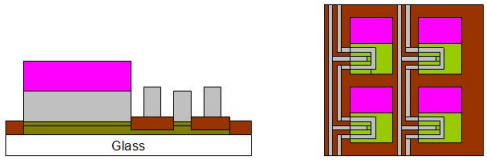

Figure 2.11: Schematic of a matrix of 4 elements after the diode island definition.

- **Step 19:**Mask exposure in DWL (diode area definition).
  This exposure defined the diode area.

- **Step 20:** 2500 Å Al_2O_3 deposition in UHV2.
  An Al_2O_3 passivation layer 2500 Å thick was deposited. This layer was used to prevent a short-circuit between the first and second metallization layers. The deposition was made in a RF sputtering system and not a CVD system, which would provide a better lateral coverage, because the latter system would need to use temperature near the Currie temperature of the ferromagnetic films of the sensor. This facts implies that the layers would loose their easy axis.

- **Step 21:** Al_2O_3 Lift-off in wet bench.
  Similarly to step 12, the PR and consequently, the Al_2O_3 above it, were removed using Microstrip 2001 and ultra-sounds. After this step the sample looked like figure 2.12.

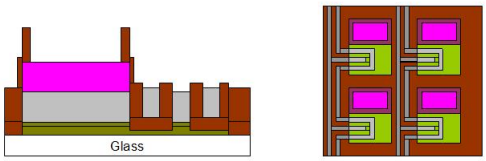

Figure 2.12: Schematic of a matrix of 4 elements after the second Al_2O_3 liftoff.

- **Step 22:** Mask exposure in DWL (row lead definition).
  This exposure defined the row lead.

- **Step 23:** 3000 Å Al + 150 Å TiW(N_2) deposition in Nordiko 7000.
  In this step, a 3000 Å Al + 150 Å TiW(N_2) layer was deposited in the Nordiko 7000 machine. This layer will be used to make the top contact lead of the diode which also corresponds to the row lead of the matrix. In terms of mask, there was an optimization accomplished in this step. In order to reduce the probability of short-circuit between this metal layer and the first one, this contact line was narrowed from 200 to 40 μm in the places where it crosses the first metal layer.

- **Step 24:** Al Lift-off in wet bench.
  Similarly to previous lift-off steps, the PR and consequently, the Al above it, were removed using Microstrip 2001 and ultra-sound. After this step the sample looked like figure 2.13.

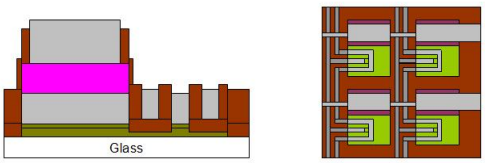

Figure 2.13: Schematic of a matrix of 4 elements after the Al Lift-off.

- **Step 25:** Mask exposure in DWL (contact pad protection from the full passivation).
  In order to protect the sensors from corrosion of fluids and short-circuits the chip had to be passivated. However, the contact pads where the wirebonding will be performed, have to be free of passivation. This exposure defines the PR mask to accomplish this.

- **Step 26:** 1000 Å Al_2O_3 deposition in UHV2.
  A passivation layer of 1000 Å of Al_2O_3 layer was deposited. This layer was the first layer of the whole passivation layer. The deposition was made in a RF sputtering system. This layer is very important since it prevent the chip from corrosion due to saline solutions that will later be put on top of it. This RF sputtered Al_2O_3 is much less porous than the RF sputtered SiO_2. However, the dextran magnetic particles used in this work tend to adsorb on the Al_2O_3 layer. Therefore, a double passivation layer composed first by Al_2O_3 and then by SiO_2 is deposited. CVD oxide deposition were also avoided in this step for the same reason than step 20.

- **Step 27:** 2000 Å SiO_2 deposition in Alcatel.
  A passivation layer of 2000 Å of SiO_2 layer was deposited. This layer was the second layer of the whole passivation layer. The deposition was made in a RF sputtering system.

- **Step 28:** Passivation layer Lift-off in wet bench.
  Similarly to previous lift-off steps, the PR and consequently, the oxides above it, were

removed using Microstrip 2001 and ultra-sounds. After this step the process is complete and the chip looked like the figure 2.14.

Figure 2.14: a) Schematic of a matrix of 4 elements after the passivation layer lift-off. b) Image of the final chip after the dicing step.

- **Step 29:** Sample dicing.
  The final sample had 8 dies (for a 2x1 inch^2 sample) or 4 dies (for a 1x1 inch^2 sample). These dies must be individualized in order to encapsulate them in a chip carrier and then to perform the measurements. An automatic dicing saw was used to cut the sample dies.

- **Step 30:** Sample annealing.
  Each die had to be annealed at 280°C for 1 hour, under a magnetic field of 5 kOe. This annealing was used to improve the exchange magnetic field in the pinned layer. This exchange magnetic field had to be relatively high (between 300-500 Oe for a standard pinned layer and above 500 Oe for a synthetic antiferomagnetic (SAF) layer) so that this layer can act properly as a reference layer. In the case of MgO barrier MTJs, this annealing temperature partly crystalized the ferromagnetic electrodes improving the MTJ signal while maintaining the linear response. Furthermore, this annealing also improved the diode characteristics since it reduces the number of structural defects.

- **Step 31:** Wire bonding.
  Finally, each die was mounted on a chip carrier, which is a holder with 40 contacts for this matrix-based biochip (figure 2.15 a)). A PCB chip carrier with 34 contacts was also used for standard spin-valve and MTJ biochips (figure 2.15b)). To connect the chip to the chip carrier contacts, a wirebonding technique was used. This technique uses ultrasonic vibrations to weld a thin aluminum wire to the metal contact on the chip. The detection experiments consist in dispensing a solution of magnetic particles on the chip surface (see section 4.2.5). In order to prevent the fouling and corrosion of delicate contact areas, the wirebondings were covered with silicon gel (Elastocil). This was made by applying a soft gel over the wirebondings and then allowing it to harden by drying for a period of 3-4 hours at room temperature.

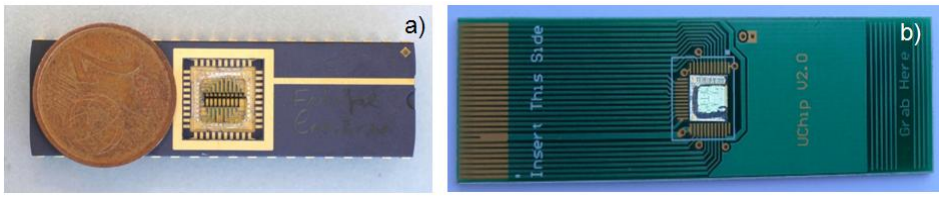

Figure 2.15: a) Matrix chip wirebonded on a 40-pin chip carrier b) Standard biochip wirebonded in a 34 pin PCB chip carrier

Microfluidics process

The microfluidic system used in this work was frabricated with two different polymers: polydimethilsiloxane (PDMS) and polymethylmethacrylate (PMMA). PDMS is one of the most widely used materials and it was chosen to replicate the channels since it uses cheap and fast casting techniques. Furthermore, the PDMS is a biocompatible material enabling gaseous exchanges between the environment and the interior of the channels. The PMMA was used to fabricate the channel master. The process for the fabrication of this microfluidic channel is described below. This microfluidic channel is further used in chapter 5.

- **Step 1:** Mold fabrication.
  For the fabrication of an U-shaped channel, three PMMA plates (2 mm thick), shown in figure 2.16, were micromachined using a CNC milling machine (TAIG Micro Mill from Super tech & Associates): one having the master of the channel (500 μm wide and 100 μm thick), the second one having the frame that defines the thickness (2mm) and the shape (5x5 mm^2) of the PDMS element and third one with 0.8 mm holes that support metallic pins to cast access to the channel (the inlet and the outlet). This last plate had also a hole used to inject the PDMS inside the mold. Two 2 mm alignment holes were also included in the side of each structures (see figure 2.16). The structures were aligned by passing a 2mm pin through these holes (one pin to each side). Since the channels are big there were not major fabrication optimization achieved.

- **Step 2:** PDMS preparation.
  A 2 ml volume of PDMS (Sylgard 184-Dow Corning) was prepared by mixing the curing agent and the base in a 1:10 mass ratio followed by a 1 hour degassing step.

- **Step 3:** PDMS curring.
  After injecting the mixture in the mold (formed by the 3 aligned plates of figure 2.16), the PDMS was cured for 1 hour at 60^{o}C.

- **Step 4:** PDMS channel uncasting.
  Finally, the solidified PDMS was released from the mold. Figure 2.17 shows the final channel after uncasting.

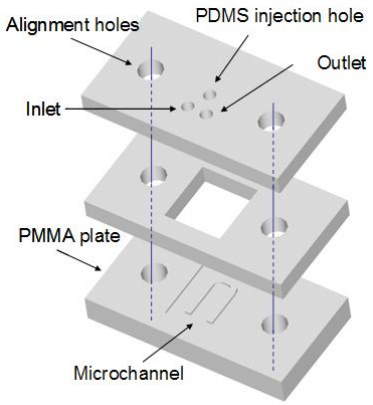

Figure 2.16: Schematic representation of the micro-drilled mold for the fabrication of PDMS microfluidic structures.

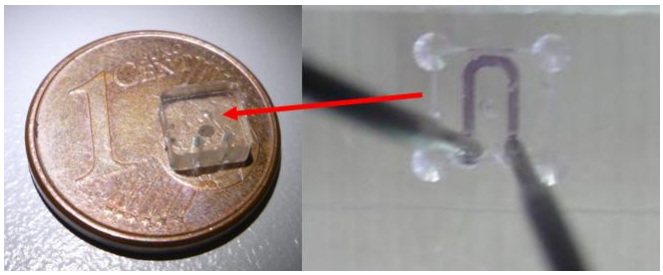

Figure 2.17: PDMS microfluidic U-shaped channel.

2.2 Characterization methods

2.2.1 Magnetic characterization

In order to characterize the magnetic moment and the magnetization of an unpatterned sample or of magnetic particles in solution, a vibrating sample magnetometer (VSM) was used. In INESC-MN facilities, a DSM 880 VSM is installed (figure 2.18). This system has two electromagnets which are able to generate static fields up to 13 kOe. The sample is mounted in a vertical quartz rod which is connected to a piezoelectric crystal. The excitation of this crystal, allows the vibration of the sample at a frequency of 200 Hz. Two pick up coils are incorporated in the gap of the electromagnets. When the sample is vibrating, an electromotive force is generated in these coils due to the change of the magnetic flux across the coils surface. This electromotive force is proportional to the magnetic moment of the sample and is thus acquired and processed delivering the magnetic moment of a sample in function of the external static magnetic field. This VSM has a resolution of 0.1 Oe in the applied field and a sensitivity down to 10^{-5}emu.

Before making magnetic moment measurements in a VSM, some calibrations have to be performed. First, the magnetic field generated by the electromagnet is calibrated using an external gaussmeter. Then, the sensitivity of the pickup coils is calibrated by measuring the

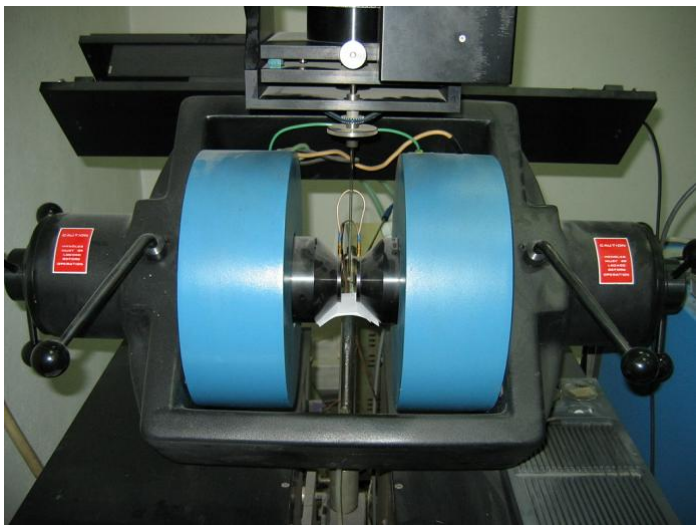

Figure 2.18: Picture of the DMS 880 Vibrating sample magnetometer

previously known magnetic moment of a standard Nickel sample (in this case $m_{StdNi} = 2.125$ emu). Finally, the diamagnetic component introduced by the quartz rod is measured in function of the static magnetic field. This contribution will be subtracted to any measured samples. A typical VSM curve of a MTJ stack is shown in figure 2.19. In this work, the VSM was used to characterize several magnetic materials (magnetization, coercive field, crystalline anisotropy...), tune the Ru thickness in synthetic antiferromagnetic (SAF) structures used in MTJs, measure the exchange field at the anti-ferromagnet/pinned layer interface and characterize magnetic particles (saturation magnetization, susceptibility...).

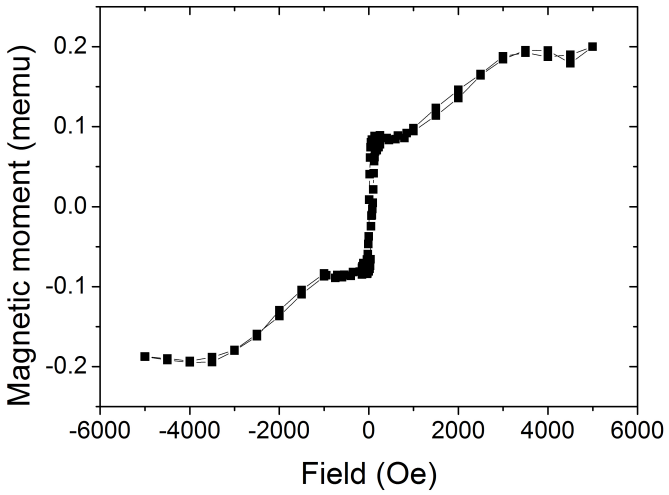

Figure 2.19: A typical MTJ stack measured by VSM. The MTJ stack is Ta 50 Å /Ru 200Å /Ta 50Å /MnIr 150Å /CoFe 30Å /Ru 8 Å /CoFeB20 40Å /MgO 11 Å /CoFeB20 30Å /Ru 50Å /Ta 50Å

2.2.2 Transport characterization

In order to characterize the transport behaviour of a magnetoresistive (MR) sensor (either spin-valve or magnetic tunnel junctions) as function of the external field, the measurement setup schematized in figure 2.20 was used. This setup can be used to measure chips already encapsulated in a chip carrier or as processed samples through the use of micro-positioner probes (resolution ~10 μm) with tungsten needles. The MR sensor is biased by a current source (Keithley 220) and the voltage is measured by a voltmeter (Keithley 182). The measurement can be done using 2 or 4 probes. The magnetic field is created by two Helmholtz coils connected in series and supplied by a current source (Kepco Bipolar operational power supply). Both current sources are controlled by a computer (GPIB connection). The voltage data is sent by the voltmeter to the computer using also a GPIB connection. Two shunt switches connected in parallel to the current source and the voltmeter are used to prevent damaging the sensors by charge accumulation at the terminal of the instruments.

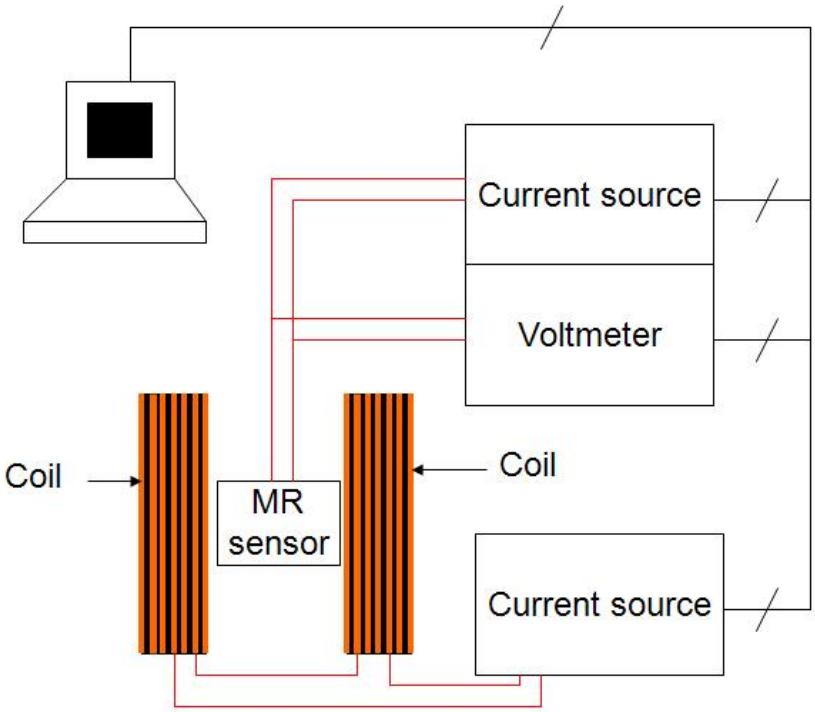

Figure 2.20: MR sensor measuring setup.

A typical linear transfer curve measured in this setup is shown in figure 2.21. In this case, it is a transfer curve of an MTJ used in a biochip. The MTJ shows a minimum resistance of 320 Ω and, as it can be observed, a TMR of ~45 %. More details about MTJs structure and transfer curves can be found in chapter 4.

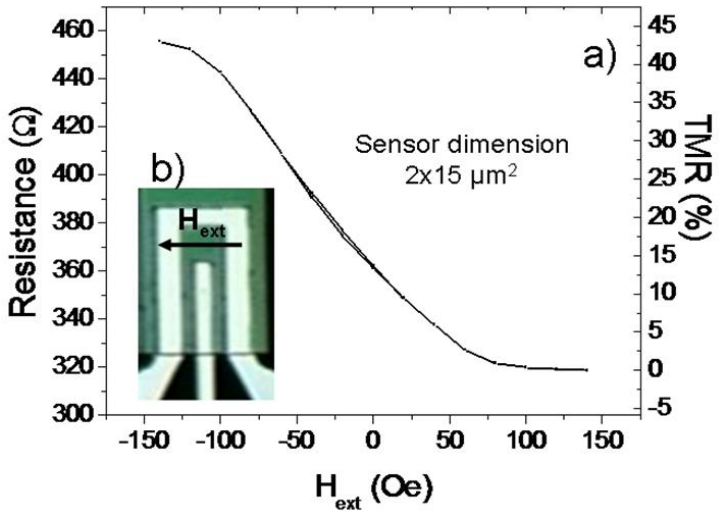

Figure 2.21: MTJ experimental transfer curve.

2.2.3 Noise characterization

Noise measurement setup

The measuring circuit (figure 2.22) is composed of three section, testing device, amplifier and spectrum analyzer. The testing device is a circuit which includes under-test device (MTJ, spin-valve, diode...), a potentiometer to regulate the current and a voltage generator (usually a battery). The under-test device signal is then amplified by a commercial amplifier from Stanford Research System (SRS) with the reference SIM910. This amplifier is a low noise amplifier with an input resistance R_{ai}=100 MΩ in parallel to a 35 pF capacitor (C_{ai}) and a maximum gain of 100 (40 dB). The amplifier power supply is composed by twenty 1.5 V batteries (± 15V) in order to avoid possible noise coming from the electrical network (specially the 50 Hz component). Finally, the amplifier is connected to a real time spectrum analyzer (Tektronix RSA3308A) which has a noise level of 90 nV/Hz$^{1/2}$.

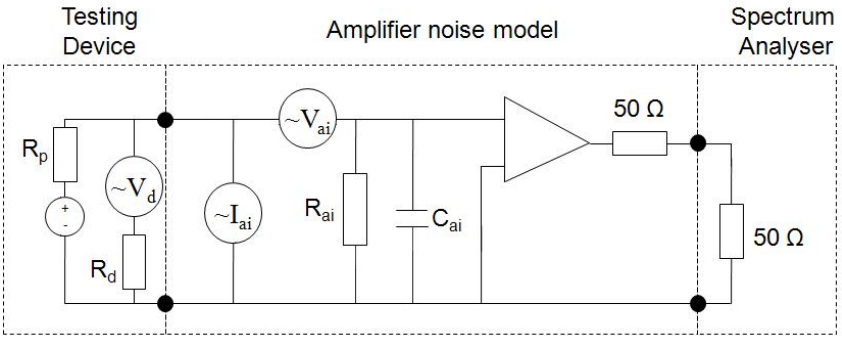

Figure 2.22: Measurement scheme for the noise characterization system.

Amplifier calibration

Before performing a noise measurement of a device, the noise of all the components of the measuring circuit have to be individually characterized. Figure 2.22 shows an equivalent circuit of the amplifier modeling the two noise sources (I_{ai} and V_{ai}) of the amplifier. To fully characterize the amplifier, three experiments were made: i) gain measurement with a network analyzer (HP 4195A), ii) V_{ai} measurement using the spectrum analyzer and an short circuit in the amplifier input and iii) I_{ai} measurement using the spectrum analyzer and a open circuit in the amplifier input. Figure 2.23 shows that the 40 dB gain remained constant from DC to 100 kHz. Although in the amplifier specification it is written that the amplifier gain is constant from DC to 1 MHz, it was found that the amplifier gain and noise sources show a non-linear behavior at frequencies above 100 kHz. This may be due to the fact that in the amplifier input the impedance is not adapted causing non-linearities at higher frequencies. As this setup was mainly designed to perform measurements at low frequency, in this work the amplifier will be used in the range of DC to 100kHz.

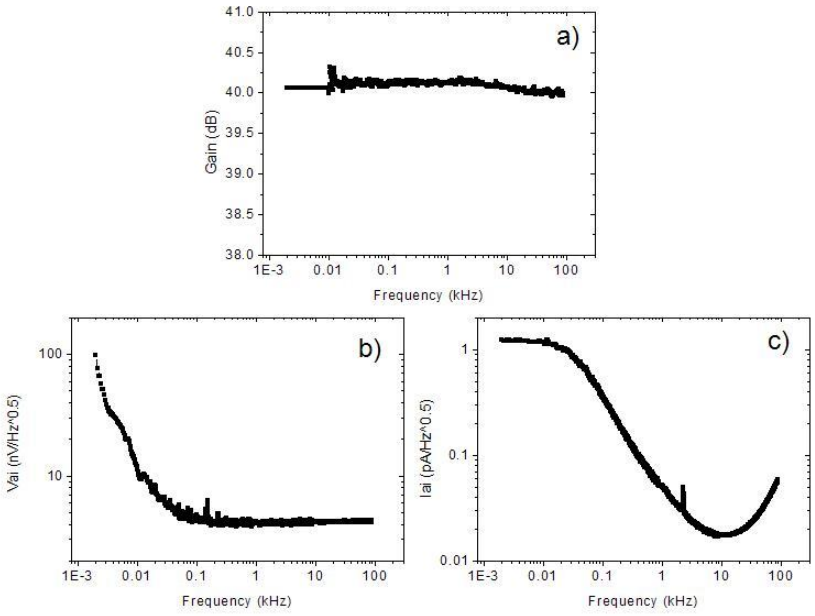

Figure 2.23: a)S21,b)Vai and c)Iai curves from the SRS SIM 910 amplifier.

To confirm that the amplifier was well characterized, a 2.2 kΩ film resistor was measured with the noise setup. These king of resistors show only thermal noise which is given by the expression $\sqrt{(4k_bTR\Delta f)}$ where k_b is the Boltzmann constant, T is the temperature, R is the resistor resistance and Δf is the bandwidth. Film resistors are then suitable to verify the correct removal of the amplifier noise from the measurements. This removal is done using the superposition principle for the circuit showed in figure 2.22, leading to the following equation:

$$V_d = \frac{[(1+\frac{R}{(R//R_{ai})})^2 + (\omega C_{ai} R)^2][V_{meas} - (V_{ai} + I_{ai} R_p//R)]}{\sqrt{(1+\frac{(R_p//R)}{R_{ai}})^2 + (\omega C_{ai} R//R_p)^2}} \tag{2.1}$$

R is the resistance of the device under test, ω is the frequency, V_{meas} is the signal measured by the spectrum analyzer, V_{device} is the noise of the device under test and R_p the resistance of the potentiometer.

Figure 2.24 shows the noise of a 2.2 kΩ film resistor after removing the noise of the amplifier. It can be observed that, in the range of DC to 100kHz, the measured noise is the same as the expected thermal noise.

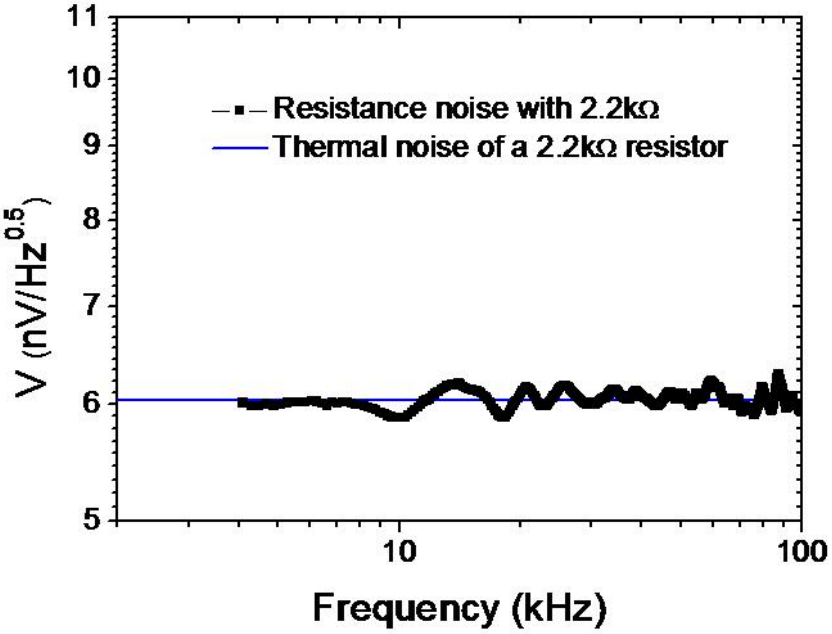

Figure 2.24: a)S21,b)Vai and c)Iai curves from the SRS SIM 910 amplifier.

2.2.4 Particle detection setup

In this work, three different experimental setups were used for the detection of a magnetic nanoparticles using MR sensors.

The first is a bench-top setup used for a DC detection (figure 2.25). This setup is composed by a current source (Keithley 220) and a voltmeter (HP 34401A) which are connected to a 32 channel multiplexer. This multiplexer board is home-made and is controlled by a computer via a NI-DAQ PCI6024E board. The MR biochip is inserted in a socket on this board. A DC voltage generator (HP 3612A) is connected to a horse-shoe electromagnet to generate an in-plane transverse external DC magnetic field over the chip. All the equipment is controlled by a computer via GPIB communication bus. The data is further saved and plotted by means of a NI-Labview program.

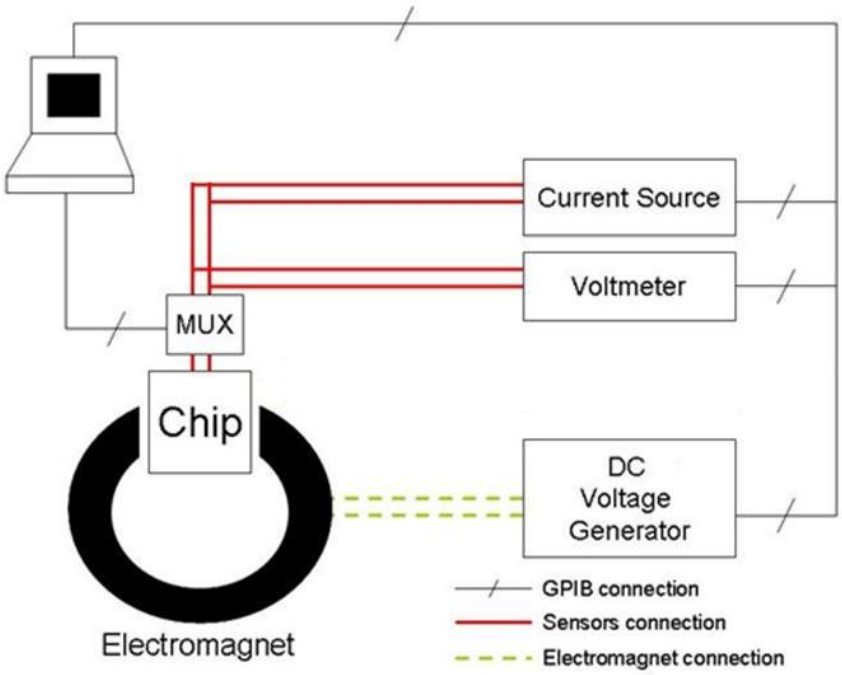

Figure 2.25: Schematic representation of the set-up used for measuring particles in DC.

Using this setup, it was possible to measure the resistance variation of the MR sensor due to the presence of magnetic particles. However, a thermal drift due to the current passing through the sensor is observed. This drift may mask the real contribution of the magnetic particles in the overall signal variation. Furthermore, the noise of a sensor is maximum in DC.

Thus, in order to reduce the effect of the thermal drift and to reduce the noise of the sensor, a second measurement setup was used. This setup is based in the previous setup since the same current source and voltmeter are used to measure the DC resistance. Then, the horse-shoe electromagnet is connected to a function generator (Agilent 33220A) which is able to apply a DC+AC voltage. The applied in- plane transversal AC field is then sensed by the MTJ or

spin-valve generating a AC voltage. This voltage is measured using a lockin amplifier (Model 5209, Princeton Applied Research). In this setup, a current source (HP 3612A) is connected to the current lines of the chips for magnetic particle attraction. As in the previous setup, all the equipment is connected via GPIB to a computer. A NI-Labview program makes the signal visualization and the data saving.

The system depicted previously is a bulky bench-top setup. In order to turn this electronic setup more compact and portable, a platform was developed in collaboration with INESC-ID (figure 2.27).

This platform provides all the electronic circuitry necessary to address, drive and readout the sensors [83]. The architecture of this platform is further detailed in section 5.2. To perform the measurement, a chip wirebonded to a PCB chip carrier (figure 2.15 b)) is plugged into the platform. A selfaligned electromagnet can generate AC fields up to 15 Oe_{rms} (211 Hz) superimposed to a DC field ranging from -40 Oe to 40 Oe. In experiments where the AC field component is not required (i.e. transfer curve measurement), DC fields from 200 Oe to 200 Oe can be generated. Furthermore, the sensors can be biased with a current ranging from 144 μA to 1.16 mA and a maximum of 30 stand alone sensors or 256 sensors in a matrix configuration (see chapter 5) can be addressed. The output signal of the sensors is then amplified with a gain of 40 and acquired by an analog to digital converter (ADC) at a sample rate 844 samples/s. Before being sent to a computer via USB or bluetooth, the signal is digitally filtered. It is important to notice that this acquisition system is powered by a battery ensuring its portability and low noise. A self-aligned microfluidic channel is also included in order automatically assist the loading of the target sample on top of the sensors. Finally, a software developed by INESC-ID in C# provides full control of the experiments and show in a graphic mode the acquired signal.

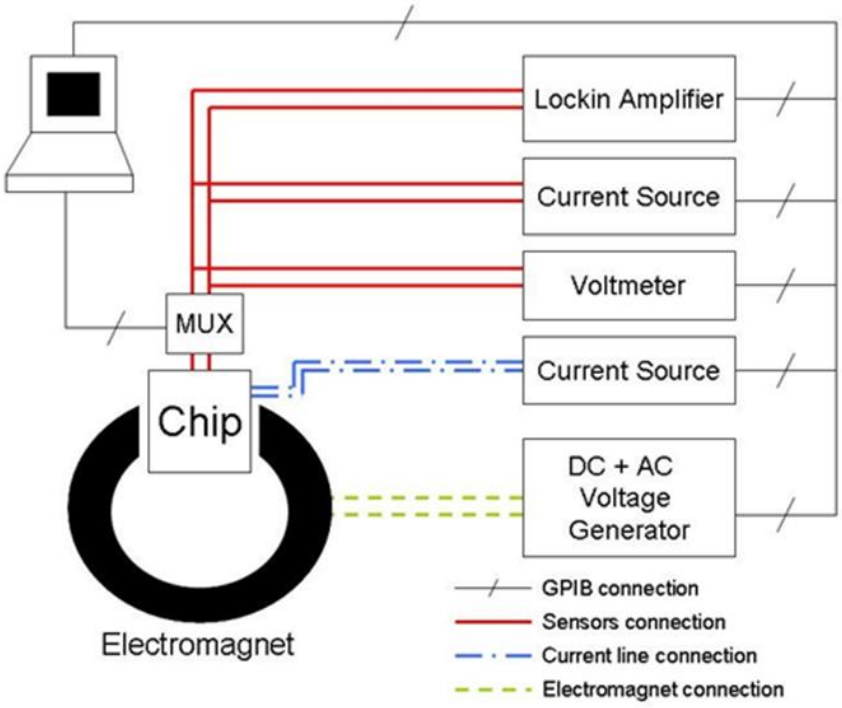

Figure 2.26: Schematic representation of the set-up used for measuring particles in AC.

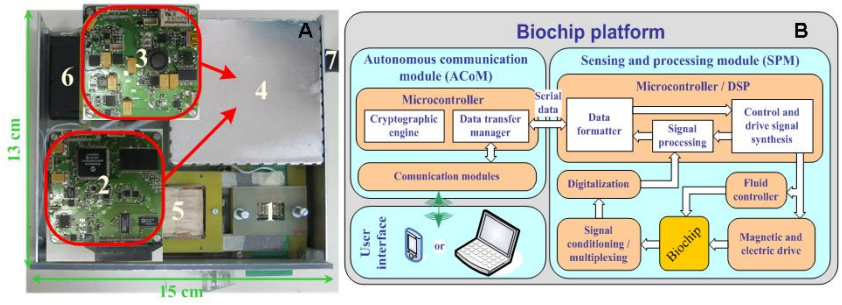

Figure 2.27: Portable platform electronic biochip read-out set-up. (A) Picture from the portable prototype system: 1- Biochip encapsulated in a PCB chip carrier; 2- Sensing and processing module; 3- Autonomous communication module and magnetic drive circuits; 4- Noise shielding enclosure; 5- Coil for the magnetic drive; 6- Battery; and 7- USB connector. (B) Schematic architecture of the biochip platform.

Chapter 3

Magnetic particles

In the past decade, magnetic particles have been used in biology and medicine in several applications including cell separation, drug delivery, contrast enhancement in magnetic resonance imaging [46],[47] and more recently in hyperthermia for cancer treatment [48]. In this thesis, magnetic particles are used as labels of target biomolecules which are recognized (via biomolecular recognition) by a probe biomolecule previously immobilized on top of a magnetoresistive sensor. The sensor will then detect the fringe field of the magnetic label indicating the binding of the target biomolecule to the specific probe. For this application, the magnetic particles should have the following characteristics:

- Size: the size of the labels should be sufficiently small in order to prevent steric hinderance in the biomolecular recognition. When trying to perform biomolecular recognition on a surface, many forces (electrostatic force, Van der Vaals force...) appear due to surface presence. This forces may hinder the biomolecular reaction. The probe is already located on a flat surface. If the DNA target is immobilized on a big particle (close to micron size), it will have an almost flat surface around which will also cause steric hindrance and therefore reduce the probbility of recognition. For DNA recognition, typically nano-sized particles with diameter ranging from 300 nm down to 10 nm are used.

- Magnetic behavior: magnetic labels should not present remanent moment in order to avoid particle clustering. Therefore, superparamagnetic particles are used.

- High magnetic moment: the labels should develop a high magnetic moment under an external magnetic field in order to provide a large fringe field for the detection.

In order to fulfill these requirements several materials can be used for the magnetic labels. An obvious approach would be to use transition metal-based particles (Co, Fe, NiFe) because they offer high moments and susceptibilities for relatively low external fields. However, below a critical diameter (70-100 nm for Co and Fe, 100 nm for NiFe) those particles become ferromagnetic and therefore may cause particle clustering. Although this particle-particle interaction may be attenuated by changing the geometry [49], it is very difficult to completely remove such dipolar interaction. Therefore, in this work FeOx-based particles were used. These particles

are typically superparamagnetic in sub-micron dimensions and show a high moment and susceptibility. In order not to poison the biological environment, these particles are encapsulated or passivated by a biocompatible material.

In this chapter, the following magnetic particles are studied: Nanomag-D 130 nm and 250 nm from Micromod (Germany), Bio-Adembeads 200 and 300 nm from Ademtech (France) and 10 nm magnetite particles (NGAP NP FeO-2204-W) from Nanogap (Spain). In the case of Micromod and Ademtech particles, characterized below, the iron oxide nano-particles are dispersed in a biocompatible polymer matrix forming a single label (spherical in the case of Ademtech labels and cluster type in the case of Micromod labels) with hundreds of nanometers in diameter. This polymer can be further functionalized with different types of biomolecules: proteins, antibodies or nucleic acids [51]. Single core 10 nm magnetite particles provided by Nanogap were also characterized. These particles are protected by a poly(acrilic acid), are monodispersed and show a very good uniformity in dimension [50].

3.1 Magnetization of magnetic particles

The magnetization M of monodisperse non-interacting magnetic nanoparticles under an applied external field H can be modelled by a Langevin-like function:

$$M = M_s \left(\coth\left(\frac{\mu_0 m_p H}{k_B T}\right) - \frac{k_B T}{\mu_0 m_p H} \right) \tag{3.1}$$

where m_p is the magnetic moment of the nanoparticles inside the matrix and M_s is the saturation magnetization. Micromod 250 and 130 nm particles, Ademtech 200 and 300 nm particles and Nanogap 10 nm particles magnetization in function of an external magnetic field was measured in a VSM system (see section 2.2.1). Typically, a volume of 20 μL of nanoparticles at the stock concentration was injected in a special recipient (which diamagnetic component was previously measured). The measured moment in the VSM system corresponds to the sum of the magnetic moment of each particles. In order to compare the different particles susceptibility, the magnetization of each particle has to be calculated. To do this, the measured magnetic moment was be devided by the number of particles in the sample and by the particle volume. The number of measured particles was estimated using the supplier information about nanoparticle concentration while the mean diameter of each nanoparticle, also given by the supplier, was used for the label volume calculation.

Figure 3.1 a) shows a typical magnetization curve. In this particular case, Micromod 250 nm particles were measured in the range of -3000 to +3000 Oe and it can be observed that Langevin-like function describes relatively well the M(H) curve. In the biochip detection system described later, a magnetic field with values varying between -50 Oe and 50 Oe is used to magnetize the magnetic particles. Analyzing this low field regime, Ademtech and Nanogap labels magnetization have shown a good fitting to the Langevin-like function (see figure 3.1 c)). On the other hand, the Micromod labels (250 nm and 130 nm) magnetization did not show a good fit (see figure 3.1 and b)). An excess of susceptibility is observed in this field range

indicating that the nanoparticles inside the label polymeric matrix may be interacting. It was already proved that for smaller Micromod (Nanomag 100 nm and 50 nm) particles with 25 % of FeOx composition did not show this excess of susceptibility at low field range [22].

Company	Particle type	Diameter	M_s (emu/cm^3)	m_p (emu)	χ (in cgs)
Micromod	Nanomag-D	250 nm	81.52	2.85×10^{-16}	0.31
Micromod	Nanomag-D	130 nm	121.11	2.91×10^{-16}	0.4
Ademtech	Bio-Adembeads	200 nm	40.50	1.86×10^{-16}	0.07
Ademtech	Bio-Adembeads	300 nm	41.08	2.09×10^{-16}	0.07
Nanogap	NGAP NP FeO-2204-W	10 nm	222.48	4.38×10^{-16}	0.88

Table 3.1: Langevin-like fitting parameters and average susceptibility for $|H| < 50$ Oe of Micromod (250 and 130 nm), Ademtech (200 and 300 nm) and Nanogap (10 nm) magnetic label.

Table 3.1 shows the m_p and M_s fitting parameters to the Langevin-like function. Although the magnetic moment of the nanoparticles inside the label matrix is basically the same, the Ademtech labels saturation magnetization is two to three times lower than Micromod's. This can be explained by the fact that Micromod has a higher FeOx composition. Furthermore, the average susceptibility of Micromod labels at low field ($|H| < 50$ Oe) is also higher than Ademtech labels mainly due to the excess of susceptibility discussed previously. Thus, for sensors designed to detect hundred nanometer particles (see chapter 4), the Micromod particles are the ones showing the best characteristics for labeling.

The Nanogap single core 10 nm particles showed higher values in the fitting parameters to the Langevin-like function and higher susceptibility. Furthermore, they did not show an excess of susceptibility (see figure 3.1) as the Micromod labels at low field range indicating that the particles are monodispersed thus there is no dipolar particle-particle interaction. Therefore, these 10 nm particles are good candidates for being used as labels providing that the sensors are designed for detecting tens of nanometer-sized particles.

3.2 Dipolar model

In order to simulate the behaviour of a magnetic particle over the free layer of the sensor, it is assumed that the particles can be approximated to a magnetic dipole. It is also assumed that the particle is spherical and that the dipole center is at the geometrical center of the sphere. The magnetic field generated by the dipole at the position $\mathbf{r}$ from the center of the dipole is given by

$$\mathbf{H}(\mathbf{r}) = \frac{1}{4\pi}\left(\frac{3(\mathbf{r}\cdot\mathbf{m})\mathbf{r}}{|\mathbf{r}|^5} - \frac{\mathbf{m}}{|\mathbf{r}|^3}\right) \tag{3.2}$$

For the label detection experiments, the magnetic particle is magnetized by applying an external field. There are two relevant direction for applying the field:

- Parallel to the sensor plane: as shown in figure 3.3 the field is applied along the x-direction.

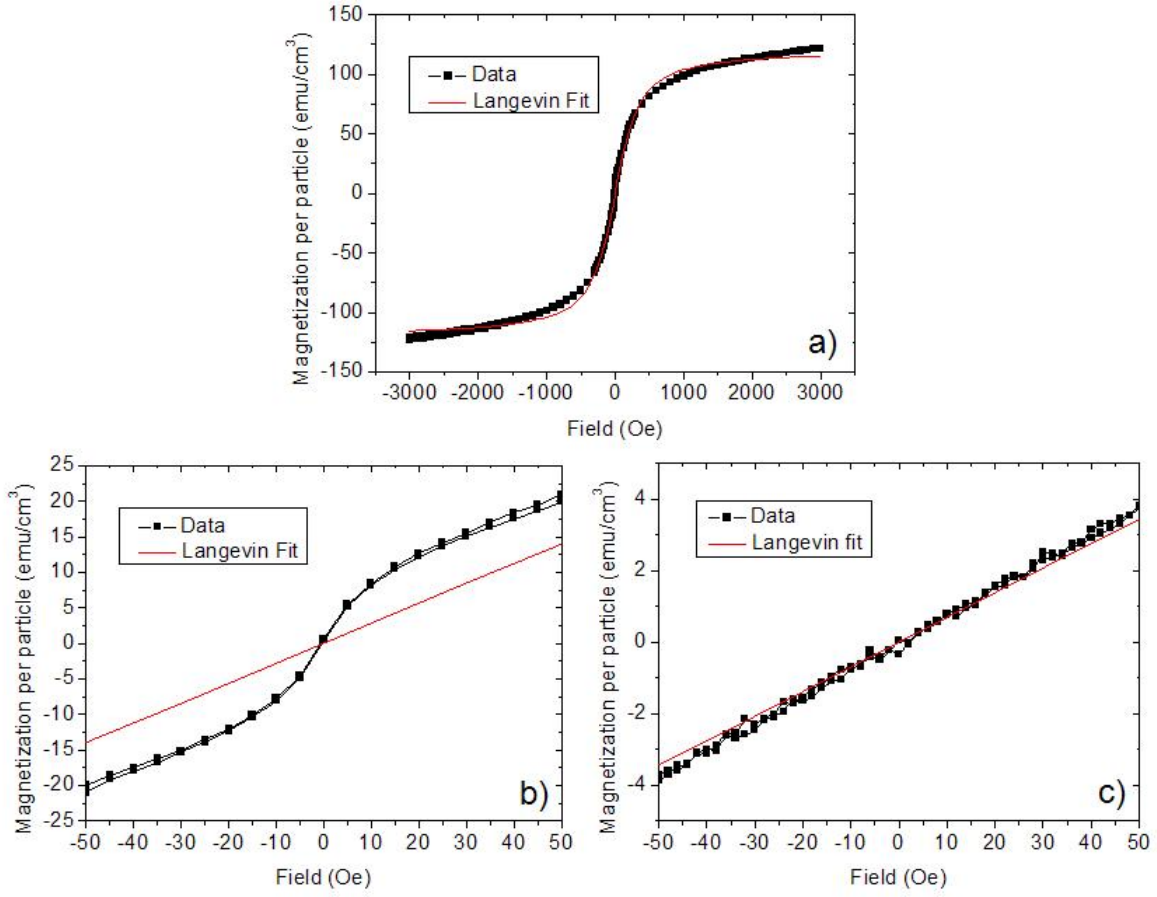

Figure 3.1: a) Typical magnetization of a magnetic particle (in this case Micromod 250 nm particles) in function of an external applied field. By fitting to a Langevin-like model the nanoparticle moment and saturation magnetization can be obtained. b) Low field M vs H of Micromod 250 nm particles. c) Low field M vs H of Ademtech 300 nm particles.

- Perpendicular to the sensor plane: as shown in figure 3.4 the field is applied along the z-direction.

As the magnetoresistive sensors used in this thesis (magnetic tunnel junction and spin valve) are only sensitive to the transverse in-plane component of the fringe field of the particle, only the x-component of the fringe field calculated using equation 3.2 has to be studied. Therefore, a particle with a radius r, a moment $m = \frac{4}{3}\pi r^3 M$ and placed in the center of the sensor show a fringe field calculated as follows, for both cases represented in figure 3.3 and 3.4:

- Magnetic moment parallel to the sensor plane ($\mathbf{m} = m_x\mathbf{i}$):

$$H_x(x,y,z) = \frac{m}{4\pi}\left(\frac{3x^2}{(x^2+y^2+z^2)^{5/2}} - \frac{1}{(x^2+y^2+z^2)^{3/2}}\right) \tag{3.3}$$

The maximum field is found to be just below the sphere at position $(0, 0, r+d)$ where d is

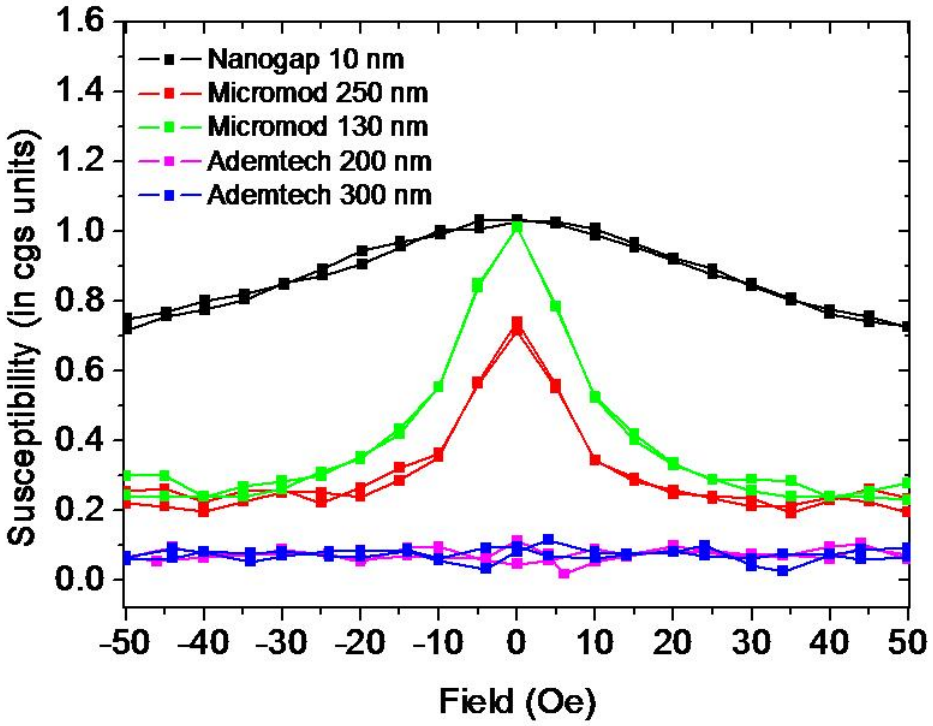

Figure 3.2: Susceptibility measurements of the different magnetic particles used.

the separation between the sensor surface and the particle bottom surface. The following expression can be used to calculate this maximum:

$$H_x^{max}(0,0,r+d) = -\frac{m}{4\pi}\frac{1}{(r+d)^3} \tag{3.4}$$

- Magnetic moment perpendicular to the sensor plane ($\mathbf{m} = m_z\mathbf{k}$):

$$H_x(x,y,z) = \frac{m}{4\pi}\frac{3xz}{(x^2+y^2+z^2)^{5/2}} \tag{3.5}$$

The field below the particle at a position $(x, y, r+d)$ is then given by the following equation:

$$H_x(x,y,r+d) = \frac{m}{4\pi}\frac{3xz}{(x^2+y^2+(r+d)^2)^{5/2}} \tag{3.6}$$

Figures 3.3 and 3.4 show the label fringe field profile for the case of a parallel and perpendicular to sensor plane, respectively. In both case, a 250 nm Micromod particle with a magnetization $M = 20.1$ emu/cm^3 at a distance $d = 0.2$ μm was assumed.

A magnetoresistive sensor is sensitive to the average fringe field generated by a magnetic particle. Therefore, the field H_x has to be averaged over the sensor area. Figure 3.5 and 3.6 show the average fringe field $< H_x >$ on a 2×100 μm^2 sensing area in function of the particle position (x,y) for the two studied cases. As previously, the particle was assumed to be at a distance

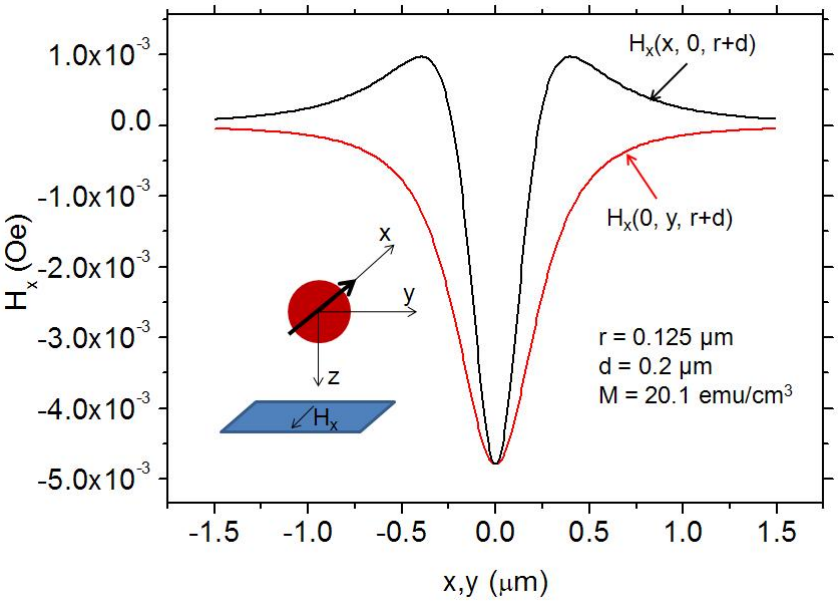

Figure 3.3: Transverse magnetic field H_x created by a 250 nm Micromod magnetic particle in function of its position on the sensor. The particle has a magnetic moment parallel to the sensor plane and it was assumed that the particle is 0.2 μm above the sensor.

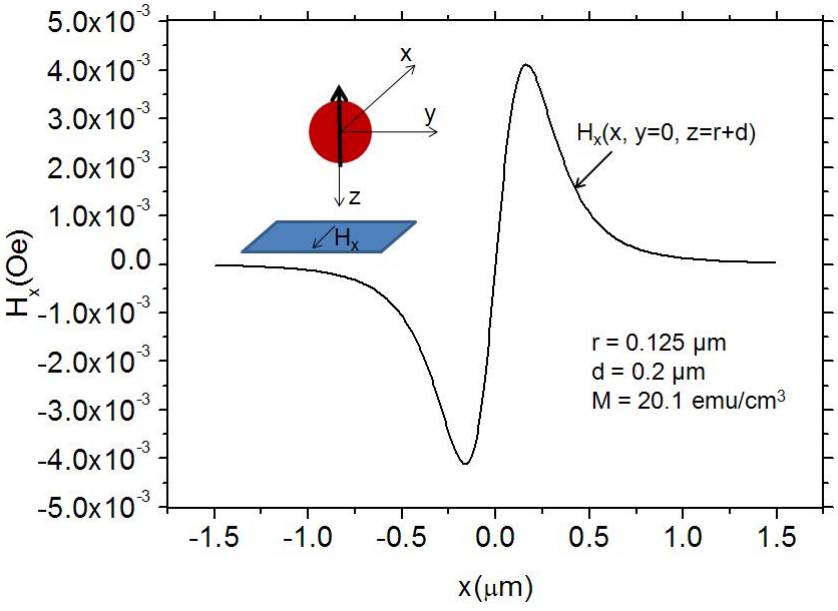

Figure 3.4: Transverse magnetic field H_x created by a 250 nm Micromod magnetic particle in function of its position on the sensor. The particle has a magnetic moment perpendicular to the sensor plane and it was assumed that the particle is 0.2 μm above the sensor.

$d = 0.2$ μm above the surface. The average magnetic fringe field of a label was calculated using an analytical expression presented by Li *et al.* in [54].

When the moment of the particle is parallel to the sensor plane, figure 3.3 shows that for

positions where $y = 0$, i.e. $(x, 0, r + d)$, the fringe field is negative for $|x| < 0.250$ μm and positive otherwise. As observed in figure 3.5, when the particle is outside the sensor the average fringe field is positive. When the particle is in the sensor area, this average field is higher and is negative. This was already observed experimentally for magnetic tunnel junctions [52] and for spin valve [53].

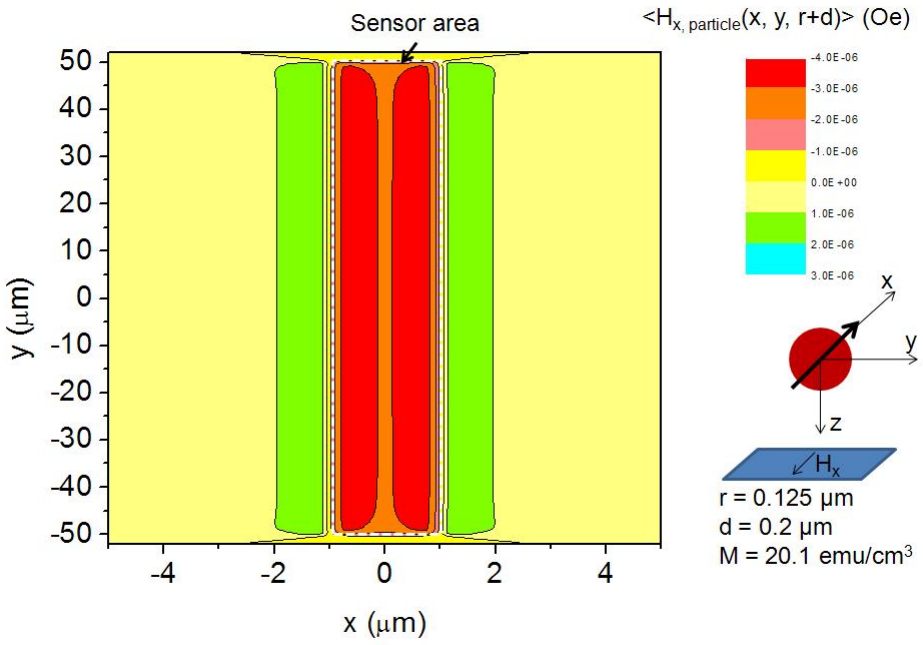

Figure 3.5: Average transverse magnetic field $< H_x >$ in the sensor area in function of the particle (x,y) position. The particle is assumed to be a at distance of d = 0.2 μm and to have a moment parallel to the sensor plane.

In the case where the moment of the particle is perpendicular to the sensor plane, a maximum positive and negative field is observed for $x \sim 0.15$ μm and $x \sim -0.15$ μm, respectively (see figure 3.4. Therefore, as observed in figure 3.6, a magnetic particle in the center of the sensor contributes with an average fringe field equal to zero and the maximum signals are attained in the edges of the sensor.

In conclusion, for each magnetizing field configurations the place where the biomolecular probes are positioned need to be carefully chosen in order to obtain a maximum signal from the biomolecular recognition event. This topic will be discussed in detail in chapter 4.

3.3 General conclusions

In this chapter, an overview of the characteristics of nanometer size superparamagnetic particles was accomplished. The Nanomag-D 130 nm and 250 nm from Micromod particles showed higher susceptibility than the ones from Ademtech with approximately the same size. Furthermore, as will be showed in more details on chapter 5, under a field of 15 Oe they show a theoretically

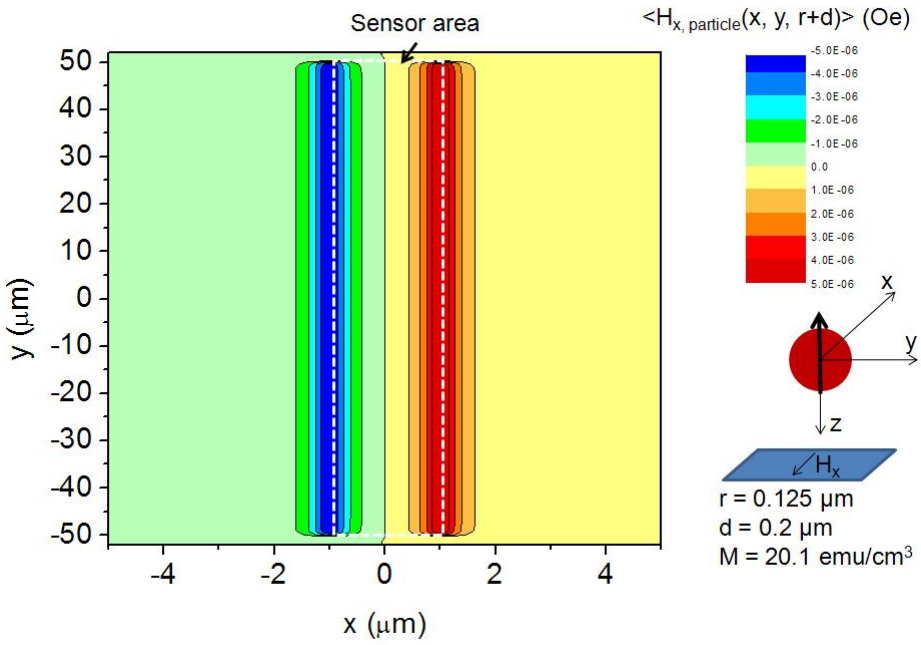

Figure 3.6: Average transverse magnetic field $< H_x >$ in the sensor area in function of the particle (x,y) position. The particle is assumed to be a at distance of d = 0.2 μm and to have a moment perpendicular to the sensor plane.

measurable signal. Joining the fact that they are nanometer-sized, these particles were chosen as labels for the rest of the thesis.

The presented 10 nm particles were only studied in a later period time of this thesis. Although few detection tests were achieved with these particles using the available magnetoresistive sensors, these results are not included in this thesis since it was found that the sensors were too large and therefore the signal too low to have a convincing detection. Nevertheless, the characteristics of these particles were compared in this chapter to larger ones and the results envisage a promising usage of them as labels providing the sensor area is reduced at least one order of magnitude.

Chapter 4

Magnetoresistive sensors for biochip applications

This chapter describes in detail de requirements for the design, fabrication and measurement of magnetoresistive sensors in a specific biological application. Two different types of magnetoresistive sensors (magnetic tunnel junction (MTJ) and spin valves (SV)) are introduced, discussed and compared in their ability to detect magnetic particles. The part of this work related to the spin valve usage for 250 nm magnetic particles detection had already been performed by a previous work [21]. All the experimental results obtained were from my own work with the exception of the ones presented in section 4.1.2 which were obtained in collaboration to with a master degree student.

The chapter is divided in four main sections. In the first section, an overview on the design of those sensors for biochip applications is accomplished and includes a general overview of the needs in biological applications, sensor engineering and design, and a summary of the different measuring systems. After that, MTJ and SV chips used in this thesis are described in detail. Their sensitivity to magnetic particles is discussed and finally a comparison of the performance of the two sensors is made.

4.1 General chip design

4.1.1 Magnetic particle average fringe field in the sensing area

The design of magnetoresistive biochips has been optimized not only to fit with the fabrication and detection systems constrains but also in order to meet the requirements of bioassay applications. These requirements mainly include:

- **Limit of detection**: the minimum concentration of the biological entity that is required to be detected.
- **Biological dynamic range**: the ability to distinguish between different concentrations of the biological target.

One of the aspects that has to be addressed in order to fulfill these requirements is the biological active area which is the area of the chip where the bio-probes will be immobilized. This area should be in optimal condition covered by the magnetoresistive sensor but in some architectures this may not be true. The biological active area is directly related with another important parameter, the biological sensitivity. This sensitivity is related to the fact that the probability of capturing one specific target biomolecule that diffuses in the test solution is proportional to the number of active probe biomolecules on the surface.Therefore, the increase of the biological active area will increase the biological sensitivity. On the other hand, the dynamic range of the sensor is directly proportional to the sensor area since a larger number of magnetic particles fit in the sensor area and can therefore be detected. However, as can be observed in figure 4.1, the average magnetic fringe field of a magnetic particle in the sensor area decreases with the increase of the sensor area. This fact directly limits the sensitivity of the sensor to magnetic particles. As the particles are used for labeling the target biomolecules, the limit of detection will therefore decrease with the increase of the sensor area. Thus, a compromise between limit of detection, dynamic range and biological sensitivity has to be made. Small sensors will be used for applications demanding low target concentration detection and small dynamic range (i.e. yes/no detection such as in disease diagnostics) while large sensors will be used for applications requiring larger dynamic ranges and higher target concentration detection (i.e. gene expression analysis, disease monitoring...).

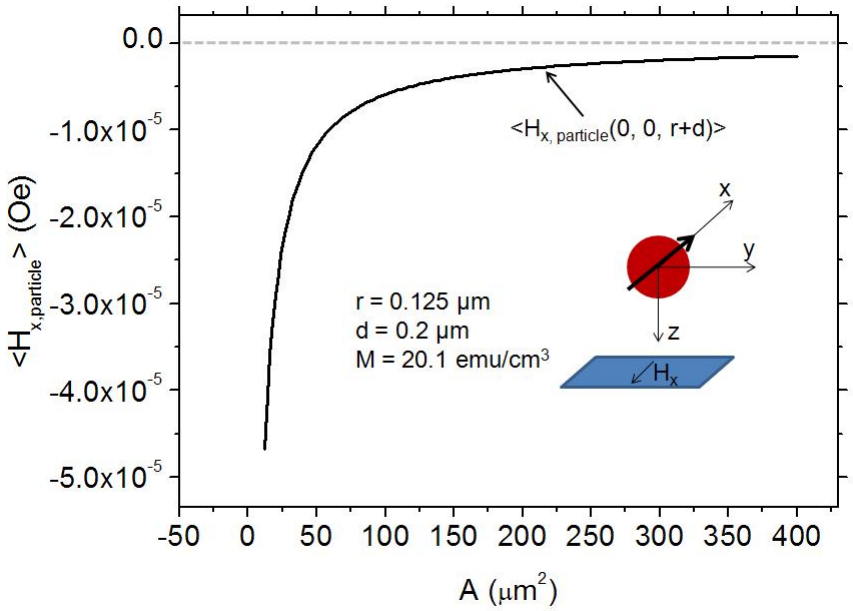

Figure 4.1: Average magnetic field of one particle in the center of the sensing area in function of the sensor area.

The first approach of magnetoresistive biochips was proposed by a group in the Naval Research Laboratory (USA) [7]. The BARC chip comprised 8 biological active areas with eight 5×80 μm^2 GMR sensors each. The probe biomolecule was spotted in each area with ~ 250 μm

in diameter. Since the sensors only covered $\sim 10\%$ of the biological active area and the magnetic particles outside the sensors are not detected, $\sim 90\%$ of the target molecule recognized by the probes were not detected. To overcome this limitation, a later version of the BARC chip was fabricated including a serpentine shape GMR sensor [8]. This sensor covered 70% of a biological active area with ~ 200 μm in diameter increasing the total amount of detected target molecules.

This idea of covering the biological active area with a sensor was further improved by a group in the University of Bielefeld. They developed a spiral shaped GMR sensor with a diameter of 70 μm in order to fit a spot of 100 μm in diameter. A chip with 206 sensing areas was used for biomolecular recognition and further compared favorably with a fluorescence-based system [9].

In parallel, another approach was pursued by INESC-MN group in order to reduce the sensor area while maintaining the same spot diameter. The goal is to increase the sensitivity of the system by attracting the magnetically labeled biomolecules into a smaller sensor area. In this architecture, one [10] or two [11] current lines were used to focus labeled biomolecules onto the sensor area. The effective biological active area is therefore reduced to the sensor area. In the case where two current lines were used, 2×6 μm^2 spin valve sensors were used for high sensitivity and low dynamic range biological experiments. Later, a chip was designed with a larger sensor (U-shaped 2.5×80 μm^2 spin valve sensor) in order to be used for gene expression experiments related to the Cystic Fabrosis disease [10]. The two current lines were replaced by a single U-shaped current line. The final chip comprised 25 spin valve sensors.

Another approach first proposed by a group in Stanford [12] and also followed at INESC-MN [105] was to immobilize the biomolecular probe in a specific area. The idea is to include in the microfabrication process a step where a specific biological active area is deposited on top of the sensor area. Upon spotting, the probes are only immobilized on this biological active area. This fact implies that the target biomolecule can only be specifically attached to this area, which corresponds to the sensitive layer. Therefore, it is no longer needed to have large sensors fitting the whole spotting area. The material used for this biological active area is different from group to group: the Stanford group used a bilayer of polymers PEI/PMMA while the INESC-MN group used a gold thin film to immobilize the biomolecular probes.

Another important aspect in the optimization of the sensor sensitivity to magnetic particles is the distance between the sensor free layer and the magnetic particle itself. Usually, in the microfabrication process, one of the last steps is to deposit a passivation layer (see chapter 2). The goal of this layer is to protect the sensor from possible corrosion caused by biochemical solutions used in the bioassays. For example, in the chips fabricated at INESC-MN the metallic contacts of the sensors are 300 nm thick (see chapter 2). Therefore, a passivation layer with at least 300 nm in thickness has to be deposited. As shown in figure 4.2 the average fringe field of a magnetic particle on the sensor area rapidly decreases with increased distance between the particle and the sensor free layer. Thus, the thickness of the passivation layer should be as small as possible. In the spin valve chips fabricated here at INESC a bilayer of 100 nm Al_2O_3/200 nm SiO_2 was used. In the Philips group this layer was even thicker (500 nm of SiN_x) in order to assure chip robustness [25]. Another approach was followed by the Stanford group. A two step passivation layer was used in order to have a thicker layer (SiO_2(100nm)/Si_3N_4(150nm)/SiO_2(100nm)) on

top of the contact and a thinner layer (SiO_2(10nm)/Si_3N_4(20nm)/SiO_2(10nm)) over the sensing area improving the signal while maintaining the sensor contact safe from corrosion [26].

In these spin valve sensors the current is passing in-plane through the sensor (CIP configuration). Therefore, there is only the passivation layer between the sensor free layer and the magnetic particles. However, in chips using magnetic tunnel junction sensors the current is passing through the sensor perpendicularly to the plane plane (CPP configuration). Therefore, besides the passivation layer, a metallic contact of at least 50 nm is additionaly separating the particles from the sensor free layer. This fact reduces the sensitivity MTJ to magnetic particles [98]. The Stanford group has proposed to replace the standard aluminium contact by gold as the top contact of the MTJ [95]. As the gold does not suffer from corrosion and can simultaneously be used as the biological active area, there is no need for an additional passivation layer on top of the sensor.

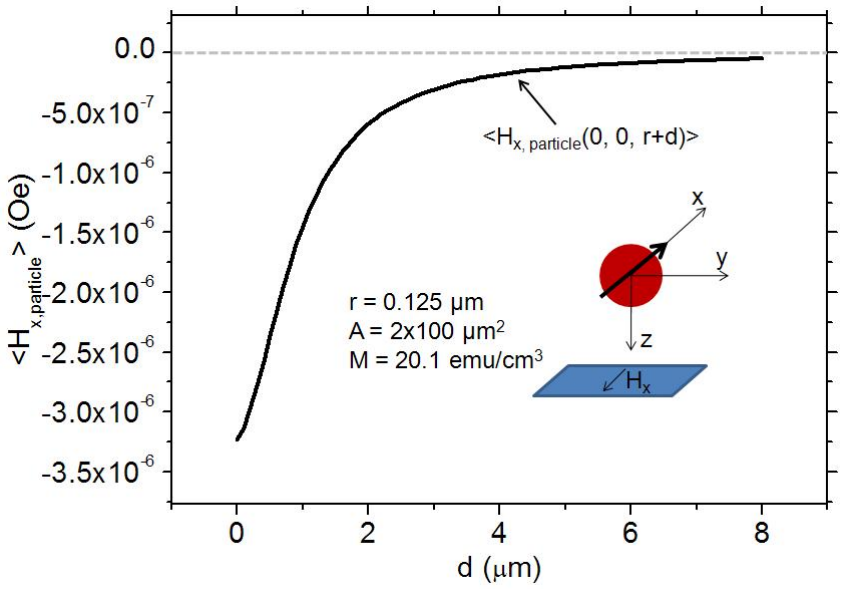

Figure 4.2: Average magnetic field of one particle in the center of the sensing area in function of the separation between the sensor and the particle.

4.1.2 Magnetoresistive sensor linearization

In this chapter, two magnetoresistive sensors (MTJ and SV) are used to detect magnetic particles. Although their transport mechanism is based on two different physical principles, their magnetic behavior is the same. Both sensors comprise two ferromagnetic layers: the pinned and free layer (figure 4.3).

A standard pinned layer comprises a ferromagnetic layer coupled with an anti-ferromagnetic layer. The interaction between these two layers fixes the orientation of the ferromagnetic layer to a specific direction. The magnetization of the ferromagnetic layer can only be reversed at fields above the exchange field (H_{exch}). This field can be as high as 500 Oe for pinned layers

comprising a single ferromagnetic and anti-ferromagnetic layer. H_{exch} can be further improved to fields up to 1000 Oe using synthetic anti-ferromagnetic (SAF) structures. The SAF structures include two ferromagnets separated by a thin Ru layer. The two magnetic layers are coupled anti-ferromagnetically as described by the RKKY theory. One of the ferromagnetic layers is further coupled to an anti-ferromagnetic layer. SAF structures are commonly used in MTJ sensors.

The free layer is typically composed by a single ferromagnetic layer. A bilayer comprising a hard and a soft ferromagnet can be also used. This can be used to soften the overall bilayer while maintaining the favorable properties of a hard ferromagnetic layer in the sensor signal. In this work, this approach is used in spin valve sensors. Finally, the free layer can be composed by two ferromagnetic layers separated by a Ru layer as the SAF in the pinned layer. This structure is called a synthetic free layer but will not be used along this thesis.

The free and pinned layers are separated by a non-magnetic layer which can be either oxide (MTJ sensor) or metal (SV sensor).

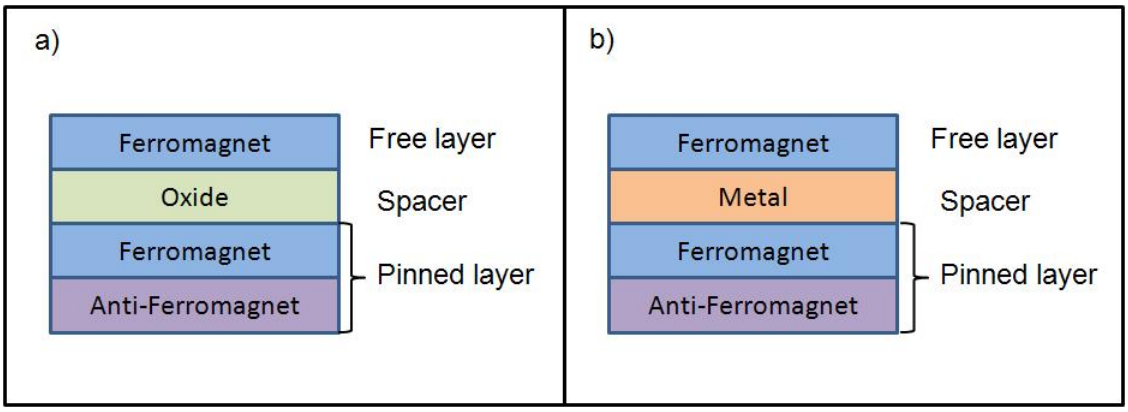

Figure 4.3: a) Global structure of a MTJ sensor comprising a magnetic free and pinned layers and a oxide spacer. b) Global structure of a SV sensor comprising a magnetic free and pinned layers and a metallic spacer.

In this section, a model assuming magnetic mono-domains for pinned and free layer is presented. An analysis of the free layer energy is further made in order to determine the conditions needed for the linearization of a magnetoresistive sensor. This analysis is divided in two different configurations of the free and pinned layers: the pinned and free layer easy axis are parallel (parallel anisotropies) , and the pinned and free layer easy axis are perpendicular (crossed anisotropies).

Parallel anisotropies

In the parallel anisotropies configuration (figure 4.4), the energy of the free layer normalized by its volume can be calculated considering the contribution of the following energy terms:

- Zeeman term: $-\mu_0 \mathbf{H} \cdot \mathbf{M^f}$ where $\mathbf{H}$ is the external applied field, and $\mathbf{M^f}$ is the magnetization of the free layer.
- Crystalline anisotropy term: $K \sin^2\theta$ where $K = \frac{1}{2}\mu_0 H_k M_s^f$ and M_s^f is the saturation magnetization of the free layer.
- Demagnetizing field of the free layer: $-\frac{1}{2}\mu_0 \mathbf{H_d^f} \cdot \mathbf{M^f}$ where $\mathbf{H_d^f}$ is the demagnetizing field of the free layer, and $\mathbf{M^f}$ is the magnetization of the free layer.
- Demagnetizing field of the pinned layer: $-\mu_0 \mathbf{H_d^p} \cdot \mathbf{M^f}$ where $\mathbf{H_d^p}$ is the demagnetizing field of the pinned layer, and $\mathbf{M^f}$ is the magnetization of the free layer.
- Néel term: $-\mu_0 \mathbf{H_N} \cdot \mathbf{M^f}$ where $\mathbf{H_N}$ is the Néel field, and $\mathbf{M^f}$ is the magnetization of the free layer.

The energy of the free layer normalized by its volume is given by the sum of all these energy terms:

$$\frac{E_f}{V} = -\mu_0 \mathbf{H} \cdot \mathbf{M^f} + K \sin^2\theta - \frac{1}{2}\mu_0 \mathbf{H_d^f} \cdot \mathbf{M^f} - \mu_0 \mathbf{H_d^p} \cdot \mathbf{M^f} - \mu_0 \mathbf{H_N} \cdot \mathbf{M^f} \tag{4.1}$$

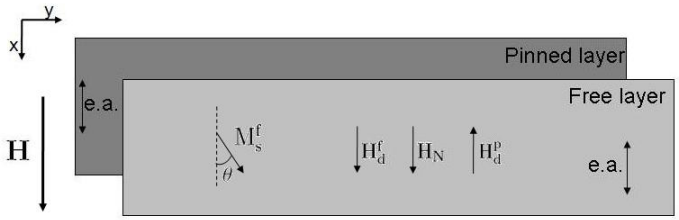

Figure 4.4: Scheme of the studied sensor composed by a pinned layer and a free layer with parallel anisotropies.

In general, the exact demagnetizing field of the free layer can only be calculated numerically. Nevertheless, for some geometries an analytical calculation can be achieved [36]. Therefore, the demagnetizing field can be assumed to be: $\mathbf{H_d^f} = -N_{xx} M_s^f \cos\theta \mathbf{i}$ where M_s^f is the saturation magnetization of the free layer and N_{xx} is the xx component of the demagnetizing matrix N [35]. The energy is then given by:

$$\frac{E_f}{V} = \mu_0 M_s^f \left[\frac{1}{2}\sin^2\theta(H_k - N_{xx}M_s^f) + \frac{1}{2}N_{xx}M_s^f - \cos\theta(H - H_d^p + H_N)\right] \tag{4.2}$$

The first derivative of the energy can be calculated:

$$\frac{\partial \frac{E_f}{V}}{\partial \theta} = \mu_0 M_s^f \sin\theta \left[\cos\theta(H_k - N_{xx}M_s^f) + H - H_d^p + H_N\right] \tag{4.3}$$

The second derivative is also important to calculate the minima of the energy.

$$\frac{\partial^2 \frac{E_f}{V}}{\partial \theta^2} = \mu_0 M_s^f \left[(H_k - N_{xx} M_s^f)(2\cos^2\theta - 1) + \cos\theta (H - H_d^p + H_N) \right] \tag{4.4}$$

The minima of energy are given when the first derivative vanishes:

$$\frac{\partial \frac{E_f}{V}}{\partial \theta} = 0 \Rightarrow \sin\theta \left[\cos\theta (H_k - N_{xx} M_s^f) + H - H_d^p + H_N \right] = 0 \tag{4.5}$$

There are then three possible solutions:

- **1-** $\sin\theta = 0 \Leftrightarrow \theta = 0$ or π
- **2-** $H_k - N_{xx} M_s^f = 0$ and $H - H_d^p + H_N = 0$
- **3-** $\cos\theta = \frac{H - H_d^p + H_N}{N_{xx} M_s^f - H_k}$

In the case of the first solution, looking to the second derivative the following solution appear:

$$\frac{\partial^2 \frac{E_f}{V}}{\partial \theta^2} > 0 \Rightarrow \begin{cases} H > H_d^p - H_N + (N_{xx} M_s^f - H_k) & \text{for } \theta = 0 \\ H < H_d^p - H_N - (N_{xx} M_s^f - H_k) & \text{for } \theta = \pi \end{cases} \tag{4.6}$$

If $H_k > N_{xx} M_s^f$, this solution show that there are only two possible states for the orientation of the free layer: $\theta = 0$ and $\theta = \pi$. Therefore, the magnetic response of the sensor will be described as in figure 4.5. As observed, the component $N_{xx} M_s^f - H_k$ defines the field at which occurs the state change while $H_d^p - H_N$ shifts the whole curve.

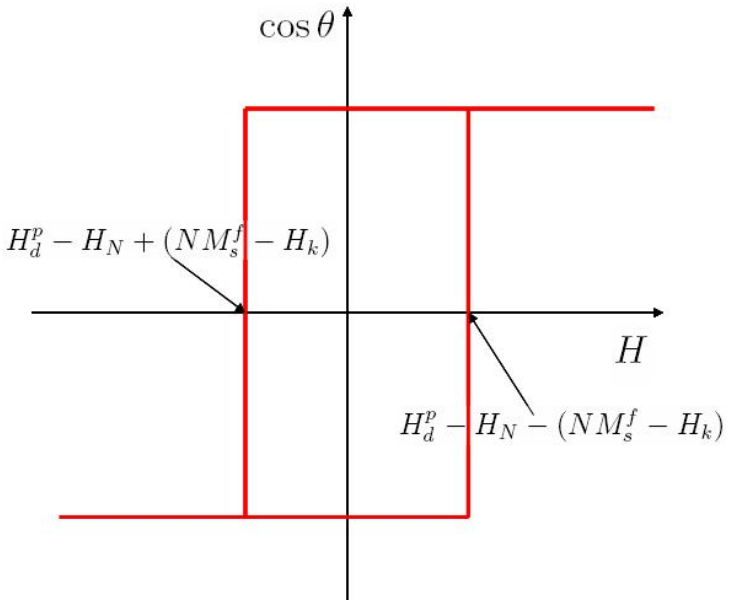

Figure 4.5: Transfer curve with hysteresis.

However if $H_k < N_{xx}M_s^f$, this solution gives an incomplete magnetic response curve. To complete the curve the third solution is taken into account. It is easy to demonstrate that this solution corresponds to a minimum of the energy if $H_k < N_{xx}M_s^f$ and to a maximum otherwise. In the case of $H_k = N_{xx}M_s^f$, all the derivatives vanish and nothing can be concluded. Therefore a linear magnetic response curve (figure 4.6) is obtained if the demagnetizing field is higher than the H_k of the material. As observed, the component $N_{xx}M_s^f - H_k$ defines the field at which the response starts to be linear while $H_d^p - H_N$ shifts the whole curve. The sensitivity of the sensor will be proportional to the slope (slope$= \frac{1}{N_{xx}M_s^f - H_k}$) as observed in figure 4.6. An increase of the demagnetizing field will reduce the slope and therefore the sensor sensitivity. However, as will be discussed in next sections, a high demagnetizing field is important to stabilize the free layer and achieve a linear sensor.

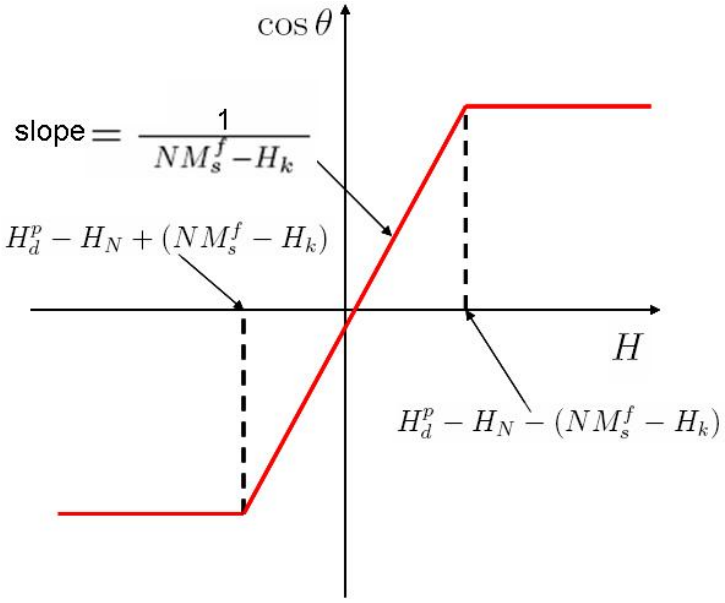

Figure 4.6: Linear transfer curve.

In summary, for parallel anisotropies there are two possible magnetic response of the sensor:

- if $H_k > N_{xx}M_s^f$: Hysteresis curve (see figure 4.5)
- if $H_k < N_{xx}M_s^f$: Linear curve (see figure 4.6)

Crossed anisotropies

In the crossed anisotropies configuration (see figure 4.7), the energy of the free layer normalized by its volume can be calculated considering the contribution of the following energy terms:

- Zeeman term: $-\mu_0 \mathbf{H} \cdot \mathbf{M^f}$ where $\mathbf{H}$ is the external applied field, and $\mathbf{M^f}$ is the magnetization of the free layer.

- Crystalline anisotropy term: $K\cos^2\theta$ where $K = \frac{1}{2}\mu_0 H_k M_s^f$ and M_s^f is the magnetization of the free layer.
- Demagnetizing field of the free layer term: $-\frac{1}{2}\mu_0 \mathbf{H_d^f} \cdot \mathbf{M^f}$ where $\mathbf{H_d^f}$ is the demagnetizing field of the free layer, and $\mathbf{M^f}$ is the magnetization of the free layer.
- Demagnetizing field of the pinned layer term: $-\mu_0 \mathbf{H_d^p} \cdot \mathbf{M^f}$ where $\mathbf{H_d^p}$ is the demagnetizing field of the pinned layer, and $\mathbf{M^f}$ is the magnetization of the free layer.
- Néel term: $-\mu_0 \mathbf{H_N} \cdot \mathbf{M^f}$ where $\mathbf{H_N}$ is the Néel field, and $\mathbf{M^f}$ is the magnetization of the free layer.

The energy of the free layer normalized by its volume is in this case given by:

$$\frac{E_f}{V} = -\mu_0 \mathbf{H} \cdot \mathbf{M^f} + K\cos^2\theta - \frac{1}{2}\mu_0 \mathbf{H_d^f} \cdot \mathbf{M^f} - \mu_0 \mathbf{H_d^p} \cdot \mathbf{M^f} - \mu_0 \mathbf{H_N} \cdot \mathbf{M^f} \tag{4.7}$$

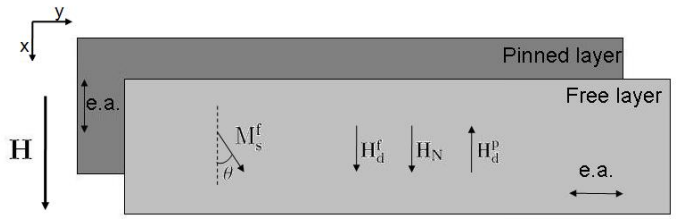

Figure 4.7: Scheme of the studied sensor composed by a pinned layer and a free layer with crossed anisotropies.

Similarly to the previous case, the demagnetizing field is assumed to be $\mathbf{H_d^f} = -N_{xx} M_s^f \cos\theta \mathbf{i}$. Thus, the energy can be written:

$$\frac{E_f}{V} = \mu_0 M_s^f \left[\frac{1}{2}\cos^2\theta (H_k + N_{xx} M_s^f) - \cos\theta (H - H_d^p + H_N)\right] \tag{4.8}$$

The first derivative of the energy can be calculated:

$$\frac{\partial \frac{E_f}{V}}{\partial \theta} = \mu_0 M_s^f \sin\theta \left[H - H_d^p + H_N - \cos\theta (H_k + N_{xx} M_s^f)\right] \tag{4.9}$$

The second derivative is also important to calculate the minima of the energy.

$$\frac{\partial^2 \frac{E_f}{V}}{\partial \theta^2} = \mu_0 M_s^f \left[(H_k + N_{xx} M_s^f)(1 - 2\cos^2\theta) + \cos\theta (H - H_d^p + H_N)\right] \tag{4.10}$$

The minima of energy are given when the first derivative vanishes:

$$\frac{\partial \frac{E_f}{V}}{\partial \theta} = 0 \Rightarrow \sin\theta \left[H - H_d^p + H_N - \cos\theta (H_k + N_{xx} M_s^f)\right] = 0 \tag{4.11}$$

There are then two possible solutions because $H_k + N_{xx}M_s^f$ is always positive:

- **1-** $\sin\theta = 0 \Leftrightarrow \theta = 0$ or π
- **2-** $\cos\theta = \frac{H - H_d^p + H_N}{N_{xx}M_s^f + H_k}$

In the case of the first solution, looking to the second derivative the following solution appear:

$$\frac{\partial^2 \frac{E_f}{V}}{\partial\theta^2} > 0 \Rightarrow \begin{cases} H > H_d^p - H_N + (N_{xx}M_s^f + H_k) & \text{for } \theta = 0 \\ H < H_d^p - H_N - (N_{xx}M_s^f + H_k) & \text{for } \theta = \pi \end{cases} \tag{4.12}$$

Contrary to the parallel anisotropies, in this case a linear magnetic response curve (figure 4.8) is the only possible solution because $N_{xx}M_s^f + H_k$ is always positive. As observed, the component $N_{xx}M_s^f + H_k$ defines the field at which the response starts to be linear while $H_d^p - H_N$ shifts the whole curve. The sensitivity of the sensor will be proportional to the slope (slope $\frac{1}{N_{xx}M_s^f + H_k}$) as observed in figure 4.8.An increase of the demagnetizing field will reduce the slope and therefore the sensor sensitivity. In principle in this configuration, the sensor should be designed to have no demagnetizing field. However, as will be discussed in next sections, the demagnetizing field is important to stabilize the free layer and achieve a linear sensor.

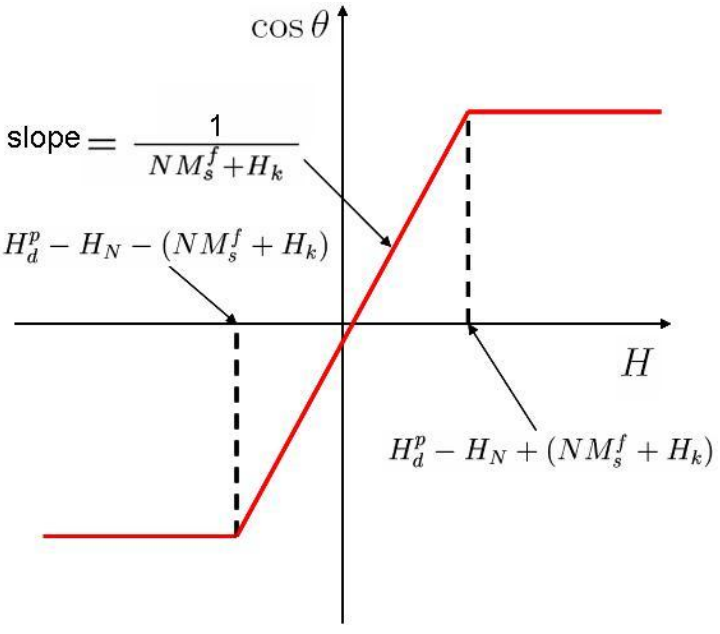

Figure 4.8: Linear transfer curve.

Demagnetizing field calculation

In the model presented above, the demagnetizing field of the free layer is a key factor in the linearization of a magnetoresistive sensors, specially in parallel anisotropies. Therefore, an

analysis of the demagnetizing field is important to understand which are the best geometries to use in order to obtain linear magnetoresistive sensors. The demagnetizing field of a magnetic layer is given by the following expression [28]:

$$\mathbf{H}_{demag}(\mathbf{r}) = -\int_V \frac{\nabla \cdot \mathbf{M}(\mathbf{r}')(\mathbf{r}-\mathbf{r}')}{|\mathbf{r}-\mathbf{r}'|^3} d^3r' + \int_S \frac{\hat{n} \cdot \mathbf{M}(\mathbf{r}')(\mathbf{r}-\mathbf{r}')}{|\mathbf{r}-\mathbf{r}'|^3} d^2r' \tag{4.13}$$

The first integral is over the whole volume V of the magnetic layer while the second integral is over the surfaces S with magnetic poles; $\hat{n}$ is the unitary vector normal to each surfaces.

Magnetoresistive sensors usually use thin magnetic layers. Assuming the magnetization is along the direction of the thickness, the surfaces with the magnetic poles will be very close to each other and the H_{demag} will be very high. Therefore, it can be assumed that the magnetization is always in the sensor plane. The demagnetizing field is then dependent on the lateral surface of the magnetic thin film. Therefore, in the same way the shorter the sensor width is the higher H_{demag}. For the magnetic materials used in magnetoresistive sensors, the magnetization may vary from 800 emu/cm^3 (NiFe) up to 1500 emu/cm^3 (CoFe). In this range of values, with parallel anisotropies, width lower than 3 μm and aspect ratios above 1:5 are needed to linearize magnetoresistive sensor. By decreasing the width, the magnetic layer is more stable but the sensitivity of the sensor will also be lower. In the case of parallel anisotropies, theoretically it would not be necessary to adjust the shape to attain a linear sensor. However, it is always good to have a shorter dimension in the pinned layer direction to stabilize the free layer.

Another approach to increase the demagnetizing field is to use a thicker free layer. By doing that, the surface of the poles is enlarged leading to an increase the H_{demag}.

In order to simulate the demagnetizing fields of the sensor, the integral of equation 4.13 has to be solved. In general, there is not an analytical solution for this integral. However, in the literature solutions for specific geometries and approximations can be found [28], [36], [35].

Comparison between the model and experimental results

The model using mono-domain magnetic layers described previously is now compared to experimental results. This work was done in collaboration with a master degree student which has used samples from the three machines available at INESC-MN (N300, N3600 and N2000). In this section, only the results concerning the N3600 system will be presented. Further results for the other deposition systems can be found in [29].

In a MgO magnetic tunnel junction deposited in the N3600 ion beam deposition system, usually a CoFeB layer (in this case $(Co_{70}Fe_{30})_{80}B_{20}$) is used as free layer. The magnetic characteristics of this layer should be independent of its thickness. However, as we go down in the thickness the magnetization of this layer decreases (figure 4.9). This is due to the fact that a magnetic layer has some atomic layers in the interfaces which are magnetically "dead" and therefore do not contribute its global magnetization. For lower thicknesses the contribution of these "dead" layers is more relevant and therefore a decrease in the magnetization value is observed.

On the other hand, the coercive (H_c) and the crystalline anisotropy (H_k) fields are increasing

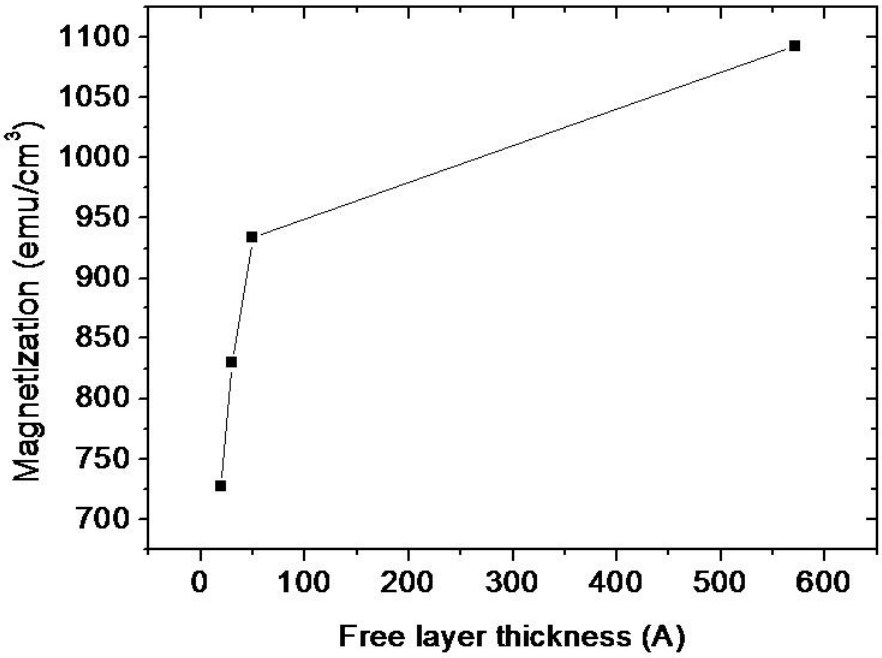

Figure 4.9: Magnetization of the $(Co_{70}Fe_{30})_{80}B_{20}$ in function of the layer thickness after annealing at 280°C during 1h under a magnetic field of 1T.

for 20 Å thicknesses (figure 4.10). Nevertheless, the Néel coupling field H_f is constant for all thicknesses. This fact was expected since the Néel coupling depends on the roughness of the layer on top of which the magnetic material was deposited. All these measurements were done using a VSM system (see section 2.2.1)

A MTJ with a MgO barrier was deposited (in the N3600 system) on a glass substrate with the following structure: Ta 50 Å / Ru 150 Å / Ta 200 Å / $(Co_{70}Fe_{30})_{80}B_{20}$ 80 Å / MgO 18 Å / $(Co_{70}Fe_{30})_{80}B_{20}$ 35 Å / Ru 9 Å / $Co_{80}Fe_{20}$ 25 Å / $Mn_{74}Ir_{26}$ 150 Å / Ta 50 Å . The free and pinned layers were deposited with crossed anisotropies under a 100 Oe magnetic field. The MTJs were further patterned with widths and lengths ranging from 1 to 3 μm and from 10 to 55 μm, respectively. This allowed for an analysis of the linearity of the MTJ not only as function of its width but also as function of its aspect ratio. As deposited the tunneling magnetoresistance ratio (section 4.2.1) of these MTJs is not higher than 20 %. This ratio was further increased up to 60 % by annealing the sample at 300°C during 1h under a magnetic field of 1T. This annealing is important to crystalize the MgO and the CoFeB electrodes. However, doing this the magnetic layers easy axis anisotropies are reset to parallel anisotropies. Therefore, the MTJ transfer curves were compared with the model including parallel anisotropies.

Figure 4.11 shows the global evolution of transfer curves varying the dimensions in simulated or experimental sensor. For the top and bottom curves, the experimental sensor exhibited the same behavior than the simulated curve (i.e. a hysteresis curve when the long direction is in the easy axis direction and a linear curve otherwise). Therefore, in these extreme conditions the model agrees with the experimental results. However, in the case where the width of the MTJ

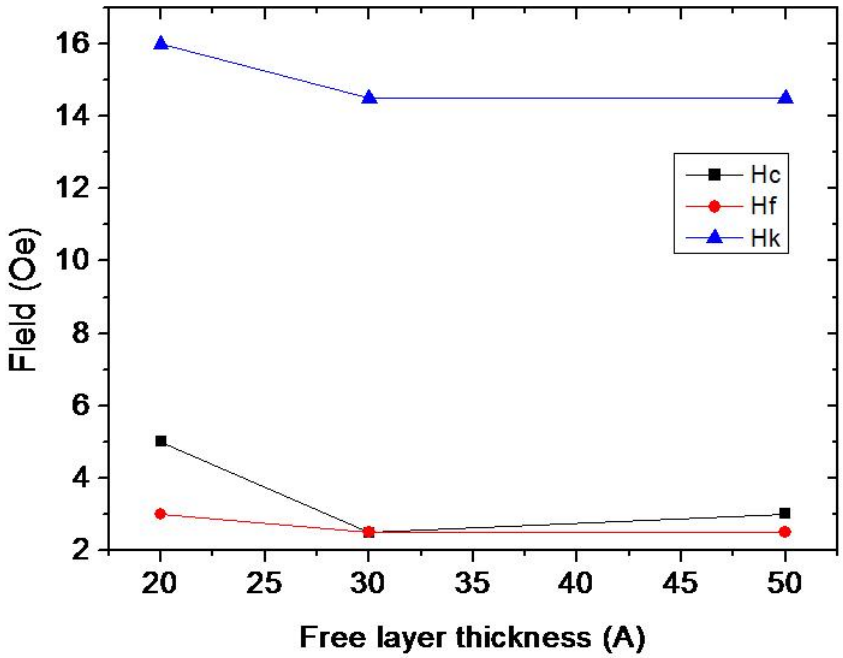

Figure 4.10: Hk, Hc and Hf of the $(Co_{70}Fe_{30})_{80}B_{20}$ as function of the layer thickness.

is 2 μm, a linear transfer curve was expected by the presented model. However, experimentally a mixture of linear response and hysteresis is observed. This means that the free layer of the MTJ is not behaving as a mono-domain. In order to model exactly this observed behavior, a micro-magnetic simulation has to be done.

For the biochip applications, it is important to know the sensitivity of the magnetic sensor. Although the proposed model is unable to predict transition cases, it can be used to predict the sensitivity of the MTJs when they show a linear response. Figure 4.12 shows that in MTJs with low or zero coercivity the measured sensitivity agrees with the one predicted.

In order to determine the best aspect ratio and the best thicknesses of the free layer giving a linear sensor, two more MTJ were processed with the same structure but with different free layer thicknesses (150 Å and 250 Å). In general, linear responses were measured in MTJ with aspect ratio higher that 30 and thick free layers (figure 4.13). In fact, few MTJs with 80 Å thick free layer exhibited linear responses and only with high aspect ratios. A decrease in sensitivity with the increase of the free layer thickness was also observed. This can be explained by the fact that the magnetization and therefore the demagnetization field of the free layer increase with its thickness (figure 4.9). Thus, as the sensor sensitivity is inversely proportional to the demagnetizing field, the sensor sensitivity should decrease with the increase of the free layer thickness.

In conclusion, the model assuming a mono-domain free layer can be used to predict the sensitivity of a MTJ when low or no coercivity is experimentally observed. These conditions are only attained in sensors with a width below 2 μm, an aspect ratio above 30 and free layer

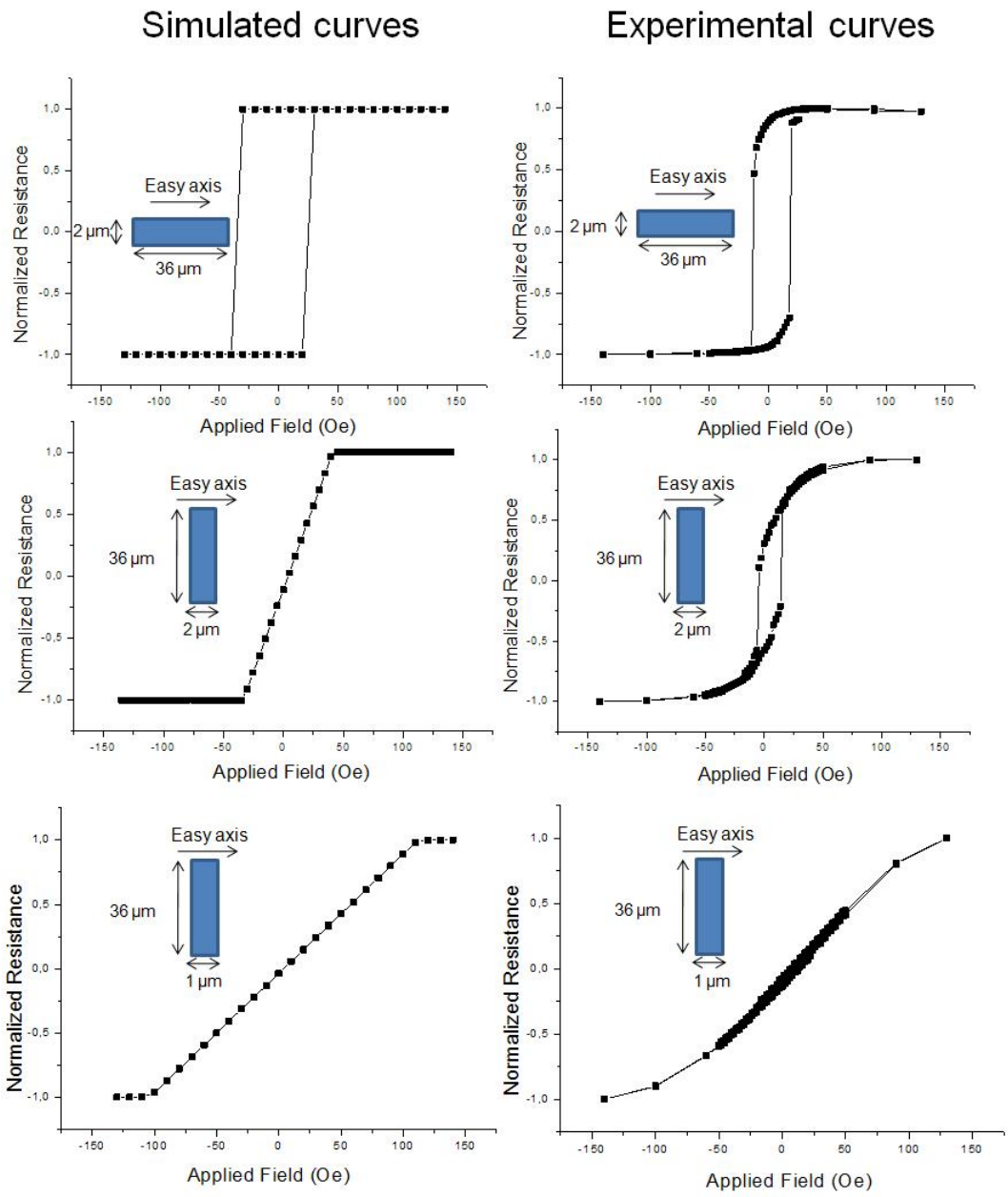

Figure 4.11: Comparison of the evolution of the experimental sensor transfer curve (right) and the modeled sensor transfer curve (left).

thicknesses above 100 Å for a CoFeB layers with a saturation magnetization and a crystalline anisotropy (H_k) of 1000 emu/cm^3 and 14 Oe, respectively.

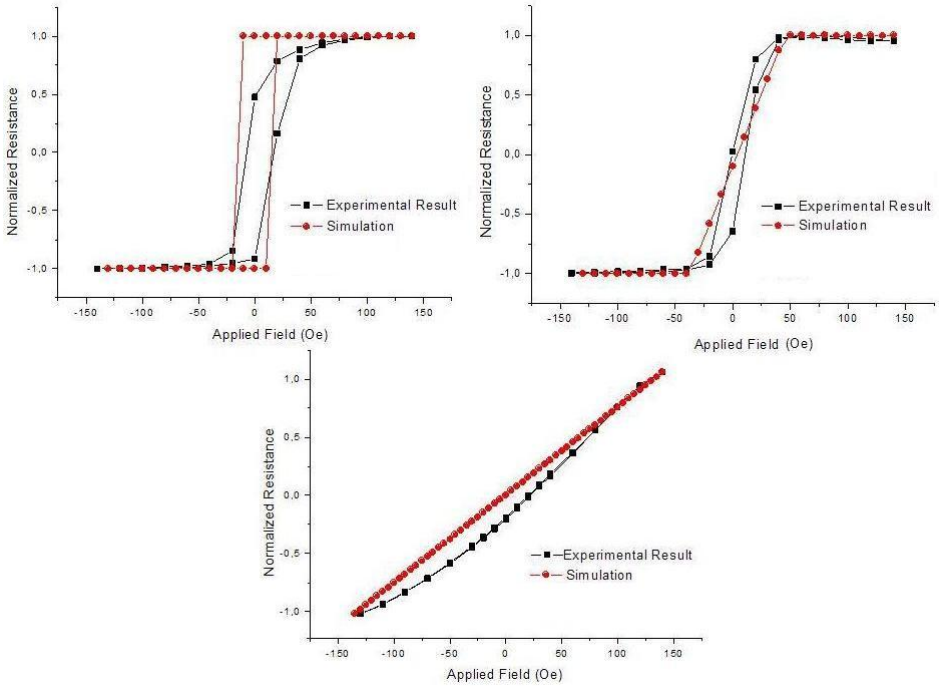

Figure 4.12: Comparison of the sensitivity of experimental sensor transfer curve and the modeled sensor transfer curve.

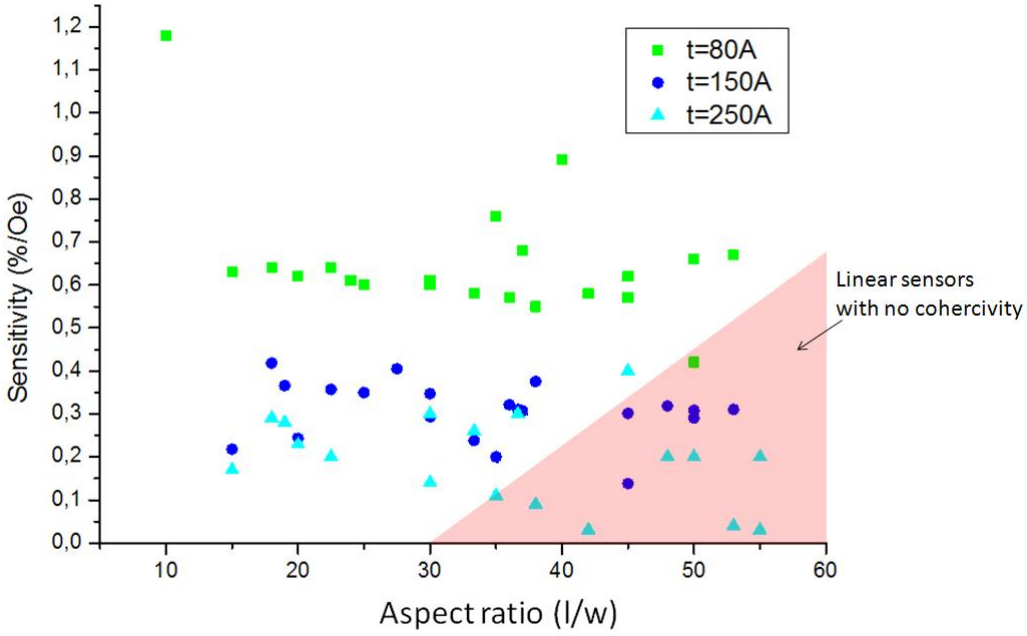

Figure 4.13: Sensitivity of magnetic sensors as function of their aspect ratio and free layer thickness.

4.1.3 Effect of magnetic layers on the magnetic particle position

The magnetic field generated by the magnetic layers of a sensor have been proved to have an important role in the detection of magnetic particles [23]. In fact the magnetic fields created by the ferromagnetic layers of a sensor are non-negligible when compared to the magnetic fields used in the detection of magnetic particles. Therefore, it is important to take them into account when performing these measurements.

Besides the amplitude of these magnetic fields, the magnetic layers also generate non-negligible magnetic gradient. These gradients may interfere in the particles position on the sensors. In this section these magnetic gradients are studied and experimental observations in different structures are compared to the theoretically expected behavior of magnetic particles.

Once introduced near a magnetoresistive sensor, a magnetic particle responds to the demagnetizing fields generated by the sensor free and pinned layers. The sum of these fields $\mathbf{H}$ induce not only a change in the magnetic moment $\mathbf{m}$ of the particle but also in its magnetic energy: $E_m = -\mu_0 \mathbf{m} \cdot \mathbf{H}$, where μ_0 is the magnetic permeability of the vacuum.

In a first experiment, a MTJ deposited by ion beam in a N3600 system with the structure 50 Å / Ru 100 Å / $Mn_{74}Ir_{26}$ 150 Å / $Co_{80}Fe_{20}$ 30 Å / Ru 9 Å / $(Co_{70}Fe_{30})_{80}B_{20}$ 40 Å / MgO 18 Å / $(Co_{70}Fe_{30})_{80}B_{20}$ 100 Å / Ru 50 Å / Ta 50 Å was used. The pinned layer comprised two anti-ferromagnetically coupled magnetic layers forming a SAF configuration. The easy axis of this layer is along the x-direction (figure 4.14). Due to the shape anisotropy of the sensor ($2 \times 100\ \mu m^2$), when no external field is applied, the free layer magnetization is perpendicular to the pinned layer (section 4.1.2). For the demagnetizing field calculation, magnetizations of 800 emu/cm^3 and 900 emu/cm^3 were used for the 40 Å and 100 Å thick CoFeB. A magnetization of 1400 emu/cm^3 was used for the CoFe layer. The distance between the particles and the sensor free layer was assumed to be 2050 Å corresponding to the total thickness of the Cr/Au used as the sensor top contact.

In this experiment, 10 μL of 250 nm magnetic particles (Micromod, Germany) with a concentration of 5×10^6 particle/μL was introduced on top of the chip. As the particles settle down, they tend to move to the position of the energy minima. As depicted in figure 4.14, in the case of a 50 Oe external magnetic field applied in the parallel or antiparallel direction, the particles agglomerated in the edge of the sensor. This position corresponded to the energy minima in this configuration. In the case, where no external magnetic field is applied, the energy minima are still located at the edge of the sensor. However, as a great amount of particles are used, once the positions in the corner are occupied, the particles should go to the next low energy position. As the energy maxima are located outside the sensor area, the particles are expected to be attracted to the sensor area. However, as can be observed in figure 4.14, the particle instead tend to agglomerate near the top and bottom corners of the sensor.

In fact, in this configuration the free layer of the sensor is along the y-direction. Therefore, the magnetic poles of this layer are located in the top and bottom corner. On the other hand, as the magnetic layers of the pinned layer are antiparallel the overall magnetic field generated from these layers is small. Computing the energy, it was found that energy minima on the top

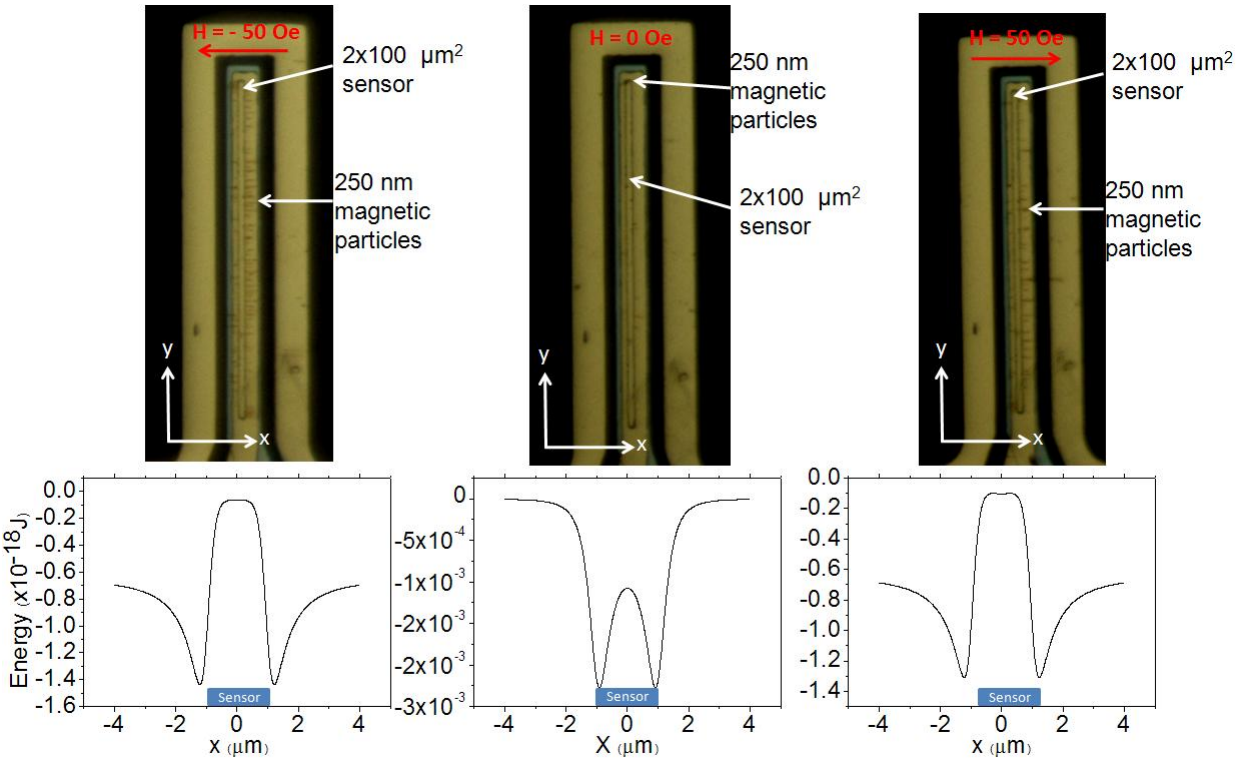

Figure 4.14: Effect of ferromagnetic layers on the position of 250 nm magnetic particle in function of the external magnetic field (-50 Oe, 0 Oe and 50 Oe). The MTJ structure deposited in N3600 system is Ta 50 Å / Ru 100 Å / $Mn_{74}Ir_{26}$ 150 Å / $Co_{80}Fe_{20}$ 30 Å / Ru 9 Å / $(Co_{70}Fe_{30})_{80}B_{20}$ 40 Å / MgO 18 Å / $(Co_{70}Fe_{30})_{80}B_{20}$ 100 Å / Ru 50 Å / Ta 50 Å. The energy was calculated assuming a magnetization of 1400 emu/cm^3 for the CoFe, 800 emu/cm^3 for the CoFeB of the pinned layer and 900 emu/cm^3 for the CoFeB of the free layer.

and bottom corner of the sensor are 500 times higher than those on the right and left edges of the sensor. Thus, the magnetic particles are expected to be attracted to the sensor corners.

As already discussed in chapter 3, when magnetizing the particles in the x-direction, the maximum average magnetic field is obtained for particles on top of the sensor area. For particles positioned on the corner of the sensor, the average field is lower and with the opposite signal.

In order to overcome this limitation, sensors were redesigned in order to attract the magnetic particles into the sensor area. The following three sensors structures were studied

1. Balanced SAF: Ta 50 Å / Ru 180 Å / Ta 30 Å / MnPt 200 Å / $Co_{90}Fe_{10}$ 20 Å / Ru 8 Å / $(Co_{50}Fe_{50})_{80}B_{20}$ 30 Å / MgO 15 Å / $(Co_{50}Fe_{50})_{80}B_{20}$ 100 Å / Ru 50 Å / Ta 50 Å .

2. Unbalanced SAF: Ta 50 Å / Ru 180 Å / Ta 30 Å / MnPt 200 Å / $Co_{90}Fe_{10}$ 20 Å / Ru 8 Å / $(Co_{50}Fe_{50})_{80}B_{20}$ 40 Å / MgO 15 Å / $(Co_{50}Fe_{50})_{80}B_{20}$ 100 Å / Ru 50 Å / Ta 50 Å .

3. Normal pinned layer: Ta 50 Å / Ru 180 Å / Ta 30 Å / MnPt 200 Å / $Co_{90}Fe_{10}$ 20 Å / $(Co_{50}Fe_{50})_{80}B_{20}$ 30 Å / MgO 15 Å / $(Co_{50}Fe_{50})_{80}B_{20}$ 100 Å / Ru 50 Å / Ta 50 Å .

These MTJs were deposited in N2000 sputtering system. For simulation means, magnetiza-

tions of 900 emu/cm^3 and 1000 emu/cm^3 were used for the CoFeB layers with 40 Å and 100 Å in thickness, respectively. For the CoFe layer a magnetization of 1400 emu/cm^3 was assumed.

The first structure is the standard structure of a linear MTJ and was optimized in order to have a maximum TMR. The SAF of this structure is almost balanced meaning that the effective magnetization of the pinned layer is zero. Therefore, there is no magnetic field generated by this layer and the particles will only follow the position of the free layer magnetic poles.

In order to increase the field generated by the pinned layer, an unbalanced SAF was used (structure n°2). The thickness CoFeB layer was increased while maintaining the thickness of the CoFe. Finally, a third sample including a normal pinned layer was fabricated. The field created by the pinned layer in this sample is much higher since both magnetic layers are oriented in the same direction.

In fact, the increase of the magnetic field created by the pinned layer of a MTJ structure dramatically increased the attraction of 250 nm magnetic particles when no external fields were applied. In the case of structure n°1, almost no particles were found on top of the sensor area. In structure n°2, a higher amount of particles in the sensor area was observed while in structure n°3 this area was completely covered (figure 4.15). However, all the energy graphics show a maximum outside the sensor area and minima in the sensor edges. Therefore, the particles should tend to completely cover the sensor.

The magnetic particles area moving into the energy minima by means of the magnetic force generated by magnetic layer. This force is given by:

$$\mathbf{F_{mag}} = -\nabla E_m = \mu_0 \nabla(\mathbf{m} \cdot \mathbf{H}) \tag{4.14}$$

The magnetic force in the xx direction is therefore the derivative of the energy graphics of figure 4.15. Thus, the force will be directly proportional to the minimum energy value since in all the cases the maximum energy is zero. The energy minima on sample 1 and 2 are, respectively, four and two order of magnitude lower than in sample 3. This means that the magnetic particles feel a higher magnetic force in sample 3 making them being attracted into the sensor area.

As the particles are suspended in a fluid, besides the magnetic force they additionally feel a drag force given by $\mathbf{F_{drag}} = -6\pi\eta R_p \mathbf{v}$ where η is the viscosity of the fluid (assumed to be 0.001 N s/m^2 in water) and R_p is the radius of the magnetic particle. Therefore, in order to be attracted into the sensor area the magnetic force felt by the particles has to be higher than the drag force. This is exactly what happens in sample 3. Concerning the other samples, the drag force is high enough to allow most of the particles to be attracted only until the edges of the sensor.

Another important issue is the distance between the free layer of the sensor and the magnetic particle. The magnetic field that a particle senses increases as the particle is closer to the free layer. Therefore, an increase of the magnetic force would be also expected as the separation between the sensor and the particles decreases. Since in the presented architecture this separation corresponds to the thickness of the gold top contact of a MTJ (section 4.2.4), there may be room to improve the magnetic particle attraction by using thinner layers.

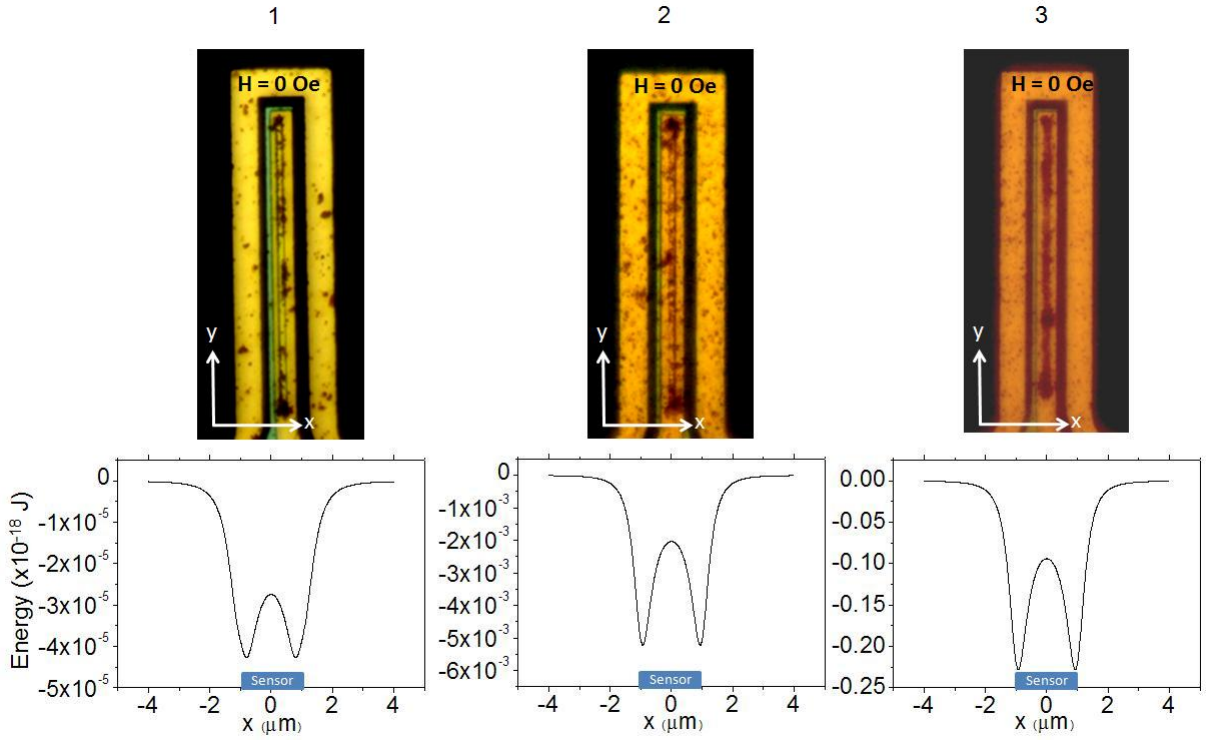

Figure 4.15: Effect of ferromagnetic layers on 250 nm magnetic particle position for three different MTJ structures: 1 - Balanced SAF: Ta 50 Å / Ru 180 Å / Ta 30 Å / MnPt 200 Å / $Co_{90}Fe_{10}$ 20 Å / Ru 8 Å / $(Co_{50}Fe_{50})_{80}B_{20}$ 30 Å / MgO 15 Å / $(Co_{50}Fe_{50})_{80}B_{20}$ 100 Å / Ru 50 Å / Ta 50 Å ; 2 - Unbalanced SAF: Ta 50 Å / Ru 180 Å / Ta 30 Å / MnPt 200 Å / $Co_{90}Fe_{10}$ 20 Å / Ru 8 Å / $(Co_{50}Fe_{50})_{80}B_{20}$ 40 Å / MgO 15 Å / $(Co_{50}Fe_{50})_{80}B_{20}$ 100 Å / Ru 50 Å / Ta 50 Å ; 3 - Normal pinned layer: Ta 50 Å / Ru 180 Å / Ta 30 Å / MnPt 200 Å / $Co_{90}Fe_{10}$ 20 Å / $(Co_{50}Fe_{50})_{80}B_{20}$ 30 Å / MgO 15 Å / $(Co_{50}Fe_{50})_{80}B_{20}$ 100 Å / Ru 50 Å / Ta 50 Å . These structures were deposited in N2000 system. The energy was calculated assuming magnetization of 1400 emu/cm^3 for the CoFe, 900 emu/cm^3 for the CoFeB of the pinned layer and 1000 emu/cm^3 for the CoFeB of the free layer.

Figure 4.16 describes the behavior of the magnetic force as function of the thickness d of this gold layer in the case of structure n°1. As expected, the force decreased with d. When there is no gold over the sensor, the magnetic particles were attracted to the sensor area while with a gold contact the particle remained in the edge. Therefore, the thickness of the top contact of a MTJ should be tailored in order to control the position of magnetic particles on top of the sensor. However, this thickness must not be too low since it increases the contact resistance of the MTJ reducing in this way its TMR.

In conclusion, the magnetic particle position over a magnetoresistive sensor directly depends on the sensor structure and on the vertical distance, which they are from the sensor. The tested structure with better particle attraction included a normal pinned layer. In this case, a lower TMR was observed when compared to the other samples. As will be explained in the next sections, this fact will also reduce the sensor sensitivity. Therefore, a MTJ has to be carefully designed in order to achieve high sensitivities while optimizing the number of particles on the

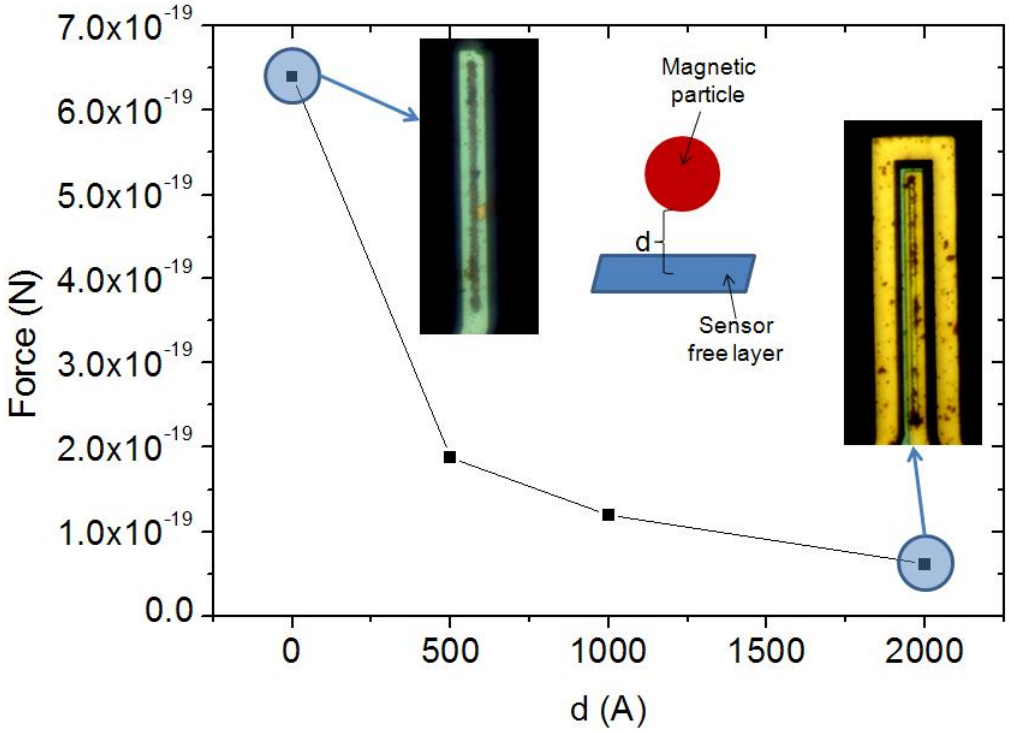

Figure 4.16: Magnetic force as function of the separation between 250 nm magnetic particles and the sensor free layer. These simulations were made for the MTJ structure: Ta 50 Å / Ru 180 Å / Ta 30 Å / MnPt 200 Å / $Co_{90}Fe_{10}$ 20 Å / Ru 8 Å / $(Co_{50}Fe_{50})_{80}B_{20}$ 30 Å / MgO 15 Å / $(Co_{50}Fe_{50})_{80}B_{20}$ 100 Å / Ru 50 Å / Ta 50 Å . Images for d=2000 Å and d=0 Å are shown.

sensor area. For example, a good option would be to use a sensor stack similar to structure n°2 while reducing the thickness of the gold contact.

4.1.4 Magnetic particles detection schemes

Several methods of detecting magnetic particles with magnetoresistive sensors have been already studied. Since the magnetic particles have no remanent magnetic field, all these methods use a magnetic polarizing field which magnetizes the particles. Therefore, the magnetic particles produce a fringe field which is detected by a magnetoresistive sensor. As explained in detail in the next sections, the resistance of these sensors changes with an external magnetic field. The measuring systems are therefore designed to acquire a resistance variation of a magnetoresistive sensor which was produced by the fringe field of magnetic particles.

The magnetic particles can be polarized by using dc or ac field. These two excitation modes will directly influence the strategy used to measure the resistance change.

DC mode

In this mode, the magnetic particles are excited by an external constant magnetic field. This field can be applied in one of the three directions x, y or z. It is important to notice that the magnetoresistive sensors will only be sensitive to the xx direction (figure 4.17).

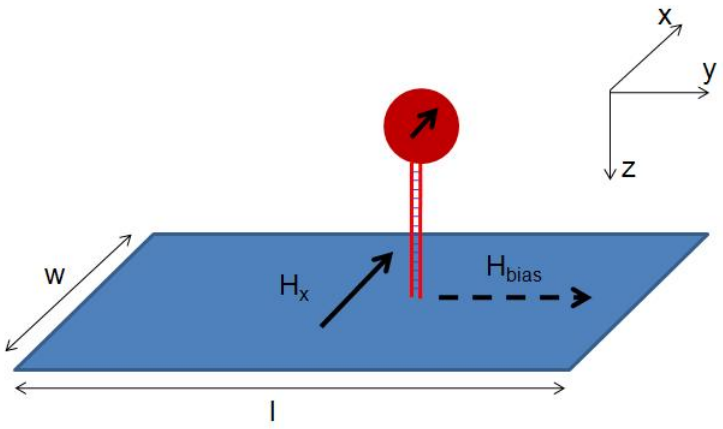

Figure 4.17: Detection system using a polarizing dc magnetic field in the x-direction. A bias magnetic field in the y-direction, may be used in order to stabilize the free layer.

The more obvious way to magnetize the magnetic particles is to apply the polarizing field in the x-direction (H_x) as depicted in figure 4.17. In this case, a magnetic particle generates a fringe field in x-direction with a sign opposite to the polarizing field (see chapter 3). Therefore, after adding the magnetic particles, the field in sensing direction is $H_x - H_{particle}$. Furthermore, a biasing magnetic field (H_{bias}) in the y-direction can be also applied. This field increases the free layer magnetic anisotropy in the y-direction and can be used if the demagnetizing field (see section 4.1.2) is not high enough to linearize the sensor. As the demagnetizing field, if the bias field is too high a loss in the sensor sensitivity may occur. Moreover, another coil or external magnet has to be used for generating this bias field. Therefore, in order to simplify the measuring system, in this thesis, this bias field is not used and the sensor are designed in

such a way that the demagnetizing field is high enough to linearize sensor response.

Figure 4.18 b) shows a typical resistance variation of a magnetoresistive sensor as function of the external magnetic field in the x-direction. The sensor resistance changes linearly with an applied field in the range of ~ -25 Oe to ~ 25 Oe. Outside this range the resistance is non-linear or constant and we call it the saturation regime. Therefore, the excitation field has to be chosen in such a way that the sensor is not saturated otherwise no resistance variation due to the presence of magnetic particles can be observed.

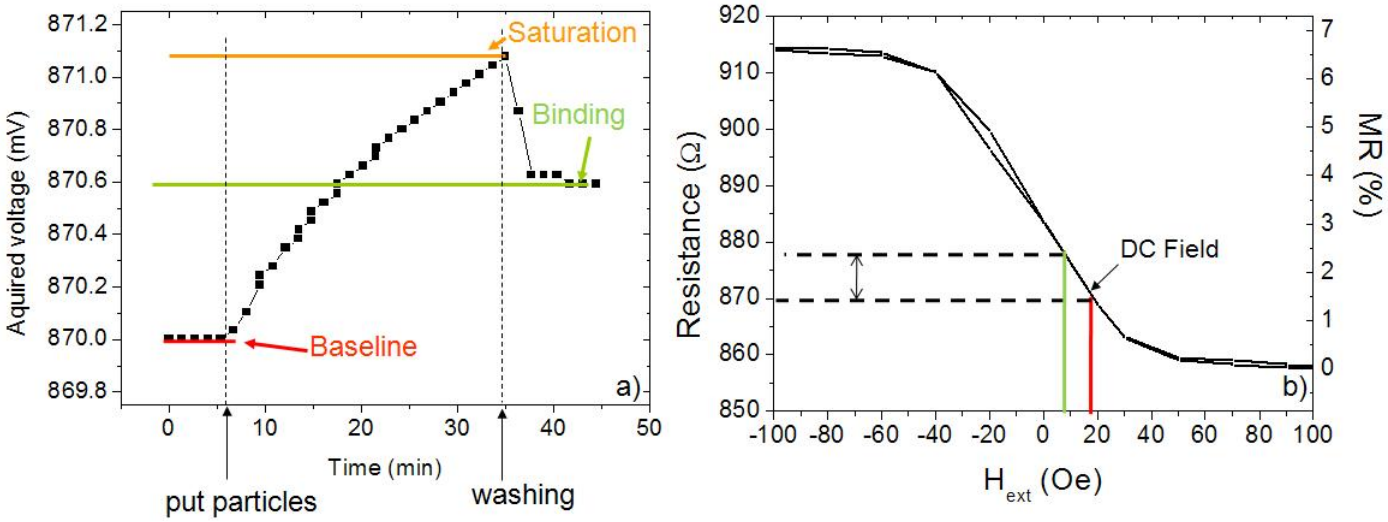

Figure 4.18: a) Signal variation due to dc external magnetic field in the x-direction. b) Sensor response to an external magnetic field in the x-direction

The measurement of the sensor resistance is achieved by applying a constant current and measuring the voltage drop over the sensor (see 2.2.4). A typical signal observed in a biodetection assay is shown figure 4.18 a). Applying a field $H_x = 15$ Oe, the resistance of the sensor is $R \sim 870\ \Omega$. Therefore, applying a current $I = 1$ mA the measured voltage is $V = 870$ mV. Initially, the signal without particles is acquired during 5 minutes and is called the baseline. After this period a certain amount of particles (i.e. 10 μL of 250 nm particles at a concentration of $\sim 5 \times 10^8$ particles/μL) in introduced on top of the sensor. As the particles are settling down, the fringe field of the particles reduces the overall magnetic field on the sensor implying an increase in the output voltage. After 30 minutes a saturation is attained meaning that the sensor is fully covered of particles and the addition of more particles does not produce any increase in voltage. At that time, the particles are washed with a buffer solution. Due to the biological recognition, some of the particles will remain on top of the sensor. Therefore, the signal does not drop down to the baseline, which would occur if the particles were completely washed out, and stabilizes at a certain voltage called the binding signal. In this measurement configuration, the difference between the baseline and the binding signal is directly proportional to the number of particles immobilized over the sensor as the average field of a magnetic particle is more or less independent of its position on the sensing area (see chapter 3).

Another possible configuration would be to apply a perpendicular magnetic field (in z-direction) as shown in figure 4.19 a). In this configuration, a high H_z magnetic field can be applied since in the z-direction the demagnetizing field of the sensor free layer is very high. This is an advantage because the fringe field of the particle is proportional to the polarizing field. However, if a particle stands in the middle of the sensor, as the fringe field of a particle is spherically symmetric (see chapter 3), the average fringe field will be zero. As shown in figure 3.6 on chapter 3, the average signal is higher on the edge of the sensor. Thus, only the magnetic particles on the edges would be detected. Furthermore, the particles near left and right edges have opposite sign. This means that if the same number of particles are on the left and right edge the total signal will be zero.

Taking these facts into account, two strategies can be adopted to observe a signal variation. The first approach would be to immobilize the biological probes only on one of the edges of the sensor. In this way the average signal is just either positive or negative and as high (or even higher) than when an in-plane magnetic field (in the $x$direction) is applied (see chapter 3). However, the area with high particle fringe field is smaller than the sensor area. Therefore, this may reduce the biological dynamic range. The second strategy would be to introduce a magnetic field along the x-direction. In this way, a particle on the center of the sensor would generate a non-zero magnetic field. However, as already discussed previously the addition of an extra magnetic field source complicates the measuring system. Furthermore, from a practical point of view, the alignment of the magnetic field generator is never perfect. Therefore, some unwanted components in the x- and y-directions may appear. If the field is high enough, these components may either saturate the sensor or reduce its sensitivity. The approach where the polarizing field is in the x-direction is not so sensitive to misorientation of the magnetic field source.

Up to now, only a static measurement where the biological probe is immobilized on top of the sensor was discussed. However, another detection method that does not require the immobilization of a probe can be envisioned. Figure 4.19 shows an example of a dynamic measurement. The magnetically labeled biological target, which in this example is a cell, passes over the sensor and the fringe field of the particle is detected. The cells are passing through a microfluidic channel and the magnetic particles labeling them are polarized with a perpendicular magnetic field. The measurement is accomplished as function of the time and a high signal will be observed when the cells pass the edges of the sensor. This strategy was already demonstrated for the detection of magnetic particles ([24]).

The measurements systems using dc external magnetic field to polarize the magnetic particles show some limitations. On one hand, as the sensors are generally biased with relatively high current (i.e. few mA) the temperature of the chip may increase. The magnetoresistive sensors in study (SV and MTJ) show a resistance dependency with the external temperature. Therefore, a thermal drift will be observed in these measurements. Furthermore, as will be discussed later in this section, the noise of the sensor is maximum when a dc measurement is accomplished. In order to assess these limitations, an ac measurement can be achieved. As the frequency of the measurement increases, the noise will be reduced. By using an AC measurement mode the

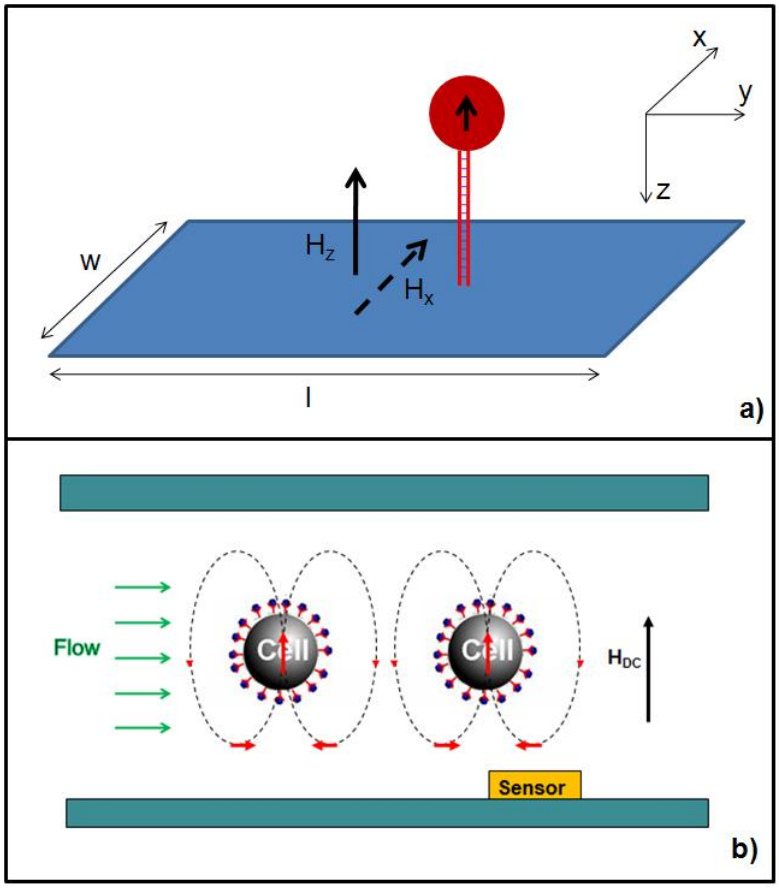

Figure 4.19: a)Detection system used a polarizing dc magnetic field in the z-direction. In this configuration, a magnetic field in the x-direction is needed so that the average particle fringe field on the sensing area is not zero. b) Dynamic detection of magnetically labeled cells passing over a magnetoresistive sensor under a perpendicular magnetic field.

thermal drift can be vanished. This is due to the fact that although there is a linear variation of the sensor resistance with the temperature, the sensor MR and sensitivity do not change. If an AC magnetic field is used to magnetize the particles the measured sensor voltage will depend on the sensor sensitivity and therefore will be independent on the thermal drift.

AC mode

In order to make an ac detection, the magnetic particle moment has to be modulated at a certain frequency. This can be accomplished by generating an ac polarizing magnetic field. As in the dc mode, the more obvious approach is to apply this ac field in the x-direction as depicted in figure 4.20. This polarizing field will make the resistance of the sensor change as function of time. As a constant current is applied, the voltage will also vary as function of time. Therefore, lock-in technique can be used for the detection. In this case, the voltage frequency will be the same as the excitation frequency (i.e. frequency of the polarizing field). When the magnetic particles are introduced over the sensor, their moment will be polarized generating a fringe field

with the same frequency of the polarizing field. This fringe field will change the sensor output voltage enabling the particle detection.

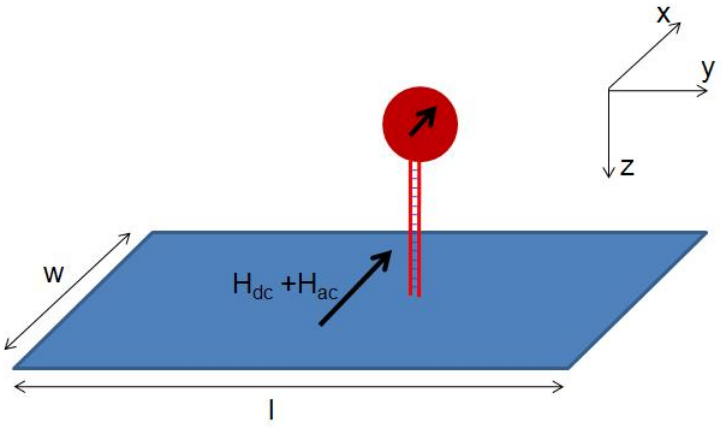

Figure 4.20: Detection system using a polarizing dc+ac magnetic field in the x-direction.

Using the same kind of sensor response of the dc mode (Figure 4.21 b)), a typical particle detection experiment can be performed. In the case reported in figure 4.21, an external ac field H_{ac} = 13.5 Oe rms was superimposed on a dc magnetic field H_{dc} = 30 Oe. The sensor was biased with a 1 mA dc current. As in the dc mode, without any particle on top, the sensor shows a signal which is called the background signal (see figure 4.21 a)). This signal is acquired during 5 minutes. After that, 10 μL of 250 nm particles (with a concentration of 5×10^8 particles/μL) was introduced over the sensor. The acquired signal decreases while the particles are settling down attaining the saturation after 30 minutes. The saturation signal corresponds to the case where the magnetic particles occupy the whole sensing area and the addition of more particles does not increase the signal. Finally, the particles, which did not bind to the sensor surface via biomolecular recognition, are washed. The remaining particles, produce a signal which is called the binding signal. The difference between the baseline and the binding signal is proportional to the number of particles bound to the sensor surface.

In this experiment, an external dc magnetic field was added to the ac polarizing magnetic field. This was accomplished because at zero dc field, it was observed (in the case of the spin valve sensors used in this thesis) that very low signal variations were acquired. In fact, as demonstrated in figure 4.22, a H_{dc} = 30 Oe field has to be applied in order to obtain a maximum particle detection signal. This may seem counter-intuitive since the sensor show higher sensitivity at 0 Oe dc field and therefore should be more sensitive to magnetic particles in this region. However, as demonstrated by H.A. Ferreira [23], the demagnetizing fields of free and pinned layers will be also sensed by the magnetic particles. These fields are therefore added or subtracted (depending on the direction) to the external fields originating a maximum particle sensitivity at a field of H_{dc} = 30 Oe for the spin valve structure used in this thesis.

Since the signal without particles is relatively high, because the dynamic range of the electronics system is limited it may be difficult to detect small voltages variation in such a high

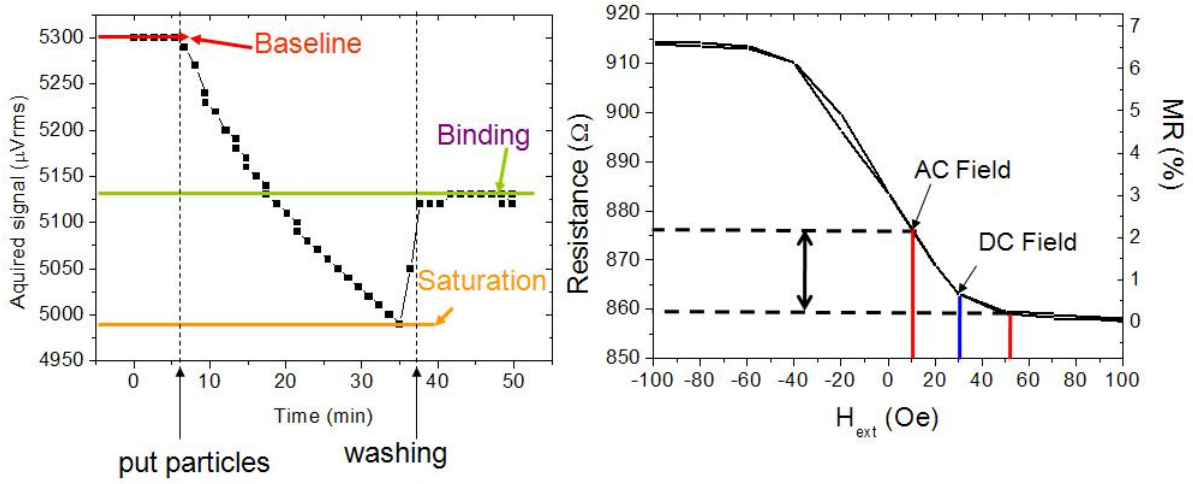

Figure 4.21: a) Signal variation due to dc+ac external magnetic field in the x-direction. b) Sensor response to an external magnetic field in the x-direction

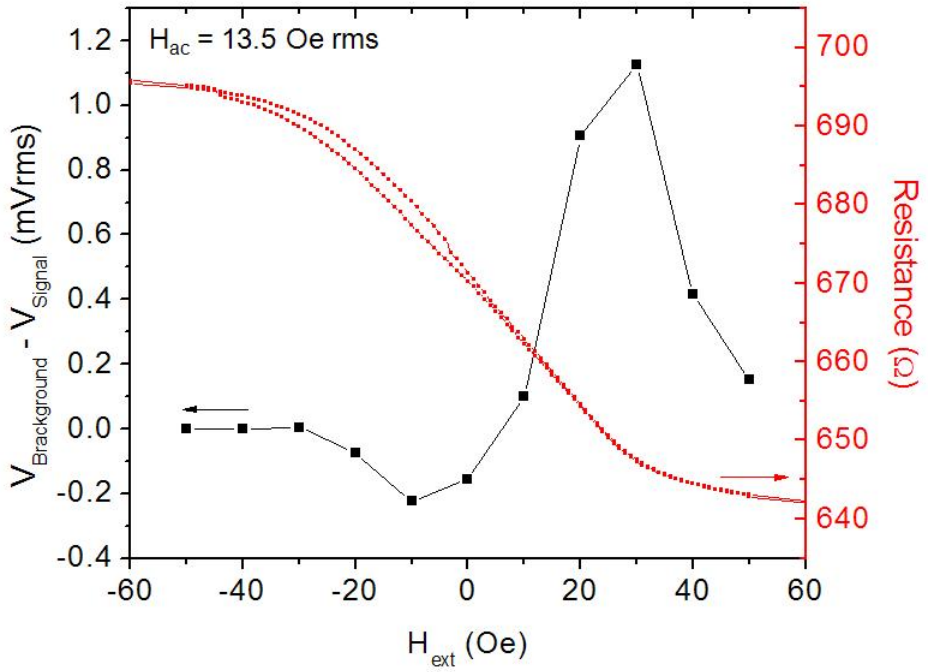

Figure 4.22: Particle sensitivity in function of the external dc magnetic field. An 13.5 Oe rms was used to detect 10 μL of 250 nm particles at a concentration of 5×10^8 particles/μL.

signal. In order to overcome this limitation, systems using sensors mounted in a Wheatstone bridge have been used [27]. The bridge is composed by two spin valves and two resistors. One of the spin valve sensors is functionalized with a biomolecular probe while the other is not functionalized and used as a reference. The resistors are dimensioned in order that the output voltage of the bridge is zero. If the sensors are close to each other in the chip, this configuration

has also the advantage of removing possible thermal drift occurring during the experiments.

Finally, other configurations for ac measurements were also tested in other groups. A measurement system applying a perpendicular (z-direction) ac field and a transverse (y-direction) dc field was used by Stanford group [12]. In this case, the magnetic particle signal appears at twice the excitation frequency. At this frequency the signal without particles on top of the sensor is near zero. Therefore the observed signal is only due to the presence of magnetic particles. However, as already shown in the dc mode, there are experimental limitations associated to this approach.

An integrated polarizing field generator was also introduced by a group in Philips [15]. In this approach, an ac polarizing field, at frequency f_1, is generated by an integrated current line which is parallel to a spin valve sensor. Since the line is in the same plane as the sensor, the magnetic field over the sensor area is perpendicular and therefore no output signal is acquired. When a magnetic particle is on top of the sensor, a signal due to the particle fringe field is detected. However, due to electrical coupling through the dielectric of the chip, when performing this experiment a non-zero signal appears at frequency f_1. Therefore, the sensor is biased by an ac current at a different frequency f_2. The magnetic signal is then acquired at the frequency f_1+f_2 or f_1-f_2 as detailed in [15]. This approach has the main advantage of needing an external magnetic field generator simplifying driving and the measurement electronic system. However, as the generated magnetic field is perpendicular to the sensor it has the same drawbacks discussed previously for this configuration.

4.2 Magnetic tunnel junction biochip

4.2.1 Spin dependent tunnelling theory

The operation of magnetic tunnel junctions is described by the spin-dependent tunnelling effect. In this phenomenon, electrons tunnel across an insulating barrier (I) between two ferromagnetic electrodes (FM). The device composed by FM1/I/FM2 is called a magnetic tunnel junction. For a sufficient thin insulating layer and applying a voltage across the electrodes, the electrons will be able to tunnel through the insulator. As the tunnelling effect conserves the spin of electrons, electrons at the Fermi level of FM1 will tunnel into free equivalent spin states at the Fermi level of FM2. The conductance G, that correspond to the number of electrons flowing through the device, will be proportional to the product of densities of states at the Fermi level in FM1 and FM2. In that case, when both the ferromagnetic layers have the same magnetization direction, the conductance G_p is given by:

$$G_p \propto D_1^{\uparrow} D_2^{\uparrow} + D_1^{\downarrow} D_2^{\downarrow} \tag{4.15}$$

where $D_i^{\uparrow}$ and $D_i^{\downarrow}$ correspond respectively to the spin up and spin down density of states in electrode i (with i =1,2). The magnetic moment of a transition metal is due to the splitting in energy of the spin up and spin down bands. At a certain Fermi level, there is an imbalance in the density of spin up and spin down states. Figure 4.23 shows this effect as well as the

tunnelling process when both electrode are in a parallel or antiparallel alignment. For the parallel configuration, tunnelling will occur between majority spin states $D^{\uparrow}$ and between minority spin states $D^{\downarrow}$. However, in the opposite magnetic configuration, the spin band correspondence for tunnelling is inverted. In that case, electrons in majority spin band will tunnel to their equivalent band that has a small available spin state. Then, the conductance G_{ap} when both ferromagnetic layers show antiparallel magnetization, can be written as:

$$G_{ap} \propto D_1^{\uparrow} D_2^{\downarrow} + D_1^{\downarrow} D_2^{\uparrow} \tag{4.16}$$

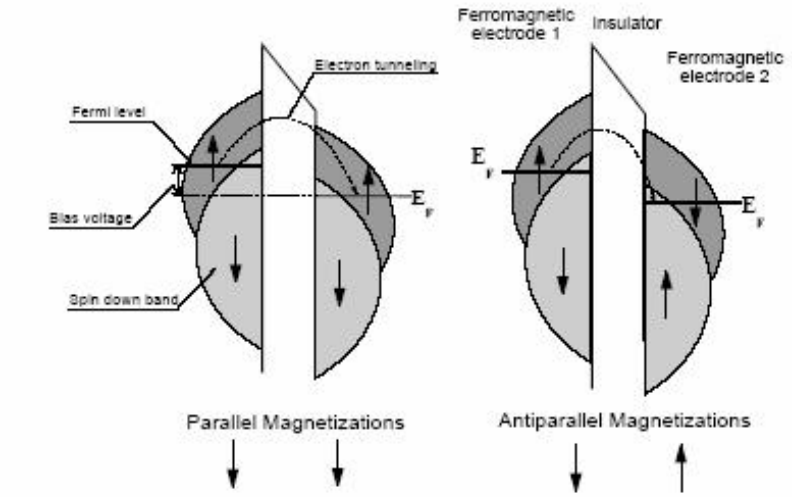

Figure 4.23: Band diagram of the tunnelling mechanism of a magnetic tunnel junction.

The conductance for the parallel (G_p) and antiparallel (G_{ap}) electrode magnetizations are different and $G_p > G_{ap}$ since it is assumed that $D^{\uparrow} > D^{\downarrow}$.

The definition of electron spin polarization of the electrode i is:

$$P_i = \frac{D_i^{\downarrow} - D_i^{\uparrow}}{D_i^{\downarrow} + D_i^{\uparrow}} \tag{4.17}$$

The tunnelling magnetoresistance (TMR) signal is defined as:

$$TMR = \frac{R_{ap} - R_p}{R_p} \tag{4.18}$$

As the resistance is defined as $R = 1/G$, the lower resistance states corresponds to the state with higher conductance, in this case it corresponds to the parallel state ($R_p = 1/G_p$). In the other hand, the antiparallel state corresponds to the high resistance level ($R_{ap} = 1/G_{ap}$). Using equations 4.15, 4.16, 4.17 and 4.20 the TMR can be written as:

$$TMR = \frac{G_p - G_{ap}}{G_p} = \frac{2P_1P_2}{1 - P_1P_2} \tag{4.19}$$

In this calculation, the electrode were considered independent. In fabricated devices with usual barrier materials, the TMR will not be exactly given by this expression since there are interactions between the two ferromagnetic electrodes. Therefore, a more generalized model was developed by Slonczewski [37] and Kubo/Laudauer [38]. These models predict an increasing TMR for an increase of the barrier height and a decrease of the barrier thickness.

In 2001, W.H. Buttler pushed forward the understanding of tunnelling magnetoresistance [39]. He calculated the electronic band structures of the materials composing a Fe/MgO/Fe trilayer. It was assumed a bcc Fe lattice with [100] texture and a MgO simple cubic lattice (NaCl structure) with [100] texture as well. The wavefunction was then calculated assuming a periodic lattice potential in each layer and matching the Block functions at the interfaces. This model predicted very large magnetoresistance (up to 1000%) causing a very strong interest in these kind of structures.

The experimental confirmation of Buttler's predictions was made in 2004 by S. Yuasa [40] and S. Parkin [41]. TMR up to 250% at room temperature was demonstrated for Fe/MgO/Fe based structures. Since then many investigation have been performed on structures based on MgO barriers leading to a maximum TMR of $\sim 500\%$ at room temperature [42].

4.2.2 Magnetic tunnel junction characteristics

In this section, the different electrical characteristics of the MTJs will be described.

Resistance

As shown in the previous section, the MTJ resistance depends on the relative magnetization orientation of the ferromagnetic layers. The resistance will change from minimum (R_{min}) to maximum ($R_{max} = R_{min}(1 + TMR)$) values. Therefore, the TMR can be also given by:

$$TMR = \frac{R_{max} - R_{min}}{R_{min}} \tag{4.20}$$

For an angle θ between the magnetization direction of the two electrodes, the resistance corresponds to a fraction of parallel ($\theta = 0^{o}$) and antiparallel ($\theta = 180^{o}$) alignment so the total resistance of the MTJ is given by:

$$R = R_{min}[1 + \frac{TMR}{2}(1 - \cos\theta)] \tag{4.21}$$

The MTJ minimum resistance is inversely proportional to the junction area. This results from the fact that the number of tunnelling electrons are directly proportional to the total electrode area. The higher the area is, the higher the tunnelling current will be. Therefore, the higher the area is, the lower the resistance will be. So, for a MTJ with an area A, the resistance will be given by:

$$R = \frac{\rho_0}{A} \tag{4.22}$$

where ρ_0 is called the resistance area product (R×A product). It is important to know the R×A product of a MTJ (commonly expressed in $\Omega \times \mu m^2$) is constant since it allows the comparison of samples with different MTJ areas. The R×A product is a characteristic that only depends on the barrier thickness. In the point of view of biochip design, this fact enables the choice of the area of the sensor and the resistance of the sensor independently. This means that an adequate sensor area can be chosen for a certain application (discussed in section 4.2.5) while a sensor resistance optimizing the sensor signal-to-noise ratio can be chosen (discussed in section 4.2.3). As will be shown later, this is not the case for spin valve sensors.

IV characteristic

Although a MTJ can be considered a resistance that depends on the external magnetic field, in general its IV characteristic is not the same as the one of a simple resistor. Simmons developed a model that give the IV characteristic of a MTJ [43] [44]. Simmons' model assumes that, from an energy point of view, the insulating layer between the metal electrodes forms a barrier for the current flow (figure 4.24).

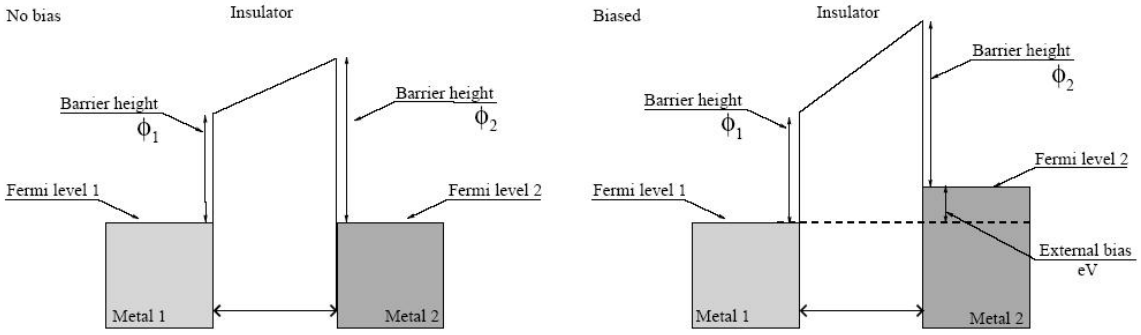

Figure 4.24: MTJ Energy barrier diagram for different electrode materials. The work needed to remove one electron from metal conduction band is traduced in the barrier height at each interface.

The barrier height at each interface is defined as the difference between the electrode Fermi level and the conduction band of the insulator. In general, the barrier heights ϕ_1 and ϕ_2 are different. They can be equal if the metal/insulator interface is exactly the same. A current I flows through the MTJ if a bias voltage is applied. This voltage creates a potential difference on the two metal Fermi levels. For very low bias voltages $V \sim 0$ and assuming only tunnelling conductance (i.e. ϕ_1,$\phi_2 \gg k_B T$), the current can be calculated using the following expression from Simmons [43]:

$$I = k_0 k_1 \frac{AV\sqrt{\phi}}{2t} \exp[-k_1 t\sqrt{\phi}] \tag{4.23}$$

with,

$$k_0 = \frac{q^2}{2\pi h} \quad \text{and} \quad k_1 = \frac{4\pi\sqrt{2m}}{h}\sqrt{e}$$

where A is the MTJ area, t the barrier thickness, q the electron charge, m the electron mass and h Planck's constant. In equation 4.23 it is assumed that $\phi_1 = \phi_2 = \phi$. This expression shows that for low voltages the MTJ has the same IV characteristic of a resistor.

However in several applications (including biochips) higher voltages are applied to the MTJ. In that case, the MTJ IV characteristic can also be calculated in the framework of Simmons' model. For voltages fulfilling $qV \leq \phi_{1,2}$ the current is given by:

$$I = k_0 \frac{A}{t^2}\left[(\phi - V/2)\exp[-k_1 t\sqrt{\phi - V/2}] - (\phi + V/2)\exp[-k_1 t\sqrt{\phi + V/2}]\right] \tag{4.24}$$

where k_0 and k_1 are the same constants used in equation 4.23, A is the MTJ area, t is the barrier thickness and ϕ is the effective barrier height.

Bias voltage dependance

The TMR of a magnetic tunnel junction depends on the applied voltage. The TMR is almost constant (TMR_0) until 30 mV, then it starts to decrease with the increasing bias voltage. In the range where the signal drops until half of the initial TMR (between 300-500mV), the decrease is almost linear (figure 4.25).

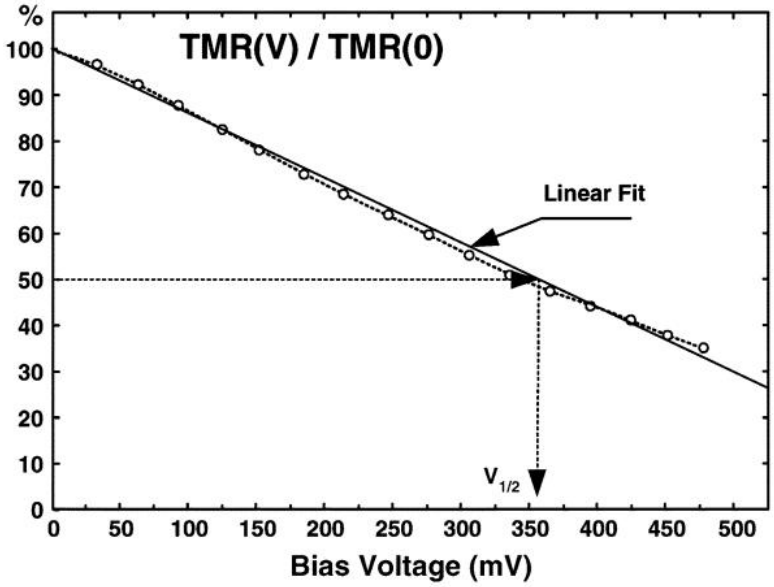

Figure 4.25: Experimental results showing that the TMR of a MTJ decreases with the applied voltage.

Therefore, the following simple model can be assumed for further calculation:

$$TMR(V) = TMR_0(1 - \frac{V}{2V_{1/2}}) \tag{4.25}$$

where $V_{1/2}$ is the voltage at which the $TMR = \frac{TMR_0}{2}$.

The MTJ has an insulator layer between two electrodes; if a high voltage is applied this layer can be destroyed. The voltage at which this phenomenon occurs is called the *breakdown voltage* (V_{break}) and is related to the dielectric strength of the insulator. V_{break} can be calculated using the following expression:

$$V_{break} = E \times t \tag{4.26}$$

where E is the dielectric strength and t is the barrier thickness. Assuming that the dielectric strength E of an Al_2O_3 insulating layer is 10^9 V/m, a 1.2 nm barrier has $V_{break} = 1.2$ V.

MTJ sensitivity

In order to be sensitive to small magnetic fields generated by the magnetic nanoparticles used in biochip applications, a MTJ sensor should have a linear response as depicted in figure 4.26. The details for the linearization of MTJ were already discussed in section 4.1.2.

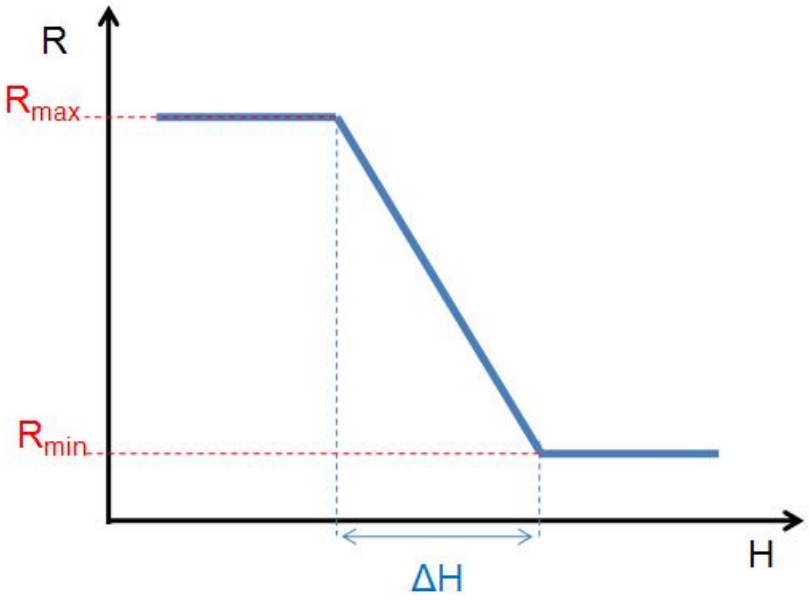

Figure 4.26: Schematic representation of the transfer curve of a linear magnetoresistive sensor

The sensitivity of the MTJ is then given by the slope of of the linear part of the transfer curve (figure 4.26). Thus:

$$S = \frac{\partial R}{\partial H} \quad [\Omega/\text{Oe}] \tag{4.27}$$

Assuming that the sensor is perfectly linear:

$$S = \frac{R_{max} - R_{min}}{\Delta H} = \frac{\Delta R}{\Delta H} \quad [\Omega/\text{Oe}] \tag{4.28}$$

In order to be able to compare the sensitivity of different sensors, the sensitivity is normalized to R_{min} and is therefore expressed given by:

$$S = \frac{\Delta R}{R_{min}\Delta H} = \frac{TMR}{\Delta H} \quad [\%/\text{Oe}] \tag{4.29}$$

Since the TMR depends on the bias voltage (see equation 4.25), the sensitivity will also depend on the voltage and from equations 4.20 and 4.29 the following expression can be found:

$$S(V) = S_0(1 - \frac{V}{2V_{1/2}}) \tag{4.30}$$

where S_0 is the maximum sensitivity of the MTJ. This maximum sensitivity is obtained at low bias voltages.

In the linear range, the resistance of a MTJ can be written as:

$$R(H) = R_0 + S(V)\ R_{min}\ H \tag{4.31}$$

where R_0 is the resistance at zero field.

Using this sensitivity, the signal variation (ΔV) on a MTJ sensor due to an external magnetic field (H) can be written:

$$\Delta V = (R(H) - R_0)I \Leftrightarrow \Delta V = S(V)\ R_{min}\ H\ I \tag{4.32}$$

4.2.3 Magnetic tunnel junction signal to noise ratio

Almost all electronic devices exhibit voltage fluctuations with a power spectral density inversely proportional to frequency. These voltage fluctuations are commonly called the $1/f$ noise. A phenomenological model proposed by Hooge [55] describes empirically this noise spectral density. Therefore, adapting this model to magnetic tunnel junctions [56] the expression describing this phenomenon is:

$$S_{1/f} = \alpha_H \frac{R^2 I^2}{fA} \quad [\text{V}^2/\text{Hz}] \tag{4.33}$$

where α_H is the phenomenological Hooge's constant, $R = \frac{\partial V}{\partial I}$ is the differential MTJ resistance, I is the current passing through the MTJ, A is the area of the MTJ and f is the operating frequency.

As the $1/f$ noise is inversely proportional to the frequency, the noise spectral density decreases with the increase of the frequency. From a certain frequency called the $1/f$ knee, the $1/f$ noise is no longer dominant and the white noise background (WNB) starts to be the dominant noise. The noise spectral density of the WNB for magnetic tunnel junctions is given by equation 4.34 which includes the thermal and shot noise [56].

$$S_{wnb} = 2qIR^2\ \coth\left(\frac{qV}{2k_BT}\right) \quad [\text{V}^2/\text{Hz}] \tag{4.34}$$

where q is the electron charge, I is the current passing through the MTJ, $R = \frac{\partial V}{\partial I}$ is the differential MTJ resistance, k_B is Boltzmann's constant and T is the absolute temperature.

Using the setup described in chapter 2.2.3, a typical noise spectrum of a MTJ was measured (figure 4.27). In this case, the $1/f$ knee was found to be ~ 300 Hz. The $1/f$ noise is dominant for frequencies below the $1/f$ knee while for higher frequencies the WNB noise is dominant. The measured MTJ showed a relatively high WNB noise due to its high resistance. Reducing the MTJ resistance would decrease the WNB noise thus increasing the $1/f$ knee frequency. Furthermore, a fitting of the curve to the $1/f$ + WNB noise can be accomplished retrieving the Hooge constant of the MTJ. In the example of figure 4.27, a Hooge constant of 1×10^{-9} μm^2 was found. This value is the expected order of magnitude for this constant and the WNB level is also similar to the theoretical one.

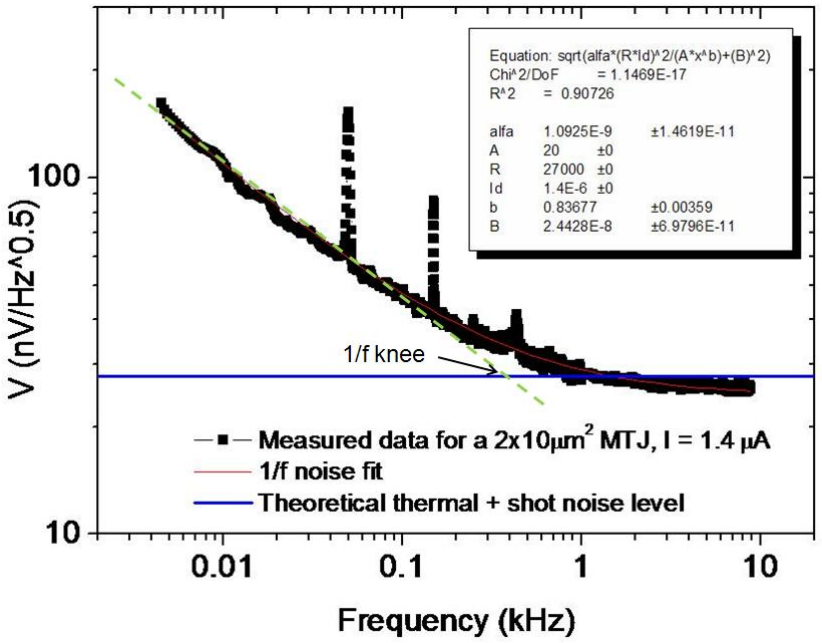

Figure 4.27: Low frequency range noise spectrum of a 27 kΩ MTJ with an area of 2×10 μm^2 and biased by a 1.4 μA current.

The SNR of a MTJ can then be calculated and its maximum can be found. This maximum is attained when the noise is minimum. As shown previously, this occurs at high frequencies when the WNB is reached.

Thus, from equations 4.32 and 4.34 can be written:

$$S/N = \frac{\Delta V}{\sqrt{S_{wnb}}} = \frac{S\ R_{min}\ H\ I}{\sqrt{2qIR^2\ \coth\left(\frac{qV}{2k_BT}\right)}} = S\ R_{min}\ H \sqrt{\frac{V}{2qR^3\ \coth\left(\frac{qV}{2k_BT}\right)}} \tag{4.35}$$

As previously explained, the sensitivity of a MTJ varies with the bias voltage. Therefore, using equation 4.30 the SNR equation can be rewritten:

$$S/N = S_0\ R_{min}\ H\left(1 - \frac{V}{2V_{1/2}}\right)\sqrt{\frac{V}{2qR^3\ \coth\left(\frac{qV}{2k_BT}\right)}} \tag{4.36}$$

The top part of this equation can be analyzed in order to determine which voltages maximizes it:

$$\frac{\partial\left[\left(1 - \frac{V}{2V_{1/2}}\right)\sqrt{V}\right]}{\partial V} = 0 \ \Leftrightarrow\ V = \frac{2}{3}V_{1/2} \tag{4.37}$$

As the $V_{1/2}$ voltages of common MTJs range from 0.3 to 0.5 V. Analyzing the bottom part of equation 4.36 in this voltage range, it can always be assumed that $qV >> 2k_BT$ because at room temperature ($T = 300$ K) $\frac{2k_BT}{q} \approx 52$ mV. Therefore,

$$lim_{\frac{qV}{2k_BT}\to+\infty} \coth\left(\frac{qV}{2k_BT}\right) = 1 \tag{4.38}$$

In conclusion, from equation 4.34 the dominant noise for high voltage bias is the shot noise, $S_{wnb} = 2qIR^2$, and from equation 4.36 the optimal SNR value is:

$$S/N = \frac{2}{3}S_0\ R_{min}\ H\sqrt{\frac{V_{1/2}}{3qR^3}} \tag{4.39}$$

The differential resistance R of a MTJ may not always be similar to the minimum resistance R_{min}. This is due to the fact the resistance of the MTJ can be up to 5 (for $TMR = 500\%$) times higher than its minimal resistance. However, from equation 4.39 it can be observed that the SNR is optimized when $R \sim R_{min}$ and the maximum SNR is given by:

$$S/N = \frac{2}{3}S_0\ H\sqrt{\frac{V_{1/2}}{3qR_{min}}} \tag{4.40}$$

As expected, the SNR is directly proportional to the sensitivity S_0 of the MTJ. Furthermore, decreasing R_{min} and increasing $V_{1/2}$ also maximize the SNR. From those parameters R_{min} is the easier to tailor. The minimum resistance of a MTJ can be reduced by reducing the barrier thickness. Nevertheless, the barrier should not be too thin since thinner barriers may show lower $V_{1/2}$ and S_0.

However, for technical reasons it may not be always possible to work in the high frequency regime. Therefore, it is important to study the SNR at low frequency. In this frequency domain, the noise of the sensor is given by the sum of the $1/f$ noise (equation 4.33) and the WNB noise (equation 4.34). Therefore, the SNR is given by:

$$S/N = \frac{\Delta V}{\sqrt{S_{1/f} + S_{wnb}}} = \frac{S\ R_{min}\ H}{R}\frac{V}{\sqrt{\alpha_H\frac{V^2}{fA} + 2qVR\ \coth\left(\frac{qV}{2k_BT}\right)}} = \frac{S_0(1 - \frac{V}{2V_{1/2}})\ R_{min}\ H}{R\sqrt{\frac{\alpha_H}{fA} + \frac{2qR}{V}\ \coth\left(\frac{qV}{2k_BT}\right)}} \tag{4.41}$$

As for the previous case, a differential resistance close to R_{min} maximizes this equation. Thus, the SNR at low frequencies is given by:

$$S/N = \frac{S_0(1-\frac{V}{2V_{1/2}})\ H}{\sqrt{\frac{\alpha_H}{fA} + \frac{2qR_{min}}{V}\ \coth\left(\frac{qV}{2k_BT}\right)}} \tag{4.42}$$

This equation is not easy to maximize therefore a graphical analysis approach will be done. Figure 4.28 shows the MTJ SNR for three different resistance values, 100 Ω, 1 kΩ and 10 kΩ. As observed, the highest SNR for low frequencies is attained for MTJ low resistance values. The voltage at which the SNR is maximized also depends on the MTJ resistance. This voltage increases with the resistance value. At a first glance, one would choose a small MTJ resistance in order to maximize the SNR. However, this fact has disadvantages. The fact that the maximum SNR is attained at a lower voltage means that for the detection of low magnetic fields, the signal variation will be small and the electronic detection system may not be able to measure it. Therefore, the MTJ resistance has to be carefully chosen.

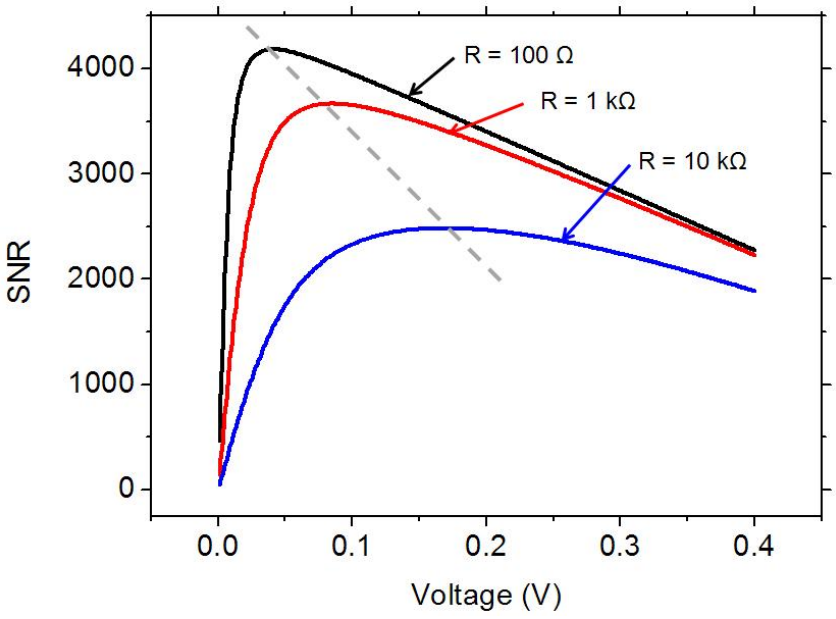

Figure 4.28: Comparison of the SNR at low frequencies of three MTJ with resistances of 100 Ω, 1 kΩ and 10 kΩ, respectively. The MTJ $A = 200\ \mu m^2$, the $S_0 = 0.0006 \times R\ \Omega/Oe$, $\alpha_H = 1.3 \times 10^{-9}\ \mu m^2$, $f = 375$ Hz and $V_{1/2} = 0.4$ V.

In this work, the MTJ will be used for detecting the fringe field of magnetic particles. Therefore, the sensor will be connected to an external electronic system (as described in section 2.2.4). The electronic systems used in this work showed a higher noise than the magnetic sensor itself. Furthermore, as will be shown in chapter 5, the diode used as a switching element of a matrix-based biochip also has a higher noise than the MTJ. It is then also important to analyze the SNR of the MTJ sensor in this case. To do that, it is assumed that the electronic measuring

system has a constant white noise S_{elec} which is the dominant noise for the working frequency. The SNR expression can then be written:

$$S/N = \frac{\Delta V}{\sqrt{S_{elec}}} = \frac{S_0\ R_{min}\ H\ V(1 - \frac{V}{2V_{1/2}})}{R\sqrt{S_{elec}}} \tag{4.43}$$

In order to find the maximum of this SNR, the S/N of equation 4.52 is differentiated with respect to the voltage and equaled to zero:

$$\frac{\partial S/N}{\partial V} = 0 \ \Leftrightarrow\ V = V_{1/2} \tag{4.44}$$

Although the SNR is lower than the one observed with the noise of the sensor, in this case the maximum of SNR is attained for higher voltages (see equations 4.44 and 4.37). It can also be demonstrated that the voltage variation ΔV given by equation 4.32 is also optimized by this voltage. For the same field, the absolute voltage variation acquired by the electronics will be higher than in the other cases and therefore more easily detected. The maximum SNR is thus:

$$S/N = \frac{S_0\ R_{min}\ H\ V_{1/2}}{2R\sqrt{S_{elec}}} \tag{4.45}$$

Again, in this case the condition $R \sim R_{min}$ maximizes the SNR and:

$$S/N = \frac{S_0\ H\ V_{1/2}}{2\sqrt{S_{elec}}} \tag{4.46}$$

It is interesting to note that when the noise of the electronic measurement system is dominant, the maximum SNR of a MTJ is independent of its resistance. Therefore, providing that the MTJ noise is not higher than the measuring system noise, the MTJ resistance can be as high as needed. This may allow more reliability ($V_{break} >> V_{1/2}$), higher process yield (since thicker barrier are needed) and lower power dissipation ($P = \frac{V_{1/2}^2}{R_{min}}$) at the optimum voltage. These are important features in the design of magnetoresistive biochips. The SNR is further improved by increasing the sensitivity S_0 and the $V_{1/2}$ of the sensor.

4.2.4 Magnetic tunnel junction biochip design

Sensor design

Taking into account what was described and simulated in the previous sections, magnetic tunnel junctions sensors were designed for high particle sensitivity (small areas like $2 \times 15\ \mu m^2$) or for medium dynamic range (larger areas like $2 \times 100\ \mu m^2$).

In the first case, the sensor was designed to be sensitive up to maximum of $\sim$ 320 250 nm magnetic particles. The small dynamic range and higher sensitivity were used in a matrix-based biochip (chapter 5) in order to be used in disease diagnostics. A typical transfer curve is shown in figure 4.29 a). Furthermore, a U-shaped current line surrounding the sensor (figure 4.29 b)) was specially designed to enable particles focusing onto the sensing area [99]. Passing a 40 mA dc current through this line generates a field gradient which will move the particles toward it.

By applying an external 30 Oe rms magnetic polarizing field, at frequencies ranging from 0.1 to 1 Hz, the magnetic particles will be alternatively attracted and repelled from the line. This movement forces the particles to pass through the sensing area and eventually to bind to the biological probes.

In the second case, a higher dynamic range (up to ~ 3200 of 250 nm magnetic particles) was targeted at the expense of reducing the magnetic particle sensitivity. This sensor was designed to be used in gene expression experiments where a high dynamic range is needed.

In both cases, several MTJ stacks were used. In the beginning of this work, smaller sensors were targeted. The stack of these sensors included AlOx barriers and standard or SAF antiferromagnetic layer. These sensor were deposited in the N3000 system. As will be shown in section 5.1, the first transfer curves were linear although with a non-negligible coercivity. The coercivity reduction was attained using the following stack due to its thicker free layer: Ta 30 Å / Ru 150 Å / $Mn_{74}Ir_{26}$ 150 Å / $Co_{80}Fe_{20}$ 40 Å / Ru 8 Å / $(Co_{80}Fe_{20})_{90}B_{10}$ 30 Å / AlOx 6 Å / $(Co_{80}Fe_{20})_{90}B_{10}$ 50 Å / Ru 100 Å / Ta 30 Å . The transfer curve is shown in figure 4.29 and shows a linear response due to the higher magnetization of $(Co_{80}Fe_{20})_{90}B_{10}$ when compared to $(Co_{70}Fe_{30})_{80}B_{20}$ used in previous sections. A maximum of ≈ 40 % of TMR was attained with those sensors.

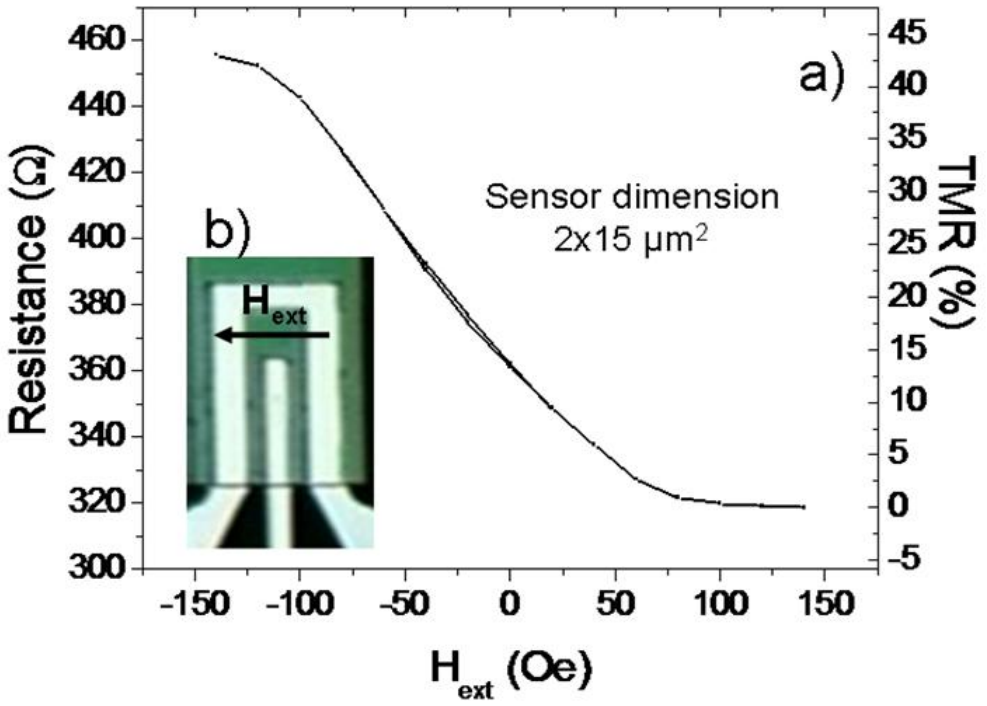

Figure 4.29: a) Magnetic tunnel junction typical transfer curve taken at a bias current of 20 μA. b) 2×15 μm^2 MTJ surrounded by a U-shaped current line used for magnetic particle focusing.

As the investigation of MTJ sensors evolved, MgO barrier were used in order to increase the TMR and thus the sensitivity of the sensors. Linear sensors with TMR up to $\approx 80 - 90$ % were fabricated. At the same time large sensors were fabricated in order to obtain the required

linearity and also to be used in another application as explained above. Three different magnetic stacks were optimized for these sensors and deposited in the N2000 system:

- Balanced SAF: Ta 50 Å / Ru 180 Å / Ta 30 Å / MnPt 200 Å / $Co_{90}Fe_{10}$ 20 Å / Ru 8 Å / $(Co_{50}Fe_{50})_{80}B_{20}$ 30 Å / MgO 15 Å / $(Co_{50}Fe_{50})_{80}B_{20}$ 100 Å / Ru 50 Å / Ta 50 Å .
- Unbalanced SAF: Ta 50 Å / Ru 180 Å / Ta 30 Å / MnPt 200 Å / $Co_{90}Fe_{10}$ 20 Å / Ru 8 Å / $(Co_{50}Fe_{50})_{80}B_{20}$ 40 Å / MgO 15 Å / $(Co_{50}Fe_{50})_{80}B_{20}$ 100 Å / Ru 50 Å / Ta 50 Å .
- Normal pinned layer: Ta 50 Å / Ru 180 Å / Ta 30 Å / MnPt 200 Å / $Co_{90}Fe_{10}$ 20 Å / $(Co_{50}Fe_{50})_{80}B_{20}$ 30 Å / MgO 15 Å / $(Co_{50}Fe_{50})_{80}B_{20}$ 100 Å / Ru 50 Å / Ta 50 Å .

The standard structure for these MgO based sensor is the first one. This structure was optimized in order to have a higher TMR. However, as already discussed, the magnetic gradients generated by the magnetic layers attract the magnetic particles to the sensor edge only. Therefore, the second and third structures were designed to be able to attract the magnetic particles to the sensing area but at the expense of reducing the TMR of the sensor.

In the beginning the contact lead used in MTJ was Al and the chip was passivated with 1000 Å Al_2O_3/2000 Å SiO_2. However, as was explained before in this chapter, in order to reduce the free layer - magnetic particle distance, the Al was replaced with Au and the passivation on top of the sensor was removed. The remaining chip is still passivated to avoid electrolysis in the fluidic sample during the biological experiments. This layer is at the same time a contact and the layer where the probe biomolecules will be immobilized. The microfabrication processes used for these two types of sensor can be found in appendix B and C.

Chip design

A magnetoresistive chip design with $2 \times 100\ \mu m^2$ was optimized in order to fulfill some predefined requirements:

- The chip can be mounted in a PCB chip carrier in order to be able to use in a portable integrated platform (section 5.2).
- Allow for the mounting of a self-aligned microfluidic PDMS channel described in section 5.2.

In this way two columns of 16 sensors separated $\sim 300\mu$m from each other were designed (figure 4.30). The separation between the sensors enables the spotting of different biomolecular probes on top of each sensor using a nanoplotter (Gesim) tool. On each column, there are two columns of 7 sensors + 1 reference sensor. The reference sensor is covered by the passivation layer so that the biomolecules are not immobilized. This sensor is used as a reference to determine the end of the washing step. An experiment is only valid if all the particles are removed from the reference sensors. Furthermore, these sensors could also be used to make a differential measurement in order to remove possible thermal drifts and improving the electrical dynamic range as discussed in section 4.1.4.

All the sensors have the same common contact which corresponds to the top left and/or right squared pad. All the other rectangular pads (except two that are used to bias the u-shaped current line) are used to address each sensors. The current should pass between one of the rectangular pads and the common pad. The voltage drop through the same two pads is measured in order to achieve the biological detection (see section 2.2.4). As depicted in figure 4.30, a U-shaped fluidic channel designed to pass through the two sensors columns.

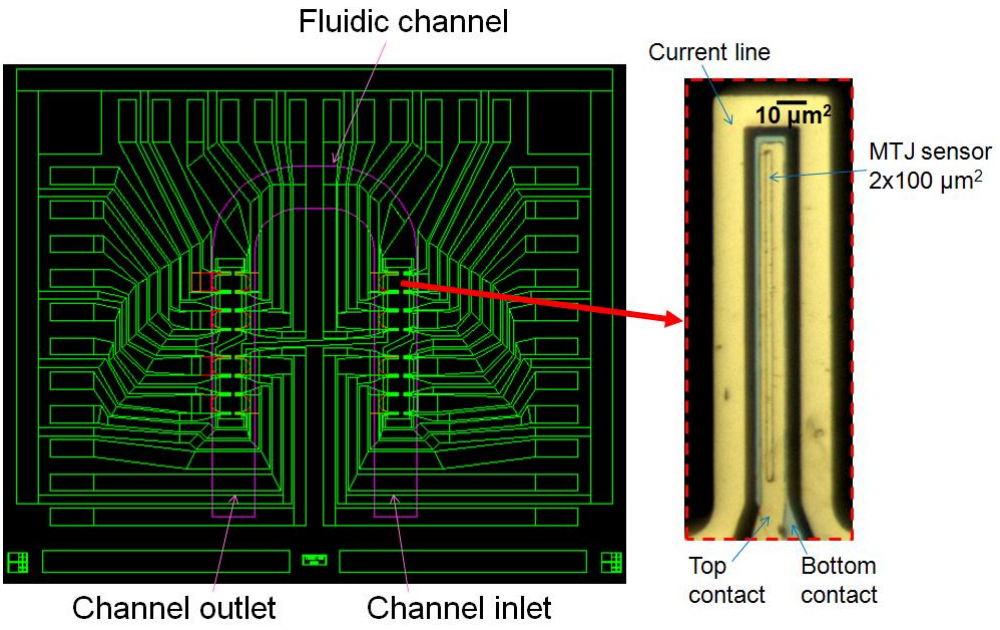

Figure 4.30: Chip design with 2 columns of MTJ sensors for integration with a microfluidic channel. Each column comprises 15 sensors and 2 reference sensors (MTJs with oxide on top of the sensor).

4.2.5 Magnetic particles detection

In this section, all the sensors were ion beam deposited in the N3600 system with parallel anisotropies and under a 100 Oe field. The microfabrication of the biochip was made following the run sheet in appendix C. The top contact of the MTJ was a 2000 Å gold layer. Half of the sensors on the chip were covered by a passivation layer of 1000 Å Al_2O_3/ 2000 Å SiO_2 (figure 4.31). The other half of the sensors remained uncovered in order to increase the sensor sensitivity as depicted in section . After, the microfabrication the sensors were diced into individual biochips and annealed at 280°C under a 1 T magnetic field. Finally, each biochip was wirebonded on a 40-pin chip carrier.

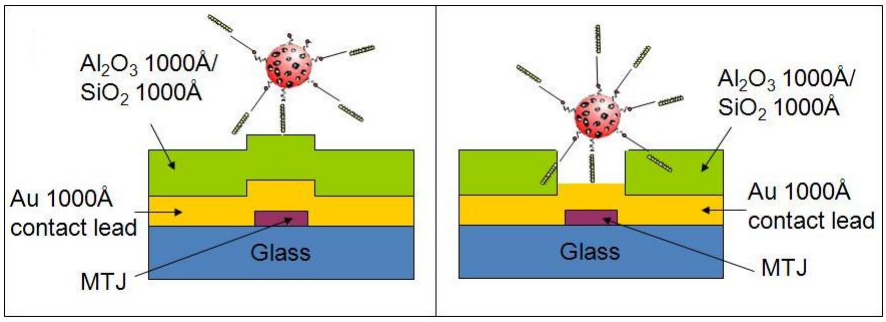

Figure 4.31: Schematic of the sensor cross section. On the left side, the top electrode is covered by the passivation layer. On the right side a liftoff of the passivation layer on top of the senor area is made reducing the distance of magnetic label to the sensor.

The MTJ were used to detect 250 and 130 nm particles (Micromod, Germany). In these experiments, an AC+DC external field configuration was chosen (section 4.1.4). The first approach was to use a SAF structure as the pinned layer of the sensor. The detection of magnetic particles was achieved in both sensors covered and not covered with the passivation layer. Finally, a sensor with a normal pinned layer was used to improve the particle attraction to the sensor area as discussed in section 4.1.3.

In a first magnetic particle detection experiment, a standard MgO stack with a SAF balanced pinned layer was used. The sensor comprised the following stacks: Ta 50 Å /Ru 200 Å /Ta 50 Å /$Mn_{74}Ir_{26}$ 150 Å /$Co_{80}Fe_{20}$ 30 Å /Ru 8 Å /$(Co_{70}Fe_{30})_{80}B_{20}$ 40 Å /MgO 18 Å /$(Co_{70}Fe_{30})_{80}B_{20}$ 50 Å /Ta 50 Å /Ru 100 Å /Ta 30Å. The sensor area size was defined to 2×15 μm^2. The MTJ showed a TMR of 60 % and a resistance in the parallel state of $\sim$ 1600 Ω (figure 4.32 inset). Finally, for the experiment the sensor was biased with a 250 μA current corresponding to the current where the $V_{1/2}$ is attained. An external fixed 15 Oe rms (31 Hz) magnetic field superimposed on a varying DC field ranging -50 to 50 Oe was applied to polarize the 250 nm magnetic particles (Micromod, Germany). The signals were acquired using a lockin technique.

After the acquisition of a the baseline signal during 10 minutes, a volume of 10 μL of particles (concentration of 5×10^7 particles/μL was put on top of the sensor. The particles were left to settle down until the signal attained the saturation. At this point the particles were washed until

the signal reached the baseline. The signal variation between the baseline and the saturation ($\Delta V = V_{baseline} - V_{saturation}$) was plotted as function of the external DC field (figure 4.32). The signal variation was further compared to the expected one.

In the case of a MTJ with the passivation layer over the top electrode, the measured signal showed a signal with the opposite sign of the simulated one for 300 particles over the sensor area (figure 4.32). This phenomenon is caused by the fact that the magnetic particle fringe field is in the opposite direction than the expected one. As already showed in chapter 3, this only happens when the magnetic particles are located outside the sensor area.

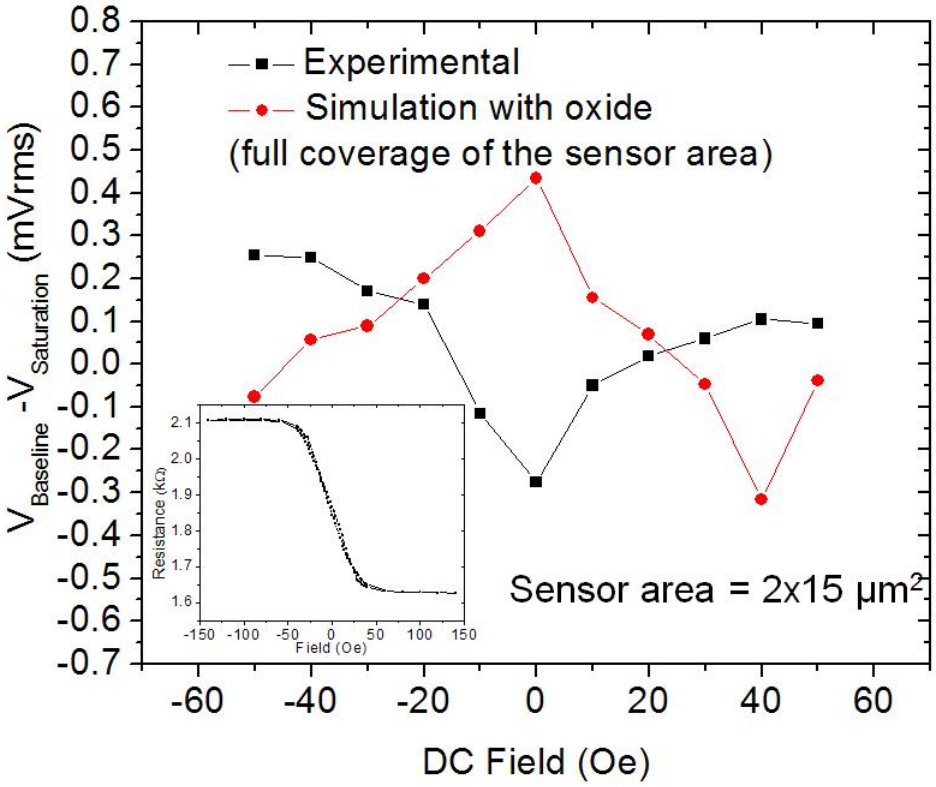

Figure 4.32: MTJ voltage variation observed in the presence of 250 nm magnetic particles as function of the external DC fields. The expected signal variation due to the full coverage of the sensor with magnetic particles is also plotted. The top electrode of the sensor was covered by a passivation layer. Inset: transfer curve of the MTJ.

On the other hand, assuming the correctness of this assumption an attenuation of the signal should also observed. In fact, taking the value at 0 Oe field, in absolute value, the measured signal is ~ 1.5 times lower than the simulated signal. This is the same attenuation factor of the average fringe field of a magnetic particle located in the edge of the sensor area when compared to a particle in the center of the sensor (chapter 3). Therefore, it can be concluded that in this experiments the magnetic particles are agglomerating on the edge of the sensor area. Figure 4.33 compares the experimental signal variation with the simulated signal obtained for 500 particles are distributed in the edges of the sensor. In the positive DC field side the simulations match

with experimental results. The discrepancies observed at negative DC fields can be explained by the fact that the sensor showed some coercivity in this zone of the transfer curve. Therefore, signal variation due to the presence of minor loops may shadow the signal created by magnetic particles.

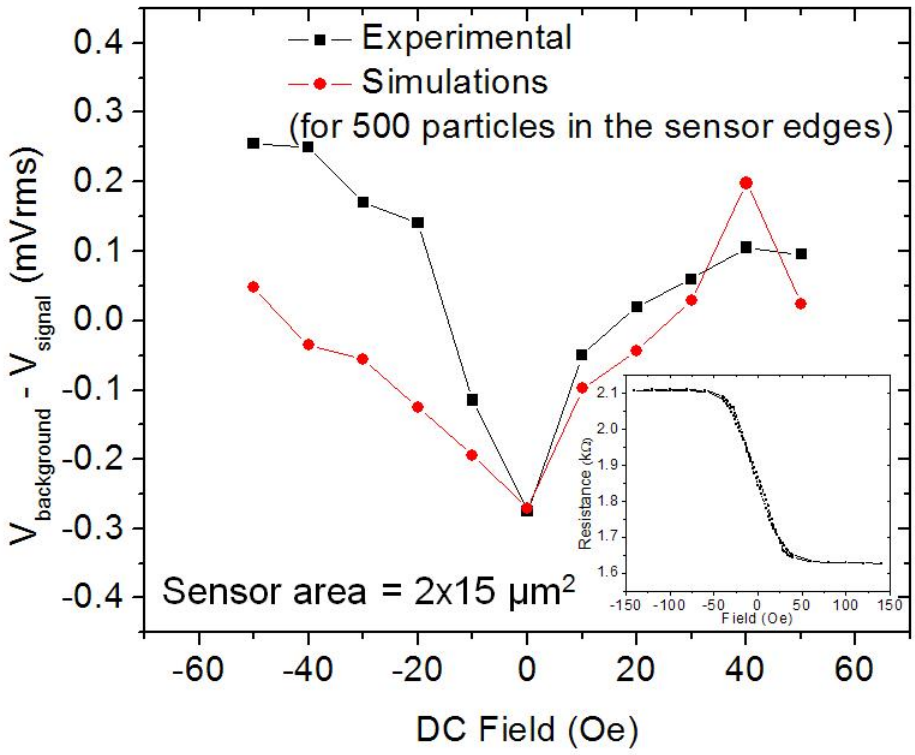

Figure 4.33: MTJ voltage variation observed in the presence of 250 nm magnetic particles as function of the external DC fields. The expected signal variation due to the presence of 500 magnetic particles on the edge of the sensor is also plotted. The top electrode of the sensor was covered by a passivation layer. Inset: transfer curve of the MTJ.

The fact that the particles are agglomerating on the edge of the sensor instead of going on top of the sensor was already addressed in section 4.1.3. In fact, the sensor used in this experiment include in its structure an almost balanced SAF pinned layer. Therefore, it is energetically more favorable for the magnetic particles to be located in the edge of the sensor.

The same experiment was carried out with a sensor without the passivation layer on top. As previously, the signal variation of the sensor due to the magnetic particles indicated that most of the particles were positioned on the edge of the sensor. However, when compared to the signal expected from 100 particles on the edge of the sensor, the signal seems attenuated by a factor of 0.6 (figure 4.34).

As discussed in section 4.1.3 the attraction force of magnetic particles increases as they are closer to the sensor. Therefore, it is probable that some particles were positioned on the sensor area. These particle contributed with a average fringe field in opposite direction than the one located on the edge of the sensor. As a result, the overall average field is lower than expected

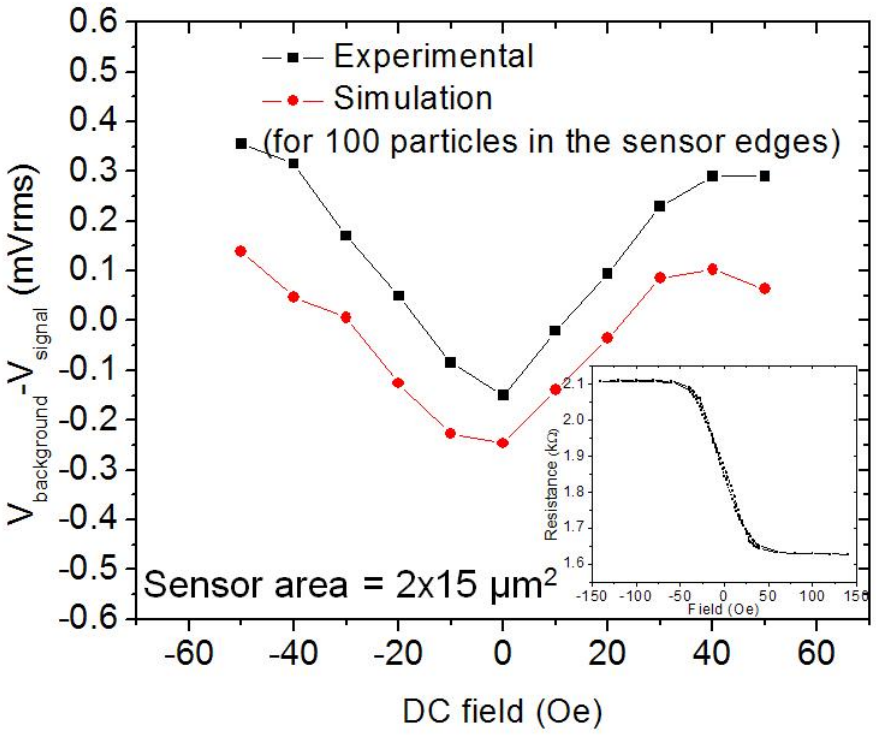

Figure 4.34: MTJ voltage variation observed in the presence of 250 nm magnetic particles as function of the external DC field. The expected signal variation due to the presence of 100 magnetic particles on the edge of the sensor is also plotted. The top electrode of the sensor was directly in contact with the particle solution. Inset: transfer curve of the MTJ.

as observed in figure 4.34. Nevertheless, the signal variation sign showed that most of the field is generated by the labels on the edge of the sensor. This fact indicates that the amount of particles outside the sensor area was still higher than the ones inside.

In order to increase the number of particles inside the sensor area, a MTJ with a normal pinned layer was fabricated included the following layers: Ta 50 Å /Ru 100 Å /$Mn_{74}Ir_{26}$ 150 Å /$Co_{80}Fe_{20}$ 15 Å /$(Co_{70}Fe_{30})_{80}B_{20}$ 25 Å /MgO 18 Å /$(Co_{70}Fe_{30})_{80}B_{20}$ 100 Å /Ru 50 Å /Ta 50Å. The MTJ showed a TMR of 40 % and a resistance in the parallel state of $\sim 710\ \Omega$ (figure 4.32 inset) for an area of $2 \times 30\ \mu m^2$. The lower TMR of this sensor is mainly caused by the fact that the pinned layer is not an SAF. In the experiment, the sensor was biased with a 500μA current. The external AC magnetic field was fixed to 10 Oe rms (31 Hz). A varying DC field ranging 0 to 35 Oe was superimposed to the AC field. The signals were acquired using lock-in technique.

A volume of 10 μL of 250 nm particles (5×10^7 particles/μL) was introduced on top of the chip. The signal variation presented in figure 4.35 was almost independent on the DC applied field. Furthermore, these signals had the same amplitude predicted by the simulation of a sensor fully covered with labels. Therefore, contrary to the previous cases the magnetic particles are mostly located in the sensor area and not on the edges.

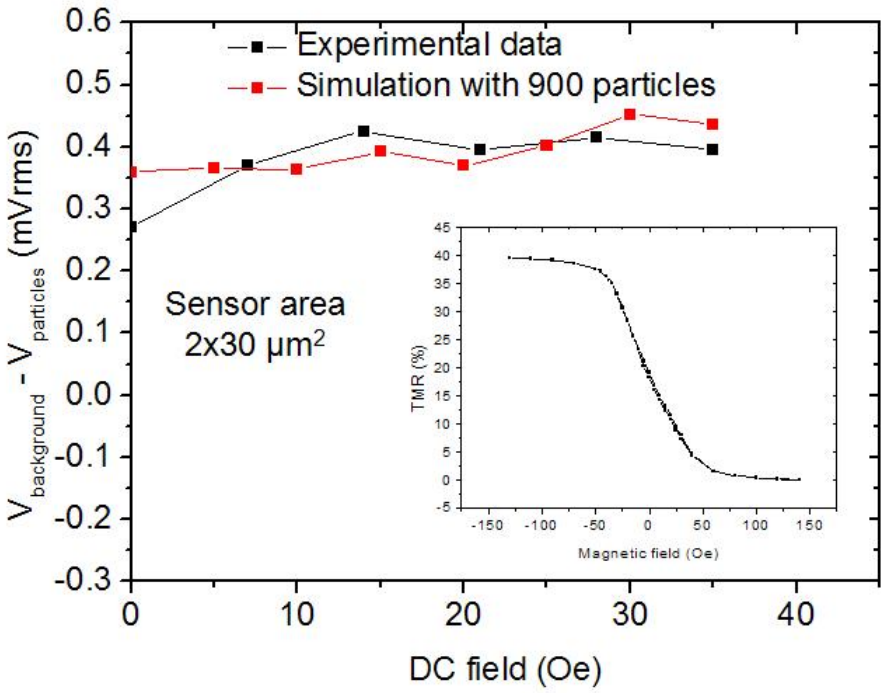

Figure 4.35: MTJ voltage variation observed in the presence of 250 nm magnetic particles as function of the external DC field. The expected signal variation due to the full coverage of the sensor area with magnetic particles is also plotted. Inset: transfer curve of the MTJ.

In conclusion, the influence of the magnetic layers of a magnetoresistive sensor on the magnetic particle position was demonstrated by the analysis of the detected signal. The distance between the sensor and the magnetic particles has proven to influence the overall signal. Upon the reduction of this distance some particles were attracted to the sensor area attenuating the dominant fringe field produced by the particles on the edge of the sensor. Finally, replacing the SAF pinned layer by a normal pinned layer produced the same signal variation expected by simulating a full covered sensor with magnetic particles.

4.3 Spin valve biochip

4.3.1 Giant magnetoresistance

The operation of a spin valve is described by the giant magnetoresistance (GMR) effect first discovered by Baibich [30]. In this phenomenon, a spin-dependent transmission of conduction electrons between two ferromagnetic (FM) layers through a metallic layer (M) is observed. This transmission depends on the relative orientation of the moments of the magnetic layers. In a spin valve device composed by FM1/M/FM2, the electrical transport can be divided into two spin-channels, currents resulting from spin-up and spin-down electrons. At the interfaces, two electrons with distinct spin have different scattering probabilities which depend on the spin-depended potential landscape and on the density of states at the Fermi-level. Therefore, an electron will have a higher scattering probability when its spin direction is opposite to the local magnetization direction of the FM layer (figure 4.36).

In a spin valve structure, the FM layers have parallel or anti-parallel moments. In the first case, spin-down electrons will have a higher scattering probability than the spin-up electrons. This fact originates a lower resistivity channel for spin-up electrons which lowers the overall resistance of the device (figure 4.36a). In the second case, spin-up and spin-down electrons will have a high scattering probability in one of the FM layers and a low scattering probability on the other creating a two channels with the same resistivity (figure 4.36b). The relative change in resistance between parallel and antiparallel configuration is called the GMR ratio, or more commonly magnetoresistive ratio (MR), and is defined by:

$$MR = \frac{R_{ap} - R_p}{R_p} \tag{4.47}$$

where R_p and R_{ap} are the device resistances of parallel and antiparallel configuration, respectively.

The principle of a spin valve sensor comprising a fixed FM layer (pinned layer) and a free layer was first introduced in 1991 by Dieny [31] and further developed and tested in 1994 [32]. This sensor typically show MR up to 8% but introducing nano-oxide layers at FM interfaces for improvement of the scattering, the MR can be increased to 15%-20% [33], [34].

4.3.2 Spin valve characteristics

Contrary to the MTJs, spin valve sensors behave like a resistor, which is sensitive to an external magnetic field. Therefore, its IV curve is given by Ohm's law ($V = R\ I$) and not by Simmons' model (see previous section).

The spin valve resistance depends on the length (l) and on the width (w) of the device. It increases with the increase of the length and decreases with the increase of the width. Thus, the resistance of a spin valve can be written:

$$R = R_{\square}\frac{l}{w} \tag{4.48}$$

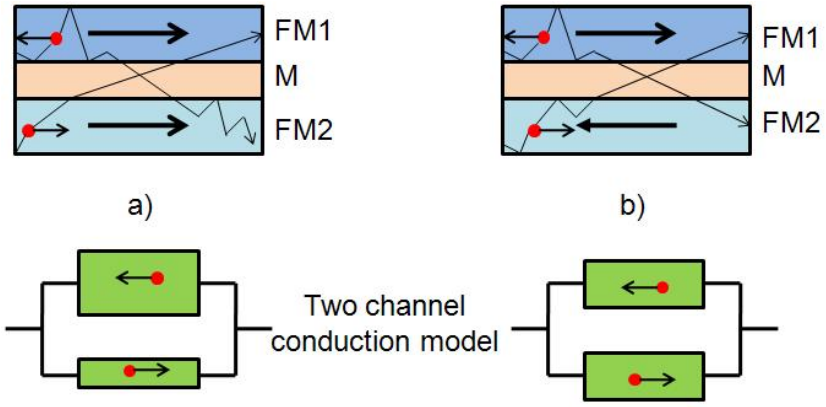

Figure 4.36: Schematic of the GMR effect in FM1/M/FM2 structure when FM1 and FM2 are parallel a) or antiparallel b). The two channel conduction model is illustrated. In this model, each spin channel is represented by a resistor. If the spin of the electron has the same orientation than the moment of the layers, the resistance is low. In the opposite case, the resistance is high. An intermediate resistance model both spin channel if the two FM are antiparallel. The overall device resistance is the parallel equivalent of the resistance of both spin-channel.

where $R_\square$ is constant for a certain spin valve structure. In the case of the spin valves studied in this thesis, $R_\square \sim 20\ \Omega$. The resistance of the spin valve is therefore dependent on its dimensions. Since the it is not as easy to change the $R_\square$ of a spin valve as the $R \times A$ product of a MTJ, a change in the area of the spin valve will directly affect its resistance. This may be a limitation in the spin valve design for biochip applications.

As for the MTJ, a spin valve sensor also has to have a linear response for biochip applications as shown in figure 4.26. Therefore, its sensitivity is also given by equation 4.29.

However, in the case of the spin valve the MR is constant for all bias voltages. Thus, the sensitivity will also remain constant with the bias voltage. In the linear range, the voltage variation due to an external magnetic field will then be:

$$\Delta V = (R(H) - R_0)I \Leftrightarrow \Delta V = S\ R_{min}\ H\ I \tag{4.49}$$

4.3.3 Spin valve signal to noise ratio

As for the MTJ, the SV sensor also exhibits low frequency voltages fluctuations with a power spectral density is inversely proportional to frequency. Adapting the phenomenological model proposed by Hooge [55] to the SV sensor, the following expression is found:

$$S_{1/f} = \gamma \frac{R^2 I^2}{N_c f} \quad [\mathrm{V}^2/\mathrm{Hz}] \tag{4.50}$$

where γ is the phenomenological Hooge constant, R is the SV differential resistance, I is the current passing through the SV, f is the operating frequency and N_c the number of charge carriers in the SV and can be calculated using the equation $N_c = VC$. C is taken as the Cu atomic concentration 8.45×10^{22} cm^{-3} and V is the volume of the spin valve (for the spin valve

used in this thesis, the area is 2.5×80 μm^2, the thickness is 7.5 nm and therefore $V = 1.5 \times 10^{-12}$ cm^3).

For higher frequencies, the SV sensor also shows a frequency independent noise. In this case, there is only the contribution from the thermal noise as for this sensor there is no shot noise effect.

$$S_{thermal} = 4k_BTR \quad [\mathrm{V}^2/\mathrm{Hz}] \tag{4.51}$$

Using the setup described in section 2.2.3, a typical noise spectrum of a SV was measured (figure 4.37). A fitting of the curve to the $S_{1/f} + S_{thermal}$ noise can be accomplished retrieving the Hooge constant of the SV. Upon this fitting a Hooge constant of $\gamma \sim 1$ and a thermal noise of $\sim 1.4 \times 10^{-17}$ V^2/Hz is obtained. The value of the Hooge constant is the expected and the thermal noise is also close to the theoretical value for a SV resistance of 650 Ω ($S_{thermal} = 1.1 \times 10^{-17}$ V^2/Hz). In this case, the 1/f knee is observed at ~ 1 kHz for 0.1 mA.

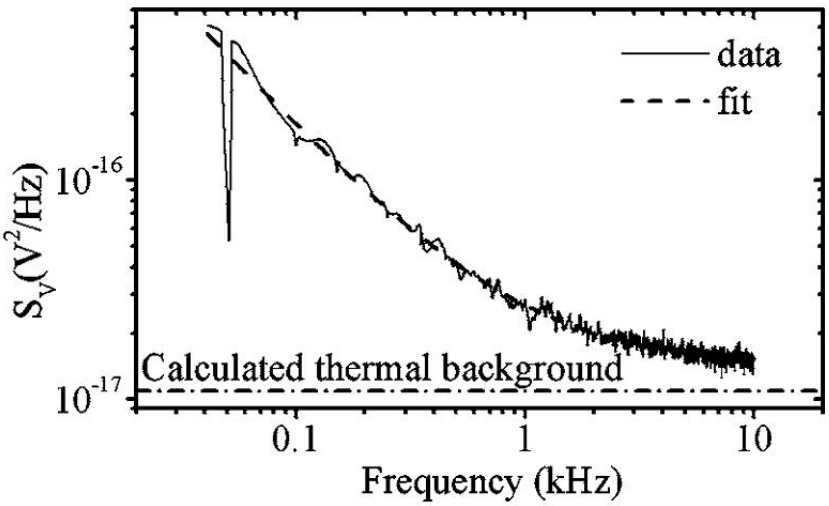

Figure 4.37: Noise spectrum for a 2.5×80 μm^2 U-shaped SV sensor in the linear regime and with a sense current of 0.1 mA. A fit is shown for the 1/f noise and thermal contributions and the calculated thermal noise is also displayed.

The SNR of a SV can now be written and its maximum calculated. Since the minimal sensor noise is obtained when the thermal noise is dominant, the SNR is:

$$S/N = \frac{\Delta V}{\sqrt{S_{thermal}}} = \frac{S\ R_{min}\ H\ V}{\sqrt{4k_BTR^3}} \tag{4.52}$$

Contrary to the MTJ sensor, the SV sensor resistance may vary at most 15 %. Therefore, it can be assumed that $R \sim R_{min}$. Therefore the SNR is given by:

$$S/N = \frac{\Delta V}{\sqrt{S_{thermal}}} = \frac{S\ H\ V}{\sqrt{4k_BTR_{min}}} \tag{4.53}$$

The SNR can be optimized by decreasing the resistance of the sensor. Furthermore, since the

SV sensitivity does not decrease with the increase of the bias voltage, the SNR of a SV sensor increases with the bias voltage. The limit is then the maximum voltage that a SV sensor can handle. However, a high current passing through the sensor heats the chip by power dissipation. This heating is critical for the biochip application since biomoleculas reactions are stable for specific temperatures. Therefore, the voltage limit for the SNR is determined by the maximum heating that the target biomolecule reaction allows since this voltage is typically much lower than the highest voltage a SV sensor can handle. In the experiments with biomolecules described in chapter 6 a maximum voltage of 1 V was used for SV with a resistance of 1 kΩ in order to minimize the heating of the chip. This voltage also avoids electrolysis when a solution is put on the chip surface.

As for the MTJ, for technical reasons it may not be always possible to work in the high frequency regime. Therefore, it is important to study the SNR at low frequency. In this frequency domain, the noise of the sensor is given by the sum of the $1/f$ noise (equation 4.55) and the thermal noise (equation 4.51). Therefore, the SNR is given by:

$$S/N = \frac{\Delta V}{\sqrt{S_{1/f} + S_{thermal}}} = \frac{S\ R_{min}\ H}{R} \frac{V}{\sqrt{\gamma \frac{V^2}{N_c f} + 4k_B T R}} = \frac{S\ R_{min}\ H}{R\sqrt{\frac{\gamma}{N_c f} + \frac{4k_B T R}{V^2}}} \tag{4.54}$$

Assuming $R \sim R_{min}$,

$$S/N = \frac{S\ H}{\sqrt{\frac{\gamma}{N_c f} + \frac{4k_B T R}{V^2}}} \tag{4.55}$$

This equation shows that the SNR increases with the voltage on the sensor. Therefore, for high voltages the SNR is given by:

$$S/N = S\ H \sqrt{\frac{N_c f}{\gamma}} \tag{4.56}$$

In this case, the SNR does not depend on the SV resistance. Therefore, large resistances can be used to minimize the power dissipation $P = \frac{V^2}{R}$ over the chip. Large sensors areas should be used in order to maximize the SNR since N_c is directly proportional to the sensor area. Finally, an increase in the sensor sensitivity or in the measuring frequency also optimizes the SNR.

It is then also important to analyze the SNR of the SV sensor when the noise of the measuring system is dominant. Therefore, a constant white noise S_{elec} is assumed for the measuring electronic system and the SNR expression can then be written:

$$S/N = \frac{\Delta V}{\sqrt{S_{elec}}} = \frac{S\ R_{min}\ H\ I}{\sqrt{S_{elec}}} \tag{4.57}$$

This case is similar to the case where the thermal noise is dominant. The SNR increases with the voltage on the sensor ($V = R_{min} I$) and the limit is given by the maximum temperature variation the experiment allows. As the maximum voltage is predefined, the SNR is independent of the sensor resistance. Therefore, as long as the SV noise is below the noise of the electronic

system, any sensor resistance can be used. This fact allows some flexibility in the sensor size design.

4.3.4 Spin valve biochip design

Sensor design

The spin valve sensor was design in order to have a medium dynamic range. In fact the 2.5×80 μm^2 U-shaped spin valve (see inset of figure 4.38) was designed to be sensitive up to $\sim$ 3200 250 nm particles. Furthermore, a U-shaped current line surrounding the sensor was specially designed to enable particles focusing onto the sensing area [99]. Passing a 40 mA dc current through this line generates a field gradient, which attracts the particles toward it. By applying an external 30 Oe rms magnetic polarizing field, at frequencies ranging from 0.1 to 1 Hz, the magnetic particles will be alternatively attracted and repelled from the line. This movement forces the particles to pass through the sensing area and eventually to bind to the biological probes.

The spin valve structure was optimized in order to achieve a linear response as shown in figure 4.38. The sensor stack deposited on a Si substrate covered by a 500 Å Al_2O_3 layer is as follows: 20 Å Ta/ 30 Å $Ni_{80}Fe_{20}$/ 25 Å $Co_{81}Fe_{19}$/ 26 Å Cu/ 25 Å $Co_{81}Fe_{19}$/ 60 Å $Mn_{76}Ir_{24}$/ 30 Å Ta/ 150 Å $Ti_{10}W_{90}$ (N). Then 3000 Å alimunium leads were defined by liftoff. After the passivation step (see appendix A), a 13×43 μm^2 Au pad is patterned on top of the spin valve defining the biological active area of the sensor. As will be described in detail in chapter 6, the biological probe molecules will be immobilized on top of this Au layer.

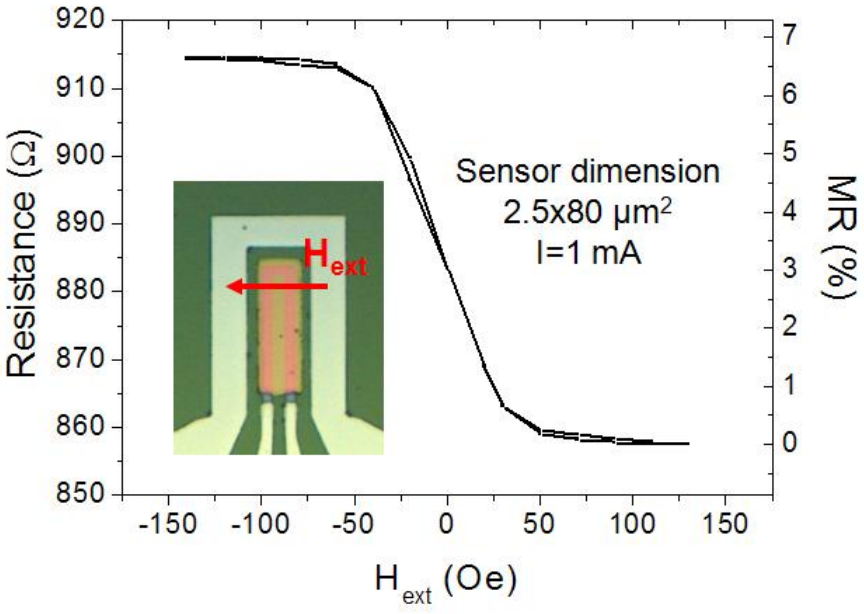

Figure 4.38: Spin valve typical transfer curve taken at a bias current of 1 mA. The inset shows the U-shaped 2.5×80 μm^2 spin valve covered by a 13×43 μm^2 gold pad. Surrounding the spin valve, a U-shaped current line is used for magnetic particle focusing.

Chip design

Up to the point that this thesis started, a biochip using 24 sensors as described previously was being used for detection of Cystic Fibrosis gene expression. This project evolved in a new european project where this chip would be integrated in a lab-on-a-chip system (further informations are provided in chapter 5.3). This fact has implied a redesign of the biochip in order to be used in the following applications:

1. **Integration with a PCR platform**: this chip was integrated in a standard microfluidic platform together with a chip which performs PCR on chip (see section 5.3).
2. **Integration in a EWOD PCR platform**: this chip was integrated in a EWOD platform which performs PCR on chip (see section 5.3).
3. **DNA detection limit**: determination of the minimum concentration of DNA and the biological dynamic range that this spin valve architecture is able to detect. (see chapter 6).

Having this application in mind, a biochip comprising 4 different areas each with 7 biological active sensors and 1 reference sensor was designed (figure 4.39). In application 1 three of the areas are used while in application 2 only one area is used. For the third application, 4 cameras surrounding each areas were made with silicon gel enabling the introduction of different biological concentrations in each area.

In each area, the sensors area disposed in two columns of 4 sensors separated from each other by ~ 300 μm. This separation enables the spotting of different biomolecular probes on top of each sensor using a nanoplotter (Gesim) tool. In this way, 7 different probes can be spotted on each area. The reference sensor (sensor without a gold pad) is not biologically active and is mainly used as an indicator of the successful washing of the chip after the hybridization. Furthermore, this sensor could also be used to make a differential measurement in order to remove possible thermal drifts and improving the electrical dynamic range as discussed in section 4.1.4.

All the sensors have the same common contact, which corresponds to the top left and/or right squared pad. All the other rectangular pads (except two that are used to bias the U-shaped current line) are used to address each sensors. The current should pass between one of the rectangular pads and the common pad. The voltage drop through the same two pads is measured in order to achieve the biological detection (see section 2.2.4).

Based on this last chip, another chip design was made in order to be integrated with a PDMS fluidic channel (see section 5.3). As depicted in figure 4.40, a U-shaped fluidic channel was designed to pass through the sensors column. The only change that was made on the chip itself is to join the areas of each column together. In this way there are no sensors on top of the inlet or the outlet.

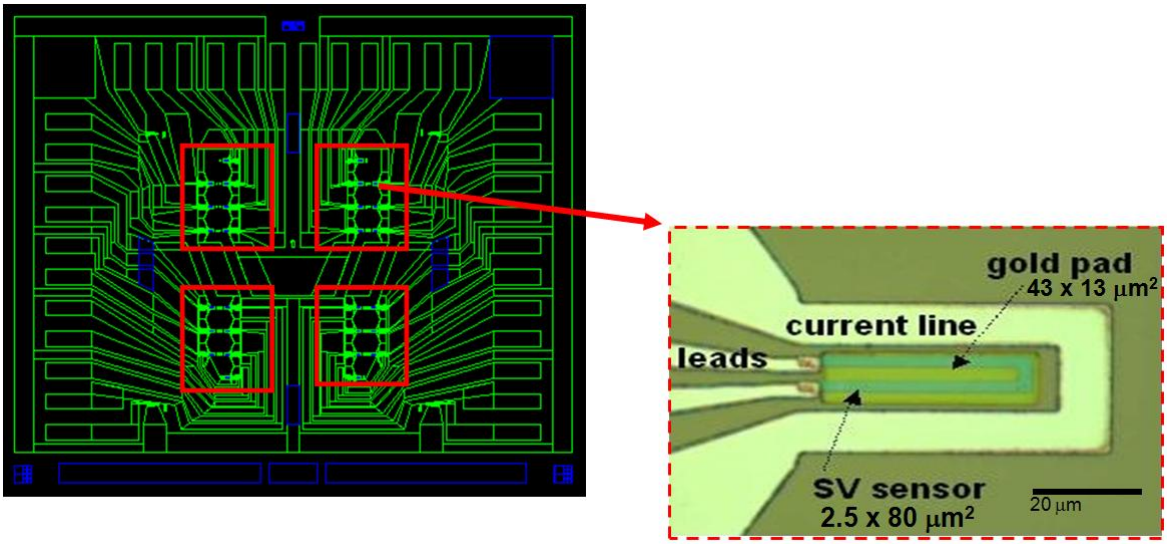

Figure 4.39: Chip design with 4 independent areas. Each area comprises 7 sensors and 1 reference sensor (spin valve without biological active area).

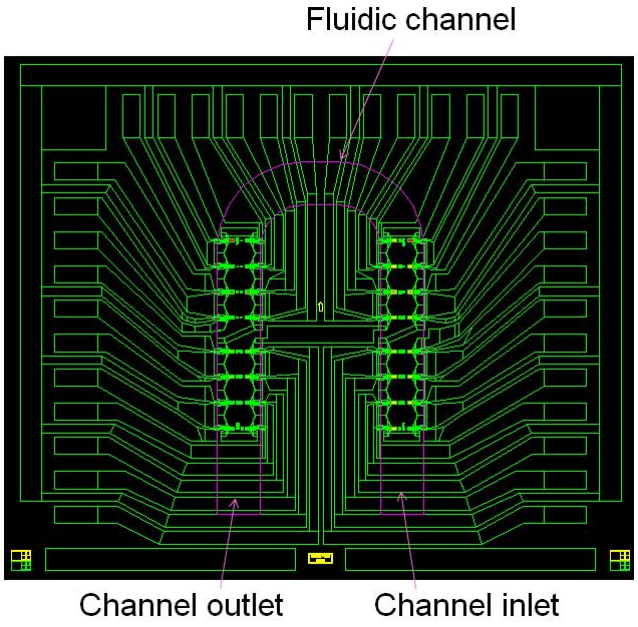

Figure 4.40: Chip design with 2 columns of spin valve sensors for integration with a microfluidic channel. Each column comprises 15 sensor and 2 reference sensor (spin valve without biological active area).

4.3.5 Magnetic particles detection

A biochip with U-shaped SV sensors and U-shaped current lines, was fabricated and used for 250 nm magnetic particle detection. The SV stack was deposited in the Nordiko 3600 system onto a Si/ Al_2O_3 500 Å substrate with the following structure: Ta 20 Å /$Ni_{80}Fe_20$ 30 Å /

$Co_{80}Fe_{20}$ 25 Å / Cu 22 Å / $Co_{80}Fe_{20}$ 25 Å / $Mn_{76}Ir_{24}$ 60 Å / Ta 30Å / $Ti_{10}W_{90}$(N) 150 Å . After the definition of a sensor area of 2.5×80 μm^2 by ion milling, contact leads of $AlSi_1Cu_{0.5}$ 3000 Å / $Ti_{10}W_{90}$(N) 150 Å were deposited by sputtering and defined by lift-off. Finally, a passivation layer composed by Al_2O_3 1000 Å / SiO_2 2000 Å was deposited over the whole chip.

In the experiment, the SV was biased with a 1 mA current. The external AC magnetic field was fixed to 13.5 Oe rms (31 Hz). A varying DC field ranging -70 to 30 Oe was superimposed on the AC field. The signals were acquired using lock-in technique.

The experiment started by acquiring a baseline signal during 5 minutes. Then, volume of 10 μL of 250 nm particles (5×10^7 particles/μL) was introduced on top of the chip and the particle were left to settle down during 30 minutes. Finally, the chip was washed with deionized water and the signal came back to the baseline.

The signal variation presented in figure 4.41 corresponds to the difference between the baseline signal and the maximum signal produced by the magnetic particles. The signal variation in function of the DC field applied was also simulated. As observed in figure 4.41 the experimental signal has the same sign, amplitude and behavior than the simulated signal. However, some discrepancies can be still observed. This is mainly due to the fact that the sensor used in this experiment exhibited some coercivity in the linear response zone (inset figure 4.41). This fact creates minor loops which will affect the signal variation and mask the real signal variation due to the the presence of magnetic particles.

In this specific case, the maximum signal variation was obtained for a DC magnetic field of -30 Oe. However, in this zone the sensor is not linear. Therefore, it would be more likely to make particle detection at a 20 Oe DC field.

In conclusion, the SV signal variation to the presence of 250 nm particles was achieved for several DC applied field in order to define which is the field optimizing the signal. A maximum signal was observed at a field of 30 Oe. However, due to the non-linearities of the SV transfer curve it was better to choose a 20 Oe as the optimum field.

4.4 Magnetic tunnel junction and spin valve comparison

In this section, MTJ and SV sensors are compared by means of their SNR. The main goal is to be able to fabricate MTJ biochips which would show an improved SNR when compared to SV biochips. On one hand, an analysis of the SNR expressions already determined will be achieved in order to determine the characteristics needed for MTJ design. On the other hand, a MTJ biochip was fabricated and compared to SV biochip.

4.4.1 Magnetic tunnel junction and spin valve SNR comparison

In this section, an analysis of the SNR of MTJs and SVs is performed. Table 4.1 summarizes the optimal SNR for both sensors assuming high frequencies, low frequencies or when the noise of an electronic measurement system is dominant. In each case, the expression of the ratio between the MTJ SNR and the SV SNR is obtained and also presented in the table. These

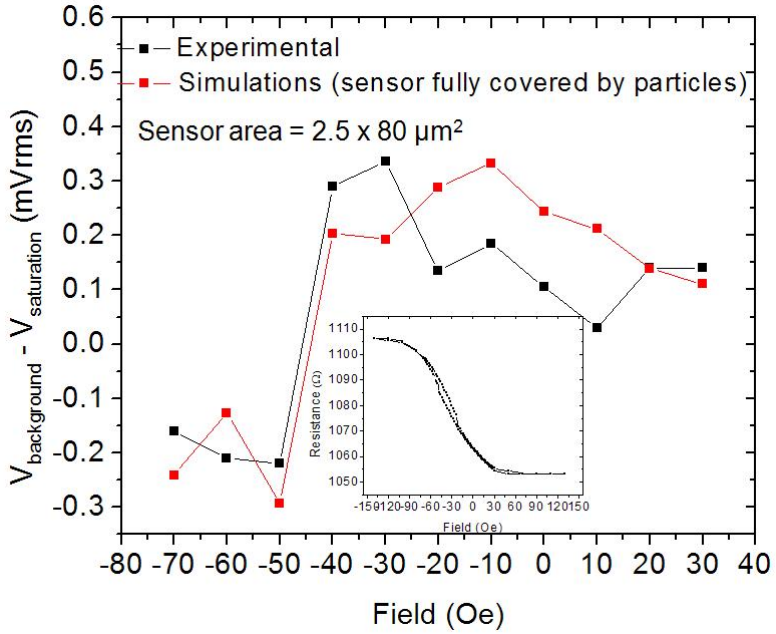

Figure 4.41: SV voltage variation observed in the presence of 250 nm magnetic particles in function of the external DC fields. The expected signal variation due to the full coverage of the sensor with magnetic particles is also plotted. Inset: transfer curve of the SV.

expressions are now analyzed assuming that the sensors have the same area ($A = 200\ \mu m^2$). For the SV sensor the following parameters were used: $N_c = 1.69 \times 10^{11}$, $\gamma = 1$, $S_SV = 0.08$ %/Oe and $R_{SV} = 1000\ \Omega$. In the case of the MTJ sensor the parameters used were: $\alpha_H = 1.3 \times 10^{-9}\ \mu m^2$, $V_{1/2} = 0.4$. The MTJ resistance R_{MTJ} and sensitivity S_{MTJ} are proportional to the corresponding parameters of the SV sensor.

Regime	SNR_{SV}	SNR_{MTJ}	SNR_{MTJ}/SNR_{SV}
High frequencies	$\frac{S_{SV}\ H\ V}{\sqrt{4k_BTR_{min}}}$	$\frac{2}{3}S_{MTJ}\ H\sqrt{\frac{V_{1/2}}{3qR_{min}}}$	$\left(\frac{2}{3}\right)^{2/3}\sqrt{\frac{2k_BT}{qV_{1/2}}}\frac{V_{1/2}}{V}\frac{S_{MTJ}}{S_{SV}}\sqrt{\frac{R_{SV}}{R_{MTJ}}}$
Low frequencies	$S_{SV}\ H\sqrt{\frac{N_cf}{\gamma}}$	$\frac{S_{MTJ}(1-\frac{V}{2V_{1/2}})\ H}{\sqrt{\frac{\alpha_H}{fA}+\frac{2qR_{min}}{V}\ \coth\left(\frac{qV}{2k_BT}\right)}}$	$\frac{S_{MTJ}}{S_{SV}}\frac{(1-\frac{V}{2V_{1/2}})\ H}{\sqrt{\frac{\alpha_H}{fA}+\frac{2qR_{min}}{V}\ \coth\left(\frac{qV}{2k_BT}\right)}}\sqrt{\frac{\gamma}{N_cf}}$
Electronic noise dominant	$\frac{S_{SV}\ H\ V}{\sqrt{S_{elec}}}$	$\frac{S_{MTJ}\ H\ V_{1/2}}{2\sqrt{S_{elec}}}$	$\frac{1}{2}\frac{S_{MTJ}}{S_{SV}}\frac{V_{1/2}}{V}$

Table 4.1: Summary of SV and MTJ SNR in the high and low frequencies and when the noise of the electronic system is dominant. In the fourth column the ratio between MTJ and SV SNR is calculated.

The optimum SNR attained by MTJ and SV sensors is observed in the high frequency limit. As already discussed before, in this limit the dominant noise observed in MTJ and SV sensors is the shot and thermal noise, respectively. As the maximum MTJ SNR is attained at $\frac{2}{3}V_{1/2}$ the SNR of both sensors can be compared by varying the bias voltage of the SV. A range between 0 and 1 V was chosen since, as proven previously, voltages higher than 1 V would affect the usability of the SV sensor in a biochip application.

Assuming an MTJ sensitivity equal to the SV sensitivity, for MTJ resistances equal or higher than the SV resistance, the SNR of the SV sensor will be always better than the MTJ SNR (figure 4.42). For lower MTJ resistance a higher MTJ SNR can be observed for low SV bias. For example, if the MTJ resistance is ten times lower than the SV resistance, below a SV voltage bias of ~ 0.3 V the MTJ SNR is better than the SV SNR. This fact would be expected since the thermal noise is typically lower than the shot noise.

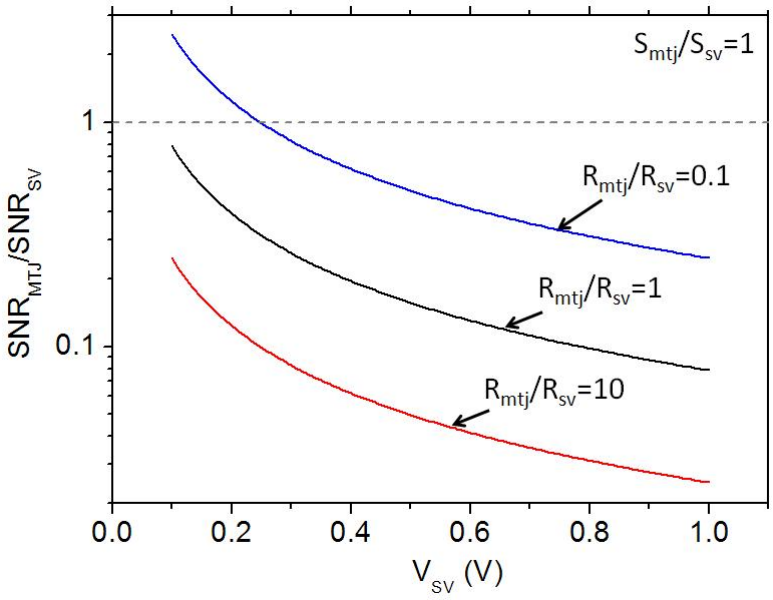

Figure 4.42: SNR_{MTJ}/SNR_{SV} in function of SV bias voltage assuming $\frac{S_{MTJ}}{S_{SV}} = 1$ and high frequencies. MTJ resistances of $0.1 \times R_{SV}$, $1 \times R_{SV}$ and $10 \times R_{SV}$ were used.

However, the interest of using MTJs as magnetoresistive sensors is their higher sensitivity. The intrinsic sensitivity of a MTJ could be up to 10 times (theoretically even more) higher than the SV intrinsic sensitivity. In this specific case, it is much easier to find a condition where the MTJ SNR is better than the SV SNR. Analyzing figure 4.43, it can directly be observed that reducing the MTJ resistance would be one of these conditions. As already highlighted previously, for a fixed sensor area the MTJ resistance can be more easily tailored than the SV resistance. Nevertheless, even if both sensors have the same resistance, there are SV biasing conditions ($V_{SV} < 0.8$ V) where the MTJ SNR is higher. Therefore, the increased sensitivity and easy of the resistance choice are key factors for replacing SV by MTJ sensors in magnetoresistive biochips for improved biological sensitivities.

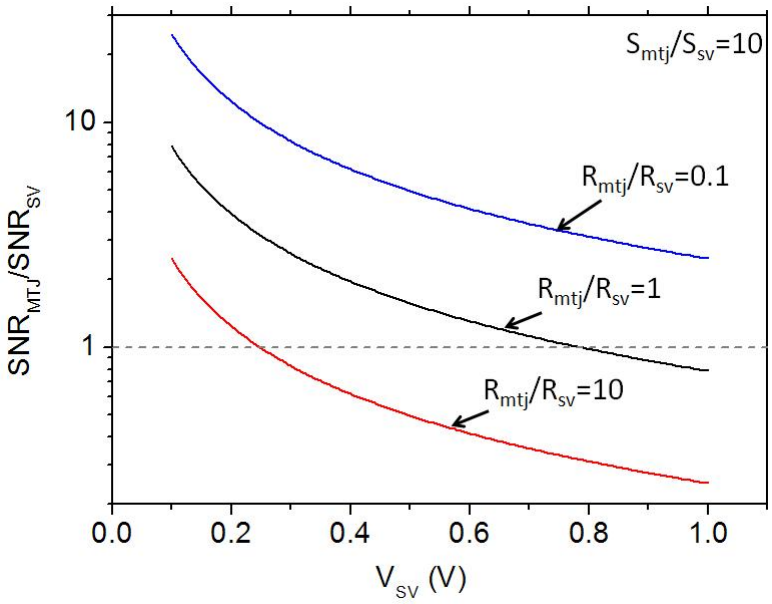

Figure 4.43: SNR_{MTJ}/SNR_{SV} in function of SV bias voltage assuming $\frac{S_{MTJ}}{S_{SV}} = 10$ and high frequencies. MTJ resistances of $0.1 \times R_{SV}$, $1 \times R_{SV}$ and $10 \times R_{SV}$ were used.

In the low frequency regime, the optimum SNR of a MTJ is attained at different voltages depending on the MTJ resistance. In contrast, the SV maximum SNR is independent on the voltage bias. MTJ and SV SNRs are therefore compared as function of the MTJ bias voltage. If both sensors exhibit the same sensitivity, the SNR of the SV will be higher than the MTJ SNR for all bias voltage (figure 4.44). However, the opposite situation occurs if the MTJ has 10 times more sensitivity than the SV. This is also true for higher MTJ resistance (up to $10 \times R_{SV}$) and bias voltages above 50 mV (figure 4.45). Therefore, in the low frequency regime an improved sensitivity of MTJ is the only requirement for attaining a higher SNR than for SV sensors.

Finally, in the case where the noise of the electronic measuring system is higher than the sensor noise, the expression comparing the MTJ and SV SNR (table 4.1) is easy to analyze. Therefore, for a maximum SV bias voltage of 1 V and $V_{1/2} = 0.4$ V the MTJ sensitivity needs to be more than 5 times higher than the SV sensitivity in order to improve the SNR of a SV-based biochip. This is further depicted in Figure 4.46.

In conclusion, the improved MTJ sensitivity is the key argument for using MTJs in biochip applications. In fact, an increase of sensitivity to biological entities is expected when MTJs sensors are used in magnetoresistive biochip instead of the SVs. Furthermore, if the measuring system is used in the high frequency regime, the flexibility on the choice of the MTJ resistance is also an advantage for using the MTJ sensors. In the following section, a comparison between MTJs and SVs in a biochip is presented.

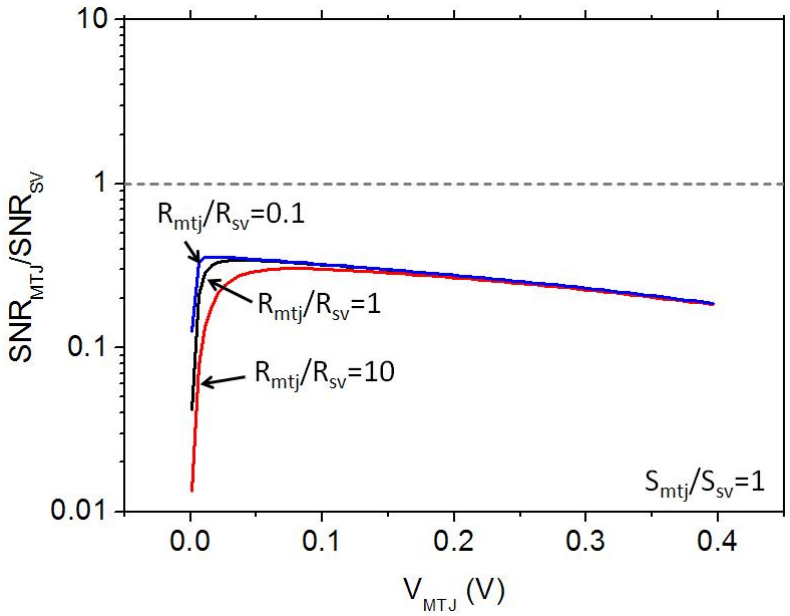

Figure 4.44: SNR_{MTJ}/SNR_{SV} in function of MTJ bias voltage assuming $\frac{S_{MTJ}}{S_{SV}} = 1$ and high frequencies. MTJ resistances of $0.1 \times R_{SV}$, $1 \times R_{SV}$ and $10 \times R_{SV}$ were used.

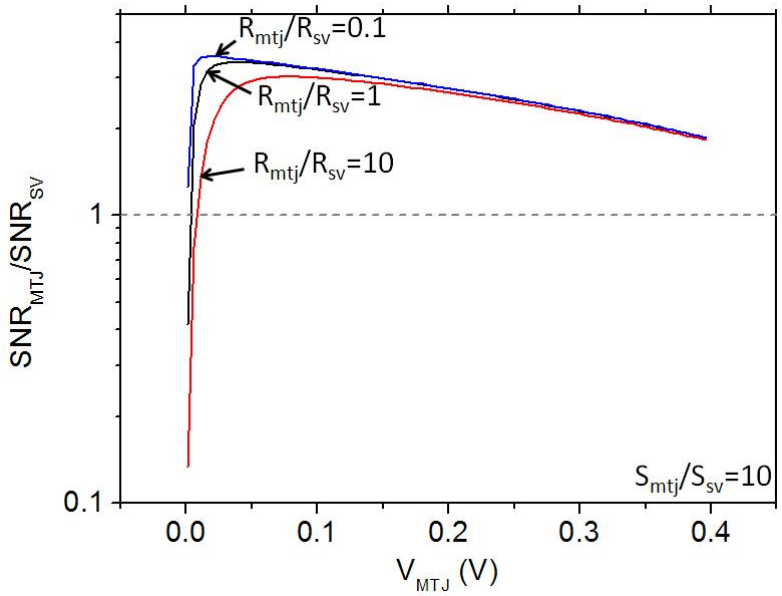

Figure 4.45: SNR_{MTJ}/SNR_{SV} in function of MTJ bias voltage assuming $\frac{S_{MTJ}}{S_{SV}} = 10$ and high frequencies. MTJ resistances of $0.1 \times R_{SV}$, $1 \times R_{SV}$ and $10 \times R_{SV}$ were used.

4.4.2 Comparison of biochips using MTJ and SV sensors.

In this section, an analysis of the signal-to-noise ratio of a MTJ sensor and a SV sensor was made using an integrated electronic platform for the measurements (section 2.2.4). The noise of the platform was compared to the noise of the sensors (MTJ or SV). Finally, magnetic particles

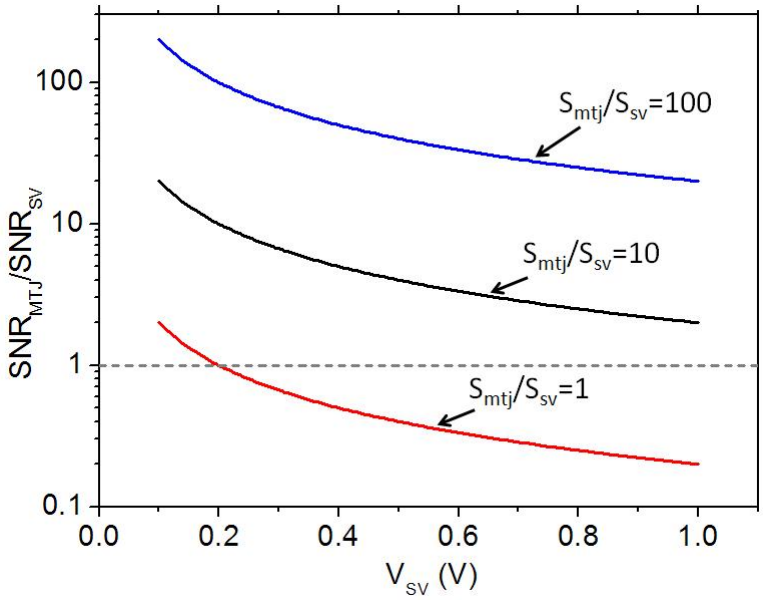

Figure 4.46: SNR_{MTJ}/SNR_{SV} in function of SV bias voltage assuming that the noise of the electronic measuring system is dominant. MTJ sensitivities of $1 \times S_{SV}$, $10 \times S_{SV}$ and $100 \times S_{SV}$ were used.

detection was performed.

The MTJ sensors were deposited onto Corning Glass 7059 substrates with the following structure: Ta 30 Å / Ru 150 Å / $Mn_{76}Ir_{24}$ 150 Å / $Co_{56}Fe_44$ 40 Å /Ru 8 Å / $(Co_{70}Fe_{30})_{80}B_{20}$ 50 Å / Al 6 Å (+oxidation)/ $(Co_{70}Fe_{30})_{80}B_{20}$ 50 Å / Ru 100 Å / Ta 30 Å. The layers were ion beam deposited in a Nordiko 3000 system and passivated with a 150 Å thick $Ti_{10}W_{90}(N)$ antireflective coating. The easy axis of the magnetic layers was defined during deposition by a 40 Oe magnetic field. The oxidation of the barrier was made by remote Ar/O_2 plasma during 15 seconds. The junction areas were defined by ion milling to have a sensor area of 2×15 μm^2 and were laterally isolated by a 500 Å thick Al_2O_3 layer. The top contact of the MTJ was defined by lift-off of a $AlSi_1Cu_{0.5}$ 2000 Å / $Ti_{10}W_{90}(N)$ 150 Å layer deposited in a Nordiko 7000 system. In order to prevent corrosion, an Al_2O_3 2000 Å / SiO_2 1000 Å stack was deposited by rf sputtering. Finally, the sample was annealed in vacuum at 280°C under a 1 Tesla magnetic field parallel to the MTJ pinned layer magnetization direction to improve the exchange bias. The MTJ sensors were part of a biochip containing U-shaped current lines for target arraying over the immobilized biological probes [10].

A second biochip with U-shaped SV sensors and U-shaped current lines, was deposited in a Nordiko 3000 system onto a Si/ Al_2O_3 500 Å substrate with the following structure: Ta 20 Å /$Ni_{80}Fe_20$ 30 Å / $Co_{81}Fe_{19}$ 25 Å / Cu 26 Å / $Co_{81}Fe_{19}$ 25 Å / $Mn_{76}Ir_{24}$ 60 Å / Ta 30Å / $Ti_{10}W_{90}(N)$ 150 Å . After the definition of a sensor area of 2.5×80 μm^2 by ion milling, contact leads of $AlSi_1Cu_{0.5}$ 3000 Å / $Ti_{10}W_{90}(N)$ 150 Å were deposited by sputtering and defined by lift-off. Finally, similarly to the MTJ, a passivation layer composed by Al_2O_3 1000 Å / SiO_2 2000 Å was deposited over the whole chip.

In the noise spectrum measurements, the MTJ and SV noise was amplified by a low-noise Stanford Research System (SRS) SIM910 amplifier and then measured using a real-time spectrum analyzer (Tektronix RSA3308A) with 2 Hz bandwidth in the DC to 1 kHz frequency range.

Magnetic labels with 130 nm diameter (Nanomag -D, Micromod, Germany) and a magnetic moment of $\sim 2.0 \times 10^{-14}$ emu for a 15 Oe magnetizing field were used in the particle detection experiments. From a stock solution with $\sim 3 \times 10^{12}$ particles/ml, four dilutions were made (1:10, 1:100, 1:1000, 1:10000). For particle detection a volume of 10 μL of each dilution was dispensed over the chip and an in-plane transverse magnetic field (25 Oe dc + 15 Oe rms at a frequency of 375 Hz) was applied on the sensors (MTJ or SV).

Figure 4.47 shows the transfer curve of the MTJ and SV sensors. The MTJ and the SV were characterized, respectively, by a magnetoresistance of 43 % and 6 %, a resistance (in the parallel state) of 319 Ω and 858 Ω, and a sensitivity of 0.23 %/Oe and 0.08 %/Oe.

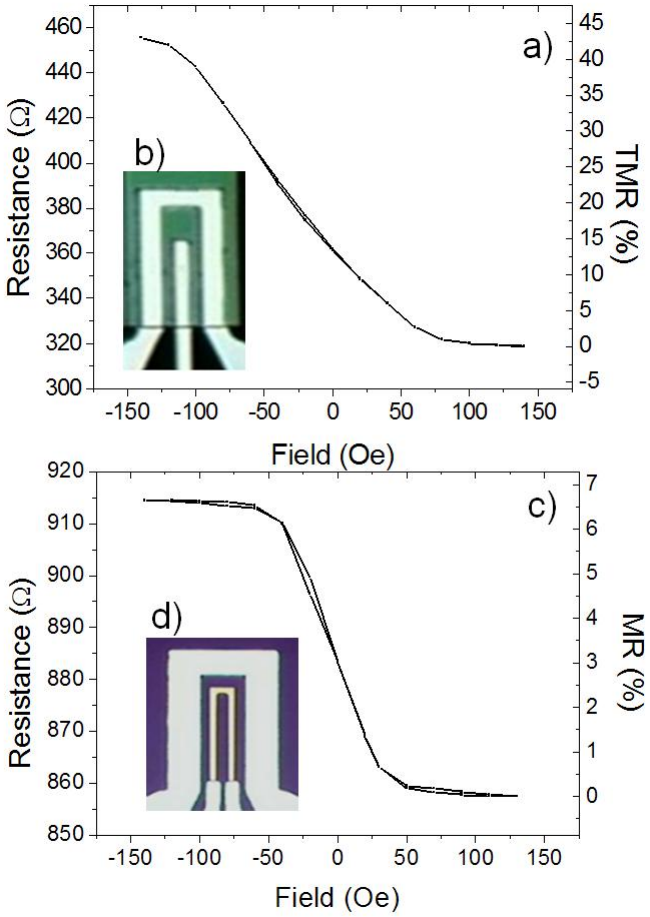

Figure 4.47: Transfer curve of a) a magnetic tunnel junction and c) a u-shaped spin valve. b) MTJ and d) SV chip layout which includes a u-shaped current line for particle focusing [99].

The signal-to-noise ratio (SNR) measurements shown in figure 2 were performed applying a bias current from 100 μA to 982 μA on each magnetic sensor (MTJ or SV). Both devices were

also excited with an AC in-plane magnetic field of 2.4 Oe rms (375 Hz) and the output voltage signal was amplified and converted to a digital representation. Finally, the signal was digitally filtered using a narrow pass-band filter with a bandwidth of 0.25 Hz. The noise (dominated by the electronic platform) and signal levels were averaged for a 10 minutes acquisition window.

From the results shown in figure 4.48, the MTJ has a SNR $\sim$ 1.5 times higher than the SV. This is the same value expected due to the MTJ higher field sensitivity. However, as the magnetoresistance of the MTJ decreases with an increase of the applied current, its SNR reaches a maximum value. In our case this maximum value is obtained for a current of 900 μA. For the SV sensor, the SNR increases continuously with the applied current and its limitation for biochip applications is related with heat generation in the SV due to Joule effect, and electrical failure through the fluid (breakdown occurs for bias voltages of 1 V). For the studied SV, a maximum current of 1 mA was chosen.

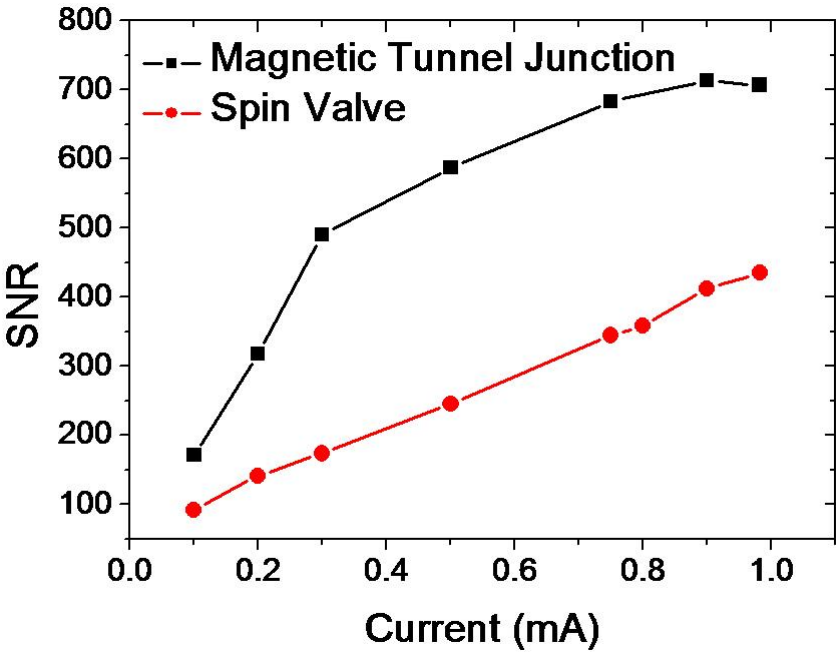

Figure 4.48: MTJ and SV signal to noise ratio in function of the applied current measured with the platform.

Figure 4.49 shows the noise contribution of each magnetic sensor and of the electronic measurement platform. At the typical platform operational frequency (375 Hz), the $1/f$ noise is the dominant noise for both sensors. Upon fitting the noise data of both sensors, the Hooge constants measured in the linear range are γ 1 and $\alpha_H = 6.03 \times 10^{-10}$ μm^2 for the SV and the MTJ sensors, respectively. An estimation of the MTJ noise for a bias current of 900 μA was made using the MTJ Hooge's constant [45]. As observed, at the used frequency (375 Hz) the platform introduces a higher noise than the sensors. In this scenario, for the same bias current the SV would have a noise two times lower than the MTJ. Nevertheless, the MTJ has three times more sensitivity than the SV meaning that in terms of SNR the MTJ would still be a

better solution if similar detection conditions are used (same external field, same sensor-particle distance).

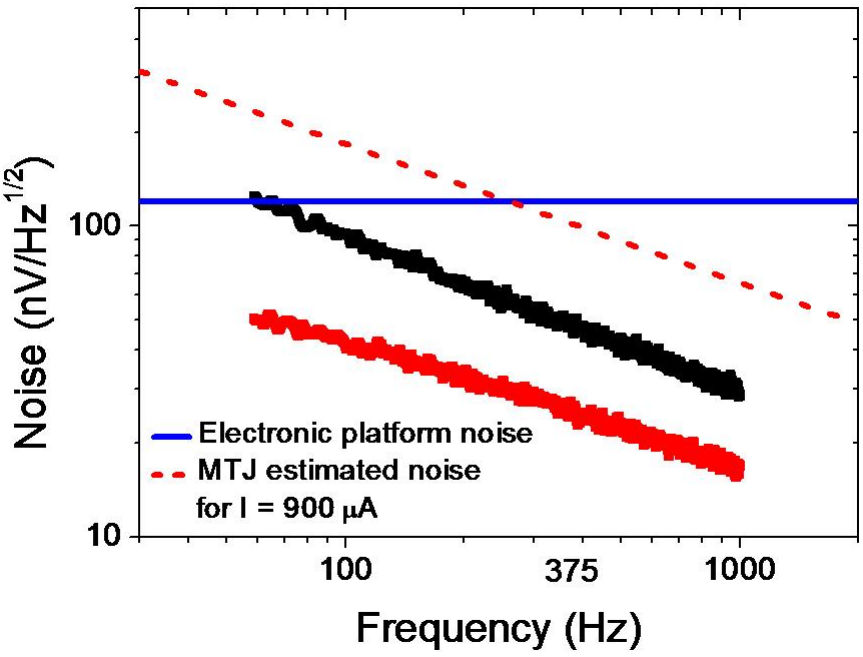

Figure 4.49: Noise of a MTJ (current bias of 200 μA), of a SV(current bias of 1 mA), of the electronic platform and an estimation of the MTJ noise for a 900 μA current bias.

For particle detection measurements, the platform was configured to deliver a bias current of 200 μA for the MTJ sensor and 1 mA for the SV sensor. The generated AC and DC magnetic fields were 15 Oe rms and 25 Oe respectively. The resulting signal was again amplified and converted to a digital representation allowing the usage of a digital narrow pass-band filter with a bandwidth of 0.25 Hz. After waiting 20 minutes for the particles to settle down on the chip surface, the signal (which attained saturation) was acquired and averaged during 10 minutes. The difference between this signal and the background signal normalized to the dc voltage was plotted on figure 4.50. The signal was normalized to the sensor dc voltage allowing the comparison between MTJ and the SV signals as shown on figure 4.50, the SV detection limit corresponds to a dilution of 1:10000 (3×10^8 particles/ml) while, for the MTJ, this detection limit was a dilution of 1:100 (3×10^{10} particles/ml). This is due to the fact that a lower current bias was used to make the measurements with the MTJ. If this current bias is increased to 900 μA (maximum SNR), a corresponding increase of the signal obtained by the presence of magnetic particles is expected.

From these experiments, SV based sensors show, for the same particle dilution, a higher signal than the MTJs. However, knowing that MTJ has a higher sensitivity, a higher signal should be expected. This discrepancy arises in part from the extra spacing between magnetic labels and the active free layers in MTJs when compared with SVs. In MTJ based biosensors the distance between the particles and the sensing layer (d =200 nm (Al) + 200 nm (Al_2O_3) +

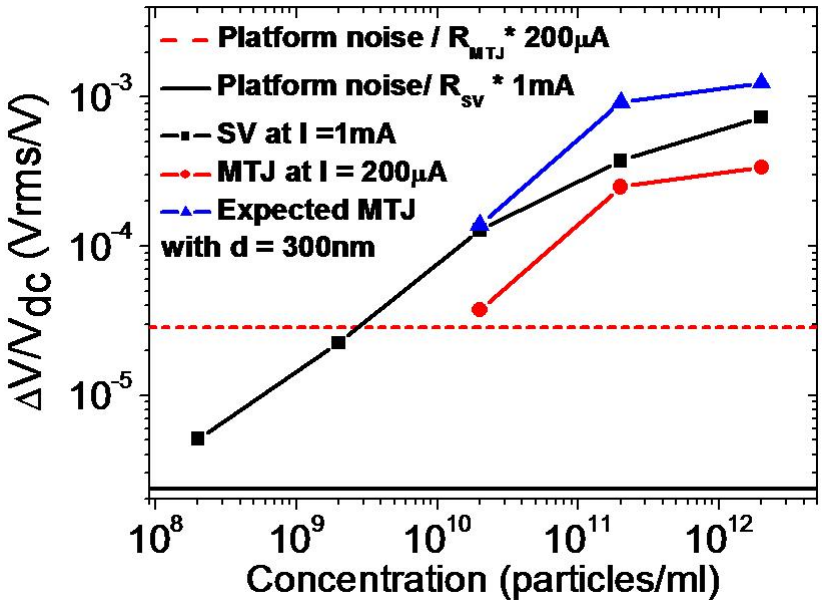

Figure 4.50: Detection of 130 nm particles (1:1, 1:10, 1:100, 1:1000, 1:10000 dilutions) by a MTJ (circles) and SV (squares) using the electronic platform. In order to be comparable, the signals were normalized to the dc voltage of the sensor. The noise was also normalized and indicates the limits of the detection system.

100 nm (SiO_2)) is higher than in the SV based biochip (d =100 nm (Al_2O_3) + 200 nm (SiO_2)). A possible solution for this extra spacing onto MTJ sensors was pointed out in [95] where the Al contact covered by a passivation layer was replaced by gold electrodes. Using the proper chemistry, biomolecules can be directly immobilized over the Au elements. Tests showed that the sensor does not get corroded with this geometry.

On another hand, the fact that the MTJ has a SAF structure the magnetic particles remained on the edges of the sensor. Therefore, besides a signal inversion the overall signal variation is also attenuated as observed in section 4.2.5.

4.5 Conclusions

In conclusion, the requirements for the design of magnetoresistive biochips were first precisely described. The importance of the thin film structure of magnetoresistive sensors was then found and tested for both sensitivity and particles positioning optimization. Detection of 250 nm and 130 nm was successfully performed and understood using both SV and MTJ sensors. Although theoretically developing a higher signal to noise ration, the MTJ showed lower particle sensitivity than the SV due to the spacing between the magnetic labels and the active free layer. The MTJ structure played also an important role in lowering the signal variation due to the magnetic particles presence. As showed in this chapter, those limitations were addressed and MTJ can therefore be used in biochips for higher particle sensitivity.

Chapter 5

Integration

In this chapter, the integration of magnetoresistive biochip with other technologies is discussed. Initially, the integration of a magnetoresistive sensor with a thin film diode in order to obtain a fully scalable matrix-based biochip is accomplished. The noise of this device is further studied. Then, magnetoresistive biochips were further integrated with a portable electronic platform and a microfluidic system. Finally, integrations accomplished on the frame of an european project (Snip2Chip) including integration with a EWOD-based PCR system and standard fluidic connections to a on-chip PCR system are depicted.

5.1 Matrix-based biochip

5.1.1 Overview

In the past twelve years, the technology of magnetoresistive biochips have been evolving in the way of increase the number of sensing sites in a chip. The first BARC chip proposed by Baselt [7] showed 8 sensing areas. Then, the number of sites were increased to 64 sensing areas for the same chip [8]. At the same time a group at Bielefeld university has developed a chip with 206 sensing sites [9]. In those chips GMR sensors were used. When INESC-MN started to work with spin-valve sensors a chip including 25 sensing areas was used for detection of Cystic Fabrosis disease [10].

In experiments for gene expression studies and diagnostics of disease the number of sensing sites available in these chips may be insufficient. However, increasing the number of sensors implies the increase of number of contact leads which may increase the complexity of the measuring electronics and the size of the chip. Therefore, to overcome this limitation in the scalability of biochips, in this work a matrix based biochip with 256 sensing sites is presented as an alternative to the above biochips. This biochip has the advantage being fully-scalable without increasing the electronics complexity (only two 16-bit multiplexers are needed for addressing 256 sensors).

The common method used to make a fully-scalable matrix of magnetoresistive sensor is to use a semiconductor device in series with the sensor to provide the necessary selectivity of the sensing site. This technique is a standard technique used for memory applications [18] [57]. The semiconductors used in these devices can be either diode or transistors. Transistors are

preferred because in general they show higher currents densities. In this thesis however, a thin film amorphous Silicon diode (a-Si:H) has been chosen for these purpose because of the available expertise at INESC-MN. Furthermore, using a two terminal device as is a diode simplifies the chip architecture. Finally, using this device it is also possible to sense the local temperature. This can be used for controlling the temperature of the chip surface enabling the choice of the temperature for a specific biological assay.

In this thesis, the matrix element is defined as the series of one TFD and one MTJ. In a matrix configuration, the matrix elements are located at the interception between a column and a row contact lead. The desired matrix element is chosen by applying a current through the column and row contact to which it is connected (figure 5.15). The TFD is therefore forward biased and almost all the current will pass through the selected matrix element. There are also several alternative paths, which are reverse biasing another matrix element. The current passing through one of these path is the reverse bias current of the TFD. When dimensioning the matrix, it is important that the sum of the current passing through all these alternative path is much smaller than the current passing through the selected matrix element. Therefore, maximum number of matrix elements is limited by the ratio between the forward and reverse bias (ON/OFF ratio) of the TFD.

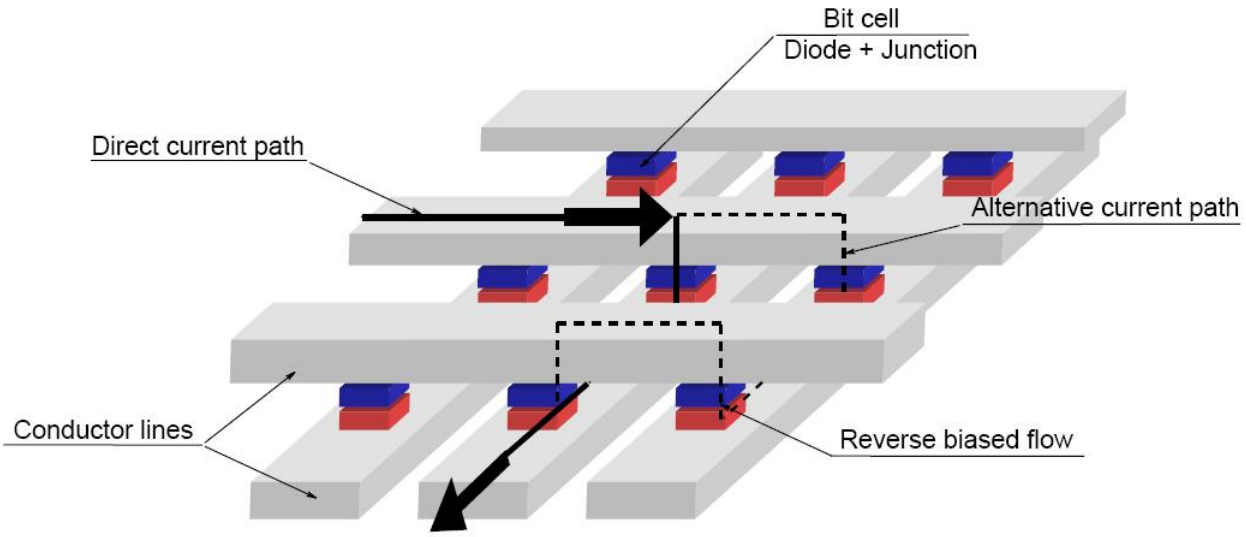

Figure 5.1: Schematic of the biochip matrix. The blue and the red elements correspond respectively to the diode and the MTJ sensor. The direct current path and one of the possible alternative current paths are also shown.

In all clean room processes there is yield associated to well functioning devices. Therefore, it may happen that one of the diodes of the matrix is damaged showing a high reverse bias current or a resistance-like behavior. In this case, a relatively high alternative current path passing through two forward biased diodes and the defective diode is possible (figure 5.2). It is then no longer possible to select only one matrix element since there is also a non-negligible

leak current passing through other elements.

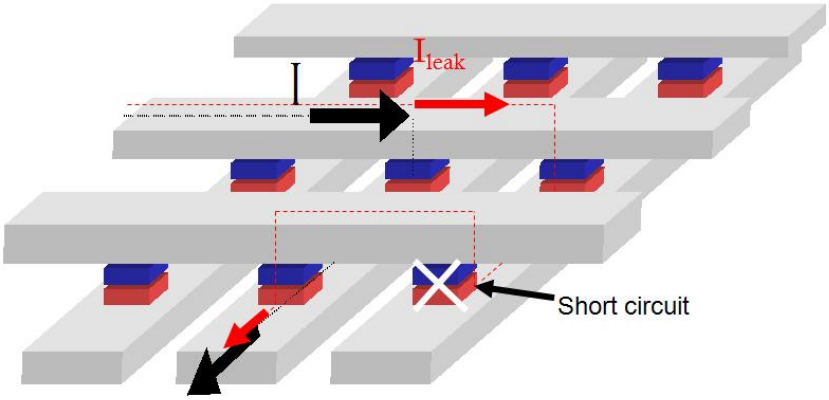

Figure 5.2: Schematic of the biochip matrix where a single diode is not working. In this case, the current is leaking through the damaged element.

As will be specified later in this section, the maximum current passing through a thin film diode (TFD) is limited to 1 mA. Therefore, the resistance of the sensor has to be carefully chosen in order to obtain a maximum signal-to-noise ratio (see chapter 4) at a current below this limit. Magnetic tunnel junction (MTJ) sensors have been chosen due to the easiness of controlling their resistance by increasing or decreasing the barrier thickness. Furthermore, as demonstrated in section 4.4 an increase in sensitivity is expected by using MTJ sensors.

In a matrix configuration system, the voltage drop over the matrix element is acquired. This voltage is given by:

$$V = V_d + V_{mtj} \tag{5.1}$$

where V_d is the voltage drop on the diode while V_{mtj} is the voltage drop on the MTJ.

Since the diode voltage is not dependent on the external magnetic field, the acquired voltage variation due to this field depends only on the MTJ voltage drop. Therefore, in an ac mode detection (section 4.1.4) where the magnetic moment of a particle is modulated by an external ac field, the acquired voltage will be the same as that observed in a stand alone MTJ. In contrast, in a dc mode detection (section 4.1.4), although the voltage variation due to the presence of a particle will only depend on V_{mtj}, the overall acquired voltage depends on V_d. The higher this voltage is the more difficult it will be to detect small voltage variations. This limitation may be overcome by using for example a Wheatstone bridge for canceling voltage drop on the diode. Those issues have to be taken into account when designing a matrix-based biochip.

5.1.2 Hydrogenated amorphous silicon (a-Si:H) diodes

Schottky barrier diode

Schottky barriers are formed when a metal is in contact with a semiconductor. These barriers have rectifying properties because an electrostatic potential barrier is formed at the interface of the semiconductor and the metal [58]. Therefore, the IV characteristic of a diode with a Schottky barrier is very similar to the IV characteristic of a P-N junction:

$$I = I_0 \left[\exp\left(\frac{qV}{nk_BT}\right) - 1 \right] \tag{5.2}$$

where n is the ideality factor (theoretically for Schottky barriers $n = 1$ and for P-N junction $n = 2$), k_B is the Boltzmann constant and T is the temperature. In the forward bias region where $qV \gg nk_BT$ this expression can be approximated by the exponential term so that:

$$I = I_0 \exp\left(\frac{qV}{nk_BT}\right) \tag{5.3}$$

In this work, the diode stack is: Al/TiW(N_2)/n+ a-Si:H/i a-Si:H/Al. The Schottky barrier of the fabricated diode is formed at the interface of an intrinsic a-Si:H layer and an Al layer. The n+ a-Si:H is an n-type doped layer, which is used to make an Ohmic contact with the bottom electrode metal. Without this layer, another Schottky barrier would be formed at the interface of the TiW(N_2) layer and the intrinsic a-Si:H layer and the device would not be a diode.

As observed in figure 5.3, the forward bias is not always exponential. In fact, the curve begins to saturate at 400-500 mV. This is due to the serial resistance that appears because of the semiconductor (a-Si:H) resistance. In semiconductors, above a certain voltage, a phenomenon called space-charge limited current (SCLC) is observed. This means that the current passing through the diode is proportional to V^2 instead of being proportional to V. So, for a device in SCLC regime, it can be written:

$$V = (R_d I)^\alpha \tag{5.4}$$

where α is a factor caused by the SCLC effect and should be equal to $\frac{1}{2}$. Taking equation 5.3 and assuming that the ideal diode has a serial resistance as is given by equation 5.4, the real diode can be modelled by:

$$V = c \ \ln\left(\frac{I}{I_0}\right) + (R_d I)^\alpha \tag{5.5}$$

with $c = \frac{nk_BT}{q}$.

Figure 5.4 shows the fitting to an experimental diode IV characteristic using the model described by equation 5.5. As it can be seen, the model fits quite well to the IV curve. The value of α and n are near the expected value.

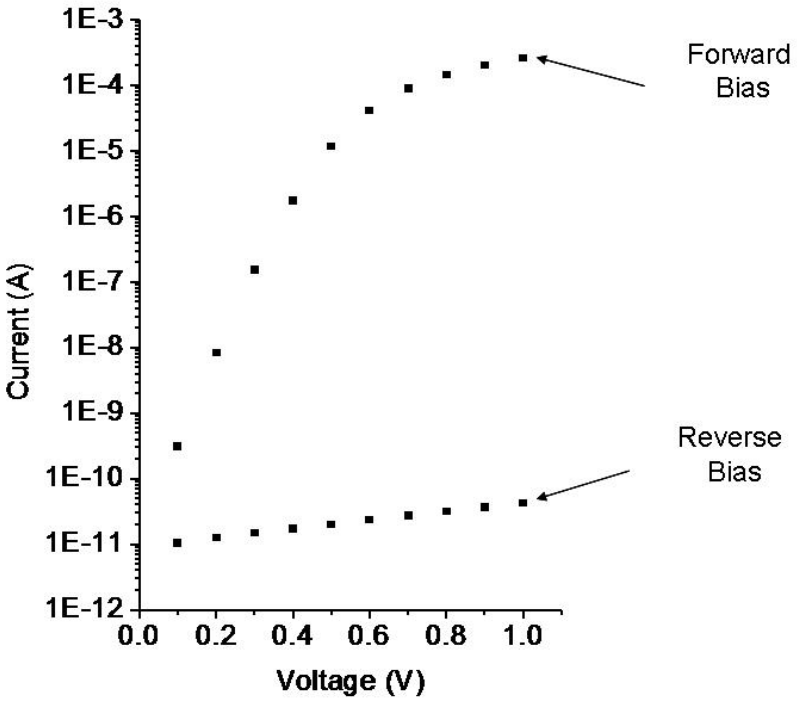

Figure 5.3: Experimental IV characteristic a-Si:H for a diode (with an area of $200\times200\mu m^2$). It was taken the absolute value of the values so that it is possible to see easily the ON-OFF ratio of this device (at 1V the ON-OFF ratio is 10^7).

p-i-n diode

Apart from Schottky barrier diode it is also possible to deposit a-Si:H p-i-n diodes. Contrary to the crystalline silicon, it is not possible to fabricate p-n junctions using a-Si:H technology. This is due to the fact that doped a-Si:H films show a high defect density shunting the p-n junction. Therefore, an intrinsic (not doped) a-Si:H layer is deposited in between the two n+ and p+ doped a-Si:H films [59].

The IV characteristic of p-i-n diodes is similar to the p-n junction for low bias voltage. Therefore, the same equations used for Schottky barriers apply to p-i-n diodes and the ideality factor in this case is ≈ 2 as in a p-n junction.

The p-i-n diodes used in this thesis were deposited with the following stack: 200 Å n+ a-Si:H/ 5000 Å intrinsic a-Si:H/ 200 Å p+ a-Si:H. As described in appendix E these films were deposited by RF plasma enhanced chemical vapor deposition [57].

A typical IV curve of a p-i-n diode is shown in figure 5.5. As deposited, these diodes showed an ON/OFF ratio 10^7. Since these diodes are integrated with a magnetoresistive sensor, after the microfabrication process an annealing step in needed to optimize the sensor characteristics. This annealing also showed benefits in the p-i-n diode characteristic. As observed in figure 5.5, the reverse bias current was reduced of one order of magnitude while the forward bias current was maintained. The ON/OFF ratio is therefore equal to 10^8. This can be explained by the

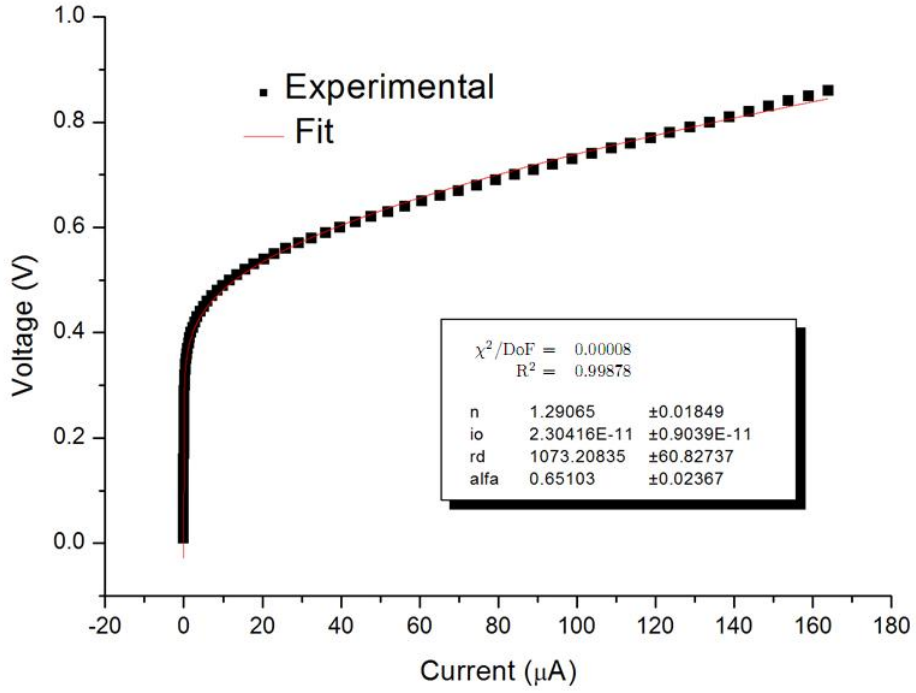

Figure 5.4: Fitting to an experimental diode IV characteristic using the model described by equation 5.5.

fact that the annealing reduces the number of defects in the intrinsic layer and therefore reduces the reverse bias current.

Schottky barrier vs p-i-n diodes

As already discussed previously, in order to be used in a matrix, diodes should have some specific characteristics. In this section the two types of diodes (Schottky and p-i-n diodes) are discussed above are compared.

In general, the diode IV characteristic depends on the area of the diode. In fact, the bigger the diode area is the higher the current passing through the diode is. Furthermore, the ON/OFF ratio remains constant for all areas. Therefore, in a first approach a large diode should be used in the integration on a matrix in order to be able to use smaller MTJ resistances (section 4.2.3). However, increasing the diode dimension would increase the overall size of the chip aswell. Thus, a compromise has to be made.

As shown in figure 5.6, 200×200 μm^2 Schottky and p-i-n diodes can deliver currents above 0.1 mA for voltages below 3 V. Therefore, a diode area of 200×200 μm^2 is a good compromise for the integration on a matrix since it deliver relatively high currents while the area it occupies is still acceptable.

When compared to the p-i-n diode, the Schottky diode has a lower ideality factor. Thus for the same current, the voltage drop is lower. As discussed above, depending on the measurement scheme chosen for the biological experiments, the voltage drop may be a limiting factor in the

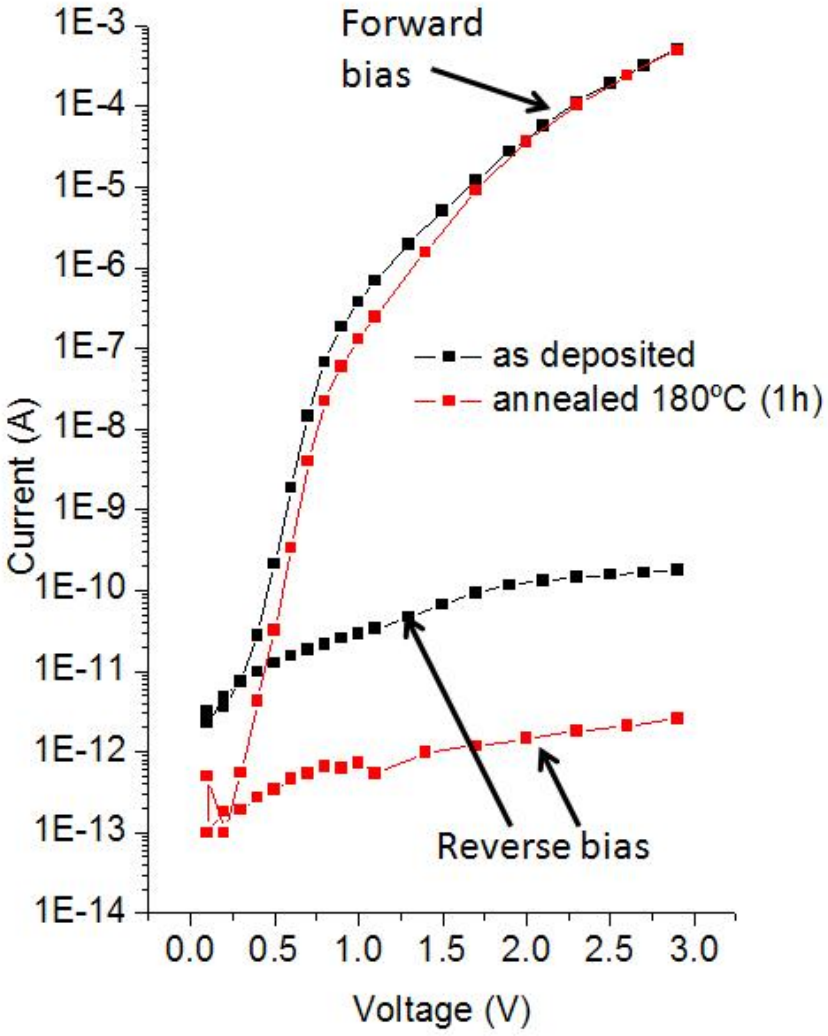

Figure 5.5: IV curve of a 200×200 μm^2 p-i-n diode as deposited and after annealing at 180ºC during 1h.

detection of low magnetic field. If that is the case, the Schottky diodes are the best choice.

However, high current densities passing through TFDs may irreversibly damage them. For 200×200 μm^2 diodes maximum currents of 0.2 mA and 1 mA can be handled by Schottky and p-i-n diodes, respectively (table 5.1). This fact shows that p-i-n diodes are more robust. Furthermore, the ON/OFF ratio of p-i-n diodes is two fold higher than the Schottky diode. As already discussed above, this is an important fact when a diode is used in matrix. In this case, a matrix made with p-i-n diodes would allow more matrix elements than a matrix made with Schottky diodes.

Finally, in matrix-based devices a very important issue is the processing yield of those diodes. The processing yield is defined by the percentage of correctly working diodes in a processed batch. Using the deposition systems available at INESC-MN and following the run sheet of appendix E both diodes types were microfabricated for yield tests. Each sample contained 60

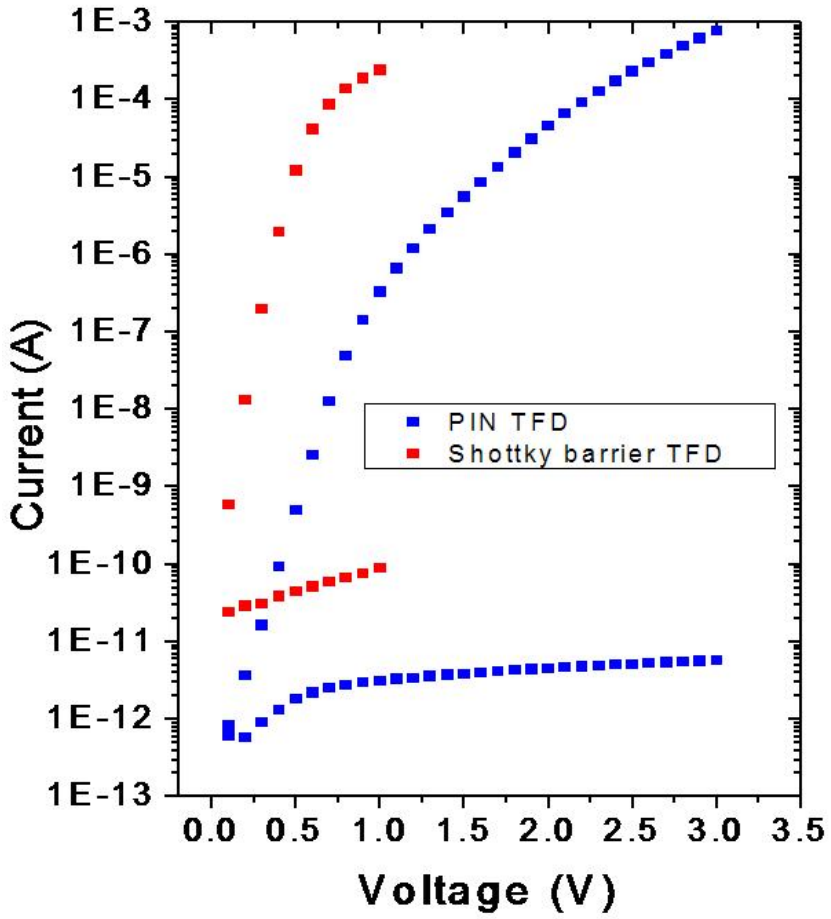

Figure 5.6: 200×200 μm^2 PIN and 200×200 μm^2 Schottky TFD IV curves.

diodes which I-V curves were measured. Diodes showing a high reverse bias current or resistor-like behavior counted as defective diodes. In this way, it was observed that Schottky diodes showed lower yield (68.8 %) than p-i-n diodes (98.4 %). As discussed before, diodes with 100 % yield should be used. The p-i-n diodes yield is close to that number but still there may be some damaged diodes in a matrix. A design to avoid having shorted matrix due to malfunctioning diodes is presented in section 5.1.3.

	Max. Current	ON/OFF ratio	Yield
Schottky	0.2 mA	10^6	68.8 %
PIN	1 mA	10^8	98.4 %

Table 5.1: Comparison table with the important characteristics of Schottky and p-i-n a-Si:H diodes.

In conclusion, for matrix-based devices p-i-n diodes are the best option since they were more robust, showed higher ON/OFF ratio and have a higher processing yield. The drawback is that their voltage drop is relatively high for a specific current and that may be a limiting factor when

a dc mode detection scheme is used.

5.1.3 Matrix design

In this thesis, a 16×16 elements matrix-based biochip was fabricated using the process depicted in section 2.1.4 and appendix D. The matrix is composed by 16 metallic rows and columns. A TFD in series with a MTJ is located in each intersection between the columns and the rows. As observed in figure 5.7, the row and the column leads connect respectively the diodes and the MTJ. A U-shaped current line surrounding each MTJ sensor was also incorporated. The superposition of a DC magnetic field created by the current lines with a low frequency, few Hz, in-plane transversal AC external field leads to attractive magnetic forces that concentrate magnetic labels in the inner region of the U-shaped line (sensing site). This in turn enables much faster (few min) biomolecular recognition processes, when compared with diffusion controlled processes [99].

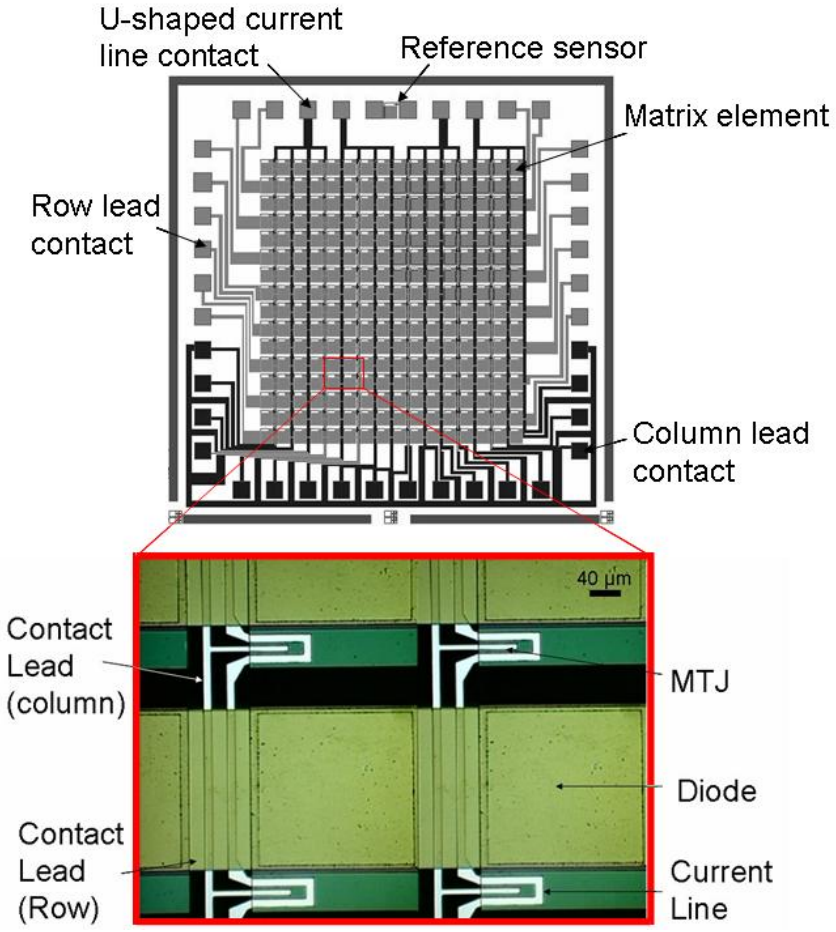

Figure 5.7: Biochip layout. Each matrix element is composed of an MTJ sensor (with an area of 10×2 μm^2) in series with a diode (with an area of 200×200 μm^2). A U-shaped line is incorporated for magnetic particle focusing.

As already noticed before, the yield of the p-i-n diodes used in this application is 98.4 %.

This means that in a 16×16 matrix ∼ 4-5 malfunctioning diodes may appear. Therefore, in each matrix element a fuse was incorporated so that a damaged element can be removed from the matrix (figure 5.8). This fuse is a narrowing (2 μm in width and 10 μm in length) of the 2000 Å aluminum contact lead which connects the column lead to one of the MTJ terminals. If a matrix element is damaged, a current higher to 60 mA is applied to it. As the fuse element is narrow, a high current density is passing through it causing the disruption of the line by electromigration. Therefore, an open circuit was created and the matrix element is no longer connected to the matrix. Although some sensors are removed, this method allows the well-functioning of a large matrix.

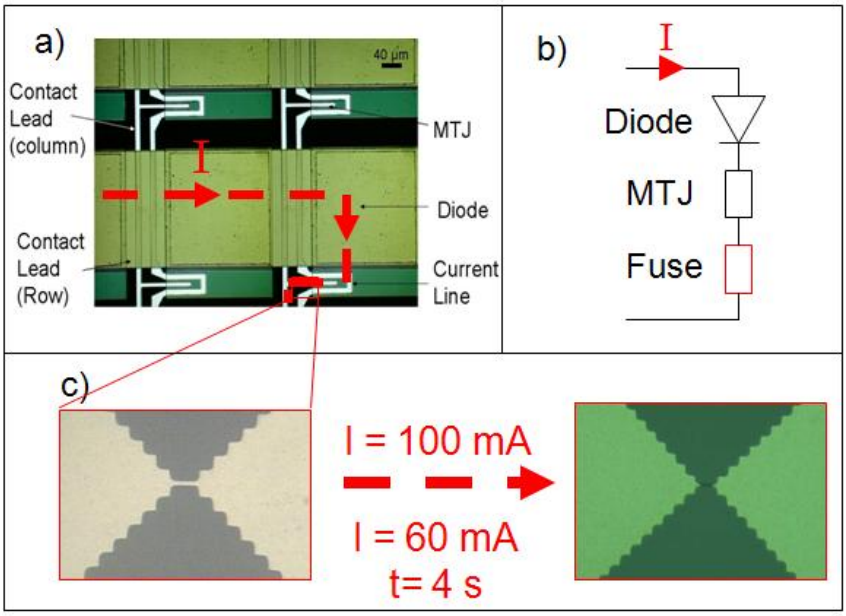

Figure 5.8: a) four matrix elements picture. A fuse is used to remove the element from the matrix if needed. b) Electrical scheme of each matrix elements. c) Aluminium fuse design. The fuse size is 2×10 μm^2 (2000 Å thick) and can be broken by 60 mA current applied during 4s or instantaneously by a 100 mA current.

In the same chip of the matrix, a reference matrix element was incorporated. This element will be under a silicon gel layer, which is cast by the chip to protect the wirebonded contacts from fluids (see section 2.1.4), such that the magnetic field created by the particles is not sensed. The reference element can be used for differential measurements using a Wheatstone bridge for example.

As discussed before this chip includes a diode with an area of 200×200 μm^2 allowing for the biasing of each matrix element with currents above 0.1 mA. The MTJ was dimensioned with an area of 2×10 μm^2 so that the chip can be used in disease diagnostics.

In the same sample used for the fabrication of this matrix, a test chip was also incorporated in order to monitor several aspects of the microfabrication proces. One of these tests is used to confirm if the oxides deposited in step 9 and step 20 (section 2.1.4) are good enough so that two metallic layer passing below and over it are not shorted. Stand alone MTJ and TFD are

also included to check their performance. Smaller matrix structures (3×3 matrix) are used as testing devices as well.

5.1.4 Magnetic particle detection with a diode+MTJ device

In this section, the fabrication and the working of a matrix element: diode in series with the MTJ, is explained. In addition, the detection of magnetic nanoparticles using this device is shown. Finally, the device response per particle was estimated based on the device and particle characteristics. The diode used in this proof-of-concept was a Schottky diode because this study was performed before the comparison between p-i-n and Schottky diodes already depicted earlier in this chapter. The whole microfabrication process and results were completely similar when Schottky diodes were replaced by p-i-n diodes.

Figure 5.9 shows a detailed cross section of the biochip at a sensing site. The process began by depositing the following MTJ structure on top of a glass substrate: Ta 90 Å / NiFe 50 Å / MnIr 250 Å / CoFeB 50 Å / Al 12 Å (+ oxidation)/ CoFeB 15 Å / NiFe 45 Å / Ta 30 Å / TiW(N) 150 Å . All the layers were deposited by ion beam in a Nordiko 3000 system. Here NiFe stands for $Ni_{80}Fe_{20}$, MnIr for $Mn_{74}Ir_{24}$, CoFeB for $(Co_{80}Fe_{20})_{90}B_{10}$ and TiW for $Ti_{10}W_{90}$, all in atomic %. The magnetic layers were deposited under a 40 Oe magnetic field to induce parallel easy axis in the pinned and free layers. The oxidation of the Al layer was done for 60 seconds. After junction definition (two ion milling steps), a 500 Å thick Al_2O_3 thick layer (ID1) was RF sputtered to laterally isolate the junction. A 2000 Å Al/ 150 Å TiW(N) (M1) thick layer was then deposited by magnetron sputtering in a Nordiko 7000 system, forming the diode bottom electrode, the column leads and the U-shaped magnetic field generating lines. M1 patterning was done by wet etching after removing the TiW(N) layer by ion milling. Diode fabrication proceeded, at 250 °C, with a RF Plasma Enhanced Chemical Vapor Deposition (PECVD) growth of 200 Å n+-a-Si:H (which forms an ohmic contact with the bottom electrode) and a 2000 Å intrinsic a-Si:H layer [57].

The diode was patterned by reactive ion etching. A second dielectric layer, 2500 Å of Al_2O_3 (ID2), was deposited by sputtering for the isolation of the column leads, and vias and contacts were opened by lift off. The final metallic layer, 3000 Å Al/ 150 Å TiW(N) (M2), was deposited to form the Schottky barrier and the row leads. Finally, the whole chip was passivated with a 1000 Å Al_2O_3/2000 Å SiO_2 (P) layer for protection against corrosion from fluids and to provide a suitable surface for bio-functionalization [10]. The MTJ and diode were patterned down to 2×10 μm^2 (MTJ) and 200×200 μm^2 (diode) dimensions. The chip was further annealed at 280 °C under a magnetic field of 0.3 T to create an exchange field in the MTJ pinned layer and to reduce diode defects.

For bio-detection applications, sensors should have a linear response to external fields. With this in mind, a sensor aspect ratio of 5:1 was chosen such that the shape anisotropy alone would be sufficient to rotate the free layer magnetization into the longer dimension, perpendicular to the pinned layer magnetization. The transfer curve for the MTJ shown in the inset of figure 5.10 still has a non-negligible coercivity (10 Oe) and is non-ideal. During experimentation

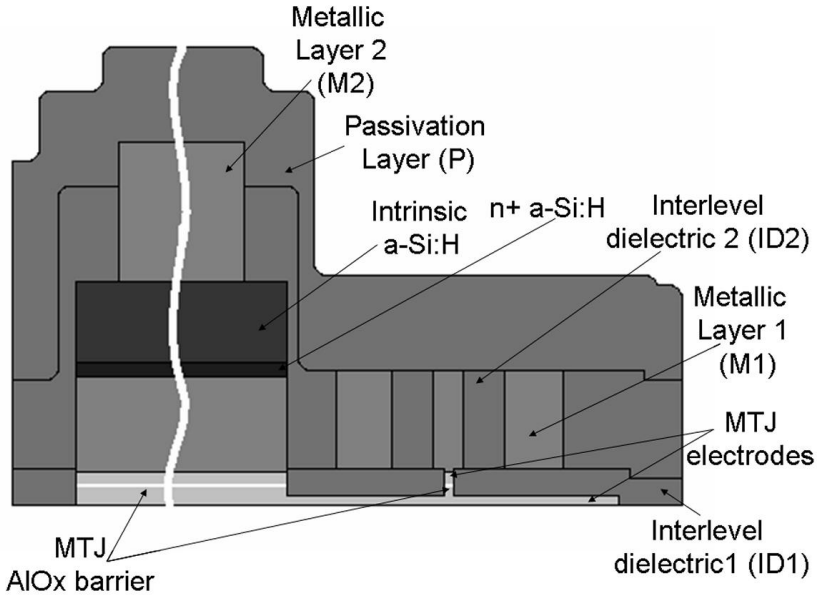

Figure 5.9: Cross sectional view of the biochip showing the MTJ sensor, diode, leads, u-shaped lines, interlevel dielectrics and passivation layers.

one of the branches of this transfer curve was used. The superparamagnetic particles used in the experiments were 250 nm diameter Nanomag -D, composed of iron oxide (magnetite) dispersed in a dextran matrix (Micromod, Germany). During magnetic nanoparticle detection experiments, a planar electromagnet was used to create an in-plane 15 Oe rms at 30 Hz + 6 Oe AC+DC bias field over the chip. The DC magnetic field is used to saturate the MTJ on the lower resistance state while the AC field is used to vary from that state into the linear part of one of the branches of the transfer curve and also to magnetize the beads. Direct connections were made to the device (MTJ + diode) and an external lockin amplifier was used to read out the data shown in this section. Small volumes (10 μL) of a magnetic nanoparticle solution (10^8 particles/μL), diluted in 1:10 and 1:100, were used. Before washing the chip with distilled water, the particles were left to settle onto the sensor surface for 10 minutes.

Individual characterization of the MTJ sensor showed a Tunneling Magnetoresistance Ratio (TMR) of 27 % and a resistance of 14.4 kΩ (figure 5.10). In addition, the diode showed an ON/OFF ratio of 10^5 at 1V, a reverse bias current density (J_0) of 5.35×10^{-7} A/cm^2 and a ideality factor n of 1.29. These values were taken after annealing the sample. Figure 5.10 shows the voltage change of the serial device discussed above, when the MTJ changed from the high resistance to the low resistance state. Device simulations for three different MTJ resistances (10, 14.4 and 20 kΩ) are also shown, and agree well with the experimental curve. The curves show a maximum signal ΔV of 50 mV for a drive current of 30 μA. The decrease of ΔV for higher biasing currents is caused by the TMR decrease at increasing bias voltage. For biochip applications, a maximum variation on the voltage is required. Increasing MTJ resistance decreases the current required to maximize signal output but at the expenses of increased sensor

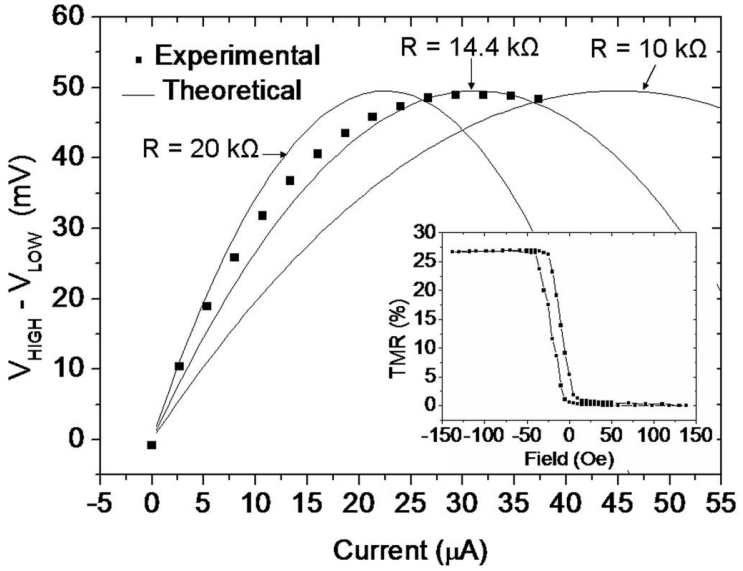

Figure 5.10: Experimental and simulated TFD-MTJ response curves vs drive current. Inset shows the transfer curve of a MTJ sensor

noise (mostly $1/f$ for low frequency applications), while lowering MTJ resistance (e. g. sensors with larger active area for similar R×A values or alternatively sensors with lower R×A for the same area) pushes the maximum signal peak to higher currents. For the used TFDs, currents in excess of few hundred μA will cause irreversible diode damage. So the MTJ area and R×A values must be optimized for maximum tolerable current through the diode. This means that more current can be applied to the device so that the MTJ resistance can be reduced by decreasing the R×A value or increasing the sensitive area. In the present demonstration, MTJ characteristics are defined by the diode.

The response of the device to 250 nm diameter magnetic nanoparticle solutions at two different dilutions is shown in figure 5.11. In this assay, the U-shaped lines were not used. Upon particle settling over the sensor, detection signals of 450 μVrms and 650 μVrms were obtained for 10 μL of 1:100 and 1:10 dilutions of a 250 nm particle solution, respectively. A device response of 14 μVrms/particle for a 15 Oe rms applied field was calculated based on model previously described in chapter 3. A magnetic moment of 1.6×10^{-13} emu/ particle was used and a magnetic dipole approximation was considered, with the dipole located at 1.125 μm above the MTJ free layer (distance between the centre of the particle and the free layer). Furthermore, in the calculations a MTJ sensor with a TMR of 27 %, a resistance of 14.4 kΩ and a sensitivity of 0.73 %/Oe was considered, and a drive current of 30 μA was used.

In conclusion, a device comprising MTJ in series with a TFD can be used for nanoparticle detection and, consequently, could be used for magnetic label based bioassays. This matrix element enables the fabrication of a fully scalable matrix based-biochip for 100s to 1000s biolog-

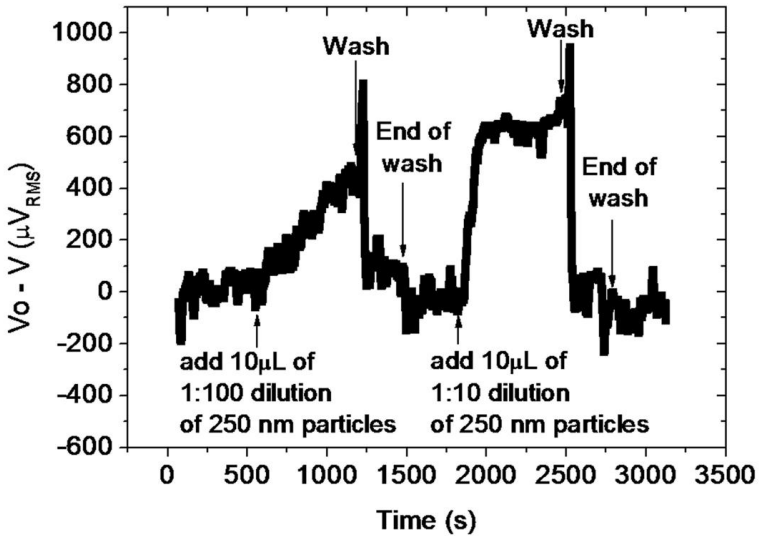

Figure 5.11: Device voltage variation to 250 nm nanoparticles at two different dilutions (1:100 and 1:10). Particles were left to settle onto the sensor surface for 10 minutes before washing the chip with distilled water.

ical probe sites. This device can be further improved, though. The sensitive area is still small (2×10 μm^2) when compared with conventional probe site areas (few hundred μm^2). Although, this limitation can be compensated by the use of U-shaped lines that concentrate particles at sensor sites [99], larger area sensors are being developed for increased biological dynamic range. In addition, in order to be able to carry high currents allowing to lower sensor resistances p-i-n diodes can be used. Furthermore, the TMR of the MTJ can be improved, up to 200 %, using MgO barriers instead of Al_2O_3 barriers. This will improve the sensitivity of the device to the magnetic markers.

5.1.5 Noise of a diode+MTJ device

In chapter 4, the noise and signal-to-noise ratio of magnetoresistive sensors were discussed. Nevertheless, when those sensors are integrated with other devices, the noise of the system may increase. Therefore, in the integration of MTJ with TFD it is important to understand which noise limits the detection. In this section, the noise of the TFD and the MTJ is measured. The reduction in the particle sensitivity is then extrapolated for different particles.

Diode noise equivalent circuits

An equivalent circuit of a diode which includes the noise sources is shown in figure 5.12. The differential resistance of the diode $R_D = \frac{nk_BT}{qI_D}$ has a shot+$1/f$ associated noise source (S_D). A shunting capacitor models the reverse bias current and the depletion zone formed in the diode

junction. Finally, a contact resistance R_c associated with a thermal noise source S_c is connected in series with the previous elements.

The experiments performed in biochip detection were achieved at frequencies below 1 KHz. In this regime, there is no current passing through the capacitor. Therefore, a simpler model of the diode associating an equivalent resistance $R_{eq} = R_c + R_D$ and an equivalent noise source, including thermal, shot and $1/f$ noise ($S_{eq} = S_c + S_D$), can be assumed (figure 5.13).

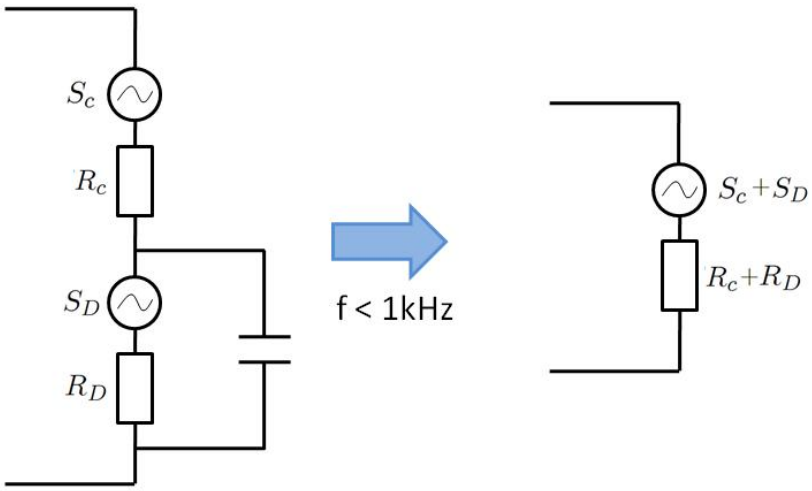

Figure 5.12: Diode equivalent circuit including the noise sources. For low frequencies (< 1 kHz) the circuit can be simplified

Since the device used in a matrix-based biochip is composed of a TFD in series with a MTJ, the equivalent circuit of this device is depicted in figure 5.13. When measuring the noise of the whole device, the TFD and MTJ noise sources are added. The equivalent differential resistance is given by the sum of the TFD and MTJ differential resistances.

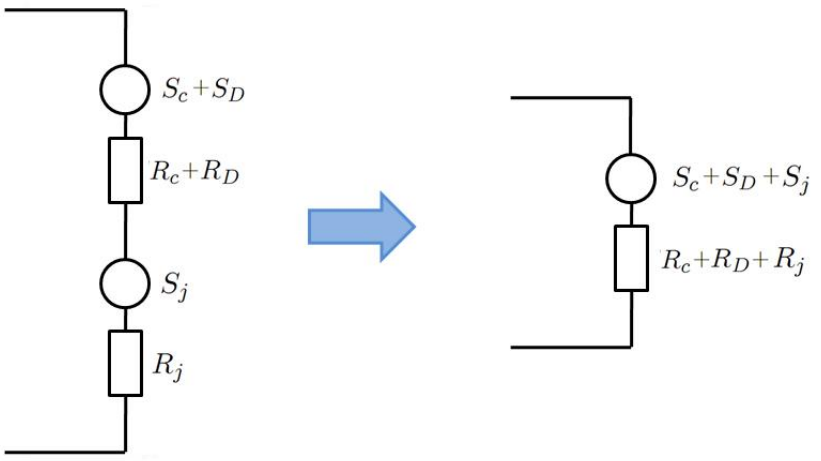

Figure 5.13: Equivalent circuit the MTJ in series with a diode including the noise sources.

TFD+MTJ magnetic particle sensitivity

In order to evaluate the sensitivity of the combined TFD+MTJ device for magnetic label detection, the noise level of the diode-MTJ series must be analyzed. In the typical MR biosensor assay, a low frequency bead magnetizing field is used (few Hz to few kHz).The excitation frequency should be chosen such as the $1/f$ noise contribution is strongly reduced (meaning working near the thermal background limit). The major goal of this work is to quantify the extra noise coming from the TFD at each matrix site (as compared to a MTJ sensor alone), and to determine the minimum number of particle markers that can be detected for a certain excitation frequency and sensor layout.

Figure 5.14 shows the schematic cross section of the fabricated TFD-MTJ matrix cell, where the diode (p-i-n or Schottky) is on the side of the MTJ. The MTJ was first deposited on top of a glass substrate using an ion beam Nordiko 3000 system with the following structure: Ta 90Å/$Ni_{80}Fe_{20}$ 70Å/$Mn_{76}Ir_{24}$ 250Å/ $(Co_{80}Fe_{20})_{90}B_{10}$ 50Å/Al 9Å(+ oxidation)/$(Co_{80}Fe_{20})_{90}B_{10}$ 50Å/ $Ni_{80}Fe_{20}$ 70Å/Ta 60Å/$Ti_{10}W_{90}$(N) 150Å(details on MTJ fabrication are given in [61]). A field of 40 Oe was used during the deposition of the magnetic layers (crossed anisotropies). The aluminum oxide tunneling barrier was obtained by remote plasma oxidation [61]. After patterning (ion milling) down to 2×10 μm^2 and isolating the MTJ electrodes with a RF sputtered 500 Å thick Al_2O_3 layer, a 2000 Å thick Al film ($AlSi_{1\%}Cu_{0.5\%}$) capped by a 150 Å thick $Ti_{10}W_{90}$(N) layer was deposited by magnetron sputtering. This layer was patterned by ion milling (to remove TiW layer) and Al wet etching forming the diode bottom contact, the matrix columns and the U-shaped particle focusing lines [99]. The hydrogenated amorphous silicon (a-Si:H) diode stacks, 200 Å n+-a-Si:H /2000 Å intrinsic a-Si:H (for Schottky diodes) or 200 Å n+-a-Si:H/5000 Å intrinsic a-Si:H/200 Å p+-a-Si:H (for p-i-n diodes) were then deposited by RF Plasma Enhanced Chemical Vapor Deposition [57]. After patterning the diodes down to 200×200 μm^2 (fig. 5.14a and 5.14b) using reactive ion etching and isolating the column lines with a 2500 Å thick layer of Al_2O_3, a 3000 Å Al/150 Å TiW(N) metallic layer deposited and patterned, forming the lines of the matrix. At last, a 1000 Å thick Al_2O_3 and a 2000 Å thick SiO_2 layer were deposited to provide a suitable surface for biomolecule immobilization and to protect the chip from corrosion during chemical and biological assays. Finally, a 280°C annealing under a 1 Tesla field in the MTJ pinned layer direction was done.

The noise of the TFD and the MTJ structures was measured using a low-noise amplifier SRS (Stanford Research System) SIM910 and a real-time spectrum analyzer with 2 Hz bandwidth in the DC to 1 kHz frequency range to respectively amplify and measure the noise spectrum [60].

The superparamagnetic particles used for device characterization are composed of magnetite (75% for Nanomag -D and 35% for Nanomag -D-spio) dispersed in a dextran matrix (Micromod, Germany) and have a diameter of 250 nm (Nanomag -D), 130 nm (Nanomag -D), 100 nm (Nanomag -D-spio) and 50 nm (Nanomag -D-spio) (see table 5.2 for the magnetic characteristics).

The I-V curves of the fabricated TFDs (Schottky and p-i-n) and the transfer curves of the

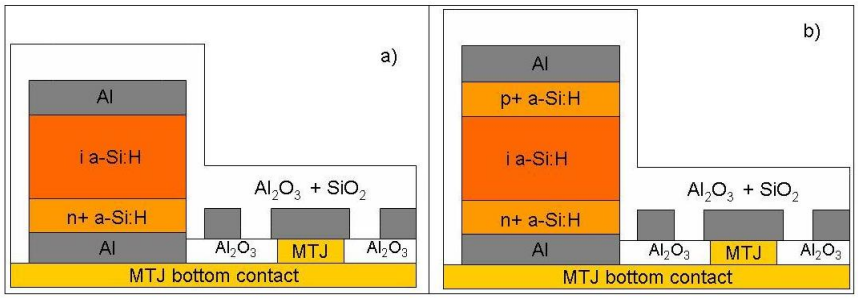

Figure 5.14: a) Film stack of a matrix element composed by a MTJ and as a-Si:H Schottky diode. b) Film stack of a matrix element composed by a MTJ and as a-Si:H p-i-n diode.

Diameter (nm)	Susceptibility (emu/Oe)	Moment under 15 Oe field (emu)	$< H_p >$ on a 2×10 μm^2 sensor area (Oe)
250	3.1×10^{-15}	1.6×10^{-13}	1.7×10^{-2}
130	4.1×10^{-16}	2.0×10^{-14}	2.7×10^{-3}
100	1.2×10^{-17}	1.8×10^{-16}	2.5×10^{-5}
50	3.7×10^{-18}	5.6×10^{-17}	7.8×10^{-6}

Table 5.2: Magnetic moment and a 15 Oe magnetic field, average susceptibility in the 0 to 40 Oe field range and average magnetic field ($< H_p >$) over the sensing area of one particle above the center of the sensor at a distance of 0.6 μm for different nano-sized superparamagnetic particles [22].

fabricated MTJs are shown in Figure 5.6 and Figure 5.15 (inset) respectively. The MTJs show a TMR of 40 % and a resistance of 30 kΩ.

A 3×3 cell matrix with p-i-n TFDs in series with MTJs as the basic cell element (Fig 5.15a) was measured. Figure 5.15 shows the voltage change (ΔV) obtained from the MTJ-TFD series, as the MTJ is switched from the parallel to antiparallel resistance states, as a function of the biasing current. Due to the TMR decrease upon bias voltage increase, a ΔV peak is observed at a certain biasing current as described in [97]. This peak depends on the MTJ resistance and TMR [97]. In the presented 3×3 matrix (fig 5.15), 7 MTJ's show this peak at the 10 μA (normally working MTJ) while two of them had a deficient MTJ showing lower TMR and higher resistance.

Figure 5.16 shows the measured noise spectrum of a 5.7 μA biased MTJ (at 0 Oe field), 4.4 μA biased 200×200 μm^2 p-i-n TFD, and a 5.3 μA biased 200×200 μm^2 Schottky TFD. In the DC to 1 kHz frequency range both devices (MTJ and TFD) are still in the $1/f$ dominated noise region. Both TFDs showed higher noise than the MTJ. The 200×200 μm^2 p-i-n diodes have a substantially higher noise level when compared with Schottky diodes despite being more suitable for matrix applications.

From the noise level measured in each device, one can now predict the minimum number of particles that the matrix cells can measure. The noise spectral density of the MTJ, MTJ+p-i-n diode and MTJ+Schottky diode was converted in voltage at each measurement frequency (1Hz

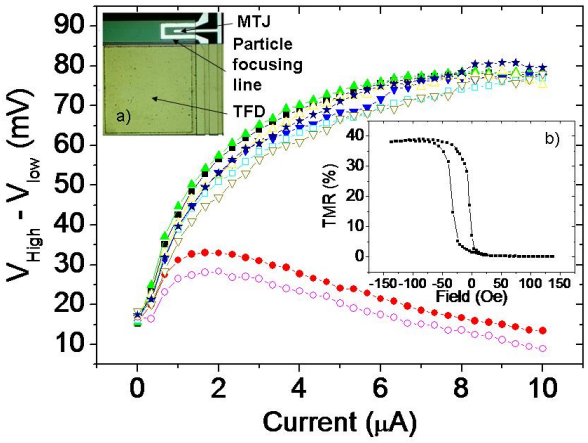

Figure 5.15: Maximum voltage change in the MTJ-Diode device (when the MTJ is switched from the parallel to antiparallel state) as a function of the applied current on each elements of a 3×3 matrix. Inset: a) Top view of a matrix element composed by a TFD and a MTJ. A U-shaped focusing line can be used to focus magnetic particles over the sensor [99]. b) Transfer curve of a MTJ with a resistance of 30 kΩ and an area of 2×10 μm^2.

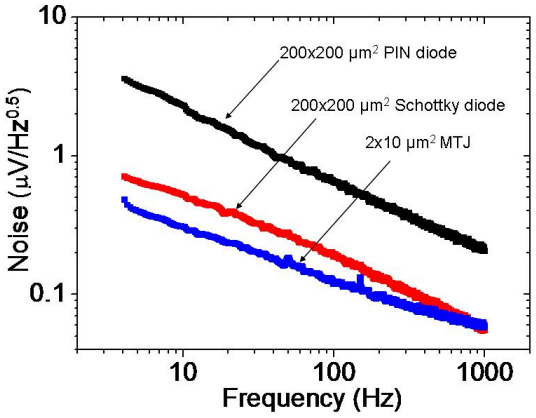

Figure 5.16: Noise spectra at a 15 Oe field of a 30 kΩ MTJ with a Hooge constant of 5×10^{-9} μm^2 and an area of 2×10 μm^2, and of a 200×200 μm^2 p-i-n and Schottky TFD.

bandwidth assumed) and then in equivalent magnetic field using the MTJ sensitivity of 0.6 mV/Oe. The number of particles required to generate the calculated field was obtained from the individual field of each particle. This field was averaged over the MTJ area (2×10 μm^2) and calculated assuming the particle placed at a distance of 0.6 μm (which corresponds to the thickness of the metallic top contact+passivation layer) above the center of the sensor with an in-plane 15 Oe (peak to peak) AC magnetizing field. It was assumed that there is no mutual interaction between beads since what is required is to determine if single particle detection is achievable Figure 5.17 shows the calculated number of particles that each device (stand alone MTJ, MTJ+p-i-n diode, or MTJ+Shottky diode) was able to detect. These calculations should be taken only for valid in the limit of small number of particles.

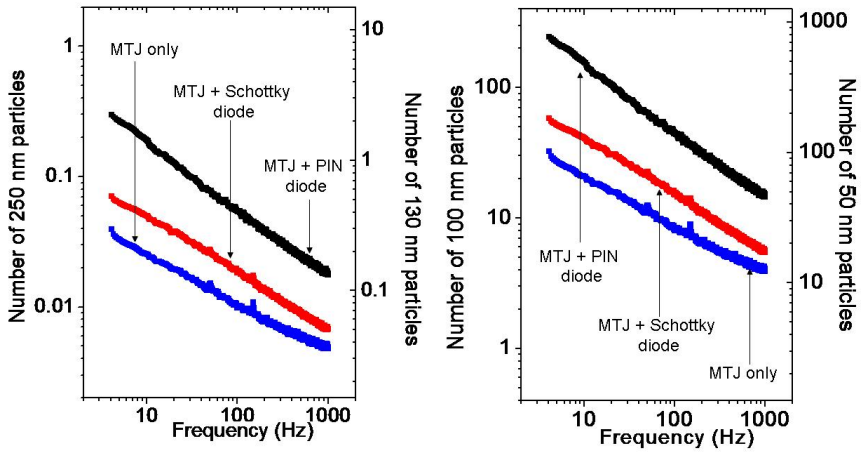

Figure 5.17: Simulated minimum number of 250 nm, 130 nm, 100nm and 50 nm particles that a MTJ, a MTJ + Schottky diode and a MTJ + p-i-n diode device allows to detect.

At 30 Hz both devices can measure a single 250 nm particle. For the 130 nm particles, only the MTJ+p-i-n diode device is not able to detect a single particle for frequencies below 30 Hz. The 100 nm and 50 nm particles have a lower magnetic moment than the previous ones and none of the devices can detect a single particle in the DC to 1 kHz range. The stand alone MTJ is the device that can detect the lower number of particles (more than ten 50 nm-sized particles and four 100 nm-sized particles) as expected from its lower noise level. The Schottky barrier TFD+MTJ configuration is the second more sensitive device, being able to detect more than seven 100 nm-sized particles and twenty 50 nm-sized particles (at 1 kHz), while at the same frequency the MTJ+p-i-n diode can only detect three times more 100 nm particles (five times with 50 nm). From the point of view of noise, the matrix-based biochips using a p-i-n diode as switching element show lower particle sensitivity than the ones using Schottky barrier TFDs. Nevertheless, if a proper detection frequency is used, at best less than one hundred of the smallest 50 nm particles can be detected by a matrix-based system.

In conclusion, a working 3×3 cell matrix was presented and the noise of the different devices (TFDs (p-i-n and Schottky) and MTJs) comprised in this matrix was studied. Simulations of the magnetic field created by superparamagnetic nanoparticles show the possibility of detecting single 250 nm and 130 nm particles, and about twenty 50 nm particles (at 1 kHz).

5.1.6 Conclusions

In conclusion, a device comprising a MTJ in series with a TFD was successfully designed, fabricated, optimized and used to detect magnetic nanoparticles. In theory, this device can further be used as a matrix element on a fully scalabe matrix-based biochip with a number of elements up to 1000. Each elements corresponds to a probe site. However, due to the process yield of the diodes (p-i-n and Schottky), only a completely 3x3 working matrix was

demonstrated. A system to remove damaged elements and allow a higher number of probe sites with these diodes was further designed and successfully tested. Finally, the noise introduced to the full device by the diodes was evaluated and compared to the expected signal needed to detect 250, 130, 100 and 50 nm particles. The possibility of detection of a single 250 and 130 nm particles as well as about twenty 50 nm particles at 1kHz was demonstrated.

5.2 Integration with a portable electronic platform

5.2.1 Overview

One of the main ideas of having a portable platform is to bring the biological analysis close to the place where it needs to be performed, independent of a laboratory or laboratory personnel. Therefore, sample handling must be simplified to a point where the user only needs to apply the sample and push a start button. To accomplish these specifications microfluidics systems are a crucial tool since they enable the development of smaller, faster, more cost-effective, and more powerful instruments and by being inherently small the size of the needed samples can be reduced from millilitres down to the range of micro- or pico-litres.

Furthermore, an autonomous portable electronic platform capable of driving and measuring the biochip is also needed. In order to fulfill these specifications, a battery powered and small size electronic system was designed, fabricated and tested. This work was performed in the scope of a national project in direct collaboration with Instituto Nacional de Engenharia de Sistemas e Computadores-Investigação e Desenvolvimento (INESC-ID) group and with Institute for Biotechnology and Bioengineering-Center for Biological and Chemical Engineering (IBB-CEBQ) group.

5.2.2 Fluidic integration in the platform

The platform discussed in this section is integrated with a microfluidic system fabricated with two different polymers: polydimethilsiloxane (PDMS) and PMMA. PDMS is one of the most widely used materials and it was chosen to replicate the channels since it uses cheap and fast casting techniques and it is biocompatible. The second polymer was used to fabricate the channel master and the holder that enables the fluidic inter-connects from the macro-world to the microfluidic device.

For the fabrication of the U-shaped channel three PMMA plates (2 mm thick) were micromachined using a CNC milling machine (TAIG Micro Mill from Super tech & Associates), one having the master of the channel (300 μm wide and 100 μm thick), the second one having the frame that defines the thickness (2mm) and the shape (5×5 mm^2) of the PDMS element and a third one with 0.8 mm holes that support metallic pins to cast the access to the channel (the inlet and the outlet). To replicate the microchannel 2 mL of PDMS (Sylgard 184–Dow Corning) is prepared by mixing the curing agent and base in a 1:10 mass ratio followed by 1 h degassing step. The mixture is finally injected in the reservoir that has access to the channel and is cured for 1 h at 60^{o}C . To seal the microchannels on the chip two different options are

available; irreversible chemical bonding between both surfaces or bonding by physical pressure. However, biochemically functionalized chips, which is the case, cannot be submitted to the chemical bonding process since an oxygen plasma activation of both surfaces (chip and PDMS) must be carried out in order to have an irreversible bonding. This plasma activation removes all the organic contaminants meaning that it would also remove the previously immobilized biomolecular probes over the sensors. On the other hand, if probe immobilization is performed after PDMS sealing, through the channels, the localized spotting of different probes over the sensors is not possible anymore. Therefore the sealing of the U-shaped channel to the chip is achieved by applying pressure over the PDMS. The pressure platform consists in two main parts: the PCB (where the biochip is electrically connected as depicted in 2.1.4) holder and the pressure element where the PDMS channel fits in (figure 5.18). The pressure is applied by two springs (placed along two screws) which are aligned with the holder in such a way that when the springs are extended the channels are sealed with a maximum error of 100 μm, meaning that the sensors are always inside the channel. By compressing the springs (pushing up the pressure element) the PCB can be replaced by a new one without needing a new channel or a new alignment step.

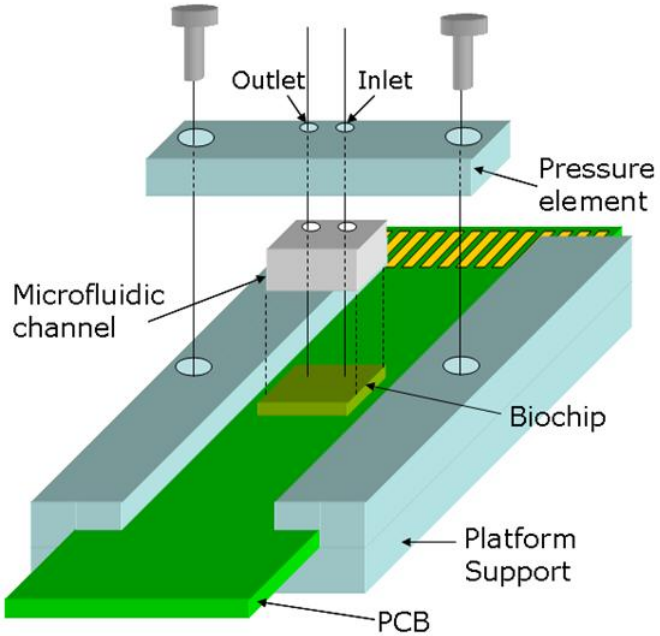

Figure 5.18: Schematic representation of the fluidic platform components showing how the alignment and sealing of the channel is achieved.

The width of the channels (300 μm) presented in figure 5.19 was chosen in agreement with the architecture and sensor's size to maximize the contact between the particles and the sensors. In order to have the particles closer to the sensors the channels height was designed to be less than 100 μm. This constriction increases the speed of the experiment when compared to thicker channels. However, from a practical point of view, smaller dimensions in a microfluidic system

are not necessarily advantageous, since the requirement for easier handling can impose some restrictions. Smaller channels are synonymous of high hydraulic resistances meaning that the pressure drop necessary to impose the flow increases with the decrease of the channel dimensions. A compromise between these two factors must be achieved, otherwise sealing and alignment problems may arise.

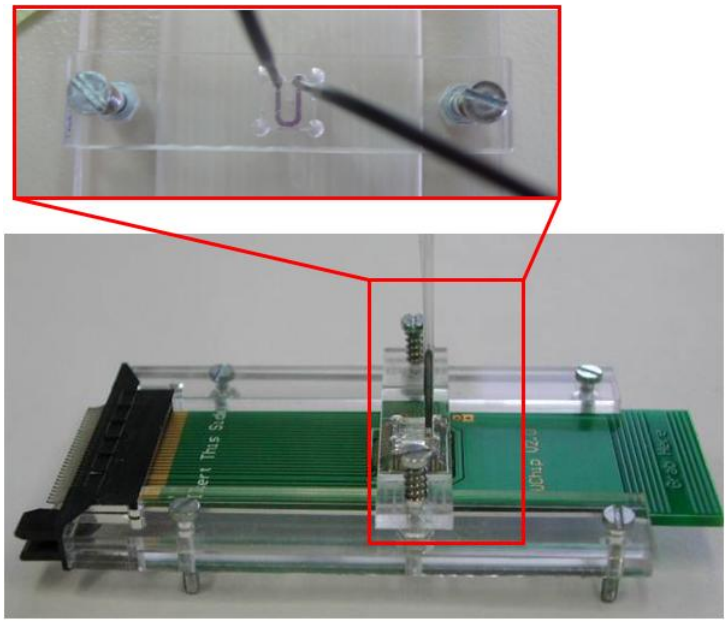

Figure 5.19: Pressure platform including the PCB aligned with the PMMA plates and with the PDMS channel. Top picture shows the PDMS element with the U-Shaped channel filled with colored fluid.

The main advantage of using a microfluidic platform is the expected reproducibility and controlled discrimination forces achieved with these systems when compared to manual processes. The cleaning protocol is crucial in order to have a clear distinction between non-specific binding and a complementary DNA binding. The biological reaction takes place in static flow but the washing step must be uniform and strong enough to wash out the particles adsorbed at the surface and the non-complementary DNA, otherwise false negatives or positives may mask the result. Having a controlled washing and sampling delivery protocol, instead of a manual one, the reproducibility among different sensors and different chips increases. The flow rates are being imposed by a syringe pump but in the future a micropump can be integrated in the fluidic system so that the portability of the system is not affected by that.

In order to test the developed microfluidic system, a test was made inserting 250 nm particles (Micromod, Germany) with a concentration of 5×10^7 particles/μL inside the channel. Once the channel was filled, the particles were let to settle down. As observed in figure 5.20 the saturation signal was attained in 15 minutes using the microfluidics system while 25 minutes was needed in an open chamber. This proves that as expected the magnetic particles settle faster in a microfluidic channel since they are closer to the chip surface. Besides the improvement in the

washing homogeneity already discussed, the use of a microfluidic channel will allow to perform faster biological assays.

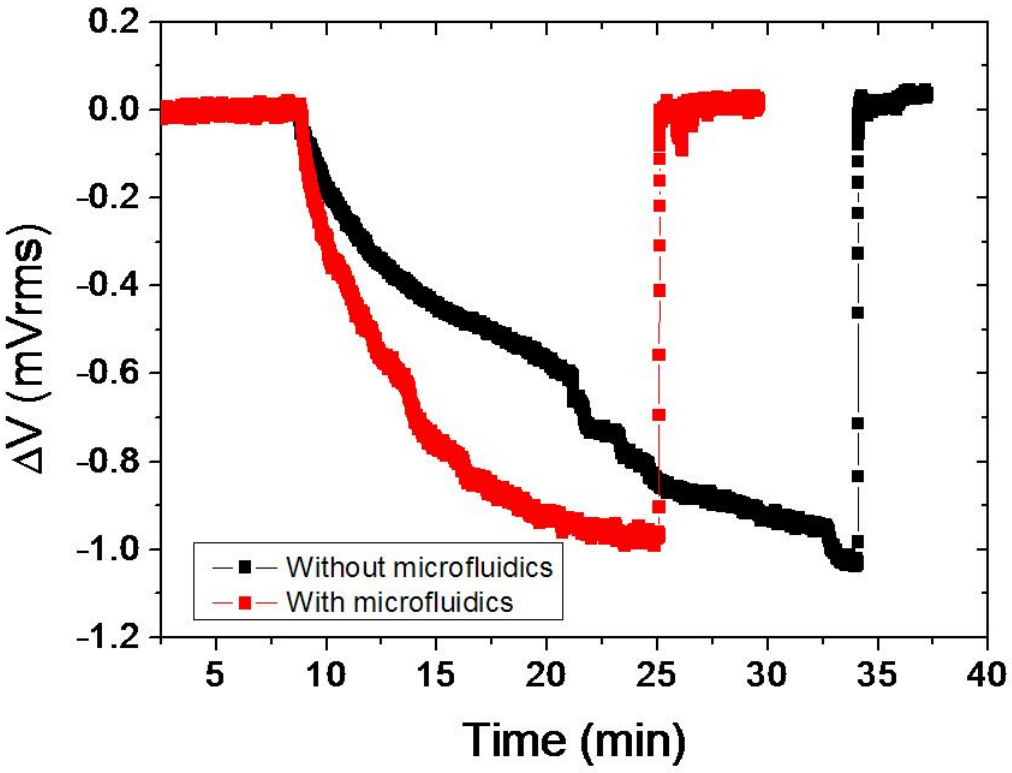

Figure 5.20: Comparison of detection of 250 nm particles (Micromod, Germany) on an open chamber and using the microfluidic system.

5.2.3 Electronic platform

An electronic platform was designed following the requirements: (i) performing real-time signal processing; (ii) the communication interfaces must use standard technologies to lower the development time and increase compatibility; (iii) the transmitted data must be encrypted; and (iv) implementing a graphical user interface (GUI), on a personal digital assistant (PDA) or a Laptop, that allows full control of the measurement procedure. The biochip is located in the sensing and processing module (SPM). The module provides the signals required to perform the magnetic and electric drive of the biochip sensors, controls the fluids, performs multiplexing of the sensor signals, and acquires the conditioned signal in order to perform digital signal processing in a DSP. The autonomous communication module (ACoM) is then responsible for encrypting the data collected at the SPM and for its transmission, to the device responsible for the user interface, using a standard communication interface (e.g. USB, Bluetooth, ZigBee). Detailed circuitry design can be found in [83]. Figure 5.21 shows a picture of the complete platform prototype.

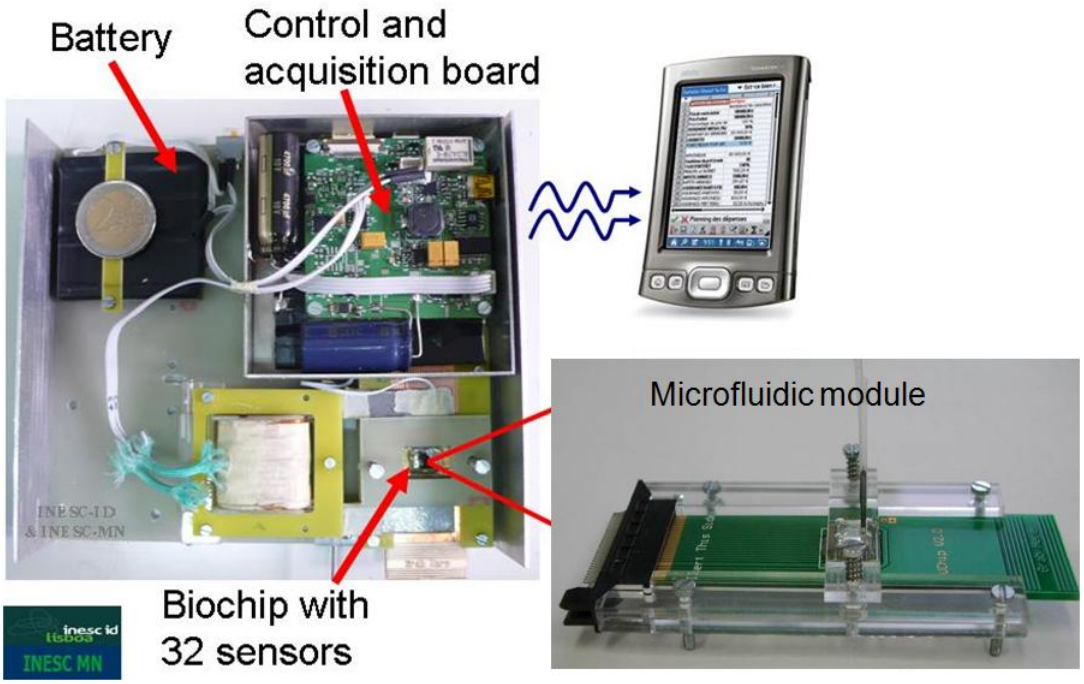

Figure 5.21: Portable platform developed for biological assays using a magnetoresistive biochip. This platform includes all the electronic circuitry needed to drive and acquire the signal from the sensors.

The bias current generators used to bias the sensors can deliver currents ranging from 144 mA to 1.16mA. The generated current is multiplexed into the biochip allowing the usage of only one current source for all the sensors. For biochips in matrix configuration up to 256 sensors can be addressed, while for linear arrays this value drops to 30. An important feature of the measurement system is the usage of a printed circuit board as chip carrier. Since the biochip is

wirebonded to a PCB that is inserted into an edge connector placed in the SPM main board, the biochip can be easily inserted from outside the noise shielding enclosure where the SPM is located. Another advantage is the possibility to perform signal routing in the chip carrier. This ensures compatibility with different biochips and allows the design to support both biochips with matrix type and linear array organization. Furthermore, since the size and shape of the PCB is fully customized, it can be adjusted to optimize the interface with a fluidic system and to ensure compatibility with conventional DNA spotters. Finally, a PCB chip carrier is less expensive than conventional one, which is an important aspect since the biochip is disposable.

The magnetic drive circuit is one the critical parts of the measurement system. To avoid low-frequency noise the measurement is performed in AC, requiring an AC magnetic field. Since the optimal DC bias field direction for a given type of sensor is unknown, the circuit must also be able to generate positive and negative DC fields. Furthermore, to achieve a portable system, power consumption, size and weight restrictions must be considered. At the frequency of 211Hz this circuit can generate a maximum AC of 15 Oe rms with a DC superimposed that can vary in the range from -40 to 40 Oe. Moreover, when the AC field is not required, it can generate a DC field from -200 to 200 Oe. The sensor signal is acquired using a single instrumentation amplifier and a high resolution analog to digital converter (ADC). The circuit must be capable of performing AC and DC measurements of different signals. The amplifier gain is digitally controlled, having a gain of 40 when in AC mode and of 1.2 when in DC mode. The sensor resistance is determined by computing the discrete Fourier transform (DFT) of the acquired signal, at the excitation frequency, in the DSP. Finally, using a USB interface, the measurement procedure is controlled and the processed sensor signals are transmitted to a laptop computer.

Using a graphical user interface (GUI), it is then possible to automatically aquire the transfer curves of all the biochip sensors and to perform a biological detection. The interface allows the user to select which sensors will be measured for the selected biochip type, and to set all the other measurement parameters. At the user interface the transmitted data is displayed in real time allowing for the observation of the measurement evolution.

5.2.4 DNA detection with the portable platform

To illustrate the measurement capabilities of the developed system, a biomolecular assay was performed using a DNA–DNA oligonucleotide hybridization model system. Two distinct single stranded DNA sequences of 20 and 25 mers were used as fully complementary and non-complementary thiolated biorecognition probes, respectively. The probes were immobilized separately at 1 mM concentration on each half of the chip. A biotinylated 20 mer target DNA strand was allowed to hybridize with both probe arrays at 1 mM DNA concentration in phosphate buffer 0.1 M, pH 7.4 and 0.2 % Tween20 surfactant (PB/Tween). The reaction occurred offline for 3 h at 42^{o}C. After hybridization the unbound target molecules were washed away by passing buffer solution in fluidic channel. A labeling solution of 130 nm magnetic particles modified with streptavidin (Nanomag-D, Micromod) was prepared diluting 2 mL of the stock suspension (2.9×10^9 particles/mL) in a 50 mL total volume of PB/Tween. Detection tests

were performed using 20 mL of this suspension dispensed on top of the sensing areas. The biochip used in these experiments was composed by 32 SV sensors with a minimum resistance of $1071 \pm 107\ \Omega$ and a magnetoresistive ratio of 6.2 ± 0.6 %. The sensors were biased with a 1 mA DC current, the magnetic drive was set to 35 Oe DC and 13.5 Oe rms AC at 211 Hz. During the assay, the sensors were sequentially addressed and the signal was measured using a gain of 40 and a sample rate of 844 samples/s. The acquired signal was then filtered with a 1 Hz bandwidth filter by using the algorithm described in [84]. Three steps are performed to analyze a solution: (1) acquire a 5 min baseline; (2) insert a 5 μL of streptavidin-coated magnetic labels suspension onto the sensors and wait 30 min for particles settle down and biotin–streptavidin biorecognition occur; and (3) wash the biochip at a 5 μL/s flow, while continuously measure the sensors signal. Figure 5.22a presents untreated sensor responses acquired sequentially from four different sensors at the same chip, two of them measuring the complementary binding signals (positive controls) and another two referring to non-complementary signals (negative controls). The sensing curves corresponding to non-complementary DNA probe sequences, as expected, returned approximately to the baseline level with an average signal for five sensor of 16 ± 5 mV, meaning that no molecular recognition occurred and the background signal from non-specific interactions is small. On the other hand, the sensing curves corresponding to complementary probes to the target molecule after two washing steps the binding signal remained about 169 ± 6 mV.

In figure 5.22b, the previous binding signals were normalized to its baseline signal, which is the out-put signal obtained from the sensor before addition of magnetic particles. The difference between a complementary and a non-complementary binding signal is higher than 90 % (figure 5.22).

5.2.5 Conclusion

In this collaboration between an applied physics group (INESC-MN), an electronic group (INESC-ID) and a biological group (BERG), some of the challenges faced during the development of a magnetoresistance-based integrated biochip device were addressed. Different areas of knowledge are involved in the development, optimization and integration of the different elements that compose the platform. Due to multidisciplinary nature of this device, some of the major challenges were found in the interfaces between the different modules.

One of the first challenge was the interface chip-electronics. Initially, the chip was mounted in a chip carrier like the one of figure 2.15 a). However, this approach is not very user-friendly and is not directly compatible with the majority of spotting systems. Therefore, a PCB chipcarrier as the one shown in figure 2.15 b) was designed with the dimensions of a glass slide (1×3 inch^2) to be compatible with spotting systems. It is also more user-friendly and much cheaper than the other approach.

The other challenge was to fabricate a support where the chip carrier can slide and enter exactly in the connector. The first prototype was made manually and there was the possibility of making bad contacts due to the big error of the system. A PCB support was therefore

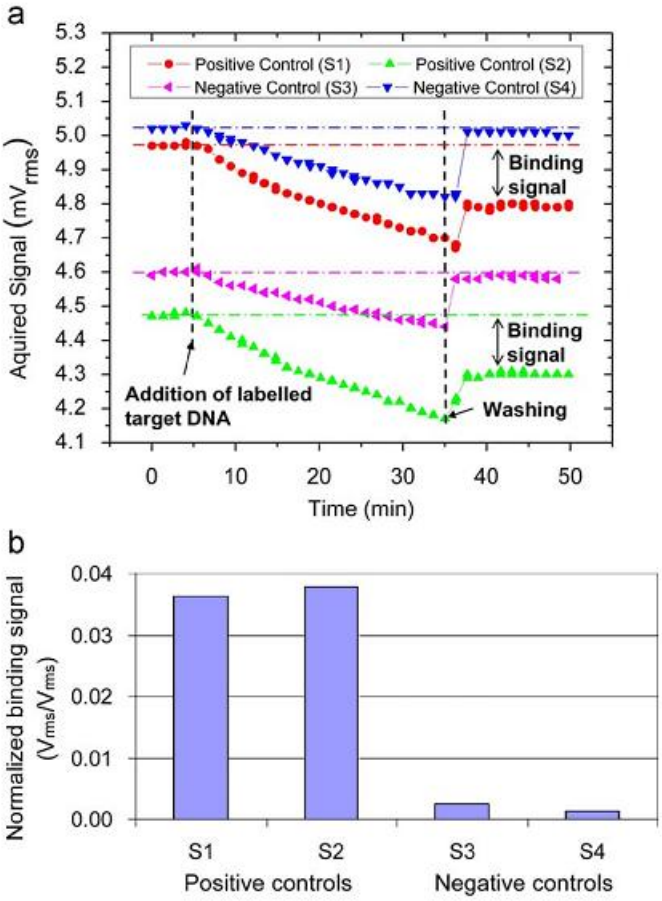

Figure 5.22: Magnetic detection of DNA-DNA biomolecular recognition using a portable platform. A concentration of 1 μM of target DNA was used in this experiment (a) Signals presented as acquired using the measurement platform. (b) Binding signal normalized to the sensor baseline signal for positiv and negative controls.

fabricated in a CNC milling machine enabling the casting of the PCB in the PCB support piece.

This PCB support piece had to be aligned with both the magnetic generator and the microfluidic system to have an auto-aligned system. The electromagnet and PCB support piece were therefore screwed to a support plate and a system to change the magnet position was made to be able to introduce the PCB.

Concerning the microfluidic system was incorporated in the PCB support system as was already depicted in this chapter. This microfluidic platform was designed and implemented to avoid the incidence of false negatives due to uncontrolled washing forces. In order to avoid false positives due to chemical adsorption a gold surface chemistry was optimized (described in detail in chapter 6).

The major achievements were presented and described culminating in a fully operational portable and autonomous platform. The device operation was demonstrated by conducting a

bioassay using a DNA–DNA oligonucleotides hybridization model. The experimental results show a clear difference between the complementary and the non-complementary binding signal.

5.3 Other integrations

5.3.1 Overview

In the past few years, the integration of biosensors on a lab-on-a-chip (LOC) platform has been pursued [62]. Typically, a LOC system includes an extraction/purification module, an amplification module (if needed) and a detection module. The extraction module is used to separate the desired molecules (DNA, RNA, proteins, cells...) from an initial sample (blood, saliva...). Then, this purified sample may be moved to a amplification module. This module is used to increase the number of biological entities in solution. For example, in the case of the DNA, a polymerase chain reaction (PCR) is usually the used technique to amplify a specific gene. Finally, the biological entity is introduced in the detection module where the bioassay is performed (DNA hybridization detection, protein detection...).

In this section, the magnetoresistive biochip developed along this thesis was integrated into a LOC platform. This work was developed in the scope of an European project called SNIP2CHIP. The goal was to integrate our biochip with an on-chip PCR system and an extraction device. The movement of the biological solution in this chip was made by electrowetting on dielectric (EWOD). Therefore, the magnetoresistive biochip was re-designed in order to be compatible with EWOD. Two different approaches have been developed in parallel along this project. The first approach consisted of integrating a standard fluidic channel connecting all the modules of the LOC system. This integration was achieved in collaboration with an Irish group, Life Science Interface group at Tyndall National Institute lead by Dr. Paul Galvin. The second approach involved the addition of process steps in the detection module microfabrication in order to include a suitable surface for droplet movement by EWOD. This approach was developed together with a French group, Leti-CEA (with Dr. Dorothée Jary), and Tyndall.

5.3.2 Integration with a standard fluidic system

A magnetoresistive biochip was integrated, in collaboration with Tyndall, in a plastic fluidic platform. This platform connects the extraction, PCR and detection modules with standard fluidic channels. The fluidic channels were designed and fabricated by Tynall using an injection molding procedure. Globally, this procedure consisted in the definition of the channel by photolithography of SU8 photoresist on Si substrate. Then, in an injection molding system, a polymer was melted over the substrate. Once cooled down, the polymer piece with the fluidic channels molded was separated from the substrate. Finally, the fluidic channel was glued over the SiO_2 of the biochip (with the architecture presented in section 4.3.4) using a UV-curable glue.

As depicted in figure 5.23a), a 1 mm wide fluidic channel passing through 3 of the 4 quadrants with sensors of the magnetoresistive biochip was designed. In this case, just the top and

right side contacts (fig. 5.23a)) of the chip are wirebonded to the PCB. The wirebonding and subsequent protection with silicon gel is performed before gluing the fluidic channel to the chip. The channel was 100 μm in height. The inlet and outlet of the channel are connected to the on-chip PCR chip and a waste reservoir, respectively. Several geometries were tested to assure the integration robustness and reproducibility. The final device including the on-chip PCR chip is shown in figure 5.23b). This platform was further used for detection of magnetic particles.

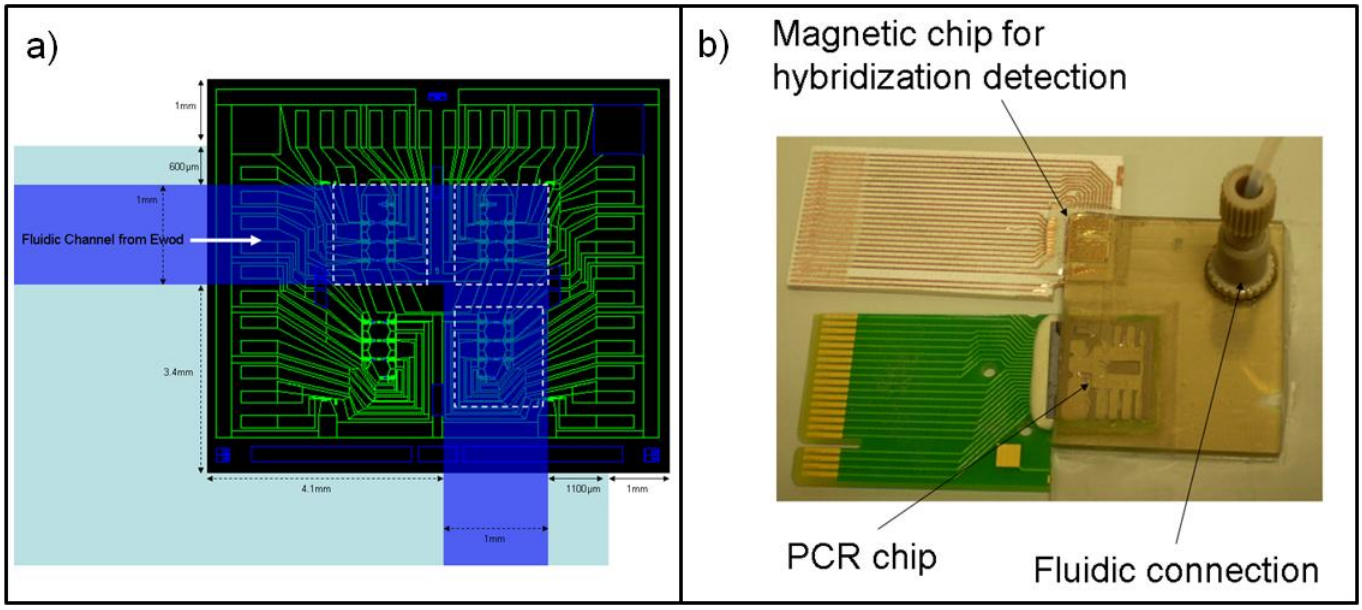

Figure 5.23: a) Schematic of a microfluidic channel passing through 3 of the 4 quadrants with sensors of the magnetoresistive biochip. b) Magnetoresistive biochip integrated by a standard fluidic lid with a DNA extraction/PCR module.

In the following experiments, a spin valve biochip as depicted in section 4.3.4 was used. The spin valve was deposited in the N3000 system with the presented stack: 20 Å Ta/ 30 Å $Ni_{80}Fe_{20}$/ 25 Å $Co_{81}Fe_{19}$/ 26 Å Cu/ 25 Å $Co_{81}Fe_{19}$/ 60 Å $Mn_{76}Ir_{24}$/ 30 Å Ta/ 150 Å $Ti_{10}W_{90}$ (N). The sensors were then patterned by ion milling with a total area of 2.5×80 μm^2 (U-shaped). Al contacts were defined by liftoff. After the passivation step, a 13×43 μm^2 Au pad was patterned on top of the spin valve defining the biological active area of the sensor.

The detection was made in the portable platform depicted in section 5.2. The sensors were biased with a 1 mA DC current and the magnetic polarizing field was set to 30 Oe DC and 13.5 Oe rms AC at 211 Hz. In a first experiment 250 nm magnetic particles (Micromod, Germany) without DNA were introduced in the fluidic channel 10 minutes after the acquisition of a baseline signal. As shown in figure 5.24, the signal changed as the particles are settling down. Finally, a phosphate buffer (PB) was used for washing the particles and the signal got back to the baseline. However, the washing was not very homogeneous along the sensor since magnetic particles were agglomerating in the corners of the channel. Therefore, the signal of the sensors close the corner did not get back to the baseline signal.

In conclusion, the spin valve magnetoresistive biochip developed along this thesis was suc-

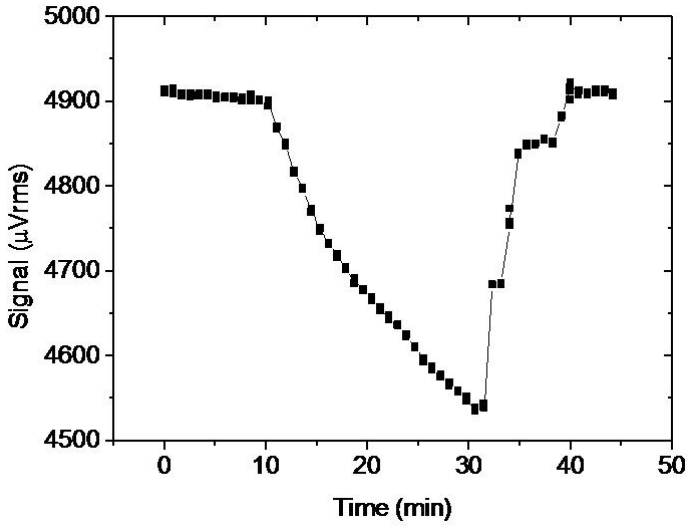

Figure 5.24: Detection of 250 nm magnetic particles on the integrated channel.

cessfully integrated in a lab-on-chip platform including an extraction chamber and a on-chip PCR module. All the modules were proven to be working with the integrated fluidic channels and the detection biochip has successfully detected 250 nm particles in the integrated system. However, the detection of DNA samples extracted from a real sample, amplified in the PCR module and detected in the magnetoresistive biochip still needs to be proven. Nevertheless, a large step in order to attain this goal was already achieved.

5.3.3 Integration with electrowetting on dielectric (EWOD)

The second integration approach used in the SNIP2CHIP project was to provide our magnetoresistive biochip the possibility to be used in a electrowetting on dielectric (EWOD). Electrowetting devices use electric fields to change the surface tension of an electrically conductive liquid [63]. These chips are usually designed with several electrodes covered by an hydrophobic material (Teflon, SiOC...). Therefore, a droplet of an aqueous solution will have a high contact angle ($> 90^{o}$) if no electrical field is applied. However, by applying an electrical field the surface tension changes and the droplet contact angle is reduced.

EWOD chips are commonly composed of several electrodes as depicted in figure 5.25. When the voltage drop between the droplet and the electrode is not zero, the surface becomes more hydrophilic and the droplet moves to that electrode. Since the droplet will always move to a more hydrophilic surface, a system with a sequence of electrodes can be constructed to move the droplets to specific positions by alternating the voltages of each electrode.

The EWOD system used in this project used a silicon wafer with electrodes to move the droplets. The surface of this chip was covered by an SiOC hydrophobic layer. A lid composed by an electrode (ITO usually used because of its transparency) and a hydrophobic layer covered the chip. The separation between the two parts was about 100 μm. The lid is used as a reference electrode while the chip has the electrodes enabling the movement of the droplets. In order

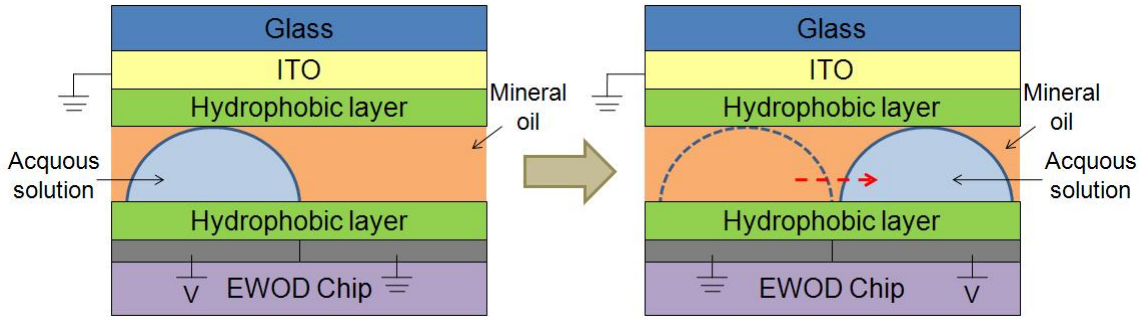

Figure 5.25: EWOD schematic including a conductive lid. The droplet moves toward the more hydrophilic surface.

to improve the droplet movement and to reduce the required voltages, the chip was filled with mineral oil. Therefore, besides the change in the surface tension, the aqueous droplet movement is helped by the opposite movement of the mineral oil.

The PCR chip was designed by Leti-CEA and comprises several reservoirs where the needed reagents were introduced (see figure 5.26). The chip was then mounted in a Peltier module in order to provide the needed temperature for each PCR step. The integration of this chip with the magnetoresistive detection chip was accomplished by replacing the lid over one of the reservoirs by the detection chip. As depicted in figure 5.26 only 1 out of 4 quadrant of sensors was used in this integration.

In order to be able to move droplets by EWOD into the detection chip, a hydrophobic layer must be added over the chip surface while maintaining the gold pad surface free for probe immobilization. The hydrophobic layer usually used by LETI is a 200 nm thick SiOC layer. However, the photoresist used in the microfabrication process at INESC-MN showed a very poor adhesion to this surface. Therefore, there is no possibility to perform another lithographic step on top of such a surface. To overcome this limitation, an approach using a liftoff step was tested. The SiOC was deposited by CVD on top of a photoresist patterned surface. Upon liftoff process it was observed that the SiOC was pealing off. This is due to the poor adhesion of SiOC to most surfaces and also due to the fact that large ultra-sound times were needed to complete the liftoff. Since it was not possible to use SiOC for further microfabrication steps, the hydrophobic layer had to be replaced by another material. The solution found was to immobilize on the chip surface, after a photolithographic step to protect the gold pads, a monolayer of a hydrophobic silane: n-octadeciltrichlorosilane (OTS).

Test samples were prepared where an 1700 Å ITO conductive layer was deposited on a glass substrate. This material was used since it is transparent and permits the visualization of droplet movements. Then, 50Å Ti/200 Å Au pads were patterned by lift-off. Finally, after covering the gold pads with photoresist by photolithography, the substrate was emerged in a toluene solution with 0.1 % of OTS during 30 minutes under agitation. The substrate was then sequentially rinsed in chloroform and ethanol. A lift-off step was then performed in microstrip or acetone to remove the photoresist of top of the gold pads surface.

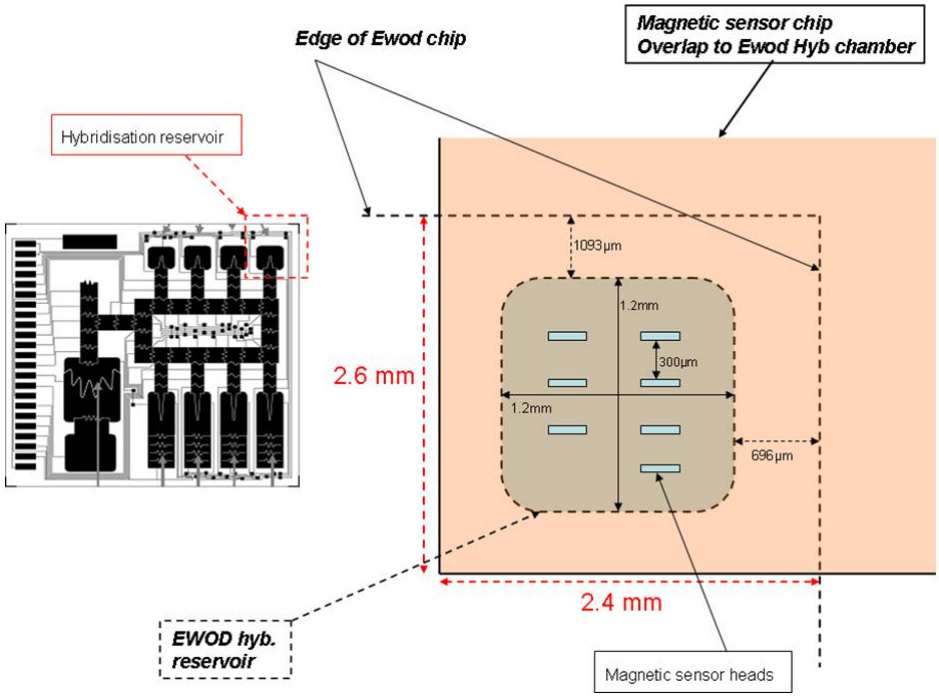

Figure 5.26: Integration of magnetoresistive biochip into the PCR chip. On the left, the PCR chip is depicted. One of the quadrants (on the right) of the detection chip is integrated on top of one of the PCR chip reservoirs

The first approach was to immobilize the OTS directly on top of the ITO (figure 5.27a)). However, it was found that the surface was not homogeneously covered by the OTS. The OTS is bonding to a surface by reacting to -OH groups on the surface. In this case, ITO many not have enough -OH groups to react with the OTS and form a perfect OTS monolayer. In order to overcome this limitation, a 2000 Å SiO_2 layer was deposited over the ITO (figure 5.27b)). After cleaning the surface during 15 minutes in an ozone plasma (UVO cleaner machine, Jelight inc.) to increase the number of -OH groups on the surface, a uniform layer of OTS was immobilized. Finally, the OTS over the photoresist was successfully removed by putting the sample on microstrip of acetone.

After this process, DNA probes are immobilized on the 43×13 μm^2 gold pads on top of the sensors. After this immobilization, the gold pads become hydrophilic. Therefore because of the EWOD requirements, these gold pads have to be small enough to not affect the large contact angles of droplets. Using the process above depicted, the surface hydrophobicity was determined by measuring the contact angle of a droplet of water. The results demonstrated that contact angle remains high enough ($> 90^o$) to move droplets by EWOD.

There is another important issue concerning the biochemistry. The droplets used in the EWOD system requires the presence of a thin layer of mineral oil covering the whole fluidic transportation surface including the biorecognition magnetic detection site. Therefore, tests were made in order to confirm if this oil layer prevents the target DNA strands from reaching by diffusion the DNA probes immobilized over the gold pads. The immobilization and hybridization

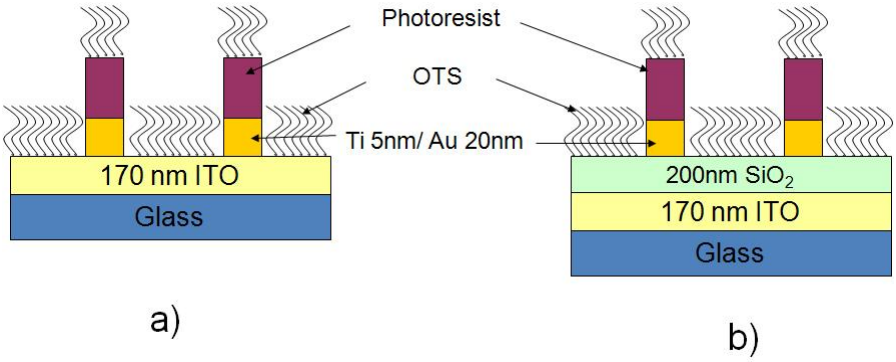

Figure 5.27: Cross section of chips fabricated for EWOD system. a) The OTS silane was directly immobilized on the ITO layer. b) An SiO_2 layer was used to improve the OTS immobilization homogeneity.

protocol optimized in chapter 6 were used. Before the addition of target DNA solution, the chip surface was covered with thin layer of mineral oil heated at 50°C (to reduce the oil viscosity). The target was further labeled by 250 nm streptavidin-coated magnetic particles (Micromod, Germany). Figure 5.28 shows that after washing the magnetic particles remained in the gold pads and almost no particles were found outside these areas. This means that the hybridization event was successful and that non-specific adsorption of DNA or particles in the OTS layer is negligible.

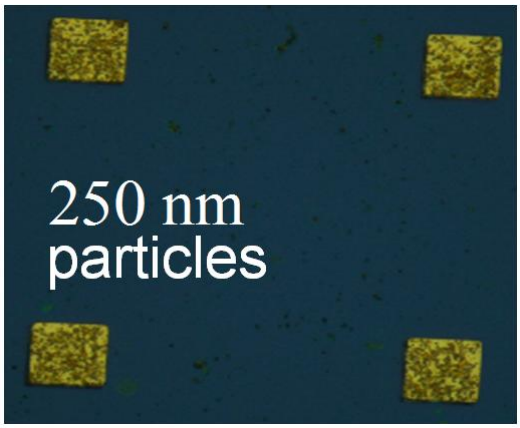

Figure 5.28: DNA hybridization of gold substrates with mineral oil mixed in the hybridization solution. 250 nm magnetic particles (Micromod, Germany) were used as labels.

These chips were finally tested in the EWOD PCR chip at Leti-CEA. As shown in figure 5.29, water droplets were successfully moved over the whole chip. The gold pads used for DNA immobilization did not have any influence in the behavior of the droplet even in the most dense structures.

In conclusion, a process to integrate magnetoresistive biochips in a EWOD system was successfully optimized. Although the full demonstration of integration and detection was not

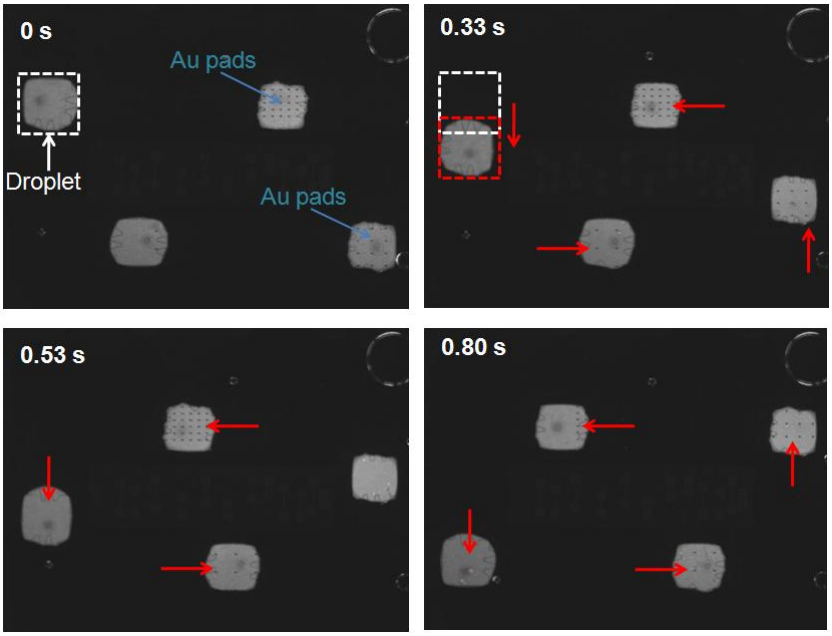

Figure 5.29: Movement of droplets in a EWOD PCR chip with a lid containing the following structure glass/1700 Å ITO/ 2000 Å SiO_2 and 50 Å Ti/ 200 Å Au patterned pads. The used hydrophobic layer was OTS.

demonstrated a large step toward this finality was accomplished.

5.3.4 Conclusions

In conclusion, a big step for the integration of magnetoresistive biochips in a standard and EWOD fluidic system was achieved. As depicted in this section, both integrations were challenging but performed successfully enabling a further full integration in the near future.

Chapter 6

Biological detection

After designing and integrating the magnetoresistive biochips, it is important to use them for what they actually were designed for: biologial detection. To do this the biological surface chemistry has to be optimized in order to reduce non-specific adsorption of magnetic particles and DNA to the surface of the chip. This reduction is essential to avoid false negatives in a future diagnostic platform. Therefore, in a first section of this chapter, the optimization of the biochemical protocol for immobilization and hybridization was performed taking into account the chip limitations. This protocol was further used in a second section where the detection limit of the platform is determined and improved by attracting the biological targets to the sensing sites.

6.1 Surface biofunctionalization

Presently, a difficulty appears associated to the biofunctionalization of most of the transducers interfaces that did not previously affect the standard planar substrates for microarrays used in optical detection [65], [66]. A great part of the recently developed systems with integrated detection technologies comprise electrical structures [67]-[69], which are sensitive to fluids and prone to corrosion and electrolysis. This greatly limits the use of biochemical solutions and functionalization protocols.

Most of the surface chemistries currently in use were developed, tested and optimized on plain solid surfaces of diverse materials for further application in unprocessed substrates, such as glass slides [70], [71], silicon wafers [72], [73], carbon electrodes [74] and gold substrates [75]. Although some of the procedures start being developed already envisioning its future application on the surface of complex devices with integrated circuits, the transposition of such procedures barely works at first.

Critical steps on chip surface preparation include activation, functionalization and derivatization methods for the construction of biomolecular arrays from inorganic materials. Several variable parameters of the process, such as, transducer/bioreceptor interface material characteristics (e.g., fabrication method, purity, roughness and thickness), environmental factors (e.g., oxidation, humidity, temperature) and biochemical reactional conditions (e.g., pH, ionic

strength, salt concentration and temperature), must be considered during the optimization of the surface chemistry, as it may considerably affect the final results.

Additionally, the magnetoresistive-based bioassays, involves the use of bioconjugated solid particles as labeling entities, which requires special carefulness to identify and avoid different types of non-specific binding events: target to substrate, label to substrate and target to probe [76]. A strong effort must still be made by all integrated biosensor platforms to proper discriminate false positive results, and even strongly discriminate false negative results, particularly in biochip for medical point-of-care diagnostics.

The selection of a proper interface between the different components of the system plays a critical role for the robustness, reliability and durability of the device. In order to conduct biological assays on top of a microelectronic system, it is crucial to protect the electrical structures from contact with the biochemical fluids, but simultaneously guarantee a uniform biochemical modification and biocompatibility. The biophysiological-related fluids present corrosive and electrolytic effects in a short- to medium-period of operation. In order to address this issue, the nature (often oxides - Al_2O_3, SiO_2 or nitrides - Si_3N_4, AlN, but also gold or polymers) and thickness of the passivation layer play an important role for the viability of the system. Some groups working in the field of magnetoresistive biochips have adopted thick passivation layers in the order of hundreds of nanometers [64] or more; however, the thickness of this protective layer takes a compromise between the robustness *versus* the sensitivity of the device. The thicker is the layer in use the higher is the distance from the magnetic labels to the sensing unit and lowers is its sensitivity. An alternative approach involves the modification of the original biochemical protocol towards a milder procedure.

The thiol-gold biochemistry adopted in this work uses a very demanding procedure. It is characterized by the usage of extremely harsh surface cleaning solutions, such as, Piranha (70 % sulfuric acid/ 30 % peroxide) [77], strong acids (HCl) or alkaline solutions (NH_4OH, NaOH) [78], to keep the gold surface free from organic contaminants. Another critical factor is the high salt concentration, up to 1 M, often reported for thiol-modified molecules immobilization in order to achieve a more stable sulphur-gold linkage [77]-[79].

This section presents the optimization of a thiol-gold chemistry protocol of reduced harshness for application in the development of a magnetoresistive biochip platform. Three main parameters were evaluated: I) the cleaning procedure before probe immobilization, II) the ionic strength (salt concentration and type of buffer) effect on immobilization, blocking, hybridization and magnetic labeling steps and III) the blocking solution efficiency. The best conditions tested were selected according the minimization of non-specific adsorption while enhancing the global performance of the magnetoresistive platform.

6.1.1 Biochemical reagents

All reagents used in the biochemical tests were of analytical grade. All solutions were prepared with ultra-pure grade water from milli-Q purifying system of Millipore. Bovine Serum Albumin (BSA) fraction V was purchased from Sigma, Tween20® was from Promega and

polyethyleneglycol, HO-PEG-SH, of 3 kDa ordered from RAPP Polymere (Tubingen, Germany). Single stranded customized 20 and 35-mer oligonucleotides (ssDNA), were synthesized by MWG-Biotech (Ebersberg, Germany), encoding for a sequence of the conservative region of the 16S rDNA from *E. coli*. Their designation, base sequences and modifications are as follows: *SH-probe-B*, 5' SH - TTT TTT TTT TTT TTT ACA CGG TCC AGA CTC CTA CG - biotin 3', *SH-probe*, 5' SH - TTT TTT TTT TTT TTT ACA CGG TCC AGA CTC CTA CG- 3'; *probe-B*, 5' biotin - CGT AGG AGT CTG GAC CGT GT- 3'; complementary target, *C-targ-B*, 5' biotin - CGT AGG AGT CTG GAC CGT GT- 3'; and 70 % non-complementary target, *NC-targ-B*, 5' biotin - TCA ATG GAG CTA CTC ATA GC - 3'.

Nanomag® -D, 250 nm, and Micromer® -D, 3 μm, magnetic particles modified with streptavidin, were obtained from Micromod, Germany. TRIS-EDTA buffer (TE) was prepared from 10 mM TRIS with addition of 1 mM EDTA and 1 M HCl to adjust pH to 7.4. Further addition of KH_2PO_4 up to 0.1 or 1 M and NaCl up to 0.1, 0.5 or 1 M concentrations was performed when stated. Phosphate buffer (PB) 100 mM consisted of a combination of monobasic sodium phosphate (NaH_2PO_4) and dibasic sodium phosphate (Na_2HPO_4), pH was adjusted to 7.4. Phosphate saline buffer (PBS) was prepared from a stock solution 10x concentrated, which consisted of a combination of Na_2HPO_4 (5.2 mM), KH_2PO_4 (1.7 mM) and NaCl (150 mM), pH 7.4 adjusted with HCl.

6.1.2 Thiol-gold surface biochemistry

The tests for optimization of surface chemistry were performed on gold substrates consisting of 5 nm titanium adhesion layer plus 20 nm of gold, sequentially sputtered (Alcatel, SCM-450) over a 3-inch silicon wafer. The wafer was protected with photoresist and diced in 7×15 mm^2 individual pieces using a dicing machine (Disco, DAD-321).

The surface biochemistry and subsequent biorecognition process in the origin of the magnetoresistive biochip comprised five sequential steps as follows: cleaning, immobilization, blocking, hybridization and labeling (figure 6.1). Different buffers were used along the various biofunctionalization steps and those are properly identified further on in section 6.1.5.

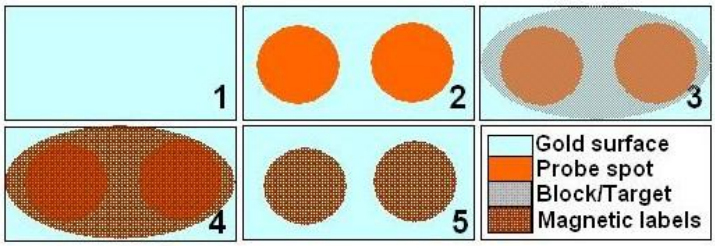

Figure 6.1: Schematic representation of the procedure used to perform probe spotting and biomolecular recognition on the surface of gold substrates. 1) Cleaned gold substrate; 2) Discrete probe spots of 2.5 μL; 3) Biorecognition, the larger circle represents the target solution covering the probe spots; 4) Magnetic labeling with magnetic particles suspension; 5) Remaining magnetic particles attached to the target molecules after washing.

In preparation for thiolated probes immobilization gold substrates went through an optimized and meticulous mild cleaning procedure. The substrates were dipped into hot (65°C) Microstrip 2001 for 2 h, copiously rinsed with isopropanol alcohol (IPA) and ultra-pure milli-Q grade water, and blow dried with a filtered (0.2 μm pore filter) compressed air stream. To completely remove traces of photoresist polymer and other organic contaminants the gold surfaces were exposed to ultraviolet light/ozone plasma for 15 min inside an UVO cleaner machine (Jelight Inc., CA, USA). Immediately after, the DNA probes were manually spotted through a procedure depicted in figure 6.1 (frame 2) in case of gold substrates or simply covered with a 50 μL droplet for processed chips. Immobilization proceeded for 2 h at 37°C. The discrete multi-spotting procedure was adopted as a strategy to get replicates and easily distinguish between specifically bound species (*in-spot*) and non-specifically adsorbed species or background (*out-of-spot*).

After immobilization, the unbound DNA was washed out by rinsing the sample with the same immobilization buffer. In the blocking step a 50 μl droplet of a blocking agent dissolved in immobilization buffer (unless otherwise stated) covers the whole surface for 1 h at 37°C. Two different blocking agents were tested, namely BSA at 5 % (w/v) and SH-PEG (1 mg/ml). Hybridization was performed for 3 h at 42°C using a target DNA (fully or 30 % complementary to the ssDNA probe) at a fixed concentration of 1 μM in the case of gold substrates.

The whole protocol from immobilization through blocking, hybridization and magnetic labeling steps was performed inside a Petri-dish in humid atmosphere to prevent evaporation.

6.1.3 Optical analysis of magnetic labeling on gold substrates

Streptavidin-coated magnetic labels of two diameters were used: 250 nm particles and 3 μm beads. The magnetic particles (MPs) right before use were collected from the stock solution by means of a magnetic concentrator (Dynal Biotech, Norway) and washed twice with phosphate buffer (PB) + 0.02 % (v/v) Tween20. MPs were then ressuspended and 10× diluted in the same buffer, unless otherwise stated. A 25 to 50 μl droplet of this suspension was placed over the functionalized gold substrate and let to settle down and react for 30 minutes at RT. Unbound or weekly bound MPs were gently washed away with buffer.

Control samples were always performed for both immobilization and hybridization steps. At immobilization both non-biotinylated probe (*SH-probe*) and non-thiolated probe (*probe-B*) were used to assess non-specific adsorption of labels to surface and non-covalent binding of target molecules, respectively. On the other hand, for hybridization a biotinylated 70% non-complementary target DNA strand (*NC-targ-B*) was tested for non-specific recognition background signals.

At the end, optical microscopic images were taken using a CCD camera and the software ImageJ used to analyze the magnetic particle density on gold surfaces. Two pictures from random sites at both spots and three pictures from outside the spots area were taken. To the original color picture a background picture (without magnetic particles) was subtracted and the resulting picture converted to grey scale. After imposing a fixed threshold delimiting the

number of pixels corresponding to magnetic particles on the surface, the surface coverage is automatically calculated in percentage of the total area. The percentage values obtained from image analysis in ImageJ must not be seen as absolute percentages but as relative results. Due to the small size of the particles combined with pictures at 800× magnification the software has no resolution to identify discrete particles. Note that the batch of pictures corresponding to surface blocking tests were analyzed using a higher threshold than the one used for buffer influence tests. The higher threshold allows us to amplify the measured value and to distinguish between very low and similar results of MP surface coverage.

6.1.4 Influence of ionic strength on thiol-gold chemistry

A referenced protocol [77] based on TE buffer was adopted and used as starting point to develop new formulations of solutions used for immobilization (I), blocking (B), hybridization (H) and labeling (L) steps. The sequence of any of these four steps is from now on identified with the correspondent initial letter, such as "I+B+H+L".

The main goals were to move towards a milder solution while maintaining the level of sulfur-gold binding capacity and minimizing the non-specific adsorption of magnetic labels. In order to understand the influence of the type of buffer and salt concentration (ionic strength) on the final surface coverage of specifically and non-specifically bound magnetic labels on the gold substrate, two groups of experiments were conducted. The first group of data is presented in the bars graph from figure 6.2. A comparison between different combinations of buffer solutions along the four biofunctionalization steps (I+B+H+L), was made in terms of percentage of gold surface coverage by 250 nm streptavidin-coated magnetic particles. For each condition tested, two probe spots were analyzed, one as positive control (probe hybridized with a biotinylated complementary DNA) and another as negative control (probe incubated with hybridization buffer without target DNA). Results for MPs coverage from positive and negative controls were designated as "specific binding" and "non-specific adsorption", respectively. The abbreviated designation and detailed compositions of all solutions used are listed in table 6.1.

From figure 6.2 two main outcomes are identified. When using TE-based labeling solutions the non-specific adsorption of MPs to non-biotinylated probe spots is significatively higher, reaching densities of the same magnitude of the corresponding specific binding. On the other hand, phosphate-based labeling solutions drastically decrease the MP binding capacity to less than 10% of surface coverage, but at the same time almost completely eliminate the non-specific adsorption to single stranded probe DNA spots.

On TE-based labeling solutions, gradually decreasing the ionic strength by decreasing the concentration of sodium chloride (NaCl) from 1 to 0.5, 0.1 M and no salt, the density of MPs in both positive and negative controls was also proportionally decreased. This can be explained by the presence of the streptavidin coating on the MPs. Streptavidin is a ∼53 kDa tetrameric protein that is known as less prone to non-specific adsorption than other related proteins, such as avidin, mainly due to the lack of carbohydrate modifications in its structure. Nevertheless, its mildly acidic isoelectric point (pI) of ∼5 turns it slightly negatively charged at the working pH

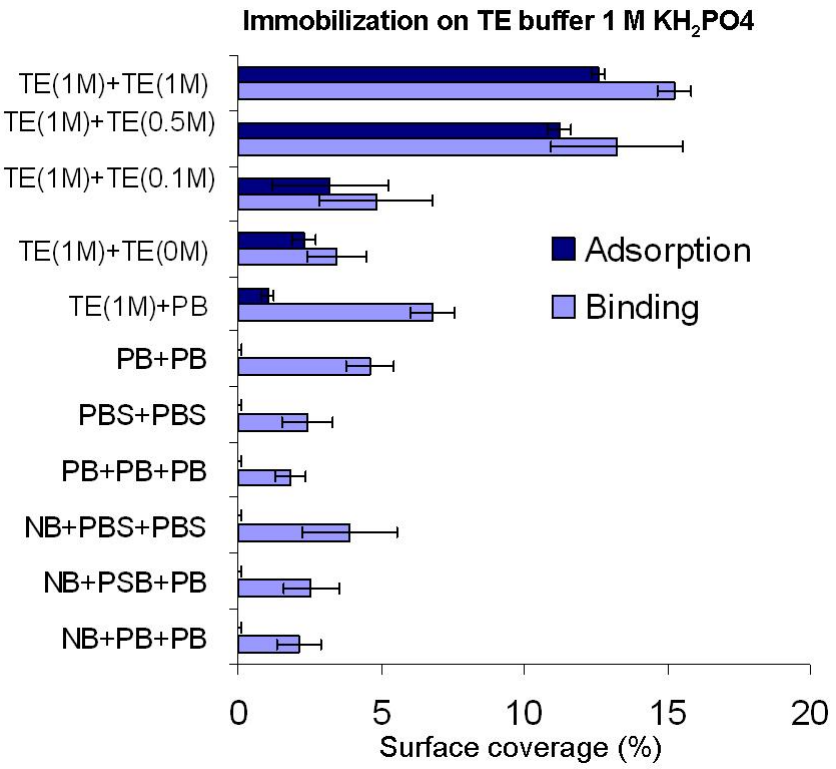

Figure 6.2: Surface coverage by 250 nm MPs on gold substrates using slightly different combinations of blocking, hybridization and labeling solutions at constant conditions for probe immobilization using TE buffer supplied with 1 M KH_2PO_4. When nothing stated the blocking buffer is the same used in the immobilization step. Data acquired from the analysis of optical microscope pictures using ImageJ software.

7.4 [80]. Negative charges potentiates the nonspecific adsorption of the protein to solid surfaces through electrostatic interactions favored at higher saline environments (e.g. PBS buffer), as reported elsewhere [81]. However, the adsorption to modified surfaces with other negatively charged biomolecules, such as DNA strands, is not favored due to electrostatic repulsion. At high ionic strength, the electrostatic repulsion between two negatively charged molecules (e.g. complementary DNA strands) is shielded, which promotes molecules interaction and favors non-specific adsorptions. Additionally, the biotin-streptavidin binding affinity is also highly dependent [82] on the ionic strength of the reactional buffer. Increasing concentrations of NaCl or other mono- or divalent salt gradually stabilizes the biotin-streptavidin interaction [82].

Meanwhile, a couple of PB-based hybridization and labeling protocols, namely "PB+PB" and "PBS+PB" were selected to perform corrosion tests on processed chips including magnetoresistive sensors and aluminum current lines. After a first complete functionalization cycle (I+B+H+L) with probe immobilization and surface blocking occurring in TE buffer 1M KH_2PO_4, the chips suffer from a general loss of sensors and corrosion on the aluminum current lines.

Another attempt on getting a milder biochemistry was conducted. A second group of data

Nomenclature	Blocking	Hybridization	Labeling
TE(1M)+TE(1M)	TE	TE 1M NaCl	TE 1M NaCl
TE(1M)+TE(0.5M)	TE	TE 1M NaCl	TE 0.5M NaCl
TE(1M)+TE(0.1M)	TE	TE 1M NaCl	TE 0.1M NaCl
TE(1M)+TE(0M)	TE	TE 1M NaCl	TE
TE(1M)+PB	TE	TE 1M NaCl	PB
PB+PB	TE	PB	PB
PBS+PBS	TE	PBS	PBS
PBS+PB	TE	PBS	PB
PB+PBS	TE	PB	PBS
PB+PB+PB	PB	PB	PB
NB+PBS+PBS	TE (no PEG)	PBS	PBS
NB+PBS+PB	TE (no PEG)	PBS	PB
NB+PB+PB	TE (no PEG)	PB	PB

Table 6.1: Description of the nomenclature used in the Y-axis of the graphs from figure 6.2 and 6.3. The immobilization solution TE corresponds to TE 1M KH_2PO_4 on figure 6.2 and TE 0.1M KH_2PO_4 on figure 6.3. When nothing is referred the blocking buffer is the same used for immobilization but containing 1 mg/ml of SH-PEG.

on magnetic label density was performed after reducing the concentration of KH_2PO_4 on the immobilization and blocking steps from 1 down to 0.1 M (figure 6.3). The specific binding after hybridization was substantially improved in about 5% of surface coverage and the non-specific adsorption to the probe spot region was kept close to while the non-specific adsorption of magnetic particles to the gold surface on the out-of-spot region was also reduced (between 0.1 and 0.3%). The hybridization improvement is explained by the fact that a higher ionic strength in the immobilization buffer promotes a more densely packed probe arraying, hampering hybridization from occur due to steric hindrance. This observation is in good agreement with what was previously reported for the adsorption of thiolated single stranded DNA molecules to gold substrates. Herne and Tarlov [77] reported that despite maximum probe coverage is achieved for 1M of KH_2PO_4 in the immobilization solution, the resulting probe hybridization array was not successful.

Assuming a compromise between the density of recognition events and the harshness level of the chemistry on the chip, in the following experiments the adopted protocol was the one identified by "PB+PB" on table 6.1.

6.1.5 Influence of the blocking step on magnetic labels non-specific adsorption

In order to better understand the effect of the blocking step on the prevention of false positives, and simultaneously assess the probe immobilization efficiency, a third group of experiments was performed. Attending to the former results, TE 0.1 M KH_2PO_4 was taken as the basis solution for the blocking tests. The three following blocking conditions were compared, TE buffer 0.1 M KH_2PO_4, BSA fraction V 5% (w/v) and 1 mg/ml of thiolated polyethylene glycol (SH-

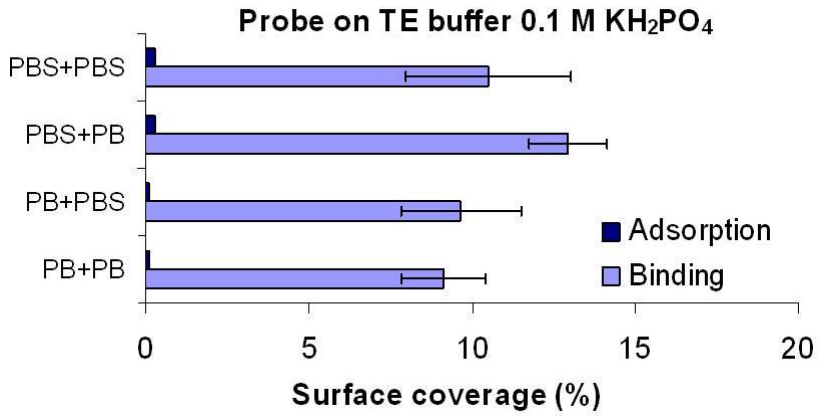

Figure 6.3: Surface coverage by 250 nm MPs on gold substrates using slightly different combinations of hybridization and labeling solutions at constant conditions for immobilization and blocking steps using TE buffer supplied with 0.1 M KH_2PO_4 (10× less concentrated compared with data from figure 6.2). Data acquired from the analysis of optical microscope pictures using ImageJ software.

PEG) both in TE 0.1 M KH_2PO_4. From figure 6.4 the efficient blocking effect of the SH-PEG is notorious at various levels, namely at immobilization and hybridization steps magnetically labeled with either nanometer sized particles (figure 6.4a and 6.4b) or micrometer beads (figure 6.4c and 6.4d). The observed specific binding signal for the different probes and targets used was proportional for the two types of magnetic particles investigated. The binding signals just differ in absolute value of surface coverage due to size disparity (10× in diameter). The binding of the particles to spotted biotinylated and non-biotinylated probes is markedly distinct varying in surface coverage from about 25 to 0% and 60 to 0% for 250 nm and 3 μm MPs, respectively. A biotinylated but non-thiolated probe clearly adsorbs to the gold surface, most probably through its nitrogen-containing bases as discussed elsewhere [77]. The MPs precisely bind to the probe spot but are more easily washed way than from thiolated probes. After 24 hours in buffer PB/Tween20 solution the probes without thiol group (*probe-B*) start to desorbing spontaneously taking along the MPs (figure 6.5 - 4), while the *SH-probe-B* remains strongly bound to the gold as proved by the well defined spot and constant particles density (figure 6.5 - 3). Magnetic labeling of immobilized and hybridized biotinylated DNA strands at 1 μM concentration present relatively the same MPs density (figure 6.5 - 3 and 6.5 - 6). A 70% non-complementary biotinylated target is not detected after hybridization (figure 6.5 - 5). In general, labeling signals from micrometer sized MPs are less reproducible than from nano-sized, presenting higher standard deviations. The large size of magnetic beads makes them more vulnerable to washing steps and prone to be inaccurately washed out.

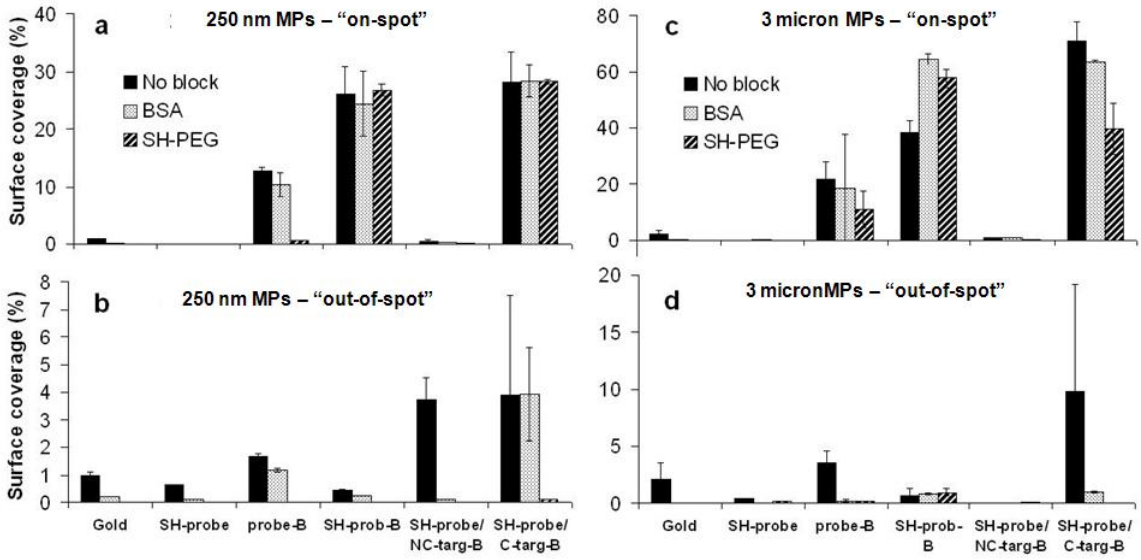

Figure 6.4: Surface coverage by MPs on gold substrates using three different blocking conditions, only buffer, 5% (w/v) BSA solution and SH-PEG 1 mg/ml, all in TE 0.1 M KH_2PO_4. Graphs **a** and **c** displays data from MPs density corresponding to surface areas inside the probe spot. Graphs **b** and **d** correspond to non-specific adsorption values of the MPs to bare gold (density of particles outside the probe spot) for 3 μm and 250 nm in diameter MPs, respectively. Data acquired from the analysis of optical microscope pictures using ImageJ software.

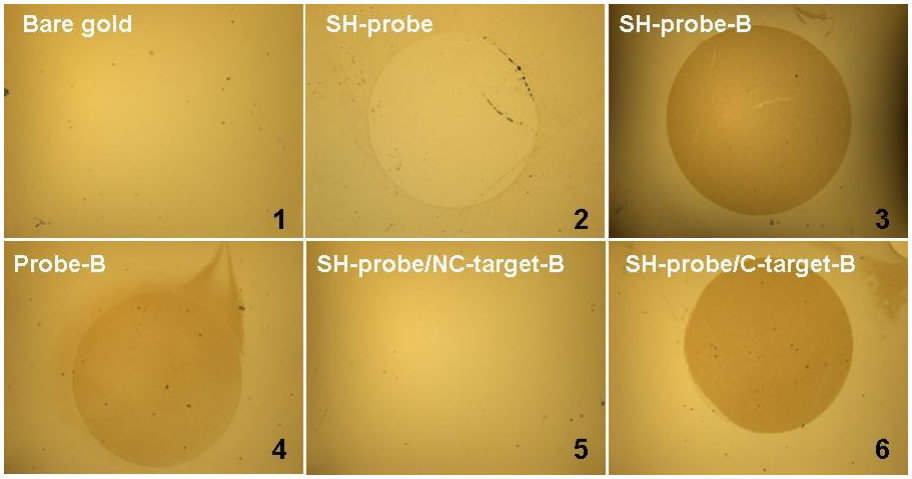

Figure 6.5: Optical microscope pictures taken at 40× magnification showing examples of functionalized gold substrates with different immobilized/adsorbed probes after reaction with 250 nm MPs. Figures nomenclature correspond to the same used in figure 6.4.

6.1.6 Conclusion

The effort undertaken towards the optimization of a surface chemistry for application in the development of a magnetoresistive biochip-based platform was successfully accomplished. Significant improvements at various levels were achieved. Less damaging biofunctionalization so-

lutions were formulated resulting in the improvement of the biorecognition event detection and simultaneously in the minimization of non-specific adsorption signal.

Therefore, the protocol used in the following sections is as follows:

1. 2h immobilization of *SH-probe* in TE buffer 0.1 M of KH_2PO_4 solution at 37°C.
2. 1h blocking with SH-PEG in TE buffer 0.1 M of KH_2PO_4 solution at 37°C.
3. 30 min hybridization of *C-targ-B* in PB buffer 0.1 M + 0.02% (v/v) Tween20 solution at room temperature.
4. 30 min settling down and target recognition (streptavidin-biotin binding) by MPs in PB buffer 0.1 M + 0.02% (v/v) Tween20 solution at room temperature.
5. washing of MPs with PB buffer 0.1 M + 0.02% (v/v) Tween20 solution.

6.2 Femtomolar limit of detection with a magnetoresistive biochip

Standard hybridization assays for both diagnostic and research applications are characterized by long hybridization times as well as poor sensitivity and high background noise, forcing the use of sample amplification methods. Usually, only a small number of copies of target nucleic acids are present in test samples either of clinical interest, environmental or food nature. For example, in water and foodstuff samples for human consumption, regulatory entities require the detection of a single pathogenic microorganism. Additionally, in biological samples the clinical significant number of infectious organisms ranges from as low as one up to one million cells. Since a microbial cell usually contains from 1 to 100 target-DNA sequences the total target-DNA available per sample ranges from approximately 10^{-24} to 10^{-16} moles. Considering average sample volumes on the order of tenth to hundreds of microliters the target molecule concentrations may range from zepto- (10^{-21} M) to femto-molar (10^{-15} M). This is far below the current limit of detection (LOD) for most of the hybridization-based systems. The optical detection systems using conventional fluorescence scanning do not go beyond the picomolar range [85]. Light absorption [86] or light scattering [87] principles using silver enhanced gold nanoparticles as labels are at the 10^{-13} to 10^{-14} M range. Electromechanical devices integrating microcantilevers [88] or quartz crystal microbalances [89] present LOD of 10^{-11} and 10^{-14}, respectively. Other systems based on electrochemical detection methods [90]-[92] are closer to the required sensitivity (10^{-14}-10^{-16}).

In order to make biological samples measurable by standard detection systems, two types of sample amplification methods may be used: the cell growth in culture media or the polymerase chain reaction (PCR). The microbial cell cultivation takes at least several hours, a day or even more, depending on the type of microorganism. A typical PCR to produce about 10 million DNA molecules from each starting target needs to undertake 40 cycles, which takes about 70 minutes.

The hybridization detection system based on magnetoresistive (MR) sensors associated to the use of superparamagnetic nano-particles as reporter systems arose with promising characteristics [93]-[95]. High sensitivity, fast performance and electronic platform compatibility leading to integrability, miniaturization, scalability and portability are its main strengths [69], [96]-[98]. MR sensors have proven to be highly sensitive to a small number of nanometer-sized magnetic labels [11]. Moreover, it offers the possibility of on-chip active transportation of the magnetically labeled molecules [99]. As the molecular diffusion of DNA fragments is typically one to three orders of magnitude smaller than the typical liquid phase diffusivity of small molecules (for which $D_{mol} = 10^{-9}$ m^2/s) the standard hybridization-based biochip analysis are relatively slow, requiring from a couple of hours to overnight hybridization periods before attaining a detectable amount of bound target molecules [100]. Using on-chip fabricated current line structures for attraction and concentration of magnetically labelled biomolecules to the sensing sites has proven to significantly reduce the biorecognition time to less than 30 min. [101], [102].

However, only few groups have demonstrated the applicability of such devices to the real detection of biological events, e.g. DNA hybridization or antibody/antigen recognition [64], [10], [103], [76]. To develop a fully functional MR biochip, a number of difficulties arise associated to the physicochemical interfaces, namely the integration of the electrical structures with the biochemical active layer. The surface biochemistry is a critical aspect that extensively influences the performance of the whole system. False negative and false positive responses due to non-specific biomolecular recognition of target molecules and magnetic labels are directly related with inappropriate surface chemistries. As MR biochip signals completely depend on the magnetic labels, a not less important factor is related to the type and characteristics of the magnetic particles (MPs) adopted, as reported elsewhere [104].

After solving those fundamental physicochemical issues related to device robustness and magnetic particle compatibility (see section 6.1), a step forward on the evaluation of the bioplatform in terms of biorecognition efficiency, reproducibility and reliability was taken. The influence of the magnetic label in the biorecognition efficiency, as well as the importance of the mechanism of target transportation (passive diffusion, magnetic focusing and upcoming microfluidics) to the sensing sites on the biological limit of detection (LOD) of the system are quantified and discussed in the present work.

The following experiments were accomplished using the spin valve chip described in section 4.3.4 and in appendix A, and the portable measuring platform depicted in section 2.2.4.

6.2.1 Pre-hybridization labeling vs Post-hybridization labeling

Following the surface chemistry optimized in section 4.3.4 after the blocking step (step 2) two different procedures can be accomplished depending on the timing at which the magnetic labeling occurs: either before (pre-hybridization labeling) or after hybridization (post-hybridization labeling) (figure 6.6). In the former case hybridization occurs between target DNA molecules immobilized by biotin/streptavidin on the surface of a MP and probes immobilized over the chip surface already connected to the measurement set-up. Hybridization proceeds for about 30

min at room temperature (∼25 °C) during on-line data acquisition as detailed in section 4.3.5. In the last case, a 50 μL sample of unlabeled biotinylated target molecules is dispensed over the chip and incubated for 3 hours at 42 °C inside a humid chamber. Solutions of 100 μL of target DNA were prepared by a series of 100-fold dilutions (1:100) from an initial stock solution of 100 μM.

In pre-hybridization labeling (pre-HL), the target DNA from an initial volume of 100 μL (target concentrations ranging from 1 μM down to 10 fM in PB, corresponding to 6×10^{13} down to 6×10^{5} absolute number of DNA molecules, respectively) is left to react for 30 min at RT with 10 μL of 250 nm MPs (4.9×10^{6} particles/μL), 100× diluted from stock. After reaction, the MPs carrying the target DNA are magnetically concentrated in a final 2 μL suspension using a permanent magnet. This volume is then dispensed over one out of the four sensing regions of the chip ($\sim 1.5\times1.5$ mm^2).

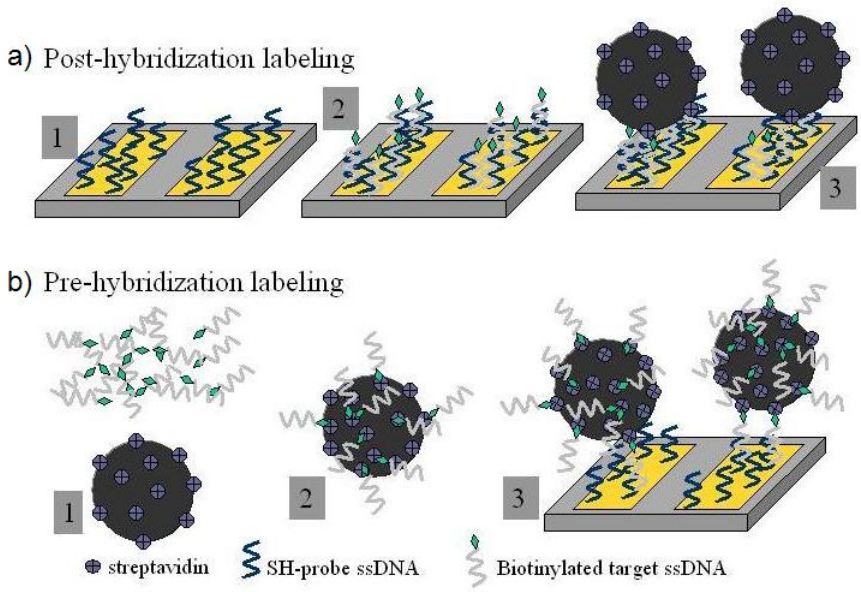

Figure 6.6: Schematic representation of two different procedures for magnetic labeling of hybridization events: (a) post-hybridization magnetic labeling (post-HL), comprising 3 steps: 1) probe immobilization over the sensor, 2) off-line hybridization of biotinylated targets with immobilized probes, 3) labeling of pre-hybridized targets with streptavidin-coated MPs and; (b) pre-hybridization magnetic labeling (pre-HL) also comprising 3 steps: 1) capture and concentration of biotinylated target DNA with streptavidin-coated magnetic particles, 2) magnetically labeled target attraction to sensor site and 3) target hybridization with immobilized probes.

The post-hybridization labeling (post-HL) takes place on-chip during the assay measurement. A 20 μL suspension of MPs (4.9×10^{7} particles/μL) is dispensed over the previously hybridized target molecules on the sensor surface and let to settle down allowing biotin/streptavidin interaction for about 30 minutes while sensors signal are acquired.

Before using the MPs its original solution is always removed and particles carefully washed and re-suspended in PB/Tween20 buffer solution. This washing step avoids the presence of

antimicrobial agents and high salt concentrations that may hamper the biomolecular recognition or damage the passivation layer.

The experiments were performed as described in section 4.3.5. The binding signals are differential voltage values identified as $\Delta V_{ac}^{binding}$, calculated from the difference between the sensor baseline (V_{ac}^{sensor}) and the signal originated from the specifically bound MPs over the sensor ($V_{ac}^{particles}$). In order to directly and accurately compare the binding signals coming from different sensors located at different chips or even among the same chip, their sensitivities must be normalized to a reference value. Each sensor response (V_{ac}^{sensor}) to the external AC excitation field (H_{ac}), typically of a few mV_{rms}, is used as its own reference. Three groups of experimental data are compared in two plots of concentration of target DNA versus normalized binding signals ($\Delta V_{ac}^{binding}/V_{ac}^{sensor}$ for each sensor).

Figure 6.7, shows data for passive hybridization experiments, where target molecules diffuse and reach the probe molecules immobilized over the sensors by a combination of pure molecular diffusion, Brownian motion and gravitational force. The difference between the two groups of data lies on the presence or absence of magnetic labels at the hybridization reaction, as described above.

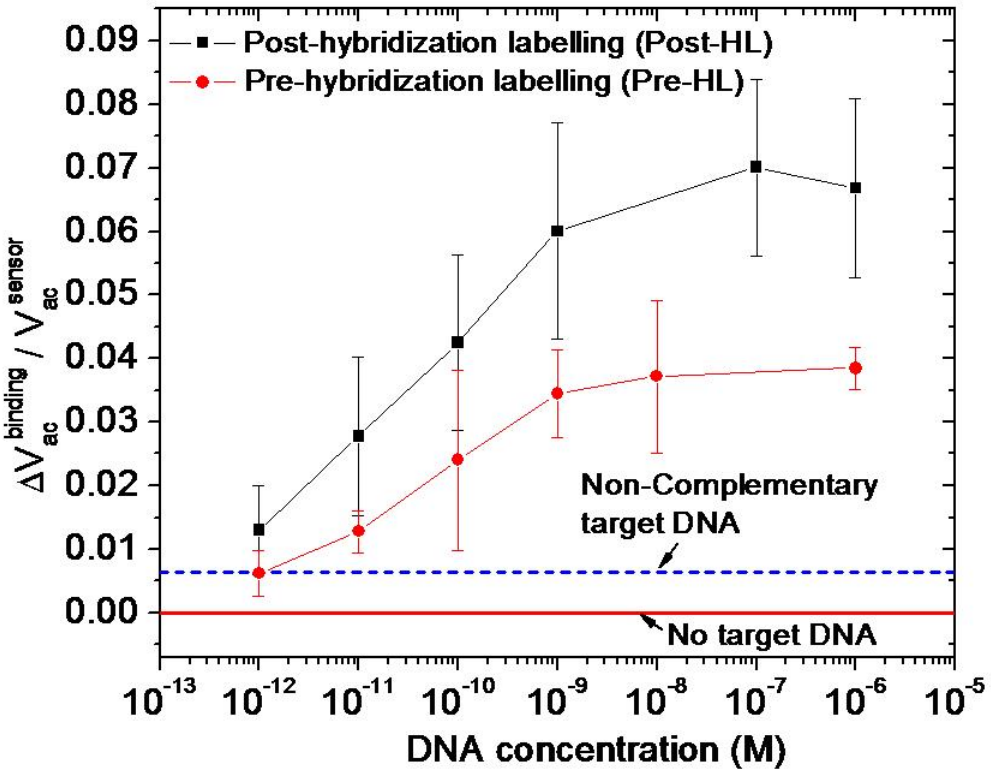

Figure 6.7: Comparison of two groups of experimental data for passive hybridization events mainly differing in the presence or absence of magnetic label during the hybridization of pre-HL and post-HL, respectively. The error bars are standard deviations of the signal coming from at least 5 sensors acquired sequentially at the same chip.

For passive hybridization assays, unlabeled target samples in comparison with magnetically

pre-labeled samples have presented significantly higher levels of hybridization for the same target concentrations. The presence of the MP during hybridization was expected to hamper the reaction, reducing its efficiency in some extent. In general, when one of the partners involved in a biomolecular reaction is immobilized on a solid surface the reaction rates are known to be slower in comparison with the same reaction but with molecules free in solution [100]. The reduction of efficiency was observed to be constant at about 43 to 50% and independent of the initial target DNA concentration, from the saturation down to the lower limit of detection which is the same in both cases (picomolar range). This efficiency reduction is extensively discussed and explained in [105].

In conclusion, the hybridization with pre-labeled target molecules showed lower signals than the hybridization of free DNA molecules which were *a posteriori* labeled. However, when the target DNA is previously attached to a magnetic particle, it can be attracted to the sensing site using an integrated U-shaped current line [99]. This may make a difference in the sensitivity of the system as studied below.

6.2.2 Attraction for improvement in sensitivity

Each spin valve sensor are surrounded by a U-shaped current line which was specially designed to enable particles focusing onto the sensing area [99]. Passing a 40 mA dc current through this line generate a field gradient which attracts the magnetic particles toward it. By applying an external 30 Oe rms magnetic polarizing field, at frequencies ranging from 0.1 to 1 Hz, the magnetic particles will be alternatively attracted and repelled from the line. This movement forces the particles to pass through the sensor area and eventually to bind to the biological probes.

Figure 6.8 shows hybridization data for pre-labelled assays, either passive (squares) or magnetically assisted (circles). The assisted hybridization has shown to be more efficient than the passive hybridization at various levels: i) presenting a 25 % higher saturation signal, ii) decreasing signal dispersion between different sensors of the same data point and iii) lowering the LOD of the system by three orders of magnitude (from pM down to fM). The trend of the curves below saturation follow with a constant separation of three orders of magnitude in target concentration between data points at the same level of binding signal.

Each data point is an average signal of the binding signal of at least 5 sensors after two or three stringent washes of the unbound labels from the surface of the sensor. The reference sensor is used to determine the washing efficiency. When the reference sensor signal returns to the baseline it is assumed that the washing step is complete. The error bars (standard deviations) associated to the passive hybridization signals are fairly high (between 9 to 69%) compared with the highest 38% achieved for the assisted hybridization data points. The random settling down of the MPs associated to the manual washing procedure is a possible cause for this variation. A micropipette is used to flush the surface of the chip in a way as reproducible as possible. The stringency of the washing differs from sensor to sensor in a way that the closest sensors to the flushing tip are subjected to stronger washing forces than the more distant ones. In

order to reduce the amplitude of the error bars, the manual washing will be replaced by a more controllable, systematic and reproducible washing procedure based on a microfluidic washing system as discussed in [106].

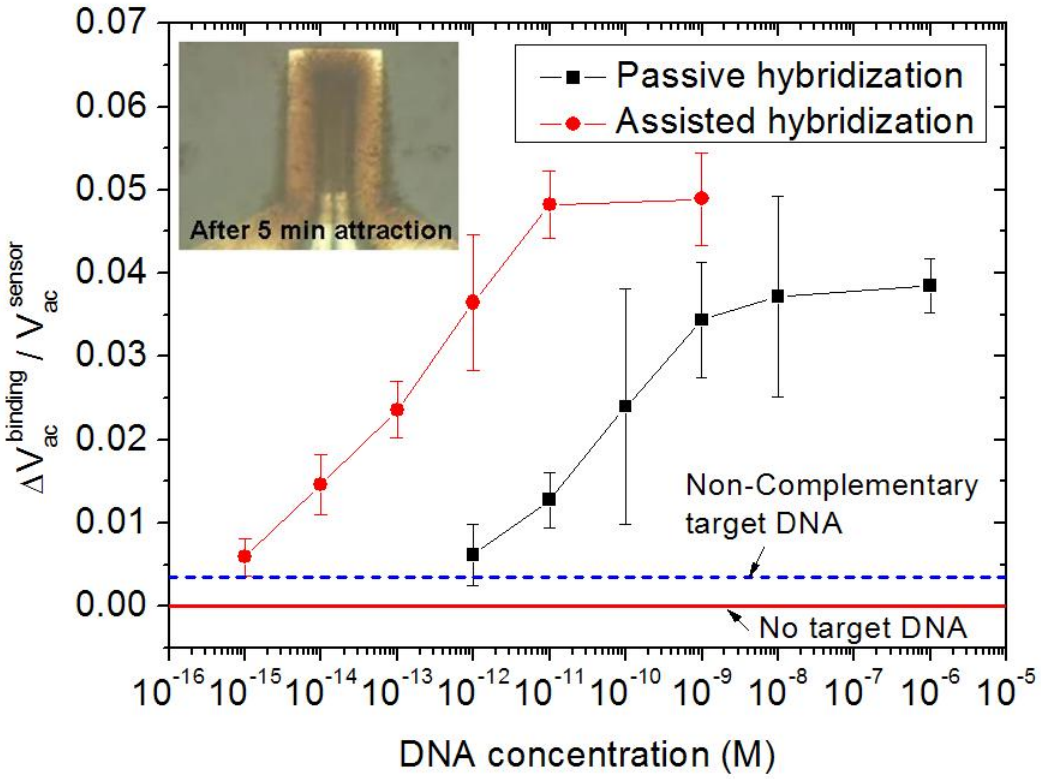

Figure 6.8: Comparison of two groups of experimental data acquired for passive and magnetically assisted hybridization events, in both cases carrying the target molecules on the surface of magnetic labels during the hybridization event. The error bars are standard deviations of the signal of at least 5 sensors acquired sequentially at the same chip. Inset picture shows an increased MPs density at the sensor site after 5 minutes of magnetic focusing using the current lines.

6.3 Conclusions

In conclusion, a protocol was first optimized in order to reduce the non-specific adsorption of both magnetic particles and biological probes. Then, the biological detection limit of the magnetoresistive biochip platform was determined and significantly improved in three orders of magnitude, from picomolar down to femtomolar, by the use of an efficient magnetic focusing system associated to pre-hybridization labeled samples. The magnetic label that initially was identified as a limitation to passive hybridization reactions, decreasing its efficiency in about 50%, easily became an advantage when associated to an active transportation system. Furthermore, as target DNA is found typically in minute quantities ($< 10^{-15}$ M) in most test samples,

since only a few copies of target DNA are present in each cell, target sequences must be at least partially purified and concentrated prior to testing. This purification and concentration is highly advantageous to be magnetically assisted with the magnetic labels.

The actual limitations of the system (washing uniformity, magnetic focusing efficiency) were identified and will be addressed by the development of an integrated microfluidic system. Besides the washing procedure some other improvements will be addressed in order to maximize the focusing efficiency of the system aiming to move further down on the LOD of the platform.

Finally, the LOD of this platform will be further determined for genomic or PCR product DNA in order to make a step forward toward the use of this platform in a real diagnostic application.

Chapter 7

Conclusions and future work

As already mentioned, magnetoresistive biochips are currently being integrated with other devices in order to obtain a fully integrated lab-on-a-chip device. The requirements for this device are: sensitivity, portability, rapidity, low cost and user-friendliness. In this thesis all of these requirements were addressed.

The first requirement discussed in this work was the sensitivity of these biochips. Several parameters including magnetic label choice, sensor structure and optimization of dimensions, detection architecture and biological protocols are important to obtain a magnetoresistive biochip with improved sensitivity. With respect to label, five different kinds of magnetic particles were characterized and tested. A compromise between susceptibility, biomolecules capturing, non-specific adsorption and steric hinderance had to be made in order to choose the best label option. On the other hand, the sensor sensitivity to magnetic fields was also optimized. This parameter depends essentially on the sensor structure, dimensions and type. Two different magnetoresistive sensors, spin valve and magnetic tunnel junction, were evaluated. Their signal-to-noise ratio was analyzed and compared in order to determine the best design conditions. Furthermore, the sensor structure and dimensions were optimized to obtain sensors with linear response and optimum sensor-labels interaction. Moreover, different sensor dimensions were used depending on the final application of the biochip. Biochips with optimized biological probe location, label positioning, signal detection and robustness were designed while enabling them to be integrated with other platforms, namely microfluidics and electronics. Different detection architectures were also studied in order to retrieve a maximum signal from these biochips while not compromising their integrability. Finally, DNA probe immobilization and target hybridization protocols with high specificity and low non-specific adsorption were optimized.

Magnetoresistive biochips were further integrated in platforms mainly to ensure portability, rapidness and user-friendliness. Since some applications require large a number of sensors, a matrix-based biochip architecture was designed, fabricated and characterized. This architecture allows for the fully scalability of the biochip without compromising its overall dimensions and complexity. After fabrication and testing, a noise characterization of the devices comprised in this architecture was achieved. Although presenting an increase of noise, matrix-based biochips are still sensitive enough to detect small amounts of magnetic particles.

A step towards portability was also achieved by integrating magnetoresistive biochips in a portable electronic platform. This portable platform performs the control and acquisition of the signals generated by magnetoresistive sensors. The acquired signals are then sent to a computer via USB or Bluetooth and further analyzed in a user-friendly software. A fluidic channel was further incorporated in order to improve the reproducibility and the rapidness of the system. The limit of detection of a spin valve biochip was determined and improved by focusing the labeled molecules to the sensing area.

Finally, a step towards the integration of magnetoresistive biochips with an EWOD-PCR system was made. A biochip microfabrication process was optimized in order to fulfill the requirements of EWOD systems. Experimental results demonstrate the compatibility of the biochip and the EWOD system.

Although along this thesis a big step was accomplished on the integration of magnetoresistive biochip, there are still some issues that have to be addressed before having a commercial device. For instance, the developed microfluidic system is still very primitive and only allows the injection of fluids over the biochip. In order to have a fully integrated biochip, a microfluidic system must be designed for target molecule labeling and extraction from a real sample. This can be achieved using magnetic separators, which are already being investigated namely for cell separation.

Furthermore, the integration with EWOD system and specially with a PCR system was not completely achieved. Biochips fabricated with the optimized process still have to be tested in real bioassays. The detection of DNA hybridization in this configuration has to be done.

On the other hand, the optimized magnetic sensors still need to be integrated in a matrix-based architecture. Bioassays involving microspotting different probes on top of each sensors and the detection of genomic or PCR product DNA has to be achieved.

Finally, competitive applications for these magnetoresistive DNA biochips have to be found. Usually gene expression and gene mutations detection require several sensors. Therefore, this would be a good application for fully scalable matrix-based biochips. New applications involving DNA detection are emerging. A very challenging and innovative application is the detection of cell free DNA (cfDNA) in blood for cancer diagnostic and monitoring. Cell free DNA are free DNA strands circulating in human blood. These strands have their origin in cells which died either by necrosis or apoptosis. Since the apoptosis dying process includes fragmentation of the cells DNA, by detecting specifics zones (e.g. ALU sequences) of the cfDNA it is possible to determine the ratio between cells dying by apoptosis or necrosis, which is expected to dramatically change in individuals suffering from cancer. The DNA biochip platform developed in this thesis can therefore potentially be used in the detection of cfDNA for cancer diagnostic and monitoring.

Appendix A

Spin valve biochip run sheet

Run Sheet for Spin Valve with current line below Fabrication process

RUN: #11

Filipe Cardoso/ Verónica Martins

Process Start : 06 / 06 / 2009 **Process Finish :** 26 / 06 / 2009

SV – 36SV105 MR= 7.0 % Hf= 10 Oe

Si/Al_2O_3 500/Ta 20/ NiFe 25/CoFe 25/Cu 20/CoFe 25/MnIr 60/Ta 20/TiW(N) 150

STEP 1 **1st Exposure –** Spin valve Definition Date: 06 / 06 / 2009

Coating PR: Vapor Prime 30 min (Recipe - 0) coat 1.5 μm PR (Recipe 6/2)

Machine: **DWL**

Mask: uchipl1 Map: uchip

Alignment mark position: X= 168 , Y= 55.7

56 dies in ¼ of 6'' wafer

Energy : 55

Power : 120mW

Focus : -50

Develop : Recipe 6/2 Development time : 1 min

Optical Inspection:

Sample	Comments
36SV105	OK

STEP 2 **Ion Milling –** Spin valve etching Date: 08 / 06 / 2009

Machine: N3000

345 A (etch rate: ~1 A/s → time:400s 55A of overetch)

Standard Etching Recipe (junction_etch) :
Junction_etch

Assist Gun: 65W/ 500V/-200V 10sccm Ar; 40% subst.rot 70º subst.pan

Wafer	samples	Etching Turn	Time	Effect
1	1 - 6			Contrast between metal and oxide

Assist Gun	Power (W)	V+ (V)	I+ (mA)	V- (V)	I- (mA)	Ar Flux (sccm)	Pan (deg)	Rotation (%)
Read Values	~65	~500	~20	~-200	~-1.0	10	70	40

Optical Inspection:

Sample	Comments
36SV105	OK

STEP 3 **2nd Exposure –** Contact Date: 09 / 06 / 2009

Coating PR: Vapor Prime 30 min (Recipe - 0) coat 1.5 μm PR (Recipe 6/2)

Machine: **DWL**

Mask: uchipl2 Map: uchip

Alignment mark position: X= 168 , Y= 55.7

56 dies in ¼ of 6'' wafer

Energy : 55

Power : 120mW

Focus : -50

Develop : Recipe 6/2 Development time : 1 min

Optical Inspection:

Sample	Comments
36SV105	1 die not well developed

STEP 4 **Contacts deposition** Date: 09 / 06 / 2009

Machine: **Nordiko 7000**

Seq.48 (svpad) – mod.2 – f.9 (1' soft sputter etch) P=60W/40W, p=3mTorr, 50 sccm Ar
mod.4 – f.1 (3000A Al, 1'20'') P=2 kW, 3mTorr, 50 sccm Ar
mod 3 – f.19 (150A TiW, 27'') P=0.5 kW, 3mTorr, 50sccm Ar + 10 sccm N_2

Readings – Module 2					
Run#	Power1	Power2	Gas flux	Pressure	
14149	F40R0	F59R6B145	50.0 sccm	3.0 mT	

Readings – Module 4					
Run#	Power	Voltage	Current	Gas flux	Pressure
14149	2.00 kW	394 V	5.1 A	50.5 sccm	3.0 mT

Readings – Module 3					
Run#	Power	Voltage	Current	Gas flux	Pressure
14149	0.5 kW	432 V	1.2 A	50.5 sccm (Ar) + 10.6 sccm (N_2)	3.0 mT

STEP 5 **Aluminum Lift-Off** Date: 09-16 / 06 / 2009

Hot μ-strip + ultrasonic
Rinse with IPA + DI water + dry N_2

Started: 09/06/2009 Stoped: 16/06/2009

Total Time in hot μ-strip : _____ Ultrasonic Time : 3-4h (in total)

Optical inspection:

Sample	Comments
36SV105	Lift-off completed in the whole sample

STEP 6 **3rd Exposure –** passivation layer Date: 16 / 06 / 2009

Coating PR: Vapor Prime 30 min (Recipe - 0) coat 1.5 μm PR (Recipe 6/2)

Machine: **DWL**

Mask: uchipl3 Map: uchip

Alignment mark position: X= 168 , Y= 55.7

56 dies in ¼ of 6'' wafer

Energy : 55

Power : 120mW

Focus : -50

Develop : Recipe 6/2 Development time : 1 min

Optical Inspection:

Sample	Comments
36SV105	OK

STEP 7 **Passivation Layer Deposition** Date: 18 / 06 / 2009

1- Al_2O_3 deposition

Machine: **UHV2**
1h30 (1000A) 200W
B.P. : 4.4 x 10^{-7} Torr

Deposition Time	Al_2O_3 thickness	Ar gas flow	Pressure	Power Source
1h30 min	1000 A	45 sccm	1.2 mT	200 W

2- SiO_2 deposition

Machine: **Alcatel**

Deposition Time	Al_2O_3 thickness	Turbo Pump Frequency	Base Pressure	Power Source
1h28min	2000 A	20 sccm	3.9 mT	140 W

STEP 8 **Oxide Lift-Off** Date: 22 - 24 / 06 / 2009

Hot μ-strip + ultrasonic
Rinse with IPA + DI water + dry N_2

Started: 18h of 22/06/2009 Stoped:14h of 24/06/2009

Total Time in hot μ-strip : _____ Ultrasonic Time : 5 x 2min

Optical inspection:

Sample	Comments
36SV105	OK

STEP 9 **4th Exposure –** Au pad for chemistry Date: 25 / 06 / 2009

Coating PR: Vapor Prime 30 min (Recipe - 0) coat 1.5 μm PR (Recipe 6/2)

Machine: **DWL**

Mask: uchipl4 Map: uchip

Alignment mark position: X= 168 , Y= 55.7

56 dies in ¼ of 6'' wafer

Energy : 55

Power : 120mW

Focus : -50

Develop : Recipe 6/2 Development time : 1 min

Optical Inspection:

Sample	Comments
36SV105	OK

STEP 10 **MTJ top Au contact** Date: 26 / 06 / 2009

Machine: **Alcatel**

50 A Cr/ 200 A Au

Material	Power	Gas flux (Ar)	Pressure	Time	Base pressure
Cr	20 Wdc	20 sccm	3.25 mT	1 min	4 x10^{-7} T
Au	10 Wrf	20 sccm	3.25 mT	5 min	4 x10^{-7} T

STEP 11 **Au lift-off** Date: 26 / 06 / 2009

Hot μ-strip + ultrasonic
Rinse with IPA + DI water + dry compressed air

Started: 11h Stoped 21h

Total Time in hot μ-strip : 10h Ultrasonic Time : 3 x 2min

Optical inspection:

Sample	Comments
36SV105	OK

Appendix B

MTJ biochip with Al contacts run sheet

Run Sheet for JUNCTION Fabrication process

RUN: Filipe Cardoso

Process Start : 09 / 08 /07 **Process Finish :** 18 / 08 / 07

MTJ sample – N2TJF01 (deposited in N2000 by Piotr Wisniowski)

STEP 4 **1st Exposure –** Main Pillar Definition Date: 09 / 08 / 07

Coating PR: Vapor Prime 30 min (Recipe - 0) coat 1.5 μm PR (Recipe 6/2)

Machine: **DWL**

Mask: biotjl1 + biotjtestl1 Map: uchip

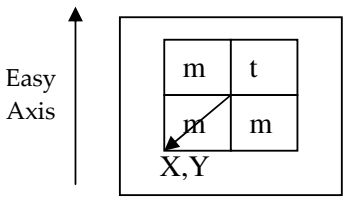

Origin: X= -5100 , Y= -3100

Energy : 80%

Power : 120mW

Focus : -50

Develop : Recipe 6/2 Development time : 1 min

Optical Inspection:

Sample	Comments
N2TJF01	First trial had 5 shift; the PR was removed in the tracks with program 8/6; New lithography made after coating; Lithography ok this time

STEP 5 **1st Ion Milling –** Total Structure Etch Date: 09/ 08 / 07

Machine: N3600

Total thickness to etch: 835 A (etch rate: ~1 A/s → time: 1000 s overetch of 155A)

Standard Etching Recipe (Junction Etch):

Etch junction stack all

Assist Gun: 105 mA +750V/-350V 12sccm Ar; Assist Neut ; 30% subst.rot ,60º subst.pan

Etching Turn	Time	Effect
1	4x250s	Etched until the glass – Sample transparent except in the areas protected by the PR
2		
3		

Assist Gun	Power (W)	V+ (V)	I+ (mA)	V- (V)	I- (mA)	Ar Flux (sccm)	Pan (deg)	Rotation (%)
Read Values	202	724.5	104.8	345.3	2.7	10.2	60	30

STEP 6 **Resist Strip** Date: 09/ 08 / 07

Hot Micro-Strip + Ultrasonic
Rinse with IPA + DI water + dry compressed air

Started: 11h15 Stoped: 15h15

Total Time in Hot Micro-Strip : 4h Ultrassonic Time : 3x2min

Optical Inspection:

Sample	**Comments**
N2TJF01	All resist removed - resist strip OK

STEP 7 **2nd Exposure –** Top Electrode and Junction Definition Date: 09 / 08 / 07

Coating PR: Vapor Prime 30 min (Recipe - 0) coat 1.5 μm PR (Recipe 6/2)

Machine: **DWL**

Mask: biotjl2 + biotjtestl2 Map: uchip

Alignment mark position: X= 168 , Y= 55.7

Easy Axis

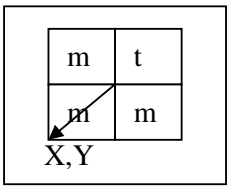

Energy : 80

Power : 120mW

Focus : -50

Develop : Recipe 6/2 Development time : 1 min

Optical Inspection:

Sample	Comments
N2TJF01	Needed more 30s of revelations - OK

STEP 8 **2nd Ion Milling –** Top Electrode and Junction Definition Date: 09 / 08 / 07

Machine: N3600

373A (etch rate: ~1 A/s → time: 400s overetch 27A)

Standard Etching Recipe (Junction etch):
Etch junction top electrode

Assist Gun: 105mA +750V/-350V 12sccm Ar; Assist Neut ; 30% subst.rot 30º subst.pan

Calibration Sample	Structure
#1	CoFe 20/Ru 8/CoFeB 30/MgO 15/CoFe 50/ Ru 50/ Ta 50/TiW(N) 150

Wafer	samples	Etching Turn	Time	Effect
1	1 - 6	1	2x150s @ 60º + 100s @ 30º	Calibration sample etched - OK

Assist Gun	Power (W)	V+ (V)	I+ (mA)	V- (V)	I- (mA)	Ar Flux (sccm)	Pan (deg)	Rotation (%)
Read Values	212	724.3	104.5	344.3	2.7	10.2	60 & 30	30

Optical Inspection:

Sample	Comments
N2TJF01	OK

STEP 9 **Insulating Layer Deposition** Date: 10 / 08 / 07

Responsible: **Fernando**
Machine: **UHV2**

Deposition Time	Al_2O_3 thickness	Ar gas flow	Pressure	Power Source
30 min	500 A	45 sccm	5.2×10^{-7} Torr	200 W

Sample	Comments
N2TJF01	OK

STEP 10	**Oxide Lift-Off**	Date: 10-12 / 08 / 07

Hot μ-strip + ultrasonic
Rinse with IPA + DI water + dry compressed air

Started: 14h (10/08/07) Stoped: 17h (12/08/09)

Total Time in hot μ-strip : 24h Ultrasonic Time : 10 x 2min

Optical inspection:

Sample	Comments
N2TJF01	OK – except 2 sensors in the test dye

STEP 11	**3rd Exposure –** Contact	Date: 13 / 08 / 07

Coating PR: Vapor Prime 30 min (Recipe - 0) coat 1.5 μm PR (Recipe 6/2)

Machine: **DWL**

Mask: biotjl3 + biotjtestl3 Map: uchip

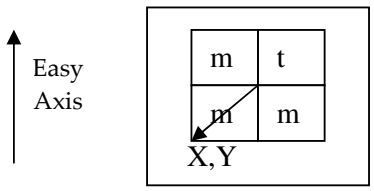

Alignement mark position : X= 168 , Y= 55.7

Energy : 80

Power : 120mW

Focus : -50

Develop : Recipe 6/2 Development time : 1 min

Optical Inspection:

Sample	Comments
N2TJF01	One die had 1 shift; the PR was removed in the tracks with program 8/6; New lithography made after coating; Lithography ok this time

STEP 12	**Contact Leads Deposition (junction top electrode)**	Date: 13 / 08 / 07

Machine: **Nordiko 7000**

Seq.48 (svpad) – mod.2 – f.9 (1' soft sputter etch) P=60W/40W, p=3mTorr, 50 sccm Ar

mod.4 – f.1 (3000A Al, 1'20'') P=2 kW, 3mTorr, 50 sccm Ar
mod 3 – f.19 (150A TiW, 27'') P=0.5 kW, 3mTorr, 50sccm Ar + 10 sccm N_2

Readings – Module 2					
Run#	Power1	Power2	Gas flux	Pressure	
12284	F40R0	F59R6B145	50.1sccm	3.0 mT	

Readings – Module 4					
Run#	Power	Voltage	Current	Gas flux	Pressure
12284	2 kW	402 V	5.0 A	50.0 sccm	3.0 mT

Readings – Module 3					
Run#	Power	Voltage	Current	Gas flux	Pressure
12284	0.5 kW	433 V	1.2 A	50.4 sccm (Ar)+ 10.8 sccm (N_2)	3.0 mT

STEP 13 **Al lift-off** Date: 13 / 08 / 07

Hot μ-strip + ultrasonic
Rinse with IPA + DI water + dry compressed air

Started: 20h00 Stoped: 21h55

Total Time in hot μ-strip : 1h55 Ultrasonic Time : 2 x 2s

Optical inspection:

Sample	Comments
N2TJF01	OK

STEP 14	**4th Exposure –** passivation	Date: 15 / 08 / 07

Coating PR: Vapor Prime 30 min (Recipe - 0) coat 1.5 μm PR (Recipe 6/2)

Machine: **DWL**

Mask: biotjl4 + biotjtestl4 Map: uchip

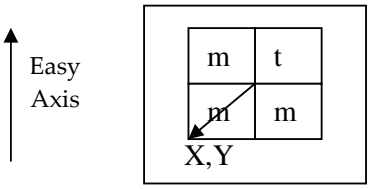

Alignement mark position : X= 168 , Y= 55.7

Energy : 80

Power : 120mW

Focus : -50

Develop : Recipe 6/2 Development time : 1 min

Optical Inspection:

Sample	Comments
N2TJF01	OK

STEP 15	**Insulating Layer Deposition**	Date: 16/ 08 / 07

Responsible: **Fernando**
Machine: **UHV2**
B.P.: 2.9 x 10^{-7}Torr

Deposition Time	Al_2O_3 thickness	Ar gas flow	Pressure	Power Source
60 min	1000 A	45 sccm	3.0 mT	200W

Sample	Comments
N2TJF01	OK

STEP 16	**Insulating Layer Deposition**	Date: 18 / 08 / 07

Responsible: **Fernando**
Machine: **Alcatel**

Deposition Time	SiO_2 thickness	Ar gas flow	Pressure	Power Source
1h28min	2000 A	20 sccm	3.9 mT	140 W

Sample	Comments
N2TJF01	OK

STEP 17	**Oxide lift-off**	Date: 18 / 08 / 07

Hot μ-strip + ultrasonic
Rinse with IPA + DI water + dry compressed air

Started: 17h Stoped: 21h

Total Time in hot μ-strip : 4h Ultrasonic Time : 2 x 2min

Optical inspection:

Sample	Comments
N2TJF01	OK

Appendix C

MTJ biochip with Au contacts run sheet

Run Sheet for JUNCTION Fabrication process

RUN: Filipe Cardoso

Process Start : 07 / 02 / 2010 **Process Finish :** 16/02/2010

STEP 1	Substrate preparing	Date: 07 / 02 / 2010

Put 1x1 inch^2 Corning glass piece in Alconox and 10 minutes of Ultra-Sounds.

Wash the sample with DI water and blow dry with compressed air gun to remove all the DI water.

STEP 2	Deposition of the magnetoresistive sensor	Date: 07 / 02 / 2010

Machine: **Nordiko 2000**
B.P.: 7.5 x 10^{-8} Torr

Seq 2: pre-sputtering of all target x2

# BioMTJ13						
Material	Time	Voltage	Power	Pressure	Gas flow	Separation
Ta 50	40 mA	343 V	10 W	4.6 mT	9.8 sccm	100%
Ru 180	40 mA	311 V	10 W	5.2 mT	7.8 sccm	100%
Ta 30	40 mA	337 V	10 W	4.6 mT	9.8 sccm	100%
MnPt 200	30 mA	294 V	-	5.1 mT	8.7 sccm	100%
CoFe 20	F34 R0B309	-	-	5.2 mT	7.8 sccm	100%
Ru 9	40 mA	302 V	10 W	5.3 mT	7.8 sccm	100%
CoFeB 30	40 mA	420 V	10 W	5.2 mT	8.8 sccm	100%
MgO cleaning	F149 R0 B307	-	-	5.0 mT	9.7 sccm	100%
MgO 15	F129 R0 B283	-	-	18.0 mT	9.5 sccm	50%
CoFeB 100	40 mA	418 V	10 W	5.2 mT	8.8 sccm	100%
Ru 50	40 mA	313 V	10 W	5.1 mT	7.7 sccm	100%
Ta 50	40 mA	339 V	10 W	4.6 mT	9.8 sccm	100%

STEP 3	150A of TiW (N2) deposition	Date: 07 / 02 / 2010

Machine: **Nordiko 7000**
Seq.48 (svpad) – mod.2 – f.9 (1' soft sputter etch) P=60W/40W, p=3mTorr, 50 sccm Ar
mod.4 – f.1 (650A Al, 18'') P=2 kW, 3mTorr, 50 sccm Ar

Readings – Module 2			
Power1	Power2	Gas flux	Pressure
F40R0	F59R6B145	50.1sccm	3.0 mT

Readings – Module 4				
Power	Voltage	Current	Gas flux	Pressure
2 kW	402 V	5.0 A	50.0 sccm	3.0 mT

STEP 4 **1st Exposure –** Main Pillar Definition Date: 08 / 02 / 2010

Coating PR: Vapor Prime 30 min (Recipe - 0) coat 1.5 μm PR (Recipe 6/2)

Machine: **DWL**

Mask: pcbchipl1 Map: uchip

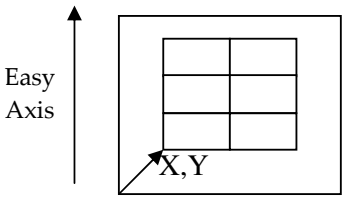

Origin: X= 5100 , Y= 3100

Energy : 80

Power : 120mW

Focus : -50

Develop : Recipe 6/2 Development time : 1 min

Optical Inspection:

Sample	Comments
BioMTJ13	Needed more 30s of revelations - OK

STEP 5 **1st Ion Milling –** Total Structure Etch Date: 08 / 02 / 2010

Machine: N3600

Total thickness to etch: 884 A (etch rate: ~ A/s → time: 1000s 116 A of overetch)

Standard Etching Recipe (Junction Etch) :

Etch junction stack all

Assist Gun: 105 mA +750V/-350V 12sccm Ar; Assist Neut ; 30% subst.rot ,60º subst.pan

Etching Turn	Time	Effect
1	5 x 200s	Sample transparent except in the structures protected with PR
2		
3		

Assist Gun	Power (W)	V+ (V)	I+ (mA)	V- (V)	I- (mA)	Ar Flux (sccm)	Pan (deg)	Rotation (%)
Read Values	228	723.8	104.6	344.5	2.7	10.2	60	30

STEP 6 **Resist Strip** Date: 08 / 02 / 2010

Hot Micro-Strip + Ultrasonic
Rinse with IPA + DI water + dry compressed air

Started: 11h00 Stoped: 16h00

Total Time in Hot Micro-Strip : 5h Ultrassonic Time : 2 x 2min

Optical Inspection:

Sample	Comments
BioMTJ13	OK

STEP 7 **2nd Exposure –** Top Electrode and Junction Definition Date: 08 / 02 / 2010

Coating PR: Vapor Prime 30 min (Recipe - 0) coat 1.5 μm PR (Recipe 6/2)

Machine: **DWL**

Mask: pcbchipl2 Map: uchip

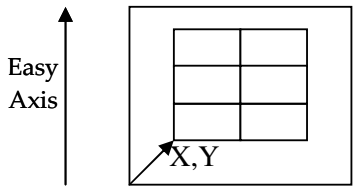

Alignment mark position: X= 168 , Y= 55.7

Energy : 80

Power : 120mW

Focus : -50

Develop : Recipe 6/2 Development time : 1 min

Optical Inspection:

Sample	Comments
BioMTJ13	OK

STEP 8 **2nd Ion Milling –** Top Electrode and Junction Definition Date: 08 / 02 / 2010

Machine: N3600
Top electrode+barrier+SAF 423A (etch rate: ~ 1 A/s → time:450s 27 A of overetch)

Base Pressure (Torr): ____

Standard Etching Recipe (Etch Junction Top electrode) :
Etch junction top electrode

Assist Gun: 105mA +750V/-350V 12sccm Ar; Assist Neut ; 30% subst.rot 60º and 30º subst.pan

Calibration Sample	Structure
#1	CoFe 20/Ru 9/ CoFeB 30/ MgO 15/ CoFeB 100/Ru 50/Ta 50/TiW 150

Wafer	samples	Etching Turn	Time	Effect
1	1 - 6	1	2x 175s @ 60º + 100s @ 30º	There is still a shadow in the calibration sample
		2	50s @ 30º	Calibration sample transparent – etch OK

Assist Gun	Power (W)	V+ (V)	I+ (mA)	V- (V)	I- (mA)	Ar Flux (sccm)	Pan (deg)	Rotation (%)
Read Values	235	723.8	104.6	344.5	2.7	10.2	60 & 30	30

Optical Inspection:

Sample	Comments
BioMTJ13	OK

STEP 9 **Insulating Layer Deposition** Date: 10 / 02 / 2010

Responsible: **Fernando**
Machine: **UHV2**
B.P.: 3.2 x 10^{-7} Torr

Deposition Time	Al_2O_3 thickness	Ar gas flow	Pressure	Power Source
60 min	1000 A	45 sccm	3.0 mT	200W

Sample	Comments
BioMTJ13	OK

STEP 10	**Oxide Lift-Off**	Date: 10 -12 / 02 / 2010

Hot μ-strip + ultrasonic
Rinse with IPA + DI water + dry compressed air

Started: 14h (10/08/07) Stoped: 17h (12/08/09)

Total Time in hot μ-strip : 24h Ultrasonic Time : 10 x 2min

Optical inspection:

Sample	Comments
BioMTJ13	OK

STEP 11	**3rd Exposure –** Contact	Date: 12 / 02 / 2010

Coating PR: Vapor Prime 30 min (Recipe - 0) coat 1.5 μm PR (Recipe 6/2)

Machine: **DWL**

Mask: pcbchipl3 Map: uchip

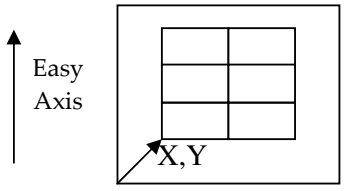

Alignement mark position : X= 168 , Y= 55.7

Energy : 80

Power : 120mW

Focus : -50

Develop : Recipe 6/2 Development time : 1 min

Optical Inspection:

Sample	Comments
BioMTJ13	OK

STEP 12 **MTJ top Au contact** Date: 13/02/2010

Machine: **Alcatel**

50 A Ti/2000 A Au

Material	Power	Gas flux (Ar)	Pressure	Time	Base pressure
Cr	20 Wdc	20 sccm	3.25 mT	1 min	4 x10^{-7} T
Au	10 Wrf	20 sccm	3.25 mT	50 min	4 x10^{-7} T

STEP 13 **Au lift-off** Date: 13/02/2010

Hot μ-strip + ultrasonic
Rinse with IPA + DI water + dry compressed air

Started: 12h30 Stoped: 16h00

Total Time in hot μ-strip : 3h30 Ultrasonic Time : 2 x 5 min

Optical inspection:

Sample	Comments
BioMTJ13	OK

STEP 14 **4th Exposure –** Passivation Date: 13/02/2010

Coating PR: Vapor Prime 30 min (Recipe - 0) coat 1.5 μm PR (Recipe 6/2)

Machine: **DWL**

Mask: pcbchipl4 Map: uchip

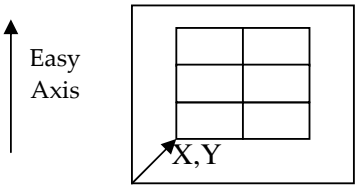

Alignement mark position : X= 168 , Y= 55.7

Energy : 80

Power : 120mW

Focus : -50

Develop : Recipe 6/2 Development time : 1 min
Optical Inspection:

Sample	Comments
BioMTJ13	Needed more 20s of revelations - OK

STEP 15	**Passivation Layer Deposition**	Date: 13-16/02/2010

1- Al_2O_3 deposition

Machine: **UHV2**

B.P: 2 x 10^{-7} Torr

Deposition Time	**Al_2O_3 thickness**	**Ar gas flow**	**Pressure**	**Power Source**
1h30 min	1000 A	45 sccm	3.0 mT	200W

2- SiO_2 deposition

Machine: **Alcatel**

Deposition Time	**SiO_2 thickness**	**Ar gas flow**	**Pressure**	**Power Source**
1h28min	2000 A	20 sccm	3.9 mT	140 W

STEP 16	**Oxide Lift-Off**	Date: 16/02/2010

Hot μ-strip + ultrasonic
Rinse with IPA + DI water + dry N_2

Started: 13h Stoped: 17h

Total Time in hot μ-strip : 4h Ultrasonic Time : 2 x 2min

Optical inspection:

Sample	**Comments**
BioMTJ13	OK

Appendix D

Matrix-based biochip run sheet

Run Sheet for DIODE+JUNCTION Fabrication process

RUN: DTJ 7 Filipe Cardoso

Process Start : 22/05/2007 **Process Finish :** 14/ 06/2007

MTJ – N2TJ85 (deposited in N2000 by Piotr Wisniowski)

STEP 4 **1st Exposure –** Main Pillar Definition Date: 22/05/2007

Coating PR: Vapor Prime 30 min (Recipe - 0) coat 1.5 μm PR (Recipe 6/2)

Machine: **DWL**

Mask: dtjml1 and dtjtl1 Map: DTJ

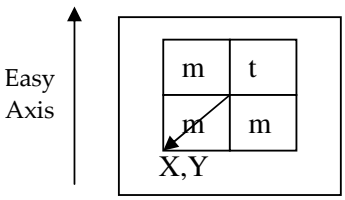

Origin: X= -8200 , Y= -8200

Energy : 47.5

Power : 120mW

Focus : +25

Develop : Recipe 6/2 Development time : 1 min

Optical Inspection:

Sample	Comments
N2TJ85	Small shift on die 3: resist strip and new litography done -> OK

STEP 5 **1st Ion Milling –** Total Structure Etch Date: 22 / 05 / 2007

Machine: N3600

Total thickness to etch: 835 A (etch rate: ~1 A/s → time: 1000 s overetch of 155A)

Standard Etching Recipe (Junction Etch):

Etch junction stack all

Assist Gun: 105 mA +750V/-350V 12sccm Ar; Assist Neut ; 30% subst.rot ,60º subst.pan

Etching Turn	Time	Effect
1	850s	A little shadow
2	150s	OK
3		

Assist Gun	Power (W)	V+ (V)	I+ (mA)	V- (V)	I- (mA)	Ar Flux (sccm)	Pan (deg)	Rotation (%)
Read Values	202	724.5	104.8	345.3	2.7	10.2	60	30

STEP 6 **Resist Strip** Date: 22/05 /2007

Hot Micro-Strip + Ultrasonic
Rinse with IPA + DI water + dry compressed air

Started:20h30 Stoped:23h00

Total Time in Hot Micro-Strip : 2h30 Ultrassonic Time : 2min

Optical Inspection:

Sample	**Comments**
N2TJ85	OK

STEP 7 **2nd Exposure –** Top Electrode and Junction Definition Date: 25/05/2007

Coating PR: Vapor Prime 30 min (Recipe - 0) coat 1.5 μm PR (Recipe 6/2)

Machine: **DWL**

Mask: dtjml2 and dtjtl2 Map: DTJ

Easy Axis

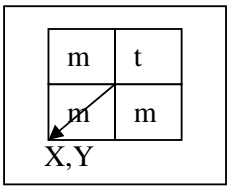

Alignment mark position: X= 168 , Y= 55.7

Energy : 47.5

Power : 120mW

Focus : +25

Develop : Recipe 6/2 Development time : 1 min

Optical Inspection:

Sample	**Comments**
N2TJ85	OK

STEP 8 **2nd Ion Milling –** Top Electrode and Junction Definition Date: 25/05 /2007

Machine: N3000
423A (etch rate: 1A/s → time: 450 s)

Standard Etching Recipe (junction_etch) :
Junction_etch

Assist Gun: 65W/ 500V/-200V 10sccm Ar; 40% subst.rot 70º and 40º subst.pan

Wafer	samples	Etching Turn	Time	Effect
1	1 - 6		200s@70º + 150s@40º	A little shadow
			50s@70º + 50s@40º	etched

Assist Gun	Power (W)	V+ (V)	I+ (mA)	V- (V)	I- (mA)	Ar Flux (sccm)	Pan (deg)	Rotation (%)
Read Values	~65	~500	~20	~-200	~-1.0	10	70 & 40	40

Optical Inspection:

Sample	Comments
N2TJ85	OK

STEP 9 **Insulating Layer Deposition** Date: 26/05/2007

Responsible: **Fernando**
Machine: **UHV2**
B.P.: 5.5×10^{-7} Torr

Deposition Time	Al_2O_3 thickness	Ar gas flow	Pressure	Power Source
30 min	500 A	45 sccm	3.0 mT	200 Wrf

Comments: Ok

STEP 10 **Oxide Lift-Off** Date: 26/05/2007

Hot μ-strip + ultrasonic
Rinse with IPA + DI water + dry compressed air

Started: 18h00 Stoped:23h00 (3 days after)

Total Time in hot μ-strip : 20h Ultrasonic Time : a lot

Optical inspection:

Sample	Comments
N2TJ85	2 or 3 MTJ per matrix are still with resist – OK to continue

STEP 11 **Contact leads Deposition** Date: 29/05/2007
(Diode Bottom electrode & junction top electrode)

Machine: **Nordiko 7000**

Seq.48 (svpad) – mod.2 – f.9 (1' soft sputter etch) P=60W/40W, p=3mTorr, 50 sccm Ar
mod.4 – f.1 (2000A Al, 54'') P=2 kW, 3mTorr, 50 sccm Ar
mod 3 – f.19 (150A TiW, 27'') P=0.5 kW, 3mTorr, 50sccm Ar + 10 sccm N_2

Readings – Module 2					
Run#	Power1	Power2	Gas flux	Pressure	
12086	F40R0	F59R6B145	50.1sccm	3.0 mT	

Readings – Module 4					
Run#	Power	Voltage	Current	Gas flux	Pressure
12086	2 kW	402 V	5.0 A	50.0 sccm	3.0 mT

Readings – Module 3					
Run#	Power	Voltage	Current	Gas flux	Pressure
12086	0.5 kW	433 V	1.2 A	50.4 sccm (Ar)+ 10.8 sccm (N_2)	3.0 mT

STEP 12 **3rd Exposure – Column (junction top contact) + current line definition** Date: 29/05/2007

Coating PR: Vapor Prime 30 min (Recipe - 0) coat 1.5 μm PR (Recipe 6/2)

Machine: **DWL**

Mask: dtjml3 and dtjl3 Map: DTJ

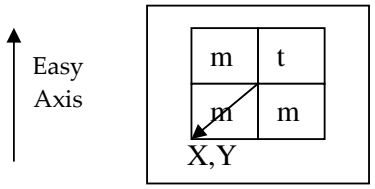

Alignement mark position : X= 168 , Y= 55.7

Energy : 47.5

Power : 120mW

Focus : +25

Develop : Recipe 6/2 Development time : 1 min

Optical Inspection:

Sample	Comments
N2TJ85	OK

STEP 13 **Lead Etching– Column (junction top contact) + current line definition** Date: 29/05/2007

1- Machine: N3600

Total thickness to etch: 150 A (etch rate: ~1 A/s → time: 250 s overetch of 100A)

Standard Etching Recipe (Junction Etch):

Etch junction stack all

Assist Gun: 105 mA +750V/-350V 12sccm Ar; Assist Neut ; 30% subst.rot ,60º subst.pan

Etching Turn	Time	Effect
1	250s	Etched TiW until the Al
2		
3		

Assist Gun	Power (W)	V+ (V)	I+ (mA)	V- (V)	I- (mA)	Ar Flux (sccm)	Pan (deg)	Rotation (%)
Read Values	155	724.5	104.8	345.0	2.4	10.3	60	30

2- Wet etch

Time: 5 min etch rate: 500 A/min

Sample	Comments
N2TJ85	Etched until the glass

STEP 14 **Resist Strip** Date: 30/05/2007

Hot μ-strip + ultrasonic
Rinse with IPA + DI water + dry compressed air

Started: 12h00 Stoped: 16h30

Total Time in hot μ-strip : 2h30 Ultrasonic Time : 5 min

Optical inspection:

Sample	Comments
N2TJ85	OK

Annealing of the sample:

Rising slope: 5ºC/min Temperature: 280 ºC Time: 1h

Measurements of the MTJ in the test die (manual setup):

RxA ≈ 60 kΩ.μm² Linearity? ▪ yes(1 x 40 μm²) □ no TMR: 50-70 %

Measurements of the metal layer crossing L1 with L3

Shorted? □ yes ▪ no R_{L3} = 428 Ω (for L3 with L6 crossing tests)

Sample ready to continue process? ▪ yes □ no

STEP 15	Diode deposition	Date: 05 /06/2007

Equipment: UHV chamber
Responsible: J.P. Conde, V. Chu

200 °A p+ doped a-Si:H + 5000 °A intrinsic a-Si:H + 200 °A n+ doped a-Si:H by PECVD

Set points:

Material	Power	Gas Flow	Pressure	Time	Temperature
p+-a-Si:H	5WRF	SiH4+B2H6/N2 10+5sccm	0,1 Torr	200 s	250°C
i-a-Si:H	5WRF	SiH4 10sccm	0,1 Torr	1h 00min 50s	250°C
n+-a-Si:H	5WRF	SiH4+PH3 10+5sccm	0,1 Torr	200 s	250°C

Read values:

Material	Power	Gas Flow	Pressure	Time	Temperature
p+-a-Si:H	5 Wrf	50.1 sccm + 10 sccm	100 mT	3min 20s	220 ºC
i-a-Si:H	5 Wrf	10 sccm	100 mT	1h00 50s	250 ºC
n+-a-Si:H	5 Wrf	50.1 sccm + 10 sccm	100 mT	3min 20s	250 ºC

Comments:
Cooling the camara until 65ºC before remove the sample

STEP 16	**4th Exposure –** Diode Definition	Date: 05/06/2007

Coating PR: Vapor Prime 30 min (Recipe - 0) coat 1.5 μm PR (Recipe 6/2)

Machine: **DWL**

Mask: dtjml4 and dtjtl4 Map: DTJ

Alignment mark position: X = 168, Y = 55.7

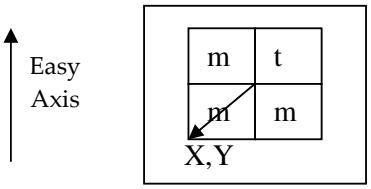

Energy : 47.5

Power : 120mW

Focus : + 25

Develop : Recipe 6/2 Development time : 1 min
Optical Inspection:

Sample	Comments
N2TJ85	OK

STEP 17 **Diode stack definition** Date: 06/06/2007

Diode Pillar etch by reactive ion etching (RIE)
Equipment: LAM Rainbow 4400

Process recipe: 6

Set points:

Power	Gas Flow	Pressure	Time
100 W (RF)	Ar+CF4+O2 200+100+10 sccm	140 mTorr	350 s

Read values:

Power	Gas Flow	Pressure	Time
100 Wrf	200+100+10 sccm	140 mT	150s+150s+150s+50s

Sample	Comments
N2TJ85	Sample etched until glass - OK

STEP 18 **Resist Strip** Date: 06/06/2007

Hot Micro-Strip + Ultrasonic
Rinse with IPA + DI water + dry N_2

Started:12h00 Stoped: 14h00
Total Time in Hot Micro-Strip : 2h Ultrassonic Time : 2min

Optical Inspection:

Sample	Comments
N2TJ85	OK

STEP 19	**5th Exposure –** Diode area definition	Date: 06/06/2007

Coating PR: Vapor Prime 30 min (Recipe - 0) coat 1.5 μm PR (Recipe 6/2)

Machine: **DWL**

Mask: dtjml5 and dtjtl5 Map: DTJ

Alignment mark position: X = 168, Y = 55.7

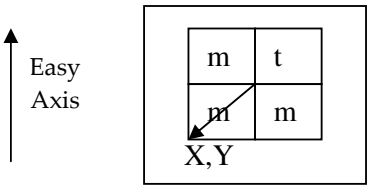

Energy : 47.5

Power : 120mW

Focus : +25

Develop : Recipe 6/2 Development time : 1 min

Optical Inspection:

Sample	Comments
N2TJ85	OK

STEP 20	**Insulating Layer Deposition**	Date: 07/06/2007

Machine: **UHV2**
2h30 (2500A) 200W

B.P: 5.1 x 10^{-7} Torr

Deposition Time	AlO_2 thickness	Gas flow	Pressure	Power Source
2h30 min	2500 A	45.1 sccm	3.1 mT	200W

STEP 21	**Oxide Lift-Off**	Date: 07/06/2007

Hot μ-strip + ultrasonic
Rinse with IPA + DI water + dry N_2

Started: 14h50 Stoped: 21h50

Total Time in hot μ-strip : 7h Ultrasonic Time : 5min

Optical inspection:

Sample	Comments
N2TJ85	OK

STEP 22 **6th Exposure –** Row (Diode contact) definition Date: 08/06/2007

Coating PR: Vapor Prime 30 min (Recipe - 0) coat 1.5 μm PR (Recipe 6/2)

Machine: **DWL**

Mask: dtjml6 and dtjtl6

Map: DTJ
Alignment mark position: X = 168, Y = 55.7

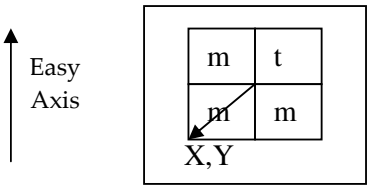

Energy : 47.5

Power : 120mW

Focus : +25

Develop : Recipe 6/2 Development time : 1 min
Optical Inspection:

Sample	Comments
N2TJ85	OK

STEP 23 Row (Diode contact) deposition Date: 08/06/2007

Machine: **Nordiko 7000**

Seq.33 (svpadnoetch) – mod.4 – f.1 (3000A Al, 1'20'') P=2 kW, 3mTorr, 50 sccm Ar
mod.3 – f.19 (150A Al, 27'') P=0.5 kW, 3mTorr, 50 sccm Ar + 10 sccm N_2

Readings – Module 4					
Run#	Pressure	Power	Voltage	Current	Gas Flux
12131	3.0 mT	2 kW	409 V	5.0 A	50.3 sccm

Readings – Module 3					
Run#	Pressure	Power	Voltage	Current	Gas Flux
12131	3.0 mT	0.5 kW	435 V	1.2 A	50.6 + 10.7 sccm

STEP 24	**Aluminum Lift-Off**	Date: 08/06/2007

Hot μ-strip + ultrasonic
Rinse with IPA + DI water + dry N_2

Started: 17h Stoped: 22h

Total Time in hot μ-strip : 5h Ultrasonic Time : 5 min

Optical inspection:

Sample	Comments
N2TJ85	OK

Measurements of metal layer crossing (L3 with L6

R_{L3} = 428 Ω R_{L6} = 370 Ω Shorted? □ yes ▪ no

Fuse burning test:

Burning? ▪yes □ no I_{burn}= 60 mA

Diode measurements:

Working? ▪ yes □ no $I_{rev\ bias}$= ~10^{-10} A (2V) $I_{forward\ bias}$= ~10^{-4} A (2V)

Sample ready to continue process? ▪ yes □ no

STEP 25	**7th Exposure –** Passivation	Date: 12/06/2007

Coating PR: Vapor Prime 30 min (Recipe - 0) coat 1.5 μm PR (Recipe 6/2)

Machine: **DWL**

Mask: dtjml7 and dtjtl7

Map: DTJ
Alignment mark position: X = 168, Y = 55.7

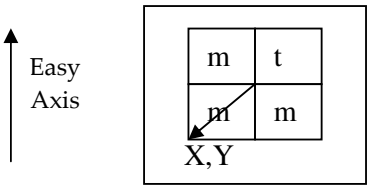

Energy : 47.5

Power : 120mW

Focus : +25

Develop : Recipe 6/2 Development time : 1 min
Optical Inspection:

Sample	Comments
N2TJ85	OK

STEP 26	**Passivation Layer Deposition**	Date: 13/06/2007

1- Al_2O_3 deposition

Machine: **UHV2**
1h30 (1000A) 200W
B.P. : 4.4 x 10^{-7} Torr

Deposition Time	Al_2O_3 thickness	Turbo Pump Frequency	Base Pressure	Power Source
1h30 min	1000 A	45 sccm	1.2 mT	200 W

2- SiO_2 deposition

Machine: **Alcatel**

Deposition Time	Al_2O_3 thickness	Turbo Pump Frequency	Base Pressure	Power Source
1h28min	2000 A	20 sccm	3.9 mT	140 W

STEP 27	**Oxide Lift-Off**	Date: 14/06/2007

Hot μ-strip + ultrasonic
Rinse with IPA + DI water + dry N_2

Started: 12h Stoped: 17h

Total Time in hot μ-strip : 5h Ultrasonic Time : 5 min

Optical inspection:

Sample	Comments
N2TJ85	OK

Appendix E

Diode run sheet

Run Sheet for DIODE p-i-n Fabrication process

RUN: D6

Filipe Cardoso

Process Start : 31/08/2006 **Process Finish :** 10/9/2006

STEP 1 **Contact Leads Deposition (Diode Bottom electrode)** Date: 31/08/2006

Machine: **Nordiko 7000**

Seq.48 (svpad) – mod.4 – f.1 (2000A Al, 54'') P=2 kW, 3mTorr, 50 sccm Ar
mod.3 - f.19 (450A $TiWN_2$, 81'') 0.5 kW, 3mTorr, 50 sccm Ar + 10sccm N_2

Readings – Module 4					
Run#	Pressure	Power	Voltage	Current	Gas Flux
11317	3.2 mT	2 kW	411 V	4.9 A	50.4 sccm

Readings – Module 3					
Run#	Pressure	Power	Voltage	Current	Gas Flux
11317	3.0 mT	0.5 kW	433 V	1.2 A	50.5 sccm (Ar) +8.2 sccm (N_2)

STEP 2 **1st Exposure –** Bottom contact definition Date: 31/08/2006

Coating PR: Vapor Prime 30 min (Recipe - 0) coat 1.5 μm PR (Recipe 6/2)

Machine: **DWL**

Mask: diodetempl1 (1), dtjt4l3 (2) Map: diode

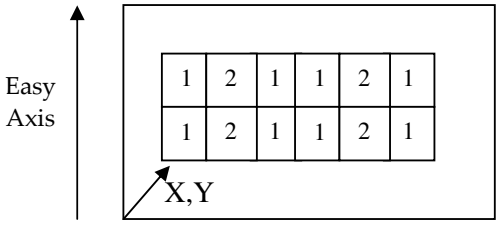

Origin: X = 6400 , Y = 6300

Energy : 60

Power : 120mW

Focus : -50

Develop : Recipe 6/2 Development time : 1 min

Optical Inspection:

Sample	Comments
D6	Needed more 15s of revelations - OK

STEP 3	**Lead Etching –** Bottom contact definition	Date: 31/08/2006

1. Ion milling

Machine: **Nordiko 3600**

Standard Etching Recipe (Junction Etch) :

Etch junction stack all

Assist Gun: 105 mA +750V/-350V 12sccm Ar; Assist Neut ; 30% subst.rot ,60º subst.pan

Etching Turn	Time	Effect
1	500 s	Ok – TiW etched
2		
3		

Assist Gun	Power (W)	V+ (V)	I+ (mA)	V- (V)	I- (mA)	Ar Flux (sccm)	Pan (deg)	Rotation (%)
Read Values	169	725.3	105.1	345.5	2.8	10.2	60	30

2. Wet etch

Time: 210s etch rate: ~11 A/s

STEP 4	**Resist Strip**	Date: 31/08/2006

Hot Micro-Strip + Ultrasonic

Rinse with IPA + DI water + dry N_2

Started: 17h15 Stoped: 20h

Total Time in Hot Micro-Strip : 2h45 Ultrassonic Time : 2 x 2min

Optical Inspection:

Sample	**Comments**
D6	OK

STEP 5	Diode deposition	Date: 01 / 09 / 2006

Equipment: UHV chamber
Responsible: J.P. Conde, V. Chu

200 °A p_+ doped a-Si:H + 5000 °A intrinsic a-Si:H + 200 °A n_+ doped a-Si:H by PECVD

Set points:

Material	Power	Gas Flow	Pressure	Time	Temperature
p+-a-Si:H	5WRF	SiH4+B2H6/N2 10+5sccm	0,1 Torr	200 s	250°C
i-a-Si:H	5WRF	SiH4 10sccm	0,1 Torr	1h 00min 50s	250°C
n+-a-Si:H	5WRF	SiH4+PH3 10+5sccm	0,1 Torr	200 s	250°C

Read values:

Material	Power	Gas Flow	Pressure	Time	Temperature
p+-a-Si:H	5 Wrf	10+5 sccm	100 mT	200s	250ºC
i-a-Si:H	5 Wrf	10 sccm	100 mT	1h 30s	250ºC
n+-a-Si:H	5 Wrf	10+5 sccm	100 mT	200s	250ºC

Comments:

Sample	**Comments**
D6	OK

STEP 6 **2nd Exposure –** Diode Definition Date: 04 / 09 / 2006

Coating PR: Vapor Prime 30 min (Recipe - 0) coat 1.5 μm PR (Recipe 6/2)

Machine: **DWL**

Mask: diodetempl2 (1), dtjt4l4 (2) Map: diode

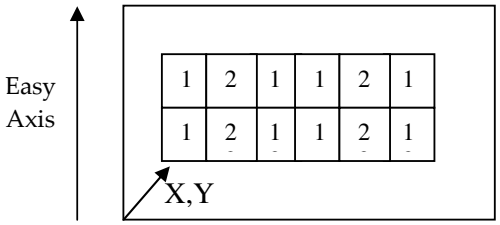

Origin: X = 6400 , Y = 6300

Energy : 60

Power : 120mW

Focus : -50

Develop : Recipe 6/2 Development time : 1 min
Optical Inspection:

Sample	Comments
D6	OK

STEP 7 **Diode stack definition** Date: 05 / 09 / 2006

Reactive ion etch

Diode Pillar etch by reactive ion etching (RIE)
Equipment: LAM Rainbow 4400

Process recipe: 6

Set points:

Power	Gas Flow	Pressure	Time
100 W (RF)	Ar+CF4+O2 200+100+10 sccm	140 mTorr	350 s

Read values:

Power	Gas Flow	Pressure	Time
100 W	200 + 100 + 10 sccm	140 mT	4 x 150s + 2 x 100s

Comments:

Sample	Comments
D6	OK

STEP 8	**Resist Strip**	Date: 05 / 09 / 2006

Hot Micro-Strip + Ultrasonic
Rinse with IPA + DI water + dry N_2

Started: 12h Stoped: 17h
Total Time in Hot Micro-Strip : 5h Ultrassonic Time : 2min

Optical Inspection:

Sample	Comments
D6	OK

STEP 9	**3rd Exposure –** Diode pad definition	Date: 05 / 09 / 2006

Coating PR: Vapor Prime 30 min (Recipe - 0) coat 1.5 μm PR (Recipe 6/2)

Machine: **DWL**

Mask: diodetempl3 (1), dtjt4l5 (2) Map: diode

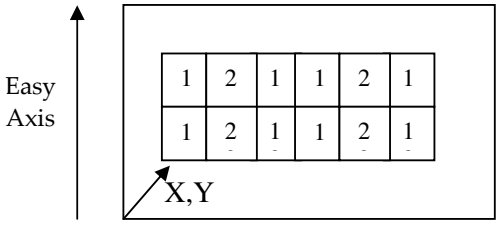

Or igin: X = 6400 , Y = 6300
Energy : 60

Power : 120mW

Focus : -50

Develop : Recipe 6/2 Development time : 1 min

Optical Inspection:

Sample	Comments
D6	Needed more 10s of revelations - OK

STEP 10	**Insulating Layer Deposition**	Date: 06 / 09 / 2006

Machine: **UHV2**
2h30 (2500A) 200W

Deposition Time	AlO_2 thickness	Ar gas flow	Pressure	Power Source
2h30 min	2500 A	45 sccm	2.6 mT	200 W

STEP 11	**Oxide Lift-Off**	Date: 06 / 09 / 2006

Hot μ-strip + ultrasonic
Rinse with IPA + DI water + dry N_2

Started: 12h Stoped: 20h25

Total Time in hot μ-strip : 8h25 Ultrasonic Time : 5 x 2min

Optical inspection:

Sample	Comments
D6	OK

STEP 12	**4th Exposure –** Diode top contact definition	Date: 07 / 09 / 2006

Coating PR: Vapor Prime 30 min (Recipe - 0) coat 1.5 μm PR (Recipe 6/2)

Machine: **DWL**

Mask: diodetempl4 (1), dtjt4l6 (2) Map: diode

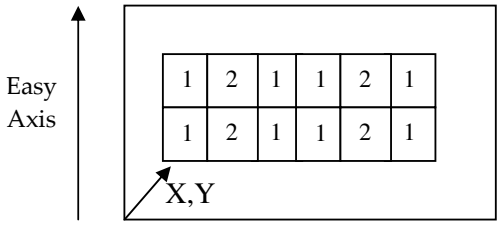

Origin: X = 6400 , Y = 6300

Energy : 60

Power : 120mW

Focus : -50

Develop : Recipe 6/2 Development time : 1 min
Optical Inspection:

Sample	Comments
D6	OK

STEP 13 Row (Diode contact) deposition Date: 07 / 09 / 2006

Machine: **Nordiko 7000**

Seq.48 (svpad) – mod.4 – f.1 (3000A Al, 1'20'') P=2 kW, 3mTorr, 50 sccm Ar

Readings – Module 4					
Run#	Pressure	Power	Voltage	Current	Gas Flux
11322	3.0 mT	2.0 kW	408 V	4.9 A	50.4 sccm

STEP 14 **Aluminum Lift-Off** Date: 07 / 09 / 2006

Hot μ-strip + ultrasonic
Rinse with IPA + DI water + dry N_2

Started: 11h45 Stoped: 19h45

Total Time in hot μ-strip : 8h Ultrasonic Time : 2 x 2min

Optical inspection:

Sample	Comments
D6	OK

STEP 15 **5th Exposure –** Sample full passivation Date: 08 / 09 / 2006

Coating PR: Vapor Prime 30 min (Recipe - 0) coat 1.5 μm PR (Recipe 6/2)

Machine: **DWL**

Mask: diodetempl5 (1), dtjt4l7 (2)

Map:

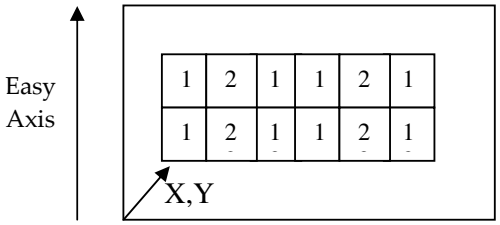

Ori gin: X = 6400 , Y = 6300
Energy : 60

Power : 120mW

Focus : -50

Develop : Recipe 6/2 Development time : 1 min
Optical Inspection:

Sample	Comments
D6	OK

STEP 16	**Passivation Layer Deposition**	Date: 09-10/09/2006

1- Al_2O_3 deposition

Machine: **UHV2**

B.P: 2.6 x 10^{-7} Torr

Deposition Time	Al_2O_3 thickness	Ar gas flow	Pressure	Power Source
1h30 min	1000 A	45 sccm	3.0 mT	200W

2- SiO_2 deposition

Machine: **Alcatel**

Deposition Time	SiO_2 thickness	Ar gas flow	Pressure	Power Source
1h28min	2000 A	20 sccm	3.9 mT	140 W

STEP 17	**Oxide Lift-Off**	Date: 10/ 09 /2006

Hot μ-strip + ultrasonic
Rinse with IPA + DI water + dry N_2

Started: 17h30 Stoped:21h00

Total Time in hot μ-strip : 3h30 Ultrasonic Time : 2 min

Optical inspection:

Sample	Comments
D6	OK

Appendix F

CURRICULUM VITAE

Name: Filipe Arroyo Cardoso
Address: Rua Forno do Tijolo nº46 5ºdto 1170-137 Lisboa-Portugal
Telephone: +351 938 407 433
E-mail: facardoso@gmail.com
Birthdate: 30/04/1982
Nationality: Portuguese and French

Skills and Competence

- **Main deposition techniques knowledge:**
  - Sputtering systems: deposition of magnetoresistive sensors (Spin Valves and Magnetic Tunnel junction with MgO barrier), deposition of metallic contacts and passivation layers (Oxides or Nitrides).
  - Ion Beam Deposition systems: deposition of magnetoresistive sensors (Spin Valves and Magnetic Tunnel Junctions with MgO and AlOx barriers).
  - Chemical Vapor Deposition system: deposition of oxide and nitride layers, deposition of amorphous silicon (intrinsic, p-doped and n-doped) for diodes fabrication.
- **Main microfabrication techniques knowledge:**
  - Photolithography using a direct write laser with a spot size of 800nm (mask design and laser usage).
  - Ion Beam milling
  - Reactive ion etching
  - Wet etching
- **Main characterization techniques knowledge:**
  - DC transport characterization of magnetoresistive sensors: magnetoresistance transfer curves, I-V curves, voltage breakdown measurements and TMR vs bias measurements
  - Low frequency spectroscopy: for magnetoresistive sensor and diode noise characterization, for signal analysis.
  - Vibrating Sample Magnetometer (VSM) measurement for magnetic material characterization (thin films and magnetic particles) and exchange bias optimization.
  - Lockin measurement technique applied to magnetoresistive biosensors.
- **Biological protocols knowledge:**
  - Surface chemistry protocols for DNA and proteins immobilization.
  - DNA labeling and hybridization protocols.

  - Protein labeling and cell recognition protocols.
  - Spotting of pL droplets with biological probes on different surfaces (glass, gold, PDMS...) using a non contact spotter (Nanoplotter, Gesim, Germany).

- **Microfluidics fabrication knowledge:**
  - Milling machine (CNC) for microfluidics channels molds and supports fabrication.
  - Microfluidics simulation, design, fabrication and testing.

- **Other knowledges:**
  - Magnetoresistive sensors simulations (materials simulations and magnetic particles detection).
  - Biochips design and microfabrication.

Education

- **2006 - Present: PhD in Physics Engineering**(defense on the 11th of February).
  Experimental work achieved at Instituto Nacional de Engenharia de Systemas e Computadores - Microsistemas & Nanotecnologias (INESC-MN, http://www.inesc-mn.pt) and degree awarded by Technical University of Lisbon in Instituto Superior Técnico (UTL-IST), Lisbon, Portugal. Thesis title: *Design optimization and integration of magnetoresistive biochips.*
  Advisor: Prof. Paulo Peixeiro Freitas
  Co-advisor: Prof. Moisés Piedade

  Projects participation during PhD
  - 2005 to 2007 - Biochip Project - national project sponsored by Portuguese Science Foundation.
  - 2005 to 2008 - SNIP2CHIP (NMP4-CT-2005-016833) - european project with the goal to make a further step toward lab-on-chip by integrating DNA extraction, on-chip PCR and detection modules.
  - 2005 to 2008 - Biomagsens (NMP4-CT-2005-017210)- european project with the goal to improve signal to noise ratio of magnetoresistive sensors.

- **2000-2005: 5 years degree (Licenciatura)** in Technologic and Physics Engineering (Engenharia Física Tecnológica), now equivalent to a MSc under Bologna Convention, awarded by UTL-IST with a final classification of 16 out of 20.
  MSC thesis title: *Magnetic tunnel junction matrix based biochips.*

Complementary education

- 22-26/06/2009 "10th Advanced Summer Course in Cell-Materials Interactions" - at Institute of molecular and cell biology (IMBC)- Faculdade de Engenharia da Universidade do Porto (FEUP).
- 31/03 e 1-2/04/2003 "Course in Software Engineering" - ESA European Space Agency - duration 27 hours
- 17 a 24/02/2001 "Introduction to astronomy course - level I" - Universidade de Lisboa, Museu de Ciência - duration 16 hours
- 1998 "Programming and analysis techniques course" - Fundação para a Divulgação das Tecnologias da Informação - duration 24 hours.

Scientific and associative experience

- 09-2003 to 08-2004 - Internship at LIP (Laboratory of Instrumentation and Experimental Particles Physics). Development of a wireless synchronization system based on the Global Positioning System (GPS).
- 18-08-2003 to 3-10-2003 - Summer internship at INESC-MN. Fabrication of a coil cooling controlling system for an annealing setup. Familiarization with Sputtering and Ion Beam Deposition systems from INESC-MN clean room.
- 2002 ro 2005 - Participation in SSETI (Student Space Exploration and Technology Initiative) project sponsored by ESA (European Space Agency). The goal of this project is to join the effort of students from different European universities to develop, fabricate and launch a micro-satellite (see http://www.sseti.org) - I was responsible for the AOCS (Attitude and Orbit Control System) simulation team. For this project participation, in November 2002, in a 1 week workshop at ESTEC-ESA in Noordwijk.
- 2001 to 2004 - Worked in Physics Students Association of IST (Instituto Superior Técnico). The goal of this association is to teach physics by simple physics experiments to general public, specially to scholar students. I participate in the organization of several events and was responsible for Astronomy section (2001/2002) and Magazine section (2002/2003)of the association.

Informatics skills

- Excel, Word, Powerpoint, LaTex.
- Programming languages: C, C++ e C#, assembly for PIC microcontrolers, mathematica

Linguistic aptitudes

- Portuguese and French: Mother tongues (15 years at the French school of Lisbon - *Lycée Français Charles Lepierre*).
- English: Proficient
- Spanish: Basic

Other interests

- Sports practiced: swimming/waterpolo, cycling, climbing
- Reading, photography.
- Bicycle traveling: performed a 3 month bicycle journey from Lisbon (Portugal) to Bethlehem (Israel). Cycled 6200 kms and passed by 12 different countries. (http://www.travelpod.com/travel-blog/fcardoso/1/tpod.html)

List of Publications

- **Book chapters**:
  - P.P. Freitas, R. Ferreira, S. Cardoso and F. Cardoso, "Magnetoresistive sensors" *J. Phys: Condens. Matter* **19**, 165221 (2007) (Special Issue).
  - P.P. Freitas, H.A. Ferreira, F. Cardoso, S. Cardoso, R. Ferreira, J. Almeida, A. Guedes, V. Chu, J.P. Conde, V. Martins, L. Fonseca, J.S. Cabral, J. Germano, L. Sousa, M. Piedade, B. Silva, J.M. Lemos, L.A. Clarke and M.D. Cabral, "Chapter 1: Nanotechnology and the detection of biomolecular recognition using magnetoresistive transducers", in book *A portrait of State-of-the-Art Research at the Technical University of Lisbon*, ed. Springer (2006).
- **Peer reviewed scientific journals**:
  - M. Donolato, E. Sogne, B.T. Dalslet, M. Cantoni, D. Petti, J. Cao, F. Cardoso, S. Cardoso, P.P. Freitas, M.F. Hansen, R. Bertacco, "On-chip measurement of the Brownian relaxation frequency of magnetic beads using magnetic tunneling junctions ", *Appl. Phys. Lett.* (submitted) (2011).
  - R. Macedo, F.A. Cardoso, S. Cardoso, P.P. Freitas, J. Germano, M.S. Piedade, "Self powered, Hybrid Antenna-Magnetoresistive Sensor for Magnetic Field Detection", *Appl. Phys. Lett.* (submitted) (2011).
  - V.C. Martins, J. Germano, F.A. Cardoso, J. Loureiro, S. Cardoso, L. Sousa, M. Piedade, L.P. Fonseca, P.P. Freitas, "Challenges and trends in the development of a magnetoresistive biochip portable platform", *J. Magnetism and Magnetic Materials* **332**, 1655-1663 (2010).

- P.A.C. Lopes, J. Germano, T.M. Almeida, L.A. Sousa, M.S. Piedade, F.A. Cardoso, H.A. Ferreira and P.P. Freitas, "Measuring and extraction of biological information on new handheld biochip-based microsystem", *IEEE Trans. on Inst. and Meas.* **vol.59**, no. 1, 56-62 (2010).
- T.M. Almeida, M.S. Piedade, L.A. Sousa, J. Germano, P.A.C. Lopes, F.A. Cardoso and P.P. Freitas, "On the modeling of new tunnel junction magnetoresistive biosensors", *IEEE Trans. Inst. Meas.* **vol.59**, no. 1, 92-99 (2010).
- V.C. Martins, F.A. Cardoso, P.P. Freitas, L.P. Fonseca, "Picomolar detection limit on a magnetoresistive biochip after optimization of a thiol-gold based surface chemistry", *J. Nanosci. Nanotechnol.* **10(9)**, 5994-6002, (2010).
- V.C. Martins, F.A. Cardoso, J. Germano, S. Cardoso, L. Sousa, M. Piedade, P.P. Freitas, L.P. Fonseca, "Femtomolar limit of detection with a magnetoresisitive biochip", *Biosens. and Bioelectron.* **24**, 2690-2695 (2009).
- J. Germano, V.C. Martins, F.A. Cardoso, T.M. Almeida, L. Sousa, P.P. Freitas and M.S. Piedade, "A portable and autonomous magnetic detection platform for biosensing", *Sensors* **9**, 4119-4137 (2009).
- F.A. Cardoso, J. Germano, R. Ferreira, S. Cardoso, V.C. Martins, P.P. Freitas, M.S. Piedade and L. Sousa, "Detection of 130 nm magnetic particles by a portable electronic platform using spin valve and magnetic tunnel junction sensors", *J. Appl. Phys.* **103**, 07A310 (2008).
- F.A. Cardoso, R. Ferreira, S. Cardoso, J.P. Conde, V. Chu, P.P. Freitas, J. Germano, T. Almeida, L. Sousa and M.S. Piedade, "Noise Characteristics and particle detection limits in diode+MTJ matrix elements for biochip applications", *IEEE Trans. Magn.* **43**, no.6, 2403-2405 (2007).
- M. Piedade, L.A. Sousa, T.M. Almeida, J. Germano, B.A. Costa, J.M. Lemos, P.P. Freitas, H.A. Ferreira anf F.A. Cardoso, "A new hand-held microsystem architecture for biological analysis", *IEEE Trans. on circuits and systems - I: regular papers* **53**, no. 11, 2384 - 2395 (2006).
- F.A. Cardoso, H.A. Ferreira, J.P. Conde, V. Chu, P.P. Freitas, D. Vidal, J. Germano, L. Sousa, M.S. Piedade, B.A. Costa, J.M. Lemos, "Diode/MTJ cell for fully-scalable matrix-based biochip", *J. Appl. Phys.* **99**, 08B307 (2006).
- H.A. Ferreira, F.A. Cardoso, R. Ferreira, S. Cardoso and P.P. Freitas, "'Magnetoresistive DNA chips based on ac field focusing of magnetic labels", *J. Appl. Phys.* **99**, 08P105 (2006).

- **Conference papers**:

  - F.A. Cardoso, V.C. Martins, L.P. Fonseca, J. Germano, L.A. Sousa, M.S. Piedade, P.P. freitas, "Spintronic microfluidic platform for biomedical and environmental applications", *Proceedings of the SPIE* **volume 7653**, pp. 765306-765309 (2010).

- V.C. Martins, F.A. Cardoso, J. Loureiro, M. Mercier, J. Germano, S. Cardoso, R. Ferreira, L.P. Fonseca, L. Sousa, M.S. Piedade and P.P. Freitas, "Integrated spintronic platforms for biomolecular recognition detection", *AIP Conf. Proceedings.* **volume 1025**, pp 150-175 (2008).
- P.A.C Lopes, J. Germano, T.M. Almeida, L. Sousa, M.S. Piedade, F. Cardoso, H. Ferreira, P. Freitas, "A new handheld biochip-based microsystem", *In International Symposium on Circuits nd Systems (ISCAS 2007), IEEE*, 2379-2382 (2007).
- L. Sousa, M. Piedade, J. Germano, T. Almeida, P. Lopes, F. Cardoso, P Freitas, "Generic Aschitecture Designed for Biomedical Embedded Systems", *Embedded system design: topics, techniques and trends* **231**, 353-362 (2007).
- T.M. Almeida, M.S. Piedade, J. Germano, P.A.C. Lopes, L. Sousa, F. Cardoso, H. Ferreira, P. Freitas, "Measurements and modelling of a magnetoresistive biosensor", *In BIOCAS 2006 - Biomedical Circuits and Systems Conference, IEEE*, 41-44 (2006)
- P.A.C. Lopes, J. Germano, T.M. Almeida, L. Sousa, M.S. Piedade, F. Cardoso, H. Ferreira, P. Freitas, "Techniques to the determination of biological expression signals on a new handheld biochip-based microsystems", *In BIOCAS 2006 - Biomedical Circuits and Systems Conference, IEEE*, 57-60 (2006)

Conferences

- 55td Conference on Magnetism and Magnetic Materials 14 - 18 November 2010, Atlanta, Georgia - Oral presentation BG-06: "Effect of magnetostatic fields from magnetoresistive sensors on the position of superparamagnetic particles" F. A. Cardoso and P. P. Freitas.
- 11th Joint MMM-Intermag Conference 18 - 22 January 2010, Washington, DC - Oral presentation AH-05: "Optimization of Magnetic Tunnel Junction for detection of magnetic particles" F. A. Cardoso, R. Ferreira, S. Cardoso, V. C. Martins, P. P. Freitas.
- 13th MicroTAS conference 1 - 5 November 2009, Jeju, South Korea - Poster presentation: "Integrated magnetoresistive platform for biomolecular recognition" F.A. Cardoso, J. Germano, V.C. Martins, S. Cardoso, L.A. Sousa, M.S. Piedade, P.P. Freitas.
- Nanospain 2008 14 - 18 April 2008, Braga, Portugal - Poster presentation: "Increasing the sensitivity of magnetoresistive-based biochips" F. A. Cardoso, S. Cardoso, V. C. Martins, P. P. Freitas.
- Intermag 2008 4 - 8 May 2008, Madrid, Spain - Oral presentation FE-07: "MTJ based biosensor with top Au electrodes and functionalization layers" F. A. Cardoso, S. Cardoso, V. C. Martins, P. P. Freitas.
- 52nd Conference on Magnetism and Magnetic Materials 5 - 9 November 2007, Tampa, Florida - Oral presentation AE-03: "Detection limit of 130 nm magnetic particles using spin valve and magnetic tunnel junction sensors" F. A. Cardoso, R. Ferreira, S. Cardoso, V. C. Martins, P. P. Freitas, J. Germano, M. S. Piedade, L. Sousa.

- 10th Joint MMM/Intermag Conference 7 - 11 January 2007, Baltimore, MD - Oral presentation GF-03: " Noise characteristic of Diode+MTJ matrix elements for biochip applications" F.A.Cardoso, R.Ferreira, S. Cardoso, J.P.Conde, V.Chu, P.P.Freitas, J. Germano, T. Almeida, L.Sousa, M.S.Piedade.

- 50th MMM conference 2005 (29/09/05 to 3/10/05) - Oral Presentation DD-04: "Portable 16x16 Diode/MTJ bioarray microsystem for DNA/cell recognition" F.A.Cardoso, H.A.Ferreira, J.P.Conde, V.Chu, P.P.Freitas, D.Vidal , J. Germano, L.Sousa, M.S.Piedade, B.Andrade, J.M.Lemos.

Bibliography

[1] M. Schena, D. Shalon, R.W. Davis, P.O. Brown, *Science* **270(5235)**, 467-470 (1995)

[2] D.J. Lockhart, H.L. Dong, M.C. Byrne, M.T. Folletie, M.V. Gallo, M.S. Chee, M. Mittmann, C.W. Wang, M. Kobayashi, H. Horton, E.L. Brown, *Nature biotechnol.* **14 (13)**, 1675-1680 (1996).

[3] J.M Bartlett and D. Stirling (eds.), *"PCR protocols"*, Springer (2003), ISBN 978-0-89603-642-0.

[4] F. Fixe, D.M.F. Prazeres, V. Chu and J.P. Conde, *Nucl. Acids Res.* **32**, e70 (2004).

[5] L.A. Pinnaduwage, V. Boiadjiev, J.E. Hawk and T. Thundatm *Appl. Phys. Lett.* **83**, 1471-1473 (2003).

[6] R. McKendry, J. Zhang, Y. Arntz, T. Strunz, M. Hegner, H.-P. Lang, M.K. Baller, U. Certa, H.J. Guntherodt and C. Gerber, *Proc. Natl. Acad. Sci. USA* **99**, 9783 (2002).

[7] D.R. Baselt, G.U. Lee, M. Natesan, S.W. Metzger, P.E. Sheehan and R.J. Colton, *Biosens. and Bioelectron.* **13**, 731-739 (1998).

[8] J. C. Rife, M. M. Miller, P. E. Sheehan, C. R. Tamanha, M. Tondra, and L. J. Whitman, *Sens. Actuat. A* **107**, 209 (2003).

[9] J. Schotter, P.B. Kamp, A Becker, A. Pühler, G Reiss, and H. Brückl, *Biosens. Bioelectron.* **19**, 1149 (2004).

[10] H.A. Ferreira, D.L. Graham, N. Feliciano, L.A, Clarke, M.D. Amaral, P.P. Freitas *IEEE Trans. Magn.* **41**, 4140-4142 (2005).

[11] D.L. Graham, H. Ferreira, J. Bernardo, P.P Freitas, J.M.S. Cabral *J. Appl. Phys.* **91**, 7786-7788 (2002).

[12] G. Li, S. Sun, R.J. Wilson, R.L. White, N. Pourmand and S.X. Wang, *Sens. Actuators A* **126**, 98-106 (2006).

[13] L. Ejsing, M. F. Hansen, A. K. Menon, H. A. Ferreira, D. L. Graham, and P. P. Freitas, *Appl. Phys. Lett.* 84, 4729-4731 (2004).

[14] W. Shen, X. Liu, D. Mazumdar, and G. Xiao, *Appl. Phys. Lett.* 86, 253901 (2005).

[15] B.M. de Boer, J.A.H.M. Kahlman, T.P.G.H. Jansen, H. Duric, J. Veen, *Biosens. and Bioelectron.* **22**, 2366-2370 (2007).

[16] V.C. Martins, J. Germano, F.A. Caroso, J. Loureiro, S. Cardoso, L. Sousa, M. Piedade, L.P. Fonseca and P.P. Freitas, *J. Magn. Magn. Mater.* **322**, 1655-1663 (2010).

[17] D.A. Hall, R.S. Gaster, T. Lin, S.J. Osterfeld, S. Han, B. Murmann and S.X. Wang, *Biosens. and Bioelectron.* **25**, 2051-2057 (2010).

[18] Ricardo Alves Ferreira Costa e Sousa, *"Magnetic Random Access Memory (MRAM) based on Spin Dependent Tunnel Junction"*, Ph.D. thesis, Instituto Superior Técnico, 2002.

[19] Ricardo Alexandre de Matos Antunes Ferreira, *"Ion Beam Deposited Magnetic Spin Tunnel Junctions targeting HDD Read Heads, Non-volatile Memories and Magnetic Field Sensor Applications"*, PhD Thesis, Instituto Superior Técnico, 2008.

[20] Susana Isabel Pinheiro Cardoso de Freitas, *"Dual-Stripe GMR and Tunnel Junction Read Heads and Ion Beam Deposition and Oxidation of Tunnel Junctions"*, PhD Thesis, Instituto Superior Técnico, 2002.

[21] Hugo Alexandre Teixeira Duarte Ferreira, *"Detection of biomolecular recognition and On-chip transport of magnetically labeled biomolecules"*, PhD Thesis, Instituto Superior Técnico, 2006.

[22] P. P. Freitas, H. A. Ferreira, D. L. Graham, L. A. Clarke, M. D. Amaral, V. Martins, L. Fonseca, and J. M. S. Cabral, in *Magnetoelectronics*, edited by M. Johnson (Academic Press, New York, 2004).

[23] H.A. Ferreira, N. Feliciano, D.L. Graham and P.P. Freitas *J. Appl. Phys.* **97**, 10Q904 (2005).

[24] J. Loureiro, R. Ferreira, S. Cardoso, P.P. Freitas, J. Germano, C. Fermon, G. Arrias, M. Pannetier-Lecoeus, F. Rivadulla and J. Rivas, *Appl. Phys. Lett.* **95**, 034104 (2009).

[25] M. Megens, F. de Theije, B. de Boer, F. van Gaal, *J. Appl. Phys.* **102**, 014507 (2007).

[26] G. Li, H. Yu, M.S. Akhras, S.-J. Han, S. Osterfeld, R.L. White, N. Pourmand and S.X. Wang, *Biosens. and Bioelectron.* **24**, 99-103 (2008).

[27] D. L. Graham, H. A. Ferreira, and P. P. Freitas, *Trends Biotechnol.* 22, 455 (2004).

[28] H.N. Bertram, *Theory of magnetic recording*, Cambridge University Press, Boston.

[29] I.C. Perdigão, *"Optimization of magnetic tunnel junction linear response for sensor applications"*, Master Thesis, Instituto Superior Técnico, 2009.

[30] M.N. Baibich, J.M. Broto, A. Fert, F.N. Van Dau, *Phys. Rev. Lett.* **61**, 2472-2475 (1988).

[31] B. Dieny, V.S. Speriosu, S. Metin, S.S. Parkin, B.A. Gurney, P. Bumgart and D.R. Wilhoit, *J. Appl. Phys.* **69**, 4774-4779 (1991).

[32] D.E. Heim, R.E. Fontana, C. Tsang, V.S. Speriosu, B.A. Gurney and M.L. Williams, *IEEE Trans. Magn.* **30**, 316-321 (1994).

[33] D. Burgler and P. Grunberg, in *Nanoelectronics and Information Tehnology.* R. Waser (Ed.), Wiley-VCH, Weinheim, Germany.

[34] P.P. Freitas, H.A. Ferreira, R. Ferreira, S. Cardoso, S. van Dijken and J. Gregg in *Advanced Magnetic Nanostructures* D. Sellmyer and R. Skomski (Eds.), Springer, Berlin, pp. 403-460.

[35] D. Craik *"Magnetism: Principles and applications"*, Wiley (1995).

[36] R. Engel-Herbert and T. Hesjedal, *J. Appl. Phys.* **97**, 074504 (2005).

[37] J. Slonczewshi, *Appl. Phys. Lett.* 39, 6995-7002 (1989)

[38] J.S. Moodera and G. Mathon , *J. Magn. Magn. Mater*, 248-273 (1999)

[39] W.H. Buttler, X-G Zhang, T.C. Schulthess, and J.M. MacLaren, *Phys. Rev. B* **63**, 054416 (2001).

[40] A. Fukushima, Y. Suzuki, S. Yuasa, T. Nagahama and K. Ando, *Nature Materials* **3**, 868 (2004).

[41] S. Parkin, C. Kaiser, A. Panchula, P.M. Rice, B. Hughes, M. Samant and S-H Yang, *Nature Materials* **3**, 862 (2004).

[42] J. Hayakawa, *Appl. Phys. Lett.* **89**, 232510 (2006).

[43] J.C. Simmons, *J. Appl. Phys.*, **34**, 1793 (1963).

[44] J.C. Simmons, *J. Appl. Phys.*, **34**, 2581 (1963)

[45] P.P. Freitas, R. Ferreira, S. Cardoso and F. Cardoso, *J. Phys.: Condens. Matter* **19** 165221, 2007.

[46] Q.A. Pankhurst, J. Connolly, S.K. Jones and J. Dobson, *J. Phys. D: Appl. Phys.* **36**, 167-181 (2003).

[47] I. Safarik and M. Safarikova, *Monatshefte fur Chemie* **133**, 737-759 (2002).

[48] S.E. Barry, *Int. J. Hyperthermia* **24 (6)**, 451-466 (2008).

[49] V.F. Puntes, W.J. Parak and A.P. Alivisatos, *Europeans cells and materials* **vol. 3**, suppl. 2, 128-131 (2002).

[50] NGAP NP FeO-2204-W particles, http://www.nanogap.es

[51] C.C. Berry and A.S.G. Curtiss, *J. Phys. D: Appl. Phys.* **36**, 198-206 (2003).

[52] C. Albon, A. Weddemann, A. Auge, K. Rott and A. Hutten, *Appl. Phys. Lett.* **95**, 023101 (2009).

[53] G. Li, S. Sun and S.X. Wang, *J. Appl. Phys.* **99**, 08P107 (2006).

[54] G. Li and S.X. Wang, *IEEE trans. Magn.* **40**, 4 (2004).

[55] F. N. Hooge and A. M. H. Hoppenbrouwers, "1/f noise in continuous gold films", **Physica 45**, 386 (1969)

[56] L. Jiang, E. R. Nowak, P. E. Scott, J. Johnson, J. M. Slaughter, J. J. Sun and R. W. Dave, "Low-frequency magnetic and resistance noise in magnetic tunnel junctions", *Phys. Rev. B* **69**, 054407 (2004)

[57] R. C. Sousa, P. P. Freitas, V. Chu, and J.P. Conde, *IEEE Trans. Magn.* **35**, 2832-2834 (1999).

[58] *Physics of Semiconductor Devices*, Michael Shur

[59] R.A. Street, *Hydrogenated amorphous silicon*, Cambidge Solid State Science Series, Cambridge University press (1991).

[60] R. Ferreira, P. P. Freitas, J. Langer, B. Ocker and W. Maass, *J. Appl. Phys.* **99**, 08K706, (2006).

[61] S.Cardoso, V.Gehanno, R.Ferreira, and P.P.Freitas, *IEEE Trans. Magn.* **35**, 2952, (1999)

[62] E. Oosterbroek and A. van den Berg (eds.), *Lab-on-a-Chip: Miniaturized systems for (bio)chemical analysis and synthesis*, Elsevier Science, second edition (2003).

[63] J. Berthier and P. Silberzan, *Microfluidics for biotechnology*, Artech House, (2006).

[64] L. Xu, H. Yu, M. S. Akhras, S. J. Han, S. Osterfeld, R. L. White, N. Pourmand, and S. X. Wang, *Biosens. Bioelectron.* **24**, 99 (2008).

[65] M. J. Heller, *Annual Review of Biomedical Engineering* **4**, 129(2002).

[66] W. Kusnezow and J. D. Hoheisel, *J. Mol. Recognition* **16**, 165 (2003).

[67] D. Goncalves, D. M. F. Prazeres, V. Chu, and J. P. Conde, *Biosens. Bioelectron.* **24**, 545 (2008).

[68] J. Fritz, M. K. Baller, H. P. Lang, H. Rothuizen, P. Vettiger, E. Meyer, G. J, uuml, H. ntherodt, C. Gerber, and J. K. Gimzewski, *Science* **288**, 316 (2000).

[69] M. Megens and M. Prins, *J. Magn. Magn. Mater.* **293**, 702 (2005).

[70] A. Kumar, O. Larsson, D. Parodi, and Z. Liang, *Nucleic Acids Res.* **28** (2000).

[71] X. Zhou, E. LeProust, H. Zhang, P. Yu, and X. Gao, *Nucleic Acids Res.* **29**, 2171 (2001).

[72] J. P. Cloarec, N. Deligianis, J. R. Martin, I. Lawrence, E. Souteyrand, C. Polychronakos, and M. F. Lawrence, *Biosens. and Bioelectron.* **17**, 405 (2002).

[73] R. Möller, A. Csáki, J. M. Köhler, and W. Fritzschea, *Nucleic Acids Res.* **28** (2000).

[74] J. Zhou and D. O. Wipf, *J. Electroanal. Chemistry* **499**, 121 (2001).

[75] A. B. Steel, R. L. Levicky, T. M. Herne, and M. J. Tarlov, *Biophys. Journ.* **79**, 975 (2000).

[76] R. L. De Palma, Chengxun; Barbagini, Francesca; Reekmans, Gunter; Bonroy, Kristien; Laureyn, Wim; Borghs, Gustaaf; Maes, Guido, *The Journal of Physical Chemistry C* **111**, 12227 (2007).

[77] T. M. Herne and M. J. Tarlov, *J. Am. Chem. Soc.* **119**, 8916 (1997).

[78] I. S. Park and N. Kim, *Biosens. Bioelectron.* **13**, 1091 (1998).

[79] A. W. Peterson, R. J. Heaton, and R. M. Georgiadis, *Nucleic Acids Research* **29**, 5163 (2001).

[80] S. Sivasankar, S. Subramaniam, and D. Leckband, *Proceedings of the National Academy of Sciences of the United States of America* **95**, 12961 (1998).

[81] X. Li, L. Jiang, Q. Zhan, J. Qian, and S. He, *Colloids and Surfaces A: Physicochemical and Engineering Aspects* **332**, 172 (2009).

[82] A. Holmberg, A. Blomstergren, O. Nord, M. Lukacs, J. Lundeberg, and M. Uhlén, *Electrophoresis* **26**, 501 (2005).

[83] J. Germano, V.C. Martins, F.A. Cardoso, T.M. Almeida, L. Sousa, P.P. Freitas and M. S. Piedade, *Sensors* **9**, 4119-4137 (2009).

[84] P.A.C. Lopes, J. Germano, T.M. Almeida et al., in *ISCAS IEEE*, 2379-2382 (2007).

[85] A.L. Ghindilis, M.W. Smith, K.R. Schwarzkopf, K.M. Roth, K.Peyvan, S.B. Munro, M.J. Lodes, A.G. Stover, K. Bernards, K. Dill, A. McShea, *Biosens. Bioelectron.* **22**, 1853-1860 (2007).

[86] T.A. Taton, C.A. Mirkin, and R.L. Letsinger, *Science* **289**, 1757-1760 (2000).

[87] J.J. Storhoff, S.S. Marla, P. Bao, S. Hagenow, H. Mehta, A. Lucas, V. Garimella, T. Patno, W. Buckingham, W. Cork, and U.R. Muller *Biosens. Bioelectron.* **19**, 875-883 (2004).

[88] M. Su, S. Li, and V.P. Dravida *Appl. Phys. Lett.* **82**, 3562-3564 (2003).

[89] L.B. Nie, Y. Yang, S. Li, N.Y. He, *Nanotechnology* **18**, 305501 (2007).

[90] J. Wang, G. Liu, A. Merkoçi, *Anal. Chim. A.* **482**, 149-155 (2003).

[91] P. Rijiravanich, M. Somasundrum, W. Surareungchai *Anal. Chem.* **80**, 3904-3909 (2008).

[92] M. Ozsoz, A. Erdem, K. Kerman, D. Ozkan, B. Tugrul, N. Topcuoglu *Anal. Chem.* **75**, 2181-2187 (2003).

[93] R.L. Edelstein, C.R. Tamanaha, P.E. Sheehan, M.M. Miller, D.R. Baselt, L.J. Whitman, R.J. Colton *Biosens. Bioelectron.* **14**, 805-813 (2000).

[94] M.M. Miller, P.E. Sheehan, R.L. Edelstein, C.R. Tamanaha, L. Zhong, S. Bounnak, L.J. Whitman, R.J. Colton, *J. Magn. Magn. Mater.* **225**, 138-144 (2001).

[95] S.X. Wang, S. Bae, G. Li, S. Sun, R.L. White, J.T. Kemp, C.D. Webb *J. Magn. Magn. Mater.* **293**, 731-736 (2005).

[96] D.L. Graham, H.A. Ferreira, P.P. Freitas, J.M.S. Cabral *Biosens. Bioelectron.* **18**, 483-488 (2003).

[97] F.A. Cardoso, H.A. Ferreira, J.P. Conde, V. Chu, P.P. Freitas, D. Vidal, J. Germano, L. Sousa, M.S. Piedade, B.A. Costa, J.M. Lemos *J. Appl. Phys.* **99**, 08B307 (2006).

[98] F.A. Cardoso, J. Germano, R. Ferreira, S. Cardoso, V.C. Martins, P.P. Freitas, M.S. Piedade, L. Sousa *J. Appl. Phys.* **103**, 07A310 (2008).

[99] H.A. Ferreira, N. Feliciano, D.L. Graham, L.A. Clarke, M.D. Amaral, P.P. Freitas *Appl. Phys. Lett.* **87**, 013901 (2005).

[100] K. Pappaert, P. Van Hummelen, J. Vanderhoeven, G.V. Baron, G. Desmet *Chem. Eng. Science* **58**, 4921-4930 (2003).

[101] H.A. Ferreira, F.A. Cardoso, R. Ferreira, S. Cardoso and P.P. Freitas *J. Appl. Phys.* **99**, 08P105 (2006).

[102] D.L. Graham, H.A. Ferreira, N. Feliciano, P.P. Freitas, L.A. Clarke, M.D. Amaral *Sens. Actuators B* **107**, 936-944 (2005).

[103] R.L. Millen, T. Kawaguchi, M.C. Granger, M.D. Porter *Anal. Chem.* **77**, 6581-6587 (2005).

[104] R. De Palma, G. Reekmans, W. Laureyn, G. Borghs, G. Maes *Anal. Chem.* **79**, 7540-7548 (2007).

[105] V.C. Martins, F.A. Cardoso, J. Germano, S. Cardoso, L. Sousa, M. Piedade, P.P. Freitas and L.P. Fonseca *Biosens. Bioelectron.* **24**, 2690-2695 (2009).

[106] C.R. Tamanaha, S.P. Mulvaney, J.C. Rife, L.J. Whitman *Biosens. Bioelectron.* **24**, 1-13 (2008).